Tada, R., Murray, R.W., Alvarez Zarikian, C.A., and the Expedition 346 Scientists
Proceedings of the Integrated Ocean Drilling Program, Volume 346

Site U1425[1]

R. Tada, R.W. Murray, C.A. Alvarez Zarikian, W.T. Anderson Jr., M.-A. Bassetti, B.J. Brace, S.C. Clemens, M.H. da Costa Gurgel, G.R. Dickens, A.G. Dunlea, S.J. Gallagher, L. Giosan, A.C.G. Henderson, A.E. Holbourn, K. Ikehara, T. Irino, T. Itaki, A. Karasuda, C.W. Kinsley, Y. Kubota, G.S. Lee, K.E. Lee, J. Lofi, C.I.C.D. Lopes, L.C. Peterson, M. Saavedra-Pellitero, T. Sagawa, R.K. Singh, S. Sugisaki, S. Toucanne, S. Wan, C. Xuan, H. Zheng, and M. Ziegler[2]

Chapter contents

Background and objectives

Integrated Ocean Drilling Program (IODP) Site U1425 is in the central part of the marginal sea surrounded by the Japanese Islands, the Korean Peninsula, and the Eurasian continent at 39°29.44′N, 134°26.55′E and 1909 meters below sea level (mbsl). The site is situated in the central part of a northeast-southwest–oriented graben in the middle of the Yamato Bank. Site U1425 is ~60 km southwest of Ocean Drilling Program (ODP) Site 799, which also sits within the graben (Fig. **F1**). A major difference between these two sites is that Site 799 is located in the deepest part of the graben and Site U1425 is situated on a terrace that is one step higher than the bottom of the graben (Fig. **F2**). The higher topographic setting of Site U1425 was chosen to minimize the influence of turbidites, which were numerous at Site 799.

Site U1425 is the northernmost site of the southern half of the latitudinal transect targeted by IODP Expedition 346 and the middepth site of the depth transect. Preliminary site survey results suggested that Site U1425 was characterized by very slow yet continuous sedimentation (4 cm/k.y.) during the last 600 k.y., which is ideal for detecting the contribution of eolian dust from the Asian continent. Based on the relatively low geothermal gradient of ~100°C/km (observed at nearby Site 799), the opal-A/opal-CT boundary at Site U1425 was predicted to be at ~400 m core depth below seafloor (CSF-A) (see the **"Methods"** chapter [Tada et al., 2015b]) (Ingle, Suyehiro, von Breymann, et al., 1990). At this site, we expected to recover unconsolidated sediment back to 10 Ma or older, permitting reconstruction of eolian dust flux and provenance changes over this period. In combination with other sites in the marginal sea, it will be possible to reconstruct changes in the position of the atmospheric Westerly Jet stream axis during the last ~5 m.y.

Site U1425 is located on the Subpolar Front in the marginal sea and is under the influence of the first branch of the Tsushima Warm Current (TWC) during summer. Sediment from Site U1425 will be used to reconstruct sea-surface temperature changes associated with the north–south movement of the Subpolar Front, which is considered to be influenced by the strength of the TWC (Isoda, 2011). In addition, the sea ice margin may have reached the site location during glacial periods, and the sedimentary record at this site will help constrain the southern limit of ice-rafted debris events. Together with results from IODP Sites U1422–

[1] Tada, R., Murray, R.W., Alvarez Zarikian, C.A., Anderson, W.T., Jr., Bassetti, M.-A., Brace, B.J., Clemens, S.C., da Costa Gurgel, M.H., Dickens, G.R., Dunlea, A.G., Gallagher, S.J., Giosan, L., Henderson, A.C.G., Holbourn, A.E., Ikehara, K., Irino, T., Itaki, T., Karasuda, A., Kinsley, C.W., Kubota, Y., Lee, G.S., Lee, K.E., Lofi, J., Lopes, C.I.C.D., Peterson, L.C., Saavedra-Pellitero, M., Sagawa, T., Singh, R.K., Sugisaki, S., Toucanne, S., Wan, S., Xuan, C., Zheng, H., and Ziegler, M., 2015. Site U1425. *In* Tada, R., Murray, R.W., Alvarez Zarikian, C.A., and the Expedition 346 Scientists, *Proc. IODP,* 346: College Station, TX (Integrated Ocean Drilling Program). doi:10.2204/iodp.proc.346.106.2015

[2] **Expedition 346 Scientists' addresses.**

U1424, Site U1425 will enable us to reconstruct temporal changes in the southern limit of sea ice in the marginal sea during the last 4 m.y. Lastly, we will reconstruct changes in deepwater oxygenation and calcium carbonate compensation depth (CCD) during the last 4 m.y. by combining results from the Expedition 346 depth transect sites.

Operations

Site U1425 (proposed Site Y-1) was occupied at two different times during Expedition 346, first following operations at Site U1424 on 28 August 2013 and then ~3 weeks later after revisiting IODP Site U1427 on 24 September (see below) to acquire additional material for postcruise studies. The return to Sites U1425 and U1427 was possible because all scientific and operations objectives were met ~5 days before the end of the expedition; therefore, the remaining time available was spent reoccupying these two important sites drilled earlier in the expedition. We drilled Hole U1425E during the revisit.

Four holes were cored at Site U1425 using the full and half advanced piston corer (APC) and the extended core barrel (XCB) (Table **T1**; see also Fig. **F2** in the "Expedition 346 summary" chapter [Tada et al., 2015a]). Hole U1425A was cored to 9.5 m CSF-A, Hole U1425B was cored to 407.2 m CSF-A, Hole U1425C was cored to 25 m CSF-A, Hole U1425D was cored to 427 m CSF-A, and Hole U1425E was drilled 3 weeks later to 113.1 m CSF-A. A total of 148 cores obtained 955.5 m of sediment (97% recovery). The advanced piston corer temperature tool (APCT-3) was deployed four times.

Transit from Site U1424

The 180 nmi distance between Sites U1424 and U1425 was covered in 17.6 h at an average speed of 10.2 kt. The sea passage ended at 0230 h on 28 August 2013. The vessel was maneuvered over the location coordinates, thrusters were lowered into position, and the vessel was turned over to dynamic positioning control. By 0300 h, the vessel was stabilized for rig floor operations to begin.

Hole U1425A

A three-stand APC/XCB bottom-hole assembly (BHA) was assembled, and the drill string was run to the bottom. After picking up the top drive and spacing out the drill string to 1911.4 meters below rig floor (mbrf) (6 m above the observed seafloor depth on the ship's precision depth recorder), an APC core barrel was deployed. The first core barrel was recovered empty. The bit was repositioned 10 m lower at 1901.4 mbrf for the second attempt. Hole U1425A was started at 0905 h on 28 August 2013. This time, however, the core barrel was recovered full, once again missing a reliable seafloor determination.

Hole U1425B

The ship was offset 15 m north, a new APC core barrel was deployed, and the bit was positioned at 1918.4 mbrf. Hole U1425B was spudded at 1005 h on 28 August 2013, establishing a seafloor depth of 1919.1 mbrf. APC/XCB coring continued to a final depth of 407.2 m CSF-A, the scientific target depth for this site. Coring operations in Hole U1425B consisted of 28 full APC cores, 23 half APC cores, and 10 XCB cores. We recovered 397.25 m of core (98%). Three successful temperature measurements were taken using the APCT-3 temperature shoe on Cores 346-U1425B-4H, 7H, and 10H (37.3, 65.8, and 94.3 m CSF-A, respectively). The hole was circulated clean, the logging tools were moved forward to the rig floor, the top drive was set back, and the drill string was pulled to a logging depth of 80 meters below seafloor (mbsf). At 1115 h on 30 August, preparations for wireline logging were initiated. The paleo combo tool string was deployed to the bottom of the hole to 403.2 m WSF (see the **"Methods"** chapter [Tada et al., 2015b]) and recorded spectral gamma ray, caliper, magnetic susceptibility, resistivity, and lithologic density logs. The second string consisted of the Formation MicroScanner (FMS)-sonic tool string, which recorded resistivity images of the borehole, caliper, sonic velocities, and natural gamma radiation (NGR) data. The FMS-sonic string reached 396.5 m WSF, 10.5 m off the bottom of the hole (407 m CSF-A). The logging tools were rigged down, and the drill string was pulled clear of the seafloor at 0200 h on 31 August.

Hole U1425C

After offsetting the ship 15 m south of Hole U1425A, Hole U1425C was spudded at 0355 h on 31 August 2013. Core 346-U1425C-1H recovered 5.95 m, establishing a seafloor depth of 1918.9 mbrf. This core was followed by two additional full-length APC cores to 25 m CSF-A. Because these cores were for optically stimulated luminescence sampling, they were handled per the protocols established at Site U1424, taking care to shield the core from any natural or artificial light as much as possible. The drill string was pulled clear of the seafloor at 0540 h on 31 August, ending Hole U1425C operations.

Hole U1425D

The ship was offset 15 m west of Hole U1425A and Hole U1425D was spudded at 0605 h on 31 August 2013. Core 346-U1425D-1H established a seafloor depth of 1919.6 mbrf. Coring continued to a final depth of 431 m CSF-A, alternating between the full and half APC and the XCB core barrels. The coring effort consisted of 26 full APC cores, 40 half APC cores, and 4 XCB cores. Core recovery totaled 417.5 m (98%). Recovery percentages are biased in the last few cores in Hole U1425D because both the XCB and half APC systems were pushed into dolomite and siliceous claystone horizons that neither coring system was designed to handle. Despite poor recovery in the last few cores, the coring effort was scientifically successful, obtaining a dateable cored section for the last half APC core recovered (Core 72H). The top drive was set back and the drill string was recovered back aboard the ship. The positioning beacon was recovered during the pipe trip and was back aboard after lunch on 2 September. The BHA was set back in the derrick, and the vessel was secured for transit to IODP Site U1426, ending (temporarily) operations at Site U1425.

Return to Site U1425

We returned to Site U1425 after completing an additional hole at Site U1427 (3 weeks after the first visit). The 212 nmi distance between Sites U1427 and U1425 was covered in 19.5 h at an average speed of 10.9 kt. Sea passage ended at 1430 h on 24 September 2013. The vessel was maneuvered over the location coordinates, thrusters were lowered into position, and the vessel was turned over to dynamic positioning control. By 1500 h, the R/V *JOIDES Resolution* was stabilized and rig floor operations began again at the site.

Hole U1425E

Deployment of a positioning beacon was deemed unnecessary for this hole because the weather was good, water depth was <2000 m, and the anticipated penetration depth was only ~100 m CSF-A. Nonetheless, a Falmouth Scientific positioning beacon (model BAP-547; SN1022, 14 KHz, 208 dB) was kept on standby in case it was required.

As at Site U1427, this hole was to provide extra core material for future sampling needs and postexpedition studies. The APC/XCB BHA was assembled, and the drill string was run to the bottom. The ship was positioned 15 m east of Hole U1425A. The top drive was picked up, and the pipe was spaced out, positioning the bit at 1913.4 mbrf. The first barrel was recovered empty (water core), so the bit was lowered 3.0 m to 1916.4 mbrf, and the process was repeated. Hole U1425E was ultimately spudded at 1945 h on 24 September. The first core barrel recovered 5.69 m of core, establishing a seafloor depth of 1920.2 mbrf. APC coring continued using full-length nonmagnetic core barrels through Core 346-U1425E-13H to a total depth of 113.1 m CSF-A. Total recovery for Hole U1425E was 107.75 m (95%). A total of 13 cores were recovered in this hole, all using full-length nonmagnetic core barrels.

The top drive was set back, and the drill string was pulled clear of the seafloor at 0435 h on 25 September. All drill collars were laid out to the forward pipe rack, and the bit was clear of the rotary table by 0910 h. The bit and bit sub were removed, and the outer barrel coring system was disassembled. The rig floor was secured for transit by 0950 h. Thrusters were raised, and the sea passage to Busan was initiated at 1012 h on 25 September, successfully ending all coring operations of Expedition 346.

Transit from Site U1425 to Busan, Korea

The transit to Busan was completed without incident. The vessel arrived at the Busan pilot station at 0600 h on 27 September 2013. The Asian Monsoon Expedition 346 officially ended 24 h early with the first line ashore at 0651 h on 27 September.

It seems only fitting during this research voyage, which is the last of this phase of IODP, that we draw attention to the fact that this expedition set the record for the most amount of core recovered during any single research cruise by IODP. That the recovery of 6135 m of sediment occurred during only ~6 weeks of drilling operations makes this accomplishment even more remarkable. In combination with the record achieved of acquiring the deepest piston core (and deepest continually piston-cored sequence at Site U1427), these achievements speak of the commitment to excellence, teamwork, and, to be direct, impressively hard work of men and women dedicated to the pursuit of scientific knowledge about Planet Earth.

Lithostratigraphy

Drilling at Site U1425 penetrated to a subbottom depth of 427 m in Hole U1425D, recovering a total of 417.5 m of sediment for a recovery rate of 98%. The shipboard lithostratigraphic program involved detailed visual assessment of sediment composition, color, sedimentary structures, and bioturbation intensity, supplemented by petrographic analysis of smear slides (141 from Hole U1425B and 157 from Hole U1425D), bulk mineralogic analysis by X-ray diffraction (XRD) (73 samples), and thin section analysis (3 samples). These objective criteria were used to describe the sediment succession, to define facies and facies associations, and to divide the stratigraphic section into major lithologic units. The sedimentary succession recovered at Site U1425 extends from the Miocene to Holocene and is dominated by clay, silty clay, diatomaceous ooze, and siliceous claystone. Numerous discrete tephra (i.e., volcanic ash) layers occur throughout the sedimentary sequence and volcaniclastic material represents a minor component of the sediment succession. The section is divided into three major lithologic units (I, II, and III, similar to Tada [1994]), distinguished on the basis of sediment composition, referring particularly to the abundance of biosiliceous and clay fractions. These units are each further divided into two subunits. The character of the sediment physical properties, including NGR, magnetic susceptibility, color reflectance parameters, and density, records the distribution of the various sediment components and lithologies (see **"Physical properties"**). The major characteristics of the sedimentary sequence at Site U1425, together with some of these additional properties, are summarized in Figures **F3**, **F4**, and **F5**. A lithostratigraphic correlation between the three holes is shown in Figure **F6**.

Unit I

Intervals: 346-U1425B-1H-1, 0 cm, to 346-U1425B-11H-1, 0 cm; 346-U1425D-1H-1, 0 cm, to 10H-5, 0 cm; 346-U1425E-1H-1 0 cm, to 11H-2, 73 cm

Depths: Hole U1425B = 0–94.30 m CSF-A; Hole U1425D = 0–86.30 m CSF-A; Hole U1425E = 0–88.43 m CSF-A

Age: Holocene to Late Pleistocene (2.7 Ma)

Lithologies and structures

Unit I consists of clay and silty clay with small amounts of diatom-bearing, diatom-rich, and foraminifer-bearing clay and rare (nonbiogenic) calcareous layers. Pyrite and volcaniclastic materials represent a minor component throughout the sediment succession. Numerous discrete millimeter- to centimeter-thick tephra layers (vitric and scoria) and pumice clasts are described throughout Unit I (total of 51 tephra beds that are >0.5 cm thick; Fig. **F7**).

The most distinguishing sedimentary feature of Unit I is the alternating decimeter-scale color-banded bedding that characterizes much of the sequence, with dark, organic-rich clay intervals interspersed with lighter colored, organic-poor intervals. The relative frequency of these color alternations and the intensity of bioturbation are used as criteria to divide Unit I into the Subunits IA and IB (Figs. **F3**, **F4**, **F5**).

Bulk mineralogy

The XRD analysis results are listed in Table **T2**. In general, sediment at this site is composed mainly of quartz, plagioclase, and clay minerals (including smectite, illite, and kaolinite and/or chlorite), as well as biogenic opal-A and minor amounts of halite and pyrite. Calcite is sparse throughout the upper 50 m of Unit I (mostly in the form of foraminifers and nannofossils). Other minor minerals are observed in smear slides, but it was not possible to detect these through XRD analysis of bulk samples.

Figure **F8** shows downcore variations of the major identified minerals in Hole U1425B. In general, the peak intensities of quartz, plagioclase, feldspar, and clay minerals (smectite, illite, and kaolinite and/or chlorite) in Unit I are higher than in other units (II and III), suggesting higher terrigenous input relative to biogenic material. In contrast, the peak height of opal-A is generally much lower in Unit I compared to other units, especially Unit II. Dolomite is only detected in two selected samples of carbonate-rich concreted yellowish sediment (Samples 346-U1425B-13X-1W, 7–9 cm, and 56X-CC, 0–2 cm), although it occasionally occurs in sediment as a minor component in smear slides.

Subunit IA

Intervals: 346-U1425B-1H-1, 0 cm, to 6H-1, 0 cm; 346-U1425D-1H-1, 0 cm, to 6H-1, 127 cm; 346-U1425E-1H-1, 0 cm, to 7H-1, 80 cm

Depths: Hole U1425B = 0–46.80 m CSF-A; Hole U1425D = 0–44.57 m CSF-A; Hole U1425E = 0–49.0 m CSF-A

Age: Holocene to early Pleistocene (1.2 Ma)

Lithologies and structures

Subunit IA is dominated by clay with subordinate amounts of diatomaceous (i.e., diatom bearing) and foraminifer-bearing clay. Tephra layers are intercalated in the clay sequence and form a minor but common component of Subunit IA. The subunit is characterized by pronounced decimeter-scale alternations of light and dark sediment intervals (Fig. **F9**). These alternations are also evident in the L*, a*, and b* records (see **"Physical properties"**). In detail, the light intervals are mainly composed of light greenish gray clay with some diatoms. Within these lighter intervals, millimeter- to centimeter-scale layers of gray, dark greenish gray, and very dark gray clay are observed forming color banding within the sediment. The lighter intervals are slightly bioturbated, although not enough to disrupt preservation of the thin, darker banding. Some prominent millimeter- to centimeter-scale olive-gray layers are also observed throughout these light intervals. Detailed examination of these layers shows they are composed of clay minerals with abundant amounts of pyrite (sometimes visible to the naked eye).

The contrasting dark layers, which dominate Subunit IA, correspond to dark grayish brown organic-rich silty clay intervals with some foraminifers and pyrite. Some of these intervals show evidence of slight bioturbation, but the dark layers are predominantly finely laminated with no apparent bioturbation (interval 346-U1425B-4H-1, 121–143 cm; Fig. **F10**). Foraminifers (mostly planktonic) are generally restricted to millimeter-scale (foraminifer-bearing) yellowish layers. These yellowish layers, however, are not present in all the dark intervals.

The lower contacts of the darker layers within Subunit IA are normally sharp, suggesting a lack of bioturbation, whereas upper contacts with the light greenish gray intervals appear more gradational because of bioturbation (at the time of deposition of the overlying light greenish gray clay). Centimeter-scale gray clay typically underlies these dark brown sediment intervals (Fig. **F11**). This gray clay is slightly bioturbated but only with the underlying light greenish gray clay (i.e., not with the overlying dark brown interval). As a result, these layers do not form from mixing of the dark brown and greenish gray intervals and probably reflect transitional depositional or early diagenetic conditions. Despite this, heavy bioturbation can occur with the formation of burrows in Subunit IA (Fig. **F12**).

Tephra layers in Subunit IA are mostly thicker than 1 cm and are interbedded within both the light greenish gray and dark brown/grayish brown clay intervals. The number of tephra per core with thickness >0.5 cm is highest in Subunit IA (Fig. **F7;** Table **T3**). Tephra are mostly white and light gray in color (i.e., vitric), but there are some very dark to black tephras (i.e., scoriaceous), with occasional gray to white pumiceous tephra layers. A notably prominent tephra layer in Hole U1425B is 26 cm thick and is made of gray vitric tephra (interval 346-U1425B-4H-7, 8.5–34.5 cm), with its equivalent found in Hole U1425D at interval 346-U1425D-5H-2, 37–67 cm.

Composition

Subunit IA sediment is composed of a mixture of terrigenous, volcanic, and biogenic grains (see Site U1425 smear slides in **"Core descriptions"**). Terrigenous components in this subunit are dominated by clay and fine silty clay fractions. In Subunit IA, the light greenish gray intervals are mostly composed of siliciclastic fine-grained material (up to 80%) dominated by clay minerals. Small pyrite framboids are distributed mainly in the dark layers. Discrete accumulations of well-developed pyrite crystals are also observed on the surface of the split section half, as well as in smear slides (Fig. **F13**). Volcanic glass accounts for nearly 100% of the tephra layers, even though sometimes the volcanic material appears to be mixed with a siliciclastic component.

Subunit IB

Intervals: 346-U1425B-6H-1, 0 cm, to 11H-1, 0 cm; 346-U1425D-6H-1, 127 cm, to 10H-5, 0 cm; 346-U1425E-7H-1, 80 cm, to 11H-2, 73 cm

Depths: Hole U1425B = 46.80–94.30 m CSF-A; Hole U1425D = 44.57–86.30 m CSF-A; Hole U1425E = 49.0–88.43 m CSF-A

Age: early Pleistocene (1.2 Ma) to late Pliocene (2.7 Ma)

Lithologies and structures

Subunit IB is a transitional sediment unit between Subunit IA and Unit II. It is identified by a decrease in the frequency of dark and light color alternation and increasing dominance of light greenish gray and light gray clay (Fig. **F14**). Some millimeter- to centimeter-scale layers of gray, dark greenish gray, very dark gray, and olive-gray clay (previously described in Subunit IA) are observed. Distinct diatom-rich laminae are evident at the top of Subunit IB (intervals 346-U1425B-6H-5, 22–54 cm, and 6H-6, 7–39 cm; Fig. **F10**), with some discrete calcite layers occurring within these structures. Bioturbation increases gradually with depth, and sediment mottling and disruption of laminae and color banding is more prevalent.

Tephra layers are intercalated in the clay sequence and form a minor but common component of Subunit IB. As with Subunit IA, tephra layers are mostly centimeter-scale light (vitric) deposits. Some of the (light) tephra layers described within the light greenish gray intervals show distinct millimeter-scale gray and grayish green laminations or cross laminations. A notable example of a thick (~18 cm) tephra made up of gray vitric tephra (interval 346-U1425B-7H-2, 9–27 cm) shows clear internal layering with normal grading of the volcaniclastic material.

Composition

The principal lithologic components of Subunit IB are terrigenous, volcanic, and biogenic in origin (see Site U1425 smear slides in **"Core descriptions"**). The major difference between the lithologies of Subunits IA and IB is the reduced occurrence of calcareous microfossils and the slightly higher contents of the biosiliceous fraction. Terrigenous materials compose the bulk (>80%) of Unit I sediment, which is dominated by clay. Volcanic glass usually occurs as a minor dispersed component (~5%) throughout the sediment. The biogenic fraction is generally low (<10%) in Subunit IB and is dominated by diatoms and sponge spicules with few calcareous microfossils.

Unit II

Intervals: 346-U1425B-11H-1, 0 cm, to 35H-1, 0 cm; 346-U1425D-10H-5, 0 cm, to 32H-3, 111 cm; 346-U1425E-11H-2, 73 cm, to 13H-6, 56 cm

Depths: Hole U1425B = 94.30–253.30 m CSF-A; Hole U1425D = 86.30–261.91 m CSF-A; Hole U1425E = 88.43–113.07 m CSF-A

Age: late Pliocene (2.7 Ma) to late Miocene (7.4 Ma)

Lithologies and structures

Unit II consists of clay, diatomaceous clay, and diatom ooze (Figs. F3, F4, F5). Pyrite and volcaniclastic materials represent a minor component throughout the succession. Discrete millimeter- to centimeter-scale tephra layers (vitric) are found throughout Unit II (a total of 18 tephra beds each with a thickness >0.5 cm). Although the majority of these layers are at most a few centimeters thick, some of the peaks in tephra thickness in Unit II (Fig. F7) are driven by rare but much thicker tephra deposits. This can be illustrated by a thick (37 cm) deposit of gray vitric tephra in interval 346-U1425B-28H-6, 61–98 cm.

Unit II is distinguished from Unit I on the basis of sediment color and an increase in overall diatom content relative to terrigenous sediment. This lithologic change is supported by NGR measurements, which show lower values in Unit II than in Unit I that are related to the relative increase of the diatomaceous to terrigenous fraction downhole (see **"Physical properties"**). Furthermore, XRD analyses show a large increase in opal-A content (see **"Bulk mineralogy"**; Fig. F8). Unit II sediment is moderately to heavily bioturbated and is often mottled (Figs. F15, F16). The degree of bioturbation changes vertically. The diatom content and intensity of bioturbation are criteria used to further divide Unit II into Subunits IIA and IIB.

Bulk mineralogy

The results of XRD analyses conducted on Hole U1425B sediment are listed in Table T2. In general, the bulk mineral composition of Unit II sediment is very similar to that of Unit I. The major difference is the disappearance of foraminifers and nannofossils in Unit II and the large increase in opal-A content (Fig. F8). The XRD results show mineral peak intensities of Subunit IIB sediment differ from Subunit IIA sediment and are more similar to those of Unit III. For example, the terrigenous minerals show much lower peak intensities in Subunit IIB and Unit III than Unit I and Subunit IIA (Fig. F8). This likely reflects the diluting influence of diatoms in units where diatom ooze dominates (Subunit IIB and Unit III).

Subunit IIA

Intervals: 346-U1425B-11H-1, 0 cm, to 20H-1, 0 cm; 346-U1425D-10H-5, 0 cm, to 16H-3, 0 cm; 346-U1425E-11H-2, 73 cm, to 13H-6, 56 cm

Depths: Hole U1425B = 94.30–131.90 m CSF-A; Hole U1425D = 86.30–130.92 m CSF-A; Hole U1425E = 88.43–113.07 m CSF-A

Age: late Pliocene (2.7 Ma) to early Pliocene (4.2 Ma)

Lithologies and structures

Subunit IIA consists dominantly of brownish and greenish diatom-bearing and diatom-rich clay, as well as clay (Fig. F15). This subunit is considered transitional from Subunit IB to the underlying Subunit IIB, which is defined by the consistent appearance of diatom ooze. In general, sediments of this unit are heavily bioturbated (Fig. F17), leading to poor preservation of original sedimentary structures, which inhibits their recognition (e.g., color banding, laminae, etc.). Tephra layers intercalated in the diatom-bearing clay and clay sequence are a minor but common component of Subunit IIA.

Composition

Subunit IIA is predominantly composed of a mixture of fine-grained material, mostly clay minerals and biosiliceous components (see Site U1425 smear slides in **"Core descriptions"**). The abundance of these components varies throughout this transitional unit, alternating with diatom ooze, clayey diatom ooze, diatom-rich clay, and clay.

Subunit IIB

Intervals: 346-U1425B-20H-1, 0 cm, to 35H-1, 0 cm; 346-U1425D-16H-3, 0 cm, to 32H-3, 111 cm

Depths: Hole U1425B = 131.90–253.30 m CSF-A; Hole U1425D = 130.92–261.91 m CSF-A

Age: early Pliocene (4.2 Ma) to late Miocene (7.4 Ma)

Lithologies and structures

Subunit IIB sediment is dominated by brownish diatom ooze with a few limited clay intervals. The abundance of diatoms and other siliceous components is key to the recognition of Subunit IIB (Fig. F16), and they typically comprise >70% (and up to 95%) of the sediment based on smear slides. A significant decrease in NGR values from Subunit IIA to

Subunit IIB coincides with the increasing diatom content of the sediment (see **"Physical properties"**). Moderate to heavy bioturbation and distinctive mottling are also displayed in some sections (Fig. **F17**). Tephra layers (vitric and scoriaceous) and occasional individual pumice stones are a minor but common component of Subunit IIB. The thickest tephra layer, with a maximum thickness of 37 cm, occurs in the lower part of Subunit IIB (see discussion above). Most of the layers, however, have thicknesses <1 cm.

Carbonate-rich zones in Hole U1425B are present as well-lithified, pale gray dolomite beds and concretions, with a 10 cm bed in the top of Section 346-U1425B-13X-1 (104.6–104.7 m CSF-A; Fig. **F18A**). Dolomitic concretions occur throughout Unit II, with 11 dolomite concretions identified in Hole U1425B and 5 dolomite concretions in Hole U1425D. Thin sections of the dolomite bed and concretions show the prevalence of pyrite within their structure along with dolomitized biosiliceous remains (Fig. **F18**). Carbonates also frequently occur as poorly lithified, yellowish brown to olive chalky patches or cements rather than as nodules or concretions. There are 27 and 16 such cements documented in Holes U1425B (~132–172 m CSF-A) and U1425D (130–210 m CSF-A), respectively.

A number of slump folds and discordant bedding are seen in Sections 346-U1425D-9H-1 to 9H-2 (71.46–72.92 m CSF-A) (Fig. **F19**) and Section 10H-6 (88.8–89 m CSF-A). These sedimentary structures are only observed in Hole U1425D. The thickness of slumped material ranges from tens of centimeters to >1.5 m. The genesis of these slumped deposits remains unknown, but it is likely to be instability or slope-related phenomena, although other types of sediment flow, such as turbidites, are not common in Hole U1425D.

Composition

The major lithologies in Subunit IIB are dominated by biosiliceous components (>70% and up to 95%) from Sections 346-U1425B-11H-1 and 346-U1425D-11H-1 downward (i.e., the Subunit IIA/IIB boundary transition) (see Site U1425 smear slides in **"Core descriptions"**). Diatoms and siliceous sponge spicules are dominant in the biosiliceous fraction (Fig. **F20**), whereas radiolarians and silicoflagellates are found only in rare or trace amounts (1%–5%). These siliceous fossil assemblages characterize both the brownish and greenish sediment in the "diatom ooze" category. Scattered glauconite grains are occasionally observed in the diatom ooze between Samples 346-U1425B-11H-5, 75 cm, and 23H-A, 75 cm.

Unit III

Intervals: 346-U1425B-35H-1, 0 cm, to 61X-CC, 42 cm; 346-U1425D-32H-3, 111 cm, to 72H-1, 25 cm
Depths: Hole U1425B = 253.30–404.04 m CSF-A; Hole U1425D = 261.91–430.95 m CSF-A
Age: Miocene (>7.4 Ma)

Lithologies and structures

Unit III consists of clay, diatom-rich clay, diatom ooze, and siliceous claystone (Figs. **F3, F4**). Unit III is distinguished from Unit II on the basis of sediment color and an increase in the terrigenous content of the sediment, though there is still significant numbers of diatoms. Unit III sediment is further divided into two subunits (IIIA and IIIB) based primarily on the degree of lithification. The upper sediment of Unit III is moderately to heavily bioturbated and often mottled, making changes between diatom ooze, diatom-rich clay, and clay difficult to distinguish. The diatom content (i.e., biogenic silica component) decreases at the deeper end of Subunit IIIA, and the indurated siliceous claystone of Subunit IIIB develops.

Bulk mineralogy

There is very little variation in peak intensities of minerals in sediment from Units II to III (Fig. **F8**), except for the general decrease in halite intensity and gradually increasing pyrite content between ~90 and 340 m CSF-A. The peak intensity of a number of minerals, including clay minerals, quartz, feldspar, halite, and amorphous opal (opal-A), decreases abruptly at ~341 m CSF-A, coincident with the first downhole occurrence of siliceous claystone in the sediment sequence and indicating the diagenetically enhanced compaction of soft sediment to well indurated claystone (Figs. **F3, F4**). At the Subunit IIIA/IIIB boundary transition, smear slides show a sharp decrease in the amount of biosiliceous material within the sediment (from 70% to 0%) over a depth range of only a few centimeters (Fig. **F21**).

An important change in the Subunit IIIB sediment is the distinct appearance of opal-CT at 378 m CSF-A. Opal-CT shows up as a large peak in intensity centered at 22° ($\Delta 2\theta$) in the XRD diagram (Fig. **F22**), suggesting opal-A is recrystallizing into opal-CT by dissolution/reprecipitation reactions. However, opal-CT likely forms a distinct peak here because the siliceous content of the claystone at 378 m CSF-A depth is high. There are small but detectable amounts of opal-CT in XRD analyses as shallow as ~342 m CSF-A, with its peak intensifying downhole as the siliceous content of the claystone increases.

Subunit IIIA

Intervals: 346-U1425B-35H-1, 0 cm, to 53H-1, 0 cm; 346-U1425D-32H-3, 111 cm, to 48H-1, 0 cm
Depths: Hole U1425B = 253.30–341.30 m CSF-A; Hole U1425D = 261.91–343.80 m CSF-A
Age: late Miocene (7.4–9.5 Ma)

Lithologies and structures

Subunit IIIA sediment is composed of alternating layers of heavily bioturbated diatomaceous ooze, clayey diatomaceous ooze, and diatom-rich clay (Fig. **F23**). These alternating layers show decimeter- to meter-scale cycles of dark gray (diatom ooze, relatively clay poor) and gray (diatom-rich clay), although these color changes can be subtle. Moderate to heavy bioturbation is generally restricted to the light layers in Unit III, but faint burrows (possibly *Chondrites*-type) are evident in the dark layers, with a large vertical burrow observed in Unit III (Fig. **F24**).

There are very few sedimentary structures within Subunit IIIA, although there is an excellent example of finely laminated diatom ooze that extends ~1.5 m in thickness and is observed in both Holes U1425B and U1425D (Fig. **F25;** 275 m CSF-A). These laminations (of approximately middle Miocene age) occur within a dark organic-rich layer in Subunit IIIA and are not seen elsewhere in the sediment sequence during the Miocene. In addition, there is evidence of slump folds from Core 346-U1425D-38H (Fig. **F19;** 294 m CSF-A). As before, their genesis is not known.

Composition

The principal lithology of Subunit IIIA is characterized by abundant diatoms (>75%) associated with the common occurrence of siliceous sponge spicules (5%–25%) and an increasing clay mineral and quartz content (5%–25%) compared to Unit II. Other siliceous components, such as radiolarians, remain rare (<5%), but organic matter, based on smear slides, increases to become more common. Toward the bottom of Subunit IIIA, the pyrite content also increases to become a more important component of the lithology. Overall, the biosiliceous and clay-size composition changes with the alternating color changes described above.

Subunit IIIB

Intervals: 346-U1425B-53H-1, 0 cm, to 61X-CC, 42 cm; 346-U1425D-48H-1, 0 cm, to 72H-1, 25 cm
Depths: Hole U1425B = 341.30–404.04 m CSF-A; Hole U1425D = 343.80–430.95 m CSF-A
Age: Miocene (>9.5 Ma)

Lithologies and structures

Subunit IIIB sediment is characterized by well-lithified gray siliceous claystone (Fig. **F26**) with occasional parallel laminations (Fig. **F25**), burrows, and carbonate concretions that appear as layers and nodules. Recovery of Subunit IIIB sediment was limited, and therefore a detailed description of lithologic changes is difficult. However, the transition from Subunit IIIA to Subunit IIIB was captured and is characterized by a rapid decrease in the amount of biogenic silica (opal-A) in the sediment (Fig. **F27**). This diagenetic loss of biosiliceous material and the formation of siliceous claystone defines the Subunit IIIA/IIIB boundary at 341.3 m CSF-A in Hole U1425B and 343.91 m CSF-A in Hole U1425D. Biosiliceous-rich clay occurs in Section 346-U1425B-57X-1 (368.4–369.07 m CSF-A), which is immediately above a distinct increase in opal-CT as documented by XRD analysis (see **"Summary and discussion"**).

Composition

The principal lithology of Subunit IIIB is characterized by abundant clay minerals and quartz (i.e., falling between 25% and 75%) and the common occurrence of pyrite and organic matter (5%–25%). The amount of glauconite varies from rare (<5%) to common (5%–25%) throughout Subunit IIIB (Fig. **F28**). All biosiliceous material is absent from smear slides in this unit.

Summary and discussion

The sedimentary sequence from Site U1425 records a history of terrigenous and pelagic sedimentation since the middle Miocene, as well as the diagenesis of silica-rich Miocene sediment and the lithification of clay at depth. The dominant lithology of Site U1425 is diatom ooze and diatom-rich clay, which extends from the late Miocene to early Pleistocene (Figs. **F3, F4**). Sedimentation is dominantly pelagic and/or hemipelagic, coupled with volcanic inputs. There is no evidence of significant turbidite inputs, but in Hole U1425D there are slump folds that likely represent downslope processes linked to either instabilities in the sediment plateau or tectonically triggered movement of sediment (Fig. **F19**).

The Holocene to Middle Pleistocene sediment at Site U1425 shows alternating dark brown organic-rich (laminated) and greenish gray and light gray clay layers (Subunit IA), followed by the appearance of slightly bioturbated light greenish gray and light gray clay (Subunit IB) (Figs. **F9, F11, F14**). This pattern parallels observations from Sites U1422 (Figs. **F8, F11** both in the "Site U1422" chapter [Tada et al., 2015c]), U1423 (Figs. F9, F11 both in the "Site U1423" chapter [Tada et al., 2015d]), and U1424 (Figs. F8, F12 both in the "Site U1424" chapter [Tada et al., 2015e]). However, it differs from Unit I at nearby Site 799 located in the Kita-Yamato Trough, which is characterized by coarse-grained and normally graded beds (fining upward) that have been interpreted as turbidite deposits (Shipboard Scientific Party, 1990).

The centimeter- to decimeter-scale alternations in Subunit IA are thought to reflect millennial-scale variations associated with Dansgaard-Oeschger cycles, with organic-rich dark layers associated with interstadials over the last glacial cycle (Tada et al., 1999). Similar to Site U1424, the dark–light alternations show dark brown intervals that are often preceded by centimeter-scale gray clay that is slightly bioturbated with the underlying light greenish gray clay (Fig. F11). Tada et al. (1999) suggest that deposition of organic-poor gray clay occurs under oxic conditions, and the organic-rich dark brown layers are deposited under suboxic to euxinic conditions as a result of changes in ventilation of the marginal sea.

The late Miocene to early Pleistocene sedimentation at Site U1425 corresponds to the deposition of Unit II, which is composed of moderately to heavily bioturbated diatom ooze and diatom-rich clay (Figs. F15, F16). This unit reflects significant pelagic and hemipelagic sedimentation at Site U1425 from the late Miocene until the early Pleistocene, whereas the high diatom abundance in the sediment indicates high biological productivity, especially in Subunit IIB. The dominance of diatoms, together with other biosiliceous components (i.e., sponge spicules and radiolarians), and the heavy bioturbation of the sediment suggests that bottom water of the marginal sea was well oxygenated and there was active circulation during at least the entire Pliocene (Tada, 1994). Bioturbation reaches a maximum in the upper part of Unit II (Subunit IIA; early Pleistocene), although the clay component increases, suggesting greater terrigenous sedimentation in the sea during this time.

Middle to late Miocene sediment is characterized by diatom ooze, clayey diatom ooze, and bioturbated diatom-rich clay that alternate in layers (Subunit IIIA; Fig. F23). The color changes associated with these sedimentary variations, however, are subtle. The changing relative abundance of biosiliceous components to clay minerals defines this sedimentary unit; these oscillations in lithology are likely related to changes in bottom water oxygenation of the sea (Tada, 1994). Fluctuations in biogenic silica content during the middle to late Miocene have been previously interpreted in terms of changes in the flux of terrigenous material to the marginal sea (Tada, 1991, 1994). Under this scenario, bottom water becomes oxic during high influx of terrigenous material and becomes anoxic during periods of reduced terrigenous input. Tada (1991, 1994) suggests that oscillations in eustatic sea level during this period changed the delivery of terrigenous material to the sea, which occurs over periodicities similar to orbital cycles.

In Subunit IIIB (middle Miocene) the diatom ooze/diatom-rich clay is replaced by siliceous claystone (Figs. F3, F4), the appearance of which defines the top of Subunit IIIB (Fig. F26) and marks a diagenetic transition from high biogenic silica content to siliceous content (Fig. F21). This lithologic change is supported by the start of a significant decrease in silica concentration in interstitial water at this time (see "Geochemistry") and a switch to higher sediment resistivity suggesting decreasing biogenic silica content in the downhole log of Hole U1425B (see "Downhole measurements"). Therefore, Subunit IIIB signifies the start of the diagenesis of diatoms and the formation of siliceous claystone.

During burial, opal-A undergoes dissolution and reprecipitation as opal-CT (Murata and Nakata, 1974). Within Subunit IIIB, opal-CT starts to precipitate at ~342 m CSF-A and with increasing depth becomes the main phase of opal, reaching a distinct peak at ~378 m CSF-A in Hole U1425B (Fig. F22). Tada and Iijima (1992) suggest that dissolution of diatom frustules (opal-A) occurs within a few meters of the shallowest occurrence of opal-CT. Therefore, the dissolution of biogenic silica and the formation of siliceous claystone mark the transition from Subunit IIIA to Subunit IIIB. The last biosiliceous-bearing clay occurs in Section 346-U1425B-57X-1 (at the top of Subunit IIIB), followed by the detection of opal-CT in XRD analyses at ~342 m CSF-A. However, there is not a distinctive peak in opal-CT until Section 58X-CC at ~378 m CSF-A (Fig. F22), likely a result of the change in siliceous content of the lithology.

Opal-A and opal-CT can coexist within a stratigraphic interval (Tada and Iijima, 1992), and therefore a transitional zone between the lower opal-A zone (i.e., disappearance of diatom frustules) and the main opal-CT phase is not unexpected. Figure F22 shows a downhole XRD profile for Hole U1425B and discrete samples from the top of Subunit IIIB. It shows there is no clearly defined opal-CT peak in Section 346-U1425B-57X-1 (which may be related to the low siliceous content), but there is a clear opal-CT peak in the sample from Section 58X-CC, suggesting the boundary between opal-A and opal-CT is likely to be between ~340 and 352 m CSF-A.

Tada (1994) defined a Miocene Unit 4 in the marginal sea, the upper portion of which is characterized by alternation of dark gray to black chert and light gray siliceous claystone. The top of this unit was found to be deeper than the first recorded appearance of opal-CT in sites drilled during ODP Leg 127. At Site U1425, there is no clear indication from the recovered lithologies or from downhole logs that this Unit 4 has been reached; therefore, our Subunit IIIB is defined to the base of the hole. Interestingly, Tada (1994) noted that Unit 4 recovery was quite poor because of the presence of chert. In Hole U1425D, drilling deeper than ~403 m CSF-A yielded only a highly disturbed slurry of coarser materials described as drilling breccia. Despite there not being an obvious change in lithology, this decrease in recovery quality near the base of the hole suggests that penetration at this site may have fallen just short of reaching the Subunit 4A previously recognized by Tada (1994).

In summary, the changes in sedimentation observed at Site U1425 since the Miocene likely reflect a combination of effects from climate oscillations, eustatic sea level changes, and volcanic processes in this marginal sea region (Tada, 1994). Site U1425 also records the volcanic history of the Japan and East Asian continent, as shown by the numerous tephra layers found throughout the sedimentary succession (Fig. F8). These environmental changes are recorded in Holes U1425B, U1425D, and U1425E (Fig. F6), although the attenuation of Subunit IIA in Hole U1425D is a consequence of the slump folds in the sediment succession. Further shore-based research will help to decipher the relative roles of these and other processes on the sedimentation history of Site U1425.

Biostratigraphy

At Site U1425, a ~431 m thick succession of Miocene–Holocene sediment was recovered. Nannofossils are present in Pleistocene sediment shallower than ~56 m CSF-A but are absent or rare deeper than this depth. Radiolarians are generally common to abundant in the sequence, although they are rare or absent deeper than 351.2 m CSF-A. Twenty radiolarian datums included in the *Eucyrtidium inflatum* Zone (middle Miocene) through the *Botryostrobus aquilonaris* Zone (Late Pleistocene) were found at this site. Diatom preservation is good throughout the succession. Overall, diatom abundance is low in most of the upper part of the succession and increases in the lower part. Seven diatom datums were identified, and the diatom-based stratigraphy spans the interval from Zone NPD 6A (middle Miocene) to NPD 12 (Late Pleistocene). The scarcity of freshwater diatoms combined with high abundance of phytoliths (Table T4) suggests wind transportation from land. The complete dissolution of diatoms and rare occurrence of radiolarians near the base of the succession coincides with the opal-A/opal-CT boundary transition. Planktonic foraminifers are mainly confined to the upper part of the succession (shallower than ~131 m CSF-A), exhibiting good to moderate preservation to ~66 m CSF-A and moderate to poor preservation between ~66 and 131 m CSF-A. Planktonic foraminiferal assemblages shallower than ~60 m CSF-A generally indicate cold and restricted environments. Benthic foraminifers occur intermittently throughout the Pleistocene to Miocene succession, showing marked variations in abundance and preservation. The overall assemblage composition indicates bathyal paleodepths. The highly variable composition of the assemblages suggests episodic oxygen depletion and intense carbonate dissolution at the seafloor, particularly during the Pliocene and Miocene. The radiolarian, diatom, calcareous nannofossil, and planktonic foraminifer datums generally agree, with only some minor inconsistencies. The integrated calcareous and siliceous microfossil biozonation is shown in Figure F29, and microfossil datums are shown in Table T5. A biostratigraphic age-depth plot is shown in Figure F30. See **"Stratigraphic correlation and sedimentation rates"** for a discussion of sedimentation rates at Site U1425.

Calcareous nannofossils

Calcareous nannofossil biostratigraphy is based on analysis of core catcher and split-core section samples from Holes U1425B and U1425D. Of the 116 samples studied, 39 contain nannofossils (Table T6).

Nannofossils are present in Pleistocene sediment shallower than 56.5 m CSF-A in Hole U1425B (Table T6), with barren intervals in Samples 346-U1425B-1H-CC, 2H-CC, 4H-CC, and 5H-2W, 25–26 cm. The majority of samples deeper than 64.8 m CSF-A lack nannofossils (Fig. F31). Sporadic occurrences are observed in core catcher samples from Cores 346-U1425B-12H through 15H, 26H, 28H, and 43H (between 104.6 and 299.2 m CSF-A). Only selected intervals were studied in Hole U1425D. Nannofossil preservation is moderate to good in Samples 346-U1425D-4H-2W, 75 cm, 4H-5W, 75 cm, and 4H-6W, 75 cm. Samples are devoid of calcareous nannofossils downhole from Samples 346-U1425D-13X-CC through 19H-CC (113.8–158.6 m CSF-A) and from Samples 59H-CC through 72H-1 (384.77–430.95 m CSF-A).

Nannofossil diversity at Site U1425 is low but higher than at previous Sites U1422–U1424. The nannofossil assemblage consists of 21 taxa, including *Braarudosphaera bigelowii, Calcidiscus leptoporus, Calcidiscus* *macintyrei, Coccolithus pelagicus, Emiliania huxleyi, Gephyrocapsa caribbeanica, Gephyrocapsa margerelii/muellerae, Gephyrocapsa oceanica, Gephyrocapsa omega, Gephyrocapsa* spp. (>4 µm), *Gephyrocapsa* spp. large (>5.5 µm), *Gephyrocapsa* spp. (<4 µm), *Helicosphaera carteri, Pontosphaera* spp., *Pseudoemiliania lacunosa, Reticulofenestra minuta, Reticulofenestra minutula, Reticulofenestra* spp., and *Umbilicosphaera sibogae*. *Reticulofenestra pseudoumbilica* is interpreted as a reworked species in Sample 346-U1425B-5H-7, 33–34 cm. Preservation is generally poor or moderate, although nannofossils exhibit good preservation at 19.4, 23.4, and 35.4 m CSF-A (Samples 346-U1425B-3H-1, 108–109 cm, 3H-4, 60 cm, and 4H-6, 9–10 cm, respectively).

Nannofossil Zones CN15/NN21 through CN13b/NN19 are recognized (Fig. F29) based on the first occurrence (FO) of *E. huxleyi*, the last occurrence (LO) of *P. lacunosa*, and the FOs of *G. oceanica* and *G. caribbeanica*. The pervasiveness of barren samples deeper than 56.6 m CSF-A (Sample 346-U1425B-6H-CC) prevents further zonal assignments.

Similar distribution, abundance, preservation, and diversity patterns were documented by Muza (1992) for Site 799 (Leg 127) drilled near Site U1425 on the Yamato Rise. At Site 799, calcareous nannofossils occur intermittently in the upper 81 m of the section. The sporadic occurrence of nannofossils in this interval is attributed to CCD fluctuations. The lack of nannofossils and other calcareous microfossils deeper than this depth is attributed by Muza (1992) to in situ dissolution and production of authigenic carbonates based on the presence of monospecific assemblages comprising overgrown specimens of the highly dissolution resistant species *C. pelagicus* (Fig. F32) concurrent with high percentages of small (1–12 µm) carbonate grains. The carbonate grains may have come from in situ dissolution of nannofossils in these horizons, and *C. pelagicus* may be all that remains of an assemblage that was originally as diverse as those documented in the upper part of the section.

Radiolarians

A total of 73 core catcher samples from Holes U1425B (60 samples) and U1425D (13 samples) were prepared for radiolarian analyses (Table T7).

Hole U1425B

In Hole U1425B, radiolarians are generally common to abundant, although they are rare or absent deeper than 351.2 m CSF-A (Sample 346-U1425B-54-CC; Fig. F31). Nineteen radiolarian datums included in the *E. inflatum* Zone (middle Miocene) through the *B. aquilonaris* Zone (Late Pleistocene) were identified in Hole U1425B (Table T5; Figs. F29, F30).

Pleistocene datums

Although key species that define the base or top of the *Stylatractus universus* and *Eucyrtidium matuyamai* Zones are not present, secondary datums include the LO of *Lychnocanoma sakaii* (0.05 Ma) at 8.8 m CSF-A (Sample 346-U1425B-1H-CC), *Spongodiscus* sp. (0.29 Ma) at 18.6 m CSF-A (Sample 2H-CC), and *Axoprunum acquilonium* (1.2–1.7 Ma) at 66.2 m CSF-A (Sample 7H-CC).

Pliocene datums

The Pleistocene/Pliocene boundary is close to the FO of *Cycladophora davisiana* (2.7 Ma) and the LO of *Hexacontium parviakitaensis* (2.7 Ma) at 75.6 m CSF-A (Sample 346-U1425B-8H-CC). The FO of *H. parviakitaensis* (3.9–4.3 Ma) is at 122.5 m CSF-A (Sample 17H-CC). The FO and LO of *Dictyophimus bullatus*, which define the top and base of the *D. bullatus* Zone (3.9–4.3 to 4.4 Ma), are at 131.2 m CSF-A (Sample 19H-CC) and 136.7 m CSF-A (Sample 20H-CC). The *Siphocampe arachnea* group is abundant at 146.3 m CSF-A (Sample 21H-CC), suggesting the acme zone of this species group is between 4.46 and 4.71 Ma. The FO of *Lipmanella redondoensis* (5.06 Ma) is at 156.0 m CSF-A (Sample 22H-CC).

Miocene datums

The FO of *Larcopyle pylomaticus* (base of the *L. pylomaticus* Zone, 5.3 Ma), which is close to the Pliocene/Miocene boundary, is at 175 m CSF-A (Sample 346-U1425B-24H-CC). Sample 25H-CC (184.5 m CSF-A) corresponds to the *A. acquilonium* Zone (5.3–6.1 Ma) lying between the FO of *L. pylomaticus* (175 m CSF-A; Sample 24H-CC) and the LO of *Lychnocanoma parallelipes* (194.1 m CSF-A; Sample 26H-CC). The rapid increase of *Lithelius barbatus* (7.1 Ma), which defines the base of the *L. barbatus* Zone, is at 221.3 m CSF-A (Sample 29H-CC). The FO of *A. acquilonium* (7.1 Ma) is at 231 m CSF-A (Sample 30H-CC). The base of the *L. parallelipes* Zone (the FO of *L. parallelipes*; 7.4 Ma) is at 244 m CSF-A (Sample 33H-CC), occurring with the LO of *Cycladophora nakasekoi* (7.4 Ma) at 253.4 m CSF-A (Sample 34H-CC). The LO of *Lychnocanoma magnacoronuta* (9.0 Ma) is at 322.7 m CSF-A (Sample 48H-CC), corresponding to the base of the *L. redondoensis* Zone and the top of the *L. magnacoronuta* Zone. Although the base of the *L. magnacoronuta* Zone (11.8 Ma) should be marked by the FO of *L. magnacoronuta* at 366 m CSF-A (Sample 56X-CC), it might be present at deeper levels because the occurrence of *C. nakasekoi* is younger than 10.1 Ma in Samples 57X-CC and 58X-CC (369.5–378.4 m CSF-A).

Sample 60H-CC (402.5 m CSF-A) lies below the LO of *Eucyrtidium inflata* (11.8 Ma) and is younger than the rapid decrease (RD) of *Cyrtocapsella tetrapera* at 12.6 Ma.

Hole U1425D

Deeper than 375.6 m CSF-A in Hole U1425D (Sample 346-U1425D-57H-CC), radiolarians are rare or absent. The FO of *L. magnacoronuta* (11.8 Ma) is at 375.6 m CSF-A (Sample 57H-CC). In the same sample, *Hexacontium akitaensis* is present, suggesting that the interval was deposited from 11.7 to 10.7 Ma (Kamikuri, 2010), in the lower part of the *L. magnacoronuta* Zone. *E. inflatum* occurs from 384.8 (Sample 59H-CC) to 404.4 m CSF-A (Sample 65H-CC), indicating the *E. inflatum* Zone (11.8–15.3 Ma). The RD of *C. tetrapera* that divided the *E. inflatum* Zone at 12.6 Ma is at 390.7 m CSF-A (Sample 61H-CC). Key biostratigraphic species were absent deeper than 408 m CSF-A (Sample 66H-CC).

Diatoms

Diatom biostratigraphy was based on smear slides from core catcher samples. Sixty core catcher samples were examined, and seven datums were identified (Tables **T4, T5**). The LO of *Neodenticula koizumii* (2.0 Ma) at 75.63 m CSF-A (Sample 346-U1425B-8H-CC) marks the boundary between the base of NPD 10 and the top of NPD 9 (Yanagisawa and Akiba, 1998), the LO of *Neodenticula kamtschatica* (2.6–2.7 Ma) at 94.82 m CSF-A (Sample 10H-CC) marks the boundary between the base of NPD 9 and the top of NPD 8 (Yanagisawa and Akiba, 1998), and the FO of *N. koizumii* (3.4–3.9 Ma) at 104.61 m CSF-A (Sample 12H-1) gives the boundary between the base of NPD 8 and the top of NPD 7B (Yanagisawa and Akiba, 1998). The LO of *Thalassiosira jackonsii* (4.81 Ma) is in Sample 23H-CC, and the last common occurrence (LCO) of *Thalassionema schraderi* (7.67 Ma) at 244.03 m CSF-A (Sample 33H-CC) marks the boundary between the base of NPD 7A and the top of NPD 6B (Yanagisawa and Akiba, 1998). The boundary between the base of Zone NPD 6B and the top of Zone NPD 6A (Yanagisawa and Akiba, 1998) is given by the LO of *Denticulopsis katayamae* (8.7 Ma) at 313.37 m CSF-A (Sample 46H-CC). The LO of *Denticulopsis dimorpha* (9.3 Ma) at 336.91 m CSF-A (Sample 51H-CC) marks the base of Zone NPD 6A and the top of Zone NPD 5A (Yanagisawa and Akiba, 1998).

Diatom preservation is good throughout the succession. Overall, diatom abundance is low (0%–20%) in most of the upper part of the cored interval and increases (20%–60%) in the lower part of the succession (Fig. **F31**). Abundance >60% occurs in Samples 346-U1425B-8H-CC through 26H-CC and 29H-CC through 51H-CC. Diatom identification was not possible in Samples 27H-CC and 28H-CC because of the presence of very fine and abundant volcanic glass. Complete dissolution of diatoms is found at the bottom of the succession, with an absence of valves and rare (<2 fragments in two slide transects), highly dissolved fragments (Samples 52H-CC through 61X-CC [last sample recovered]). This dissolution also appears in Hole U1425D in Samples 346-U1425D-46H-CC through 72H-1 (last sample recovered) and may be the consequence of the opal-A/opal-CT boundary transition.

The absence of significant abundance of freshwater diatoms combined with high abundance (>5 specimens found in two slide transects) of phytoliths (Table **T4**) suggest wind transport from land.

Planktonic foraminifers

Planktonic foraminifers were examined in core catcher samples from Holes U1425A (2 samples), U1425B (60 samples), and U1425D (18 samples). Relative abundances of taxa and visual estimates of assemblage preservation are presented in Table **T8.** Planktonic foraminifers are mainly confined to the upper part of the succession (Sample 346-U1425B-19H-CC; 131.20 m CSF-A and shallower; Figs. **F31, F33**). They are generally abundant between 8.77 and 56.56 m CSF-A (Samples 1H-CC and 6H-CC), whereas abundance varies markedly between 66.25 and 131.20 m CSF-A (Samples 7H-CC and 19H-CC). Sample 20H-CC (136.69 m CSF-A) and other samples deeper in the succession are mainly barren. Preservation is good to moderate shallower than 56.56 m CSF-A (Sample 6H-CC), becoming moderate to poor deeper than 66.25 m CSF-A (Sample 7H-CC) because of frequent fragmentation and/or pyritization. Deeper than Sample 17H-CC (122.49 m CSF-A), most of the planktonic foraminiferal tests have a yellow or orange color. These tests appear to have been partially dissolved and recrystallized when observed in the scanning electron microscope (Fig. **F34**).

Planktonic foraminiferal assemblages shallower than Sample 346-U1425B-6H-CC (56.56 m CSF-A) are characteristic of cold, subarctic, and restricted environments. They mainly consist of *Globigerina bulloides* and *Neogloboquadrina pachyderma* (sinistral and dextral) with rare occurrences of *Globigerina umbilicata, Globigerina quinqueloba, Neogloboquadrina dutertrei* (= *Neogloboquadrina himiensis*), *Neogloboquadrina incompta, Neogloboquadrina kagaensis* group (*N. kagaensis* and *Neogloboquadrina inglei*), and *Neogloboquadrina* cf. *asanoi*. The LO of *N. kagaensis* group (recorded at 0.7 Ma; Kucera and Kennett, 2000) is reported in Sample 4H-CC (37.61 m CSF-A). The change in coiling direction of *N. pachyderma* from sinistral to dextral in Sample 5H-CC (46.99 m CSF-A) corresponds to the Zone PF8/PF7 boundary in the regional zonation for the marginal sea (Maiya, 1978). The planktonic foraminiferal assemblages between Samples 11H-CC and 19H-CC (104.02 and 131.20 m CSF-A) are more diverse than in the upper part of the sequence, including *Globigerinita glutinata, Globorotalia praeinflata, Globorotalia ikebei, Orbulina universa*, and *Orbulina suturalis*, in addition to the species listed above. The FO of *G. praeinflata* in Sample 12H-CC (104.59 m CSF-A) indicates an age younger than 3.3 Ma (Lyle, Koizumi, Richter, et al., 1997). However, this datum is poorly constrained, as samples deeper than this level contain only rare planktonic foraminifers. Based on the FO of *G. praeinflata*, the Zone PF7/PF6 boundary is placed at 105.44 m CSF-A between Samples 12H-1 and 13X-CC. The occurrence of *O. universa* in Sample 12H-CC (104.59 m CSF-A) suggests an age older than 3.0 Ma (Miwa, 2014). The relatively continuous occurrences of *O. universa* and *O. suturalis* between Samples 14H-CC and 18H-CC (115.79 and 127.31 m CSF-A) together with *G. ikebei* (Sample 17H-CC) indicate that this interval corresponds to Zone PF6 (*G. ikebei/O. universa* Zone) of Maiya (1978).

Benthic foraminifers

Benthic foraminifers were examined in core catcher samples from Holes U1425A (2 samples), U1425B (60 samples), and U1425D (18 samples). The mudline sample recovered in Hole U1425B was also investigated. Samples with an average volume of ~30 cm^3 were processed from all core catchers to obtain quantitative estimates of benthic foraminiferal distribution patterns downhole. To assess assemblage composition and variability, all specimens from the >150 µm fraction were picked and transferred to slides for identification and counting. The presence and distribution of benthic foraminifers was additionally checked in the 63–150 µm fraction to ensure that assemblages in the >150 µm fraction were representative and that small species such as phytodetritus feeders or small infaunal taxa were not overlooked. Core catcher samples were also examined for the presence of ostracods during shipboard preparation of benthic foraminifer samples.

Benthic foraminifers vary substantially in abundance and preservation throughout the 408 m thick Miocene to Pleistocene biosiliceous-rich succession recovered at Site U1425 (Figs. F31, F33; Table T9). Samples 346-U1425B-1H-CC and 2H-CC (8.77 and 18.58 m CSF-A) are barren. Samples 3H-CC and 19H-CC (27.04 and 131.17 m CSF-A) contain assemblages that are intermittently diverse and show marked fluctuations in abundance. Deeper than 131.17 m CSF-A (Sample 19H-CC), samples are barren or impoverished, except for Samples 42H-CC and 43H-CC (294.53 and 299.24 m CSF-A), which contain abundant taxa that exhibit low-diversity assemblages. Preservation is generally poor to moderate, except for Samples 3H-CC, 5H-CC, 12H-1, 15H-CC, and 18H-CC, where preservation is good. The assemblages consist of calcareous and agglutinated taxa, and their overall composition indicates bathyal paleodepths throughout the Miocene to Pleistocene.

A total of 52 benthic foraminiferal taxa were identified. Table T9 summarizes the downcore distribution of benthic foraminifers in core catcher samples from Holes U1425A, U1425B, and U1425D. Figure F35 illustrates characteristic taxa found at Site U1425. Species commonly recorded in Samples 346-U1425B-3H-CC and 19H-CC (27.04 and 131.17 m CSF-A) include *Bolivina pacifica, Cassidulina laevigata, Cassidulina norcrossi, Epistominella pulchella, Globobulimina pacifica*, and *Uvigerina yabei*, which typically indicate enhanced organic flux and/or dysoxic conditions at the seafloor and within the uppermost few centimeters of the sediment (Gooday, 1993; Jorissen et al., 1995, 2007; Jorissen, 1999). Sample 12H-1 (104.56 m CSF-A) contains a slightly more diverse assemblage including *Martinotiella communis, Melonis pompilioides, Oridorsalis umbonatus, Cibicidoides mundulus, Quinqueloculina* sp., and *U. yabei*, suggesting a transient increase in deepwater oxygenation between 4 and 5 Ma.

Deeper than Sample 346-U1425B-19H-CC (131.17 m CSF-A), the agglutinated foraminifers *M. communis* and *Miliammina echigoensis* occur sporadically together with rare calcareous taxa. Samples 42H-CC and 43H-CC (294.53 and 299.24 m CSF-A) are dominated by the organic flux–sensitive species *E. pulchella* and include the species *G. pacifica*, which is known to be tolerant of low-oxygen conditions within pore waters (Gooday, 1993; Jorissen et al., 1995, 2007; Jorissen, 1999). Samples 346-U1425B-60H-CC and 61H-CC (402.45 and 403.83 m CSF-A) and 346-U1425D-63H-CC through 67H-CC (397.66–408.86 m CSF-A) contain impoverished agglutinated assemblages including *M. communis, Kareriella* sp., and *Spirosigmoilinella compressa*. Sample 346-U1425D-65H-CC (404.42 m CSF-A) additionally contains three specimens of *Uvigerina*. These two intervals, which are characterized by low-diversity agglutinated assemblages and are older than 12.5 Ma, may be correlative in Holes U1425B and U1425D. However, they do not correspond to the more diversified *Cibicidoides wuellerstorfi* Assemblage Zone defining the "First Foram Sharp Line" (~14 Ma), which was identified at ODP Site 797 in the Yamato Basin by Nomura (1992). This more diversified calcareous assemblage was not recovered at Site U1425.

Overall, the highly variable composition of assemblages at Site U1425 suggests marked variations in oxygenation at the seafloor and intense carbonate dissolution, in particular during the Pliocene and Miocene. Moderately to well-preserved diatoms and radiolarians are common to abundant in residues >150 and >63 µm throughout the succession, becoming dominant deeper than ~134 m CSF-A. Ostracods were not found in any of the samples examined.

Mudline samples

Mudline samples from Holes U1425B and U1425C were gently washed in order to preserve fragile agglutinated specimens with extremely low fossilization potential. The mudline sample from Hole U1425B contains planktonic foraminifers that show partial dissolution. The planktonic foraminifers include *N. pachyderma* (sinistral), *G. bulloides, G. umbilicata*, and *G. quinqueloba*. Benthic foraminifers include mainly *M. echigoensis, B. pacifica, Haplophragmoides sphaeriloculum*, and *Paratrochammina challengeri* with rare *Cassidulina teretis* and *Reophax scorpiusus* (Fig. **F36**). The thin, delicate tests of *B. pacifica* and the fragile, organically cemented agglutinated tests of *H. sphaeriloculum, P. challengeri*, and *R. scorpiusus* have extremely low fossilization potential in contrast to *M. echigoensis*, which frequently occurs in Pleistocene core catcher samples at this site. The mudline sample from Hole U1425B also contains calcareous nannofossils with moderate to poor preservation. Specimens of *C. pelagicus* (Fig. **F32**) and *G. oceanica* were found together with broken shields of *E. huxleyi* (according to light microscope and scanning electron microscope observations). Diatoms are abundant, but no ostracods were recorded in the mudline sample from Hole U1425B.

Geochemistry

Site U1425 is located on the Yamato Rise, ~54 km northeast of Site 799 (see **"Background and objectives"**). With the fairly comprehensive geochemistry data sets of Site 799 (Shipboard Scientific Party, 1990) as guidance, we returned to our basic Expedition 346 sample program (**"Geochemistry"** in the "Methods" chapter [Tada et al., 2015b]), but with three modifications.

We initially planned to collect two squeezed interstitial water (IW-Sq) samples per core on the deepest hole until the base of APC coring. However, we scaled this back, given our newly acquired appreciation for sample flow through the Chemistry Laboratory. We instead took two IW-Sq samples per core through the upper 100 m and one IW-Sq sample per core deeper than this depth.

By arrival at Site U1425, some geochemical results from Site U1424 had emerged. Among these exciting results, the analyses of Rhizon interstitial water (IW-Rh) samples from across Core 346-U1424A-1H (a "mudline" core) suggested prominent inflections in dissolved NH_4^+, Mn, and Fe profiles within the uppermost 1 m below the seafloor (see **"Geochemistry"** in the "Site U1424" chapter [Tada et al., 2015e]). Presumably, the inflections represent thin depth horizons where microbes consume the three species. Encouraged by our ability to connect detailed interstitial water profiles across key intervals to broader interstitial water profiles generated through conventional squeezing, we offered a plan to collect numerous Rhizons across mudline cores at Site U1425 (Fig. **F37**).

A series of light and dark intervals characterize the uppermost lithologic unit at Sites U1422–U1424 as well as at other locations throughout the marginal sea (Föllmi et al., 1992; Tada et al., 1992). To aid shore-based sampling and research, we thought it desirable to quantify differences in organic carbon between some of these intervals.

Sample summary

During operations at Site U1425, the geochemistry group collected and analyzed a range of samples. These included the following (Tables **T10, T11, T12, T13, T14**):

- 2 mudline (ML) samples from bottom water poured from the uppermost core liner at Holes U1425B and U1425D.
- 55 interstitial water samples from whole-round squeezing (IW-Sq) from Hole U1425B. Most whole rounds were nominally 5–6 cm long.
- 84 interstitial water samples from Rhizons (IW-Rh) from Holes U1425A (7), U1425B (27), U1425D (23), and U1425E (27). The samples from Hole U1425A were used to evaluate whether water flow increased and sediment cracking decreased if Rhizons were dipped in deionized water prior to insertion. The Rhizons from Hole U1425D were taken because during operations the presence of a mudline was not certain for Hole U1425B. The Rhizons from Hole U1425E were taken on our second visit to the site to complement onshore studies.
- 56 sediment samples from the interstitial water squeeze cakes.

- 12 additional sediment samples from Core 346-U1425B-1H to examine changes in solid-phase chemistry associated with light and dark cycles (Table **T11**).
- 71 headspace (HS) gas samples.

No Vacutainer (VAC) samples were taken at this site.

Carbonate and organic carbon

The solid-phase geochemistry profiles at Site U1425 (Fig. **F38**) are fairly similar to those at Site 799 (Shipboard Scientific Party, 1990). In general, sediment samples have low $CaCO_3$ contents. Higher quantities (0.4–11.2 wt%; mean = 4.6 wt%) are found at the top within Unit I, whereas very small amounts (mean = 0.9 wt%) are found in basal units. Nonetheless, compared to results from Sites U1422–U1424, Unit I at Site U1425 has the highest overall $CaCO_3$ contents observed so far during Expedition 346. One sample at 100.25 m CSF-A in Subunit IIA has a very high $CaCO_3$ content of 17.7 wt%.

Site U1425 appears to have lower $CaCO_3$ values than sediment at Site 799 (Shipboard Scientific Party, 1990). Carbonate contents over the uppermost 400 m at Site 799 average 6.9 wt%, with a range between 0.2 and 51.7 wt%. As the water depths of Sites U1425 (1971 m) and 799 (2073 m) are similar, the difference in $CaCO_3$ content may be a consequence of our sampling strategy, where most sediment samples are the remains of IW-Sq samples. Certainly, numerous carbonate layers exist at both locations (see **"Lithostratigraphy"**).

In contrast to $CaCO_3$, organic carbon contents are moderately high for marine sediment (Müller and Suess, 1979; Emerson and Hedges, 1988). This is particularly true for the upper portion of Subunit IA and for Unit III (Fig. **F38**). The total organic carbon (TOC) contents of Subunit IA average 1.23 wt% with a range of 0.29–2.46 wt%. Subunits IB and IIA have lower TOC contents, on average 0.8 and 1.0 wt%, respectively. Subunit IIB has low TOC contents until ~200 m CSF-A, where values increase with depth, eventually reaching 2.4 wt%. Subunits IIIA and IIIB are the richest regarding TOC, with an average of 3.1 wt% and a range of 1.5–4.7 wt% across both units. Interestingly, the transition between these two units has lower TOC, although values are still ~2 wt%, which is high for marine sediment (Müller and Suess, 1979; Emerson and Hedges, 1988).

When examining the overall TOC profile (Fig. **F38**), it is important to consider that squeeze cakes are compressed intervals 5–10 cm in length and arbitrarily selected with regard to lithologic horizons. As such, a different result is obtained when centimeter-scale samples are taken from light and dark sediment layers of Subunit IA (Table **T11**). Between 0 and 7.4 m CSF-A, discrete sediment samples representing different color intervals (see **"Physical properties"**) show high variability, from 0.4 to 5.1 wt% (average = 2.3 wt%).

In summary, the total carbon (TC) contents of sediment at Site U1425 derive from organic and inorganic carbon at shallow depths (<200 m CSF-A), especially in Unit I. At deeper depths, organic carbon content mainly controls the abundance of TC.

The mean value of total nitrogen (TN) is 0.24 wt%. With the exception of some samples from Subunit IA where TN can exceed 0.5 wt%, the maximum TN content is 0.41 wt% at 328.6 m CSF-A. Minima in TN contents of 0.16 wt% are found at 100.25 and 176.05 m CSF-A. Deeper than 200 m CSF-A, TN contents clearly track TOC contents. In fact, the C:N ratio for samples from Unit III averages 8.2.

Manganese and iron

Dissolved Mn and Fe exhibit intriguing profiles with respect to depth when analyses from mudline, IW-Sq, and IW-Rh samples are merged (Figs. **F39, F40**). Notably, downhole changes in these species, particularly Fe, occur over stratigraphic distances too short to examine with the size (10 cm long) and spacing (>1 m) of samples typically taken for squeezing (Fig. **F39**).

Manganese is ~1 µM in the mudline sample. Within 5 cm of the apparent seafloor, concentrations rise to 76 µM (Fig. **F40**). From this depth, dissolved Mn decreases to 35 µM at 0.9 m CSF-A and then more gradually decreases to 2 µM by 17 m CSF-A (Fig. **F39**). Manganese concentrations remain low until 52 m CSF-A then increase, reaching almost 77 µM by 245 m CSF-A. Dissolved Mn decreases to <35 µM between 320 and 360 m CSF-A, which is the opal-A–opal-CT transition (see **"Silica"**). Mn concentrations of IW-Rh samples are similar to those of IW-Sq from similar depths (Fig. **F40**).

The Mn profile at Site U1425 is similar to that at Site 799 (Shipboard Scientific Party, 1990), except that concentrations are significantly higher at the new drill location. The cause of the basic Mn profile at both sites has been discussed, in both previous chapters of this volume and in chapters of ODP Leg 128 (Ingle, Suyehiro, von Breymann, et al., 1990). Assuming that dissolved Mn concentrations at depth are related to equilibrium with Mn carbonate phases (Middelburg et al., 1987), a basic explanation for the differences in dissolved Mn concentrations between the sites is that alkalinity is lower at Site U1425 compared to Site 799. This is the case, as discussed below.

The mudline sample has an Fe concentration of 1.1 µM, which is near the detection limit (1 µM at this site). Below the seafloor and as observed at previous sites drilled during Expedition 346, the dissolved Fe profile is complicated (Fig. **F39**). Considering only the IW-Sq samples, Fe concentrations fluctuate between 2 and 6 µM until ~180 m CSF-A. From here to the base of the hole, Fe concentrations are near detection limit, except for a peak centered at ~320 m CSF-A. Importantly, the Fe profile is not "smooth," suggesting either problems obtaining precise dissolved Fe concentrations using samples from the squeezers, numerous depth zones where Fe-bearing minerals dissolve or precipitate, or some combination of both. Analyses of the IW-Rh samples from the upper 9 m (Fig. **F40**) are interesting in this regard. The Fe profile constructed using Rhizons shows peaks that suggest dissolution of a solid Fe phase in the upper 1 m and perhaps at ~2.4 m CSF-A, but almost all Fe existing in solid Fe phases across other depths. The difference between IW-Sq and IW-Rh Fe concentrations at ~6 m CSF-A could represent Fe precipitation during Rhizon collection, Fe contamination during squeezing, or both. Iron was not measured at Site 799, so there is no comparison to previous studies.

Sulfate and barium

Dissolved SO_4^{2-} concentration at the mudline was 28 mM, which is close to the expected 28.1 mM for Japan Sea Proper Water (JSPW) (Table **T10** in the "Methods" chapter [Tada et al., 2015b]). Below the seafloor, the dissolved SO_4^{2-} profile systematically decreases with a concave downward shape to between 60 and 70 m CSF-A, where SO_4^{2-} concentrations decrease below 0.5 mM (Fig. **F41**). SO_4^{2-} concentrations of IW-Sq and IW-Rh samples are similar.

The dissolved Ba profile displays a shape opposite that of SO_4^{2-} (Fig. **F42**), similar to other sites drilled in the marginal sea (von Breymann et al., 1992) and during Expedition 346. Barium concentrations are <25 µM from the seafloor to 48 m CSF-A. At this depth, values rise considerably. As described in the **"Methods"** chapter [Tada et al., 2015b]), high Ba concentrations are unconstrained and require postcruise analyses to check and rescale high Ba concentrations. Similar to previous sites, Ba concentrations of IW-Sq samples are consistently higher than those of IW-Rh samples (Fig. **F42**).

Given Fick's law (Fick, 1855) and assuming constant porosity and temperature with depth, the shape of the SO_4^{2-} profile suggests continual loss of SO_4^{2-} over the uppermost ~70 m below the seafloor. Such removal contrasts to that inferred from a linear SO_4^{2-} gradient, which suggests focused SO_4^{2-} consumption over a short depth horizon. The SO_4^{2-} profile, therefore, may indicate that organoclastic sulfate reduction, rather than anaerobic oxidation of methane (AOM), removes much of the SO_4^{2-} from interstitial water at Site U1425. The general lack of CH_4 until 60 m CSF-A (Fig. **F41**) may provide additional support for this hypothesis. Note, however, that a concave downward SO_4^{2-} profile will appear when AOM dominates net SO_4^{2-} loss across a short depth horizon if temperature increases significantly between the seafloor and the horizon of interest (Dickens, 2001). With the steep geothermal gradient of 104°C/km at Site U1425 (see **"Downhole measurements"**), numerical modeling is needed to elucidate the cause of SO_4^{2-} depletion and check the sensitivity of the system to variations in other parameters (e.g., porosity).

As discussed at previous sites, the removal of interstitial water SO_4^{2-} eventually leads to barite dissolution. In turn, such dissolution releases large quantities of dissolved Ba to interstitial water (von Breymann et al., 1992). Passage of very small barite crystals through 0.45 µm filters during squeezing or barite precipitation during Rhizon sampling may explain the differences in dissolved Ba concentrations across IW-Sq and IW-Rh samples (see **"Geochemistry"** in the "Site U1424" chapter [Tada et al., 2015e]).

Volatile hydrocarbons

The downhole CH_4 profile at Site U1425 (Figs. **F41, F43**) reflects several processes, including CH_4 production and consumption in the sediment column and degassing during coring and core retrieval.

Methane concentrations in HS samples are <20 ppmv from the seafloor to ~60 m CSF-A (Table **T14**). At this depth, which corresponds to the horizon where interstitial water SO_4^{2-} concentrations approach detection limit (Fig. **F41**), CH_4 values increase relatively slowly, reaching 17,300 ppmv at 185 m CSF-A. Deeper than this depth, CH_4 concentrations fluctuate between 19,720 and 8,800 ppmv until 320 m CSF-A. Relatively low CH_4 concentrations appear at depths of XCB drilling (i.e., 100, 283, and 330–403 m CSF-A).

Ethane concentrations range between 0 and 42 ppmv across all samples. Consequently, the C1:C2 ratio generally exceeds 500 at Site U1425.

At Site U1425, microbes use dissolved SO_4^{2-} to consume significant amounts of organic matter. However, a small fraction of organic matter passes through the sulfate reduction zone, where microbes use it to form biogenic gas, composed of almost pure CH_4. The methane gradient between 60 and 120 m

CSF-A, although difficult to quantify with HS samples from indurated sediment, is very low. The upward diffusive flux of CH_4 implied by this gradient may not be sufficient to counteract the downward burial flux of CH_4. Consequently, a prominent sulfate–methane transition, such as that found at Site U1422, does not occur at Site U1425 (Fig. F41).

Alkalinity, ammonium, and phosphate

The alkalinity, NH_4^+, and PO_4^{3-} profiles at Site U1425 (Fig. F44) are broadly similar to those at sites previously drilled during Expedition 346. The profiles using Rhizons through the upper 2 m CSF-A appear similar to those generated using squeezers (Fig. F45), although it is difficult to make rigorous comparisons given the depth frequency of samples, depth offsets between holes, and times between sample recovery and analyses. In particular, because of precruise concerns that alkalinity could not be measured on IW-Rh samples accurately, alkalinity was measured on squeezed samples as soon as water was collected but was measured on IW-Rh samples typically after waiting for >12 h. During this waiting period, IW-Rh samples were kept in original sampling syringes without any headspace and refrigerated.

Alkalinity steadily increases from 2.5 mM at the seafloor to 32 mM at 106 m CSF-A and remains at 32 mM until 133 m CSF-A (Table T12). This increase exhibits a clear concave downward profile with no prominent concave downward inflections, such as at Site U1422. The alkalinity maximum coincides with a dolomite horizon (see **"Lithostratigraphy"**). Below the maximum, alkalinity decreases steadily to 9 mM at ~400 m CSF-A. The lack of a kink in alkalinity within the upper sediment column is informative: at Site U1425, there is no evidence for significant addition of alkalinity across a short depth horizon, as would be expected if AOM was an important process.

Ammonium increases from 21 µM in the mudline sample to 4100 µM at ~329 m CSF-A. Deeper than this depth, NH_4^+ decreases to ~2800 µM at the base of the Hole U1425B (~400 m CSF-A). The profile is generally concave downward until 325 m CSF-A. Analyses of closely spaced Rhizon samples across the upper 2 m in both Holes U1425B and U1425D indicate that the steep NH_4^+ profile is nearly linear and intersects the seafloor (Fig. F45).

Phosphate increases from 9 µM at the seafloor to 83 µM at ~15 m CSF-A. Deeper than this depth, PO_4^{3-} decreases steadily to <20 µM at ~300 m CSF-A. This decrease in PO_4^{3-} has a concave downward profile. A few apparently anomalous PO_4^{3-} values occur at depth.

The general explanations for downcore variations in alkalinity, NH_4^+, and PO_4^{3-} profiles are the same as those provided in previous chapters of this volume and elsewhere (Murray et al., 1992). The only significant additional commentary on this matter is that Site U1425, along with the other sites, provides a spectrum of sites to investigate organic carbon decomposition.

Assuming the seafloor (mudline) was not missed twice during coring, NH_4^+ seems to be escaping to deep water at this location (Fig. F45). The finding is especially intriguing when one considers two comparisons: (1) the 400 m of sediment at Site U1425 is approximately one-fifth the thickness of the overlying water mass and (2) the average NH_4^+ concentration in interstitial water (~3000 µM) is ~120 times greater than the average NO_3^- concentration of water in the marginal sea (~25 µM) (Kim et al., 1992). Even considering sediment porosity, the apparently leaky subseafloor nitrogen pool, if extensive, must be extremely large relative to the overlying water mass nitrogen pool.

Bromide

The two mudline samples contain 0.84 mM Br^- (Table T12; Fig. F46). This value is identical to that expected for JSPW (Table T10 in the "Methods" chapter [Tada et al., 2015b]). Below the seafloor, Br^- concentrations slowly increase with depth, such that interstitial water samples at the base of the cored sequence have values of 0.93–0.94 mM.

The Br^- profile has a fair amount of scatter because of analytical precision. Nonetheless, the overall consistency of the profile at Site U1425 suggests that meaningful Br^- profiles might be generated using the new ion chromatograph, especially if sites with higher Br^- concentrations are encountered in the future. In terms of interpretation, the increase in dissolved Br^- with depth suggests that modest amounts of organic carbon have decomposed over time (Martin et al., 1993).

Yellowness/Absorbance

A total of 79 interstitial water samples were measured for absorbance at 325 and 227 nm (Table T13; Fig. F47). The totality examined included both IW-Sq (51) and IW-Rh (28) samples taken from three holes (Holes U1425A, U1425B, and U1425D). Because IW-Sq samples were collected from three holes with depths drilled at different times over 4 days, samples were analyzed in several batches. To assess absorbance precision, several samples were examined repeatedly.

As at previous sites during Expedition 346, interstitial water at Site U1425 did not visually appear yellow. Nevertheless, for both wavelengths examined, the absorbance of interstitial water changes systematically downhole (Fig. F47). At 325 nm, absorbance increases from 0.009 in the mudline sample to 0.257 at ~34 m CSF-A. Values then decrease to 0.034 at ~310 m CSF-A. At 227 nm, absorbance increases from 0.092 in the mudline sample to 1.638 at ~34 m CSF-A. Values then slowly decrease to 0.892 at ~310 m CSF-A. Thus, for both wavelengths, there is a steep increase in absorbance to a shallow maximum, as well as a gradual decline in absorbance with further depth, but the decrease is more pronounced at the 325 nm wavelength. However, it is not entirely certain how interstitial water absorbance scales with concentration. Samples should be diluted serially and reexamined, especially at 325 nm, where absorbance exceeds 1.0.

The downhole changes in absorbance broadly correspond to those of alkalinity and PO_4^{3-} (Fig. F44). This supports the idea that the color of interstitial water derives from some component released during the decomposition of solid organic matter, such as a fraction of dissolved organic carbon (Briucaud et al., 1981; You et al., 1993).

The above reporting on interstitial water color at Site U1425 raises two additional questions. First, for several samples from Core 346-U1425A-4H, the absorbance at 325 nm decreased after several days. Second, when dissolved $HgCl_2$ was added to several interstitial water samples from Core 4H (during poisoning for shore-based carbon isotope analyses), a yellow-brown color immediately appeared and a black solid precipitated within 2 days. The second change most likely resulted from the following reaction:

$$HgCl_{2(aq)} + H_2S_{(g)} \rightarrow HgS_{(s)} + 2H^+_{(aq)} + Cl^-_{(aq)}.$$

If this is the case and although fine-grained HgS precipitates do not exist in the interstitial water naturally, the above observations raise the possibility that, at least for some samples, some of the absorbance at low wavelengths may result from hydrogen sulfide or a fine-grained precipitate thereof.

Splits of several interstitial water samples from Site U1425 were removed for testing of absorbance after time and after experimentation, such as purging with N_2. The results are not completed at this juncture.

Calcium, magnesium, and strontium

The dissolved Ca, Mg, and Sr profiles (Table T12; Fig. F48) have similar shapes to those at several previously drilled sites in the marginal sea (Murray et al., 1992) and other locations (Gieskes and Lawrence, 1981). Mg and Ca concentrations of IW-Sq and IW-Rh samples are similar (Fig. F49). As at previous sites, Sr concentrations of interstitial water from Rhizons are significantly higher than those from squeezers.

Dissolved Ca is 10.0 mM in the mudline sample, which is slightly less than the 10.2 mM expected for JSPW (Table T10 in the “Methods” chapter [Tada et al., 2015b]). From the seafloor, Ca concentrations decrease to ~4.2 mM at ~53 m CSF-A. Deeper than this depth, Ca concentrations steadily increase to ~23 mM at ~400 m CSF-A, the base of the cored hole.

The mudline sample has a dissolved Mg concentration of 51.3 mM, which compares to 52.7 mM inferred for JSPW (Table T10 in the “Methods” chapter [Tada et al., 2015b]). Interstitial water Mg decreases below the seafloor to ~40 mM at ~53 m CSF-A. As observed at previously drilled sites during Expedition 346, the decrease in dissolved Mg concentrations within shallowly buried sediment is about twice the decrease in dissolved Ca concentrations. As also observed at the other drilled sites, Mg concentrations decrease deeper than 53 m CSF-A, reaching ~16 mM at ~400 m CSF-A.

Dissolved Sr is 92.8 µM in the uppermost IW-Sq sample below the seafloor (1.45 m CSF-A), which is slightly higher than the 90.5 µM expected for JSPW (Table T10 in the “Methods” chapter [Tada et al., 2015b]). Deeper than this depth, Sr concentrations slowly rise, reaching 234 µM at ~100 m CSF-A. Values are erratic (but high, >200 µM) from ~100 m CSF-A to the base of the cored hole.

Dolomite formation likely drives the decreases in dissolved Ca and Mg (Sayles and Manheim, 1975; Moore et al., 2004), even though AOM probably does not dominate SO_4^{2-} consumption at Site U1425. As noted previously (see **“Geochemistry”** in the “Site U1422” chapter [Tada et al., 2015c]), the key to suggesting dolomite precipitation lies in Ca and Mg flux calculations throughout the upper sediment column (Moore et al., 2004) rather than changes in Ca and Mg concentrations between the seafloor and the minimum in dissolved Ca and Mg. In any case, although AOM may enhance dolomite precipitation (Moore et al., 2004), it is not the proximal cause because all sites drilled so far have compelling evidence for dolomite precipitation, independent of whether AOM appears to be dominant or subordinate. The loss of SO_4^{2-}, irrespective of cause, may be the primary driver for dolomite formation in the sediment (Baker and Kastner, 1981).

Chlorinity and sodium

Cl^- concentration of the mudline sample is 544 mM, which compares to 544 mM for inferred JSPW (Table **T10** in the "Methods" chapter [Tada et al., 2015b]). Below the seafloor, the Cl^- profile (Table **T12;** Fig. **F50**) shows anomalously low concentrations (<540 mM) until 77 m CSF-A. This pattern is consistent with those found at Sites U1422–U1424 and supports the idea that deep water of the marginal sea was less saline sometime in the recent past, perhaps during the Last Glacial Maximum. Interestingly, deeper than 50 m CSF-A, most Cl^- values are less than that of present-day bottom water. We speculate that, on average and over the long term, deep water of the sea was less saline than modern JSPW.

The Na profile at Site U1425 (Table **T12;** Figs. **F50, F51**) shows considerable scatter, and the mudline sample has a value of 454 mM, which is significantly less than the 468 mM expected for JSPW (Table **T10** in the "Methods" chapter [Tada et al., 2015b]). Nonetheless, the Na profile generally shows lower values than present-day bottom water over much of the cored sedimentary sequence, including the upper 50 m below the seafloor.

Potassium

The K profile at Site U1425 (Table **T12;** Figs. **F50, F51**) resembles that at other sites drilled to date during Expedition 346. K concentration of the mudline sample is 10.8 mM, which is close to the 10.2 mM expected for JSPW (Table **T10** in the "Methods" chapter [Tada et al., 2015b]). Immediately beneath the seafloor, K concentrations increase significantly, a phenomenon observed at all sites. The increase in K is greater in IW-Sq samples (to ~12.9 mM) than in IW-Rh samples (to ~11.5 mM) (Fig. **F51**). K then systematically decreases with depth, reaching 4 mM at the base of the cored sequence.

The rapid increase in dissolved K beneath the seafloor, consistent at all sites drilled, may represent a temperature effect. When clay-rich cores recovered from cold temperatures at in situ conditions are squeezed at room temperature, several studies have shown that certain ions, especially K^+, are released to interstitial water (Sayles and Manheim, 1975). In fact, the typical increase in K^+ concentration for a sample just below the seafloor is ~1.5 mM (Sayles and Manheim, 1975), which is approximately what we observe. If this explanation is correct, the Rhizons may be collecting water at colder temperature, at least for shallowly buried samples, presumably because samples are disaggregated before squeezing. The steady decrease in K toward basement results from alteration with basalt (Murray et al., 1992).

Boron and lithium

The dissolved B and Li profiles (Table **T12;** Fig. **F52**) resemble those at previous sites drilled during Expedition 346. Li concentration is 29 µm at the seafloor and increases to 45 µM at ~72 m CSF-A. Concentrations then rise more rapidly, such that Li reaches 201 µM at ~400 m CSF-A.

The B profile shows much scatter, but overall trends can still be recognized. Close to the seafloor, B concentrations range from 600 ± 50 µM. They decrease to range from 500 to 550 µM at ~10 m CSF-A. At deeper depths, B resembles the dissolved Si curve (see next section) as it increases to a maximum concentration of 826 µM and decreases rapidly at the opal-A/opal-CT horizon.

Silica

Dissolved silica (H_4SiO_4) concentrations exhibit a classic profile at Site U1425 (Table **T12;** Fig. **F52**). Concentration is 447 µm in the mudline sample, which is at 0.4°C (see **"Downhole measurements"**), and rapidly increases to >600 µm by 10 m CSF-A. Deeper than this depth, H_4SiO_4 steadily increases to ~1430 µm at 320 m CSF-A, which is at ~34°C, given the geothermal gradient of 104°C/km (see **"Downhole measurements"**). From ~320 to 360 m CSF-A, concentrations decrease to ~600 µm.

The H_4SiO_4 profile at Site U1425 is similar to those determined at other drill sites in the marginal sea (Murray et al., 1992). Consistent with this work, there appears a relatively straightforward explanation (Kastner et al., 1977; and many others). Biogenic silica begins dissolving on the seafloor and within the uppermost few meters below the seafloor. However, the amount of dissolution is limited by the solubility of opal-A, which is modest but increases with temperature. Hence, dissolved H_4SiO_4 concentrations quickly reach equilibrium with opal-A and slowly increase with depth along the geothermal gradient. At 320 m CSF-A, opal-CT begins to form, and by 360 m CSF-A, H_4SiO_4 concentration is in equilibrium with opal-CT.

Rhizon commentary

Our experimentation with Rhizon samples during Expedition 346 continued at Site U1425. As at previous sites (U1422 and U1424), the use of Rhizons during scientific drilling expeditions shows great potential but also raises some issues. Clearly, over wide concentration ranges, samples taken through conventional squeezing and Rhizons give very similar values for multiple dissolved species (Figs. F40, F41, F45, F49). In detail, however, there remain some issues.

Following the Rhizon campaign at Site U1424, the geochemistry group constructed a detailed plan for Rhizon sampling at Site U1425 before drilling commenced (Fig. F37). It was not clear if the mudline was captured in Hole U1424B, so additional Rhizons were placed at the top of Hole U1424D.

We took several Rhizons from Cores 346-U1424D-4H and 5H to see if the difficult penetration and low water flow encountered at Site U1423 recurred. They did, as these Rhizons also had water flow problems. In addition to lithology, syringe suction capabilities had an effect on extraction time. Newer syringes performed better than preused and acid-washed syringes.

After completing the interstitial water program at Site U1424 (and after collecting samples at Site U1425), we noted several issues when examining concentration data from IW-Sq and IW-Rh samples together. First, for some elements, notably Ba and Fe, samples collected from Rhizons consistently and systematically gave different values than samples obtained from squeezing. The same is true at Site U1425, as evidenced by comparing dissolved concentrations in IW-Sq and IW-Rh samples taken from short depth intervals in the same hole. For example, Ba concentrations in IW-Sq samples are consistently higher than in IW-Rh samples (Fig. F42), and Fe concentrations in IW-Sq samples are generally higher and show more scatter than in the IW-Rh samples (Fig. F40). We have not yet identified the cause of such variance, but we speculate that it may involve tiny particles of perhaps barite or microbially synthesized magnetite passing through the squeezer filter (0.45 µm) and not through the Rhizon porous membrane (0.2 µm). To examine the possibility of a Rhizon blank, we soaked two sets of Rhizons for 1 h, one in deionized water and one in synthetic seawater. We then pulled the water through the Rhizons and analyzed the water by inductively coupled plasma–atomic emission spectroscopy. Concentrations of all elements examined were below detection.

Preliminary conclusions

Similar to previous sites drilled during Expedition 346, the accumulation of organic matter and subsequent microbial diagenesis of this material strongly affect the geochemistry at Site U1425. Sediment in the upper ~200 m below seafloor averages ~1 wt% organic carbon. In the upper 1 m, reactions between this organic matter and metal oxides lead to maxima in dissolved Mn and dissolved Fe, along with increases in HCO_3^-, NH_4^+, and PO_4^{3-}. With continued burial, organic matter reacts with dissolved SO_4^{2-}, which releases additional HCO_3^-, NH_4^+, and PO_4^{3-} to interstitial water. Much of the organic matter decomposition at Site U1425 occurs through sulfate reduction, as evident by the high-resolution concave upward SO_4^{2-} profile that extends to zero concentration at 60 m CSF-A. This consumption of SO_4^{2-} and production of alkalinity also drives precipitation of authigenic carbonate, probably dolomite, within the uppermost 60 m of the sequence. Deeper than this depth, CH_4 concentrations slowly increase, eventually surpassing shipboard saturation conditions (1 atm) at ~150 m CSF-A. Dissolved H_4SiO_4 concentrations steadily increase below the seafloor until ~320 m CSF-A, where upon they decrease rapidly, presumably because opal-A converts to opal-CT.

Paleomagnetism

Paleomagnetic samples and measurements

Paleomagnetic investigations at Site U1425 included measurement of magnetic susceptibility of whole-core and archive-half split-core sections and of natural remanent magnetization (NRM) of archive-half sections. NRM was measured before and after alternating field (AF) demagnetization with a 20 mT peak field for all archive-half sections from Hole U1425B at 5 cm intervals. Because of increased core flow and limited measurement time available at the paleomagnetism station, NRM of archive-half sections from Hole U1425D were measured only after 20 mT AF demagnetization at 5 cm intervals. The FlexIT core orientation tool (see "Paleomagnetism" in the "Methods" chapter [Tada et al., 2015b]) was used to orient Cores 346-U1425B-2H through 12H and 14H. The APC-collected core orientation data for Hole U1425B that are reported in Table T15.

We collected paleomagnetic discrete cube samples (see "Paleomagnetism" in the "Methods" chapter

[Tada et al., 2015b]) from the first section of 52 cores in Hole U1425B and occasionally from deep sections when the first section was not suitable for collecting discrete cube sample (Fig. F53). Stepwise AF demagnetization on 35 discrete samples collected from Hole U1425B was performed at successive peak fields of 0, 5, 10, 15, 20, 25, 30, 40, 50, and 60 mT to verify the reliability of the split-core measurements and to determine the demagnetization behavior of the recovered sediment. Depth levels where the measured discrete samples were collected are marked as orange triangles along the inclination data column in Figure F53. To avoid potential acquisition of anhysteretic remanent magnetization (ARM) during AF demagnetization, which was observed in discrete sample measurements from Sites U1422 and U1423, especially at high AF peak fields (see **"Paleomagnetism"** in the "Site U1422" chapter and **"Paleomagnetism"** in the "Site U1423" chapter [Tada et al., 2015c, 2015d]), we followed the Expedition 318 Scientists (2011) protocol to demagnetize and measure the discrete samples multiple times at each demagnetization level. The measurements acquired at each demagnetization step were then averaged to cancel out potential ARM acquisition during AF demagnetization (see **"Paleomagnetism"** in the "Methods" chapter [Tada et al., 2015b]).

We processed data extracted from the shipboard Laboratory Information Management System (LIMS) database by removing all measurements collected from disturbed and void intervals and all measurements that were made within 10 cm of the section ends, which are slightly biased by measurement edge effects. The XCB-cored archive-half sections of Holes U1425B and U1425D frequently contain drilling "biscuits" surrounded by as much disturbed material as intact material, strongly compromising the quality of the resulting paleomagnetic data. We removed data collected within those disturbed intervals of the 11 measured XCB-cored archive-half sections. For declination data from cores in Hole U1425B where FlexIT tool data are available, we corrected the declination values for each core using estimated orientation angles. A modified version of the UPmag software (Xuan and Channell, 2009) was used to analyze the NRM data of both the split-core section and the discrete cube samples. The disturbed and void intervals used in this process are reported in Table T16. The processed NRM inclination, declination, and intensity data after 20 mT AF demagnetization are reported in Table T17 and shown in Figure F53.

Natural remanent magnetization and magnetic susceptibility

NRM intensity after 20 mT AF demagnetization in the two measured holes at Site U1425 is similar in magnitude for overlapping intervals, mostly ranging between ~10^{-5} and 10^{-2} A/m. For the top ~50 m of the recovered sediment, NRM intensity of the measured core sections after 20 mT demagnetization is on the order of 10^{-3} to 10^{-2} A/m. NRM intensity gradually decreases downcore to ~10^{-4} to 10^{-3} A/m between ~50 and ~125 m CSF-A, and to ~10^{-5} to 10^{-4} A/m between ~125 and ~250 m CSF-A. Deeper than ~250 m CSF-A until the bottom of the holes, NRM intensity appears to gradually increase from below 10^{-4} to ~10^{-3} A/m. For some cores in Hole U1425B (e.g., Cores 346-U1425B-34H and 35H) and a few cores in Hole U1425D (e.g., Cores 346-U1425D-16H to 25H and Core 32H), NRM intensity of the top part of the cores appears to be dramatically (one to two magnitudes) higher than that of the bottom part. These intensity changes are not accompanied by similar changes in magnetic susceptibility and are more likely artifacts related to remanence acquired during the coring process.

The typical well-behaved AF demagnetization behavior of 8 out of the 35 measured discrete samples is illustrated in Figure F54. Declination and inclination values acquired from the discrete sample measurement generally agree well with the split-core measurement after 20 mT AF demagnetization. All samples exhibit a steep, normal overprint that was generally removed after AF demagnetization at peak fields of ~15–20 mT, demonstrating that the 20 mT AF demagnetization is, in general, sufficient to eliminate the drilling overprint. Discrete sample measurements acquired using the Expedition 318 Scientists (2011) protocol show generally reduced ARM acquisition. However, some measured samples still appear to acquire remanence during AF demagnetization especially at high peak field demagnetization steps (>40–50 mT) (e.g., Fig. **F54B–F54E**). This is possibly related to changes in ambient field on the ship during the measurements and the fact that some of the samples are too weak to be measured accurately using the shipboard superconducting rock magnetometer.

Magnetic susceptibility measurements were taken on whole cores from all holes as part of the Whole-Round Multisensor Logger (WRMSL) analysis and on archive-half sections using the Section Half Multisensor Logger (SHMSL) (see **"Physical properties"**). The WRMSL acquired susceptibility was stored in the database in raw meter units. These were multiplied by a factor of 0.68 × 10^{-5} to convert to the dimensionless volume SI unit (Blum, 1997). A factor of (67/80) × 10^{-5} was multiplied by the SHMSL acquired susceptibility stored in the database. Magnetic susceptibility measurement is consistent between the two instruments and varies between 5 × 10^{-5} and 20 × 10^{-5} SI for sediment from the top ~80 m of the holes, and are generally <5 × 10^{-5} SI for sediment from between ~80 and ~250 m CSF-A (Fig. F53, fourth panel). Deeper than ~250 m CSF-A to the bottom of the holes, magnetic susceptibility appears to gradually increase from <5 × 10^{-5} SI to ~10 × 10^{-5} SI. Except for the intervals where NRM intensity is abnormally high in the top part of the cores (e.g., Cores 346-U1425B-34H and 35H and Cores 346-U1425D-16H through 25H and 32H), magnetic susceptibility, in general, mimics NRM intensity, suggesting that the magnetic minerals that carry NRM are the same or at least coexist with those that dominate magnetic susceptibility.

Magnetostratigraphy

Paleomagnetic inclination and declination data from Site U1425 show patterns that allow for the determination of magnetic polarity for at least the uppermost ~90 m of recovered sediment. Compared with Hole U1425D, paleomagnetic directions appear to be more stable and better preserved in Hole U1425B. Both magnetic declination and inclination after 20 mT AF demagnetization were used when possible for the magnetostratigraphic interpretation at Site U1425. The geomagnetic field at the latitude of Site U1425 (39.49°N) has an expected inclination of 58.75°, assuming a geocentric axial dipole field model, which is sufficiently steep to determine magnetic polarity in APC cores that lack horizontal orientation. We identified the Brunhes/Matuyama boundary (0.781 Ma) and the Jaramillo (0.988–1.072 Ma) and Olduvai (1.778–1.945 Ma) Subchrons, as well as the Matuyama/Gauss boundary (2.581 Ma) in both Holes U1425B and U1425D (Table T18).

The Brunhes/Matuyama boundary (0.781 Ma) is recorded at ~33.7 m CSF-A in Hole U1425B and at ~34.2 m CSF-A in Hole U1425D. Above this boundary, inclination values after 20 mT AF demagnetization vary closely around the expected positive inclination at the site location in both holes (Fig. F53A, F53C). In Hole U1425B, the FlexIT-corrected declination values show a shift from ~0° to ~180° at this boundary (in Core 346-U1425B-4H). Our interpretation agrees well with the LO of planktonic foraminifer *N. kagaensis* (0.7 Ma) at ~27.04–37.58 m CSF-A in Hole U1425B (see **"Biostratigraphy"**) and is consistent with the results of discrete samples from 20.33 and 38.06 m CSF-A in Hole U1425B. Stepwise demagnetization of discrete samples from 20.33 m CSF-A in Hole U1425B (Fig. F54A) shows a stable and positive inclination that was likely acquired during the Brunhes Chron. The results of a discrete sample from 38.06 m CSF-A in Hole U1425B (Fig. F54B) appears to record negative inclination that is consistent with the interpreted Matuyama age.

We interpret the positive inclination intervals between ~39.2 and 41.4 m CSF-A in Hole U1425B and between ~38.5 and 40.5 m CSF-A in Hole U1425D as recording the Jaramillo Subchron (0.988–1.072 Ma) in both holes. In Hole U1425B, this positive inclination interval is accompanied by FlexIT-corrected declinations varying around 0°. Declinations near the top and bottom of this interval in the two holes both show an apparent ~180° shift, supporting the two depth levels as polarity boundaries suggested by the inclination data.

Between ~57.2 and 69.50 m CSF-A in Hole U1425B, the FlexIT-corrected declination values vary mostly around 0° or 360°, with inclination dominated by positive values close to the expected normal polarity dipole value of the site. We interpret this interval as the Olduvai Subchron (C2n; 1.778–1.945 Ma) recorded in Hole U1425B. In Hole U1425D, the Olduvai Subchron is identified between ~54.2 and 68.4 m CSF-A, during which inclination after 20 mT AF demagnetization appears to be mostly positive and close to the expected normal polarity dipole value. The depth levels of the Olduvai Subchron in the holes are consistent with the LO of radiolarian *A. acquilonium* (1.2–1.7 Ma) at ~46.96–56.53 m CSF-A and the LO of calcareous nannofossil *C. macintyrei* (~1.6 Ma) at ~54.03–56.53 m CSF-A in Hole U1425B (see **"Biostratigraphy"**).

The Matuyama/Gauss boundary (2.581 Ma) was recorded at ~87.8 m CSF-A in Hole U1425B and at ~85.2 m CSF-A in Hole U1425D. The paleomagnetic inclination of samples from the holes after 20 mT AF demagnetization apparently switches from dominantly negative values above this boundary to mostly positive values right below the boundary. In Hole U1425B, the inclination pattern change is accompanied by FlexIT-corrected declination values switching from an average of ~180° to ~0°. Declination of samples from Hole U1425D, although not oriented, also shows an ~180° shift around this boundary in Core 346-U1425D-10H. The depth level of the Matuyama/Gauss boundary in the holes is consistent with a list of biostratigraphic events identified in Hole U1425B (see **"Biostratigraphy"**).

Deeper than ~90 m CSF-A in both holes, NRM intensity is weak and is generally on the order of 10^{-5} to 10^{-4} A/m. NRM inclination after 20 mT AF demagnetization shows mostly positive values that are apparently steeper than the expected dipole inclination. Increased coring disturbance, strong drill string overprint, and the largely scattered paleomagnetic directions makes magnetostratigraphic interpretations difficult for the deep part of the holes at Site U1425.

Physical properties

Physical properties measurements at Site U1425 were conducted to provide high-resolution data on the bulk physical properties and their downhole variations in Holes U1425B and U1425D using the same plan as at previous Sites U1423 and U1424. *P*-wave velocity that was measured in Sections 1, 2, and 3 of each core with the WRMSL was consolidated as one data set using measurements from Holes U1425B and U1425D.

After the sections reached thermal equilibrium with the ambient room temperature of ~20°C, thermal conductivity (one per core) and NGR measurements (eight per full section) completed the suite of whole-core measurements. One half of each split core was reserved for archiving and the other half was for analysis and sampling (working half). Shear stress measurements were performed (most commonly one per core) from 0 to 300 m CSF-A on the working halves of Hole U1425B. Moisture and density (MAD) measurements were performed on discrete core samples (most commonly 1 or 2 per core) collected from the working halves of Hole U1425B and the lower part of Hole U1425D. We also collected MAD samples and accompanying shear stress data from pairs of organic-rich and hemipelagic sediment in Unit I in order to compare the physical properties of two types of sediment layers. Diffuse spectral reflectance (most commonly at 1 cm intervals) and point magnetic susceptibility (most commonly at 2 cm intervals) were measured using the SHMSL on the archive halves. Physical properties measurements are presented in Figures **F55, F56, F57,** and **F58.**

Thermal conductivity

Thermal conductivity was measured once per core using the full-space probe, usually near the middle of Section 4. Thermal conductivity values range from ~0.8 to ~1.2 W/(m·K) and decrease from 0 to ~150 m CSF-A before increasing to the bottom of the recovered section. This broad minimum at ~150 m CSF-A corresponds to lithologic Unit II with low gamma ray attenuation (GRA) bulk density suggesting a compositional control on this parameter.

Moisture and density

Although measurement errors exist in GRA bulk density data because of the presence of air between a core and a core liner, in general, GRA bulk density tends to reflect the characteristic of each lithologic unit (Fig. **F55;** see **"Lithostratigraphy"**). Between 0 and ~200 m CSF-A, GRA bulk density at Site U1425 is largely similar in pattern to previous Sites U1422–U1424. GRA bulk density is highly variable in the uppermost part (between 0 and 69 m CSF-A), roughly coinciding with lithologic Unit I, with values ranging from 1.2 to 1.7 g/cm³ (Fig. **F55**). As at previous sites, high variations of GRA bulk density dominate in Unit I with alternating very dark brown to black organic-rich sediment and lighter olive and green hemipelagic sediment. Low-value GRA bulk density remains stable between ~90 and ~180 m CSF-A, with relatively less scatter. Deeper than ~180 m CSF-A, GRA bulk density gradually increases with depth to ~330 m CSF-A, which is approximately consistent with the lithologic Subunit IIIA/IIIB boundary. From ~330 to ~340 m CSF-A, GRA bulk density increases abruptly, and the highest values of GRA bulk density occur from ~340 m CSF-A to the bottom of the hole with high scatter. This high scatter is closely related to biscuited and possibly disturbed sediment between ~340 m CSF-A and the bottom, which had limited recovery. The above GRA bulk density trends at Site U1425 correlate well with the density log acquired in open Hole U1425B (see Fig. **F59** and **"Downhole measurements"**).

Although discrete wet bulk density and grain density are relatively constant for the entire core interval, ranging from 1.2 to 1.8 g/cm³ and from 2.3 to 3.1 g/cm³, respectively, the primary trends agree well with GRA bulk density (Fig. **F56**). Porosity and water content show generally reversed trends when compared to density, ranging from 53.1% to 87.4% and from 31.0% and 75.9%, respectively. The higher resolution MAD measurements performed in the uppermost part (between 0 and 50 m CSF-A) in organic-rich versus organic-poor hemipelagic sediment (Figs. **F56, F57**) show the large range of variability for discrete wet bulk density, grain density, porosity, and water content in Subunit IA. Discrete bulk density and grain density of organic-rich sediment (average = 1.38 and 2.61 g/cm³, respectively) are lower than hemipelagic sediment (average = 1.46 and 2.76 g/cm³, respectively), whereas porosity and water content (average = 77.6% and 57.7%, respectively) are higher than hemipelagic sediment (average = 74.8% and

52.6%, respectively). These differences in physical properties of two sediment layers are probably related to sediment texture because grain density between two sediment layers shows the largest difference.

Subsequently, discrete bulk density and grain density generally decrease with depth to ~180 m CSF-A, where porosity and water content of the sediment increase, except in an interval of relatively high bulk density and low porosity and water content between 78 and 82 m CSF-A. The decrease in bulk density and increase in porosity and water content with depth, which is contrary to the typical trends in marine sediment, is closely related to the downhole increase in diatom silica as discussed at Site U1424. Between ~180 and ~330 m CSF-A, discrete bulk density increases, whereas porosity and water content decrease with depth. At ~330 m CSF-A coinciding with the lithologic Subunit IIIA/IIIB boundary, discrete bulk density, ranging between 1.2 and 1.5 g/cm^3 shallower than ~330 m CSF-A, increases rapidly to an average of 1.7 g/cm^3, whereas porosity and water content show large step decreases averaging 14.5% and 16.7%, respectively.

These abrupt changes of GRA and discrete bulk density, porosity, and water content at ~330 m CSF-A strongly suggest that the lithologic Subunit IIIA/IIIB boundary corresponds to the diagenetic transition from opal-A to opal-CT. This transition is confirmed by both XRD and biogenic silica dissolution as seen in smear slides (see **"Lithostratigraphy"** and **"Geochemistry"**).

Magnetic susceptibility

Magnetic susceptibility at Site U1425 shows a different pattern compared to previous Sites U1422–U1424 (Fig. **F55**). Low magnetic susceptibility is typical for the entire drilled sequence without a high magnetic susceptibility peak in the uppermost part. The initial lack of magnetic carriers or perhaps their diagenetic dissolution may explain the poor paleomagnetic records at this site (see **"Paleomagnetism"**). Point magnetic susceptibility from the SHMSL closely tracks whole-core magnetic susceptibility with mean values for the site between 0 and 23 × 10^{-5} SI. Magnetic susceptibility linearly decreases with depth from 0 to 134 m CSF-A except for a small step decrease near ~85 m CSF-A. Magnetic susceptibility only appears to be highly variable between ~134 and ~322 m CSF-A because the values are so low. Relatively high magnetic susceptibility, ranging from 8 × 10^{-5} to 23 × 10^{-5} SI, occurs from 338 m CSF-A to the bottom of the hole because the diatom ooze/diatom-rich clay is replaced by siliceous claystone at the bottom of lithologic Subunit IIIA and the top of Subunit IIIB (see **"Lithostratigraphy"**).

Natural gamma radiation

The variation patterns of NGR are conformable with GRA bulk density (Fig. **F55**) and correlate well with the total gamma ray log acquired in open Hole U1425B (Fig. **F59**). Between 0 and 10 m CSF-A, the total NGR counts show a large step increase from 10 to 57 cps and then gradually increase to 50 m CSF-A (Fig. **F55**), coinciding with the lithologic Subunit IA/IB boundary, with strong cyclicity. As discussed at previous sites, these variation patterns of NGR may be explained by increased uranium content associated with organic-rich layers in Unit I. This is supported by the downhole spectral gamma ray measurements, which indicate, despite the through-pipe attenuation of the signal, a higher mean uranium content shallower than ~50 mbsf compared to the deeper interval (~50–80 mbsf) (Fig. **F60**). After sharply decreasing at 50 m CSF-A, NGR counts decrease to 94.3 m CSF-A, which corresponds to the lithologic Unit I/II boundary, and then low NGR counts remain stable to 187 m CSF-A with relatively less scatter. These meter-scale patterns of the total NGR counts in Unit I are very similar to the ones at previous Sites U1422–U1424, exhibiting a one-to-one correlation. Subsequently, NGR counts increase between 187 and 253 m CSF-A and then decrease to 322 m CSF-A. Deeper than ~322 m CSF-A, NGR counts largely increase and show the highest values, ranging between 45 and 65 cps, in the opal-A–opal-CT transition zone.

Compressional wave velocity

Compressional *P*-wave velocity was measured with the WRMSL in Sections 1, 2, and 3 of each core for Holes U1425B and U1425D following the same strategy as at Site U1423. Because of poor sediment-to-liner coupling or the influence of small cracks in the relatively stiff and brittle sediment, results from the WRMSL include significantly higher or lower values than a typical data set. These values were removed manually and then the *P*-wave velocities were combined as one data set of values from each hole (Fig. **F55**). *P*-wave velocity at Site U1425 varies from 1470 to 1740 m/s (average = 1545 m/s) and generally increases with depth. *P*-wave velocity shows a similar trend pattern with GRA bulk density in lithologic Unit I, inversely decreasing to 68 m CSF-A after increasing between 0 and 50 m CSF-A. Subsequently, although *P*-wave velocity gradually increases to 322 m CSF-A with a little variation, the trend is not clear enough to reflect the lithologic changes. *P*-wave velocity, however, largely increases from 1560 to 1625 m/s between 322 and 341 m CSF-A, which coincides with the lithologic Subunit IIIA/IIIB boundary. The highest value *P*-wave velocities occur with high scatter deeper than 340 m CSF-A, in the opal-A–opal-CT transition zone and the lowest part of Subunit IIIB.

Vane shear stress

Shear stress measurements were performed (generally one per core) from 0 to 300 m CSF-A on the working halves of Hole U1425B using an analog vane shear device. Deeper than 300 m CSF-A, high sediment strength did not allow measurements. Although shear strength was generally measured one per core, higher resolution measurements were performed between 0 and 50 m CSF-A to compare the shear strength of organic-rich and hemipelagic sediment. Shear strength ranges from 4.4 to 118.9 kPa and generally increases with depth (Fig. **F56**). Between 0 and 50 m CSF-A, shear strength linearly increases from 4.5 to 31.2 kPa in lighter olive and green hemipelagic sediment, whereas shear strength measured on very dark brown to black organic-rich sediment shows higher average values (~5.2 kPa). This higher shear strength encountered in organic-rich sediment may be explained by sediment texture and possible differential compaction. Deeper than ~80 m CSF-A, shear strength is highly scattered and does not reflect the lithologic units. This scattering shear strength may be related to the highly diatomaceous layers composing lithologic Unit II. As discussed at previous sites, the highly diatomaceous layers often show low shear strength values.

Diffuse reflectance spectroscopy

Similar to previous drilled sites, color reflectance data measured on the split archive-half sections at Site U1425 show high variability, especially in Subunit IA, reflecting the variegated colors of the decimeter- to centimeter-scale lithologic packages (Fig. **F58**). Subunit IA is generally characterized by high variability in luminance (L*), red-green ratio (a*), and yellow-blue ratio (b*), as very dark brown to black organic-rich sediment occurs here and alternates with lighter olive and green hemipelagic sediment. Although the dark bands fade out downhole below Subunit IA, the color reflectance shows little variation to the bottom of the hole.

Summary

Physical properties measured at Site U1425 generally show trends that follow lithostratigraphy. Magnetic susceptibility, bulk density, and NGR have higher values in lithologic Unit I than in Unit II, whereas porosity and water content show an opposite trend. *P*-wave velocity and shear strength generally increase with depth because of sediment compaction, although shear strength data are highly scattered in the highly diatomaceous layers deeper than ~80 m CSF-A. Color reflectance shows higher variation in Unit I than in Unit II, and the variations are closely related to the lithology of Unit I, which consists of alternating very dark brown to black organic-rich bands and lighter olive to green hemipelagic sediment. All physical property values were largely changed at the opal-A–opal-CT transition zone, when entering in Subunit IIIB.

Downhole measurements

Logging operations

Downhole logging measurements at Site U1425 were conducted in Hole U1425B after completion of APC/XCB coring to a total depth of 407.3 m CSF-A. Several hard dolomite layers were encountered during coring, but the hole was reported to be in good condition. Seawater was circulated to clean the hole, and the bit was pulled up to 80 m CSF-A. Two tool strings were deployed in Hole U1425B: the paleo combo and FMS-sonic (Fig. **F61**) (see **"Downhole measurements"** in the "Methods" chapter [Tada et al., 2015b], see also Table **T12** in the "Methods" chapter [Tada et al., 2015b] for tool acronyms). The Hostile Environment Natural Gamma Ray Sonde (HNGS) was included in the FMS-sonic tool string to increase precise depth match processing between logging strings and passes.

On 31 August 2013 at 0355 h (UTC), the paleo combo tool string (comprising resistivity, density, natural and spectral gamma radiation, and magnetic susceptibility tools) descended from the rig floor into the pipe. A downlog was taken at ~600 m/h. There was some difficulty descending past ~350 mbsf, but after a few attempts the tool passed that depth and reached the bottom of the hole at 403.2 m WSF. The hole was logged up to ~302 m WSF (Pass 1) at 540 m/h. The tool string returned for a main pass from the bottom of the hole (~404.2 m WSF) to the seafloor.

The FMS-sonic was rigged at ~0915 h on 31 August. A downlog was taken at 850 m/h, from which we established the best settings for the source frequency and the automated picking of *P*-wave velocity from the sonic waveforms. The tool string reached the bottom of Hole U1425B at ~396.5 m WSF rather than the total depth of ~404 mbsf. The hole was either collapsing or filling in by the time the FMS-sonic run was conducted. Two uphole passes of the FMS-sonic were run, the first pass to ~123 m WSF and the main pass to the seafloor, both at 550 m/h. Rig down was completed at 1855 h.

The seafloor depth was given by the step in the gamma logs. The paleo combo downlog found the seafloor at 1916.3 mbrf and the uplog (main pass) found it at 1918.9 mbrf. The main pass of the FMS-sonic found the seafloor at 1916.7 mbrf, compared to the drillers mudline tagged at 1919.1 mbrf (Hole U1425B). Heave was relatively high (~0.6 and ~1.8 m peak-to-peak) and is likely the cause of the offset between the FMS-sonic and the paleo combo downlog and uplog seafloor depths. Despite the use of the wireline heave compensator for each uplog pass (see **"Downhole measurements"** in the "Methods" chapter [Tada et al., 2015b]), depth matching may be required to correct for possible heave-related depth discrepancies.

Logging data quality

Tool calibration was performed both before and after the logging runs to ensure quality control. In Hole U1425B, the borehole conditions were medium with a diameter ranging from 11 to 16 inches (Fig. **F60,** Column 1) with a decreasing trend downhole. The hole was asymmetrical as evidenced from the FMS caliper, and the bottom of the hole was unstable. Deeper than 370 mbsf, the borehole diameter was ~12 inches when the paleo combo tool string was run, but when the FMS-sonic was run, the caliper subsequently read some values <5 inches. The gamma ray log (Fig. **F60,** Column 2) generally anticorrelates with the caliper log. This is partly because, despite borehole diameter corrections, less gamma radiation reaches the detector in a wider borehole. Also, there is lithologic control, with less clayey sediment being more easily washed out. Despite moderately good borehole conditions and high heave during downhole logging data acquisition, log data quality is generally good.

Agreement between physical properties and logging data is excellent for the density and NGR logs along almost the entire borehole (Fig. **F59,** Columns 2 and 3). As a result of caliper closure (see **"Downhole measurements"** in the "Site U1423" chapter [Tada et al., 2015d]) from ~115 mbsf to the pipe entrance, the gamma ray uplogs deviate from the core NGR data to lower values and no longer overlap the downlogs (Fig. **F59,** Column 2). For the same reason, the density log shows much lower values than the core data over the same interval. Deeper than ~370 mbsf, gamma ray logs from the FMS-sonic tool are also affected by borehole size, as the FMS caliper was not fully opened because of the very tight diameter of the bottom-hole section. Also, natural and spectral gamma ray data recorded shallower than 80 mbsf should only be used qualitatively because of the attenuation of the signal through the pipe (Fig. **F59**). The resistivity curve worked well, except for a few noisy peaks, starting ~50 m below the pipe and increasing uphole. Once corrected for temperature drift (see **"Downhole measurements"** in the "Site U1423" chapter [Tada et al., 2015d]), the Magnetic Susceptibility Sonde (MSS) (Fig. **F59,** Column 5) should be an indicator of the magnetic signal variability in the formation. The temperature drift–corrected deep-reading log is generally inversely correlated with the density and resistivity logs. The corrected high-resolution log does not correlate with magnetic susceptibility measurements on cores. This is possibly due to the very low magnetic susceptibility signal in the sediment, which may be lower than the detection limits of the tool. Further processing remains necessary. The velocity log increases downhole and shows little variability except in the lowest part of the hole (Fig. **F59,** Column 6). The increase in velocity observed deeper than ~360 mbsf is likely due to bad borehole conditions. The FMS resistivity images were of good quality despite the changes in borehole diameter (Fig. **F60**). Deeper than ~370 mbsf, the data should be used with caution because of the apparent poor borehole conditions.

Logging units

The Hole U1425B logs change gradually downhole, with no major steps in base levels. The lowermost part of the hole (from ~338 mbsf to the bottom) is characterized by higher gamma ray, density, and resistivity values than the rest of the hole. Density has a positive trend downhole when resistivity is relatively flat, increasing in the lower part of the hole deeper than ~338 mbsf. The sonic velocity log shows an increasing downhole trend, with values ranging from ~1.5 to 1.8 km/s, reflecting compaction. The HNGS signal ranges on average from 20 to 90 gAPI with one maximum value reaching 100 gAPI. The signal shows moderately high amplitude variability on a several-meter to submeter scale and most likely tracks clay and organic matter content (see **"Lithostratigraphy"**). The K and Th curves are generally well correlated (Fig. **F60**). Uranium behaves differently than K and Th because it is not chemically combined with the main terrigenous minerals. Deeper than ~132 mbsf in Hole U1425B, however, U is also generally well correlated to U and K. Uranium generally accounts for 40%–50% of the total gamma radiation signal and locally for >60%. The highest values (>4 ppm) are observed from 255 to 290 mbsf and from 341 to 390 mbsf in lithologic Unit III (see **"Lithostratigraphy"**). Three logging units have been identified on the basis of changes in character of gamma ray, resistivity, and density logs (logging Units LI–LIII; Fig. **F59**).

Logging Unit LI: base of drill pipe (~80 mbsf) to ~244 mbsf

Logging Unit LI has been divided into two subunits (LIa and LIb; Fig. **F59**).

Logging Subunit LIa: base of drill pipe (~80 mbsf) to ~132 mbsf

The upper logging subunit presents strong analogies with logging Subunit LIa identified in Hole U1423B. It is characterized by NGR > 40 gAPI and moderate- to high-amplitude swings in U, Th, and K. The gamma ray signal correlates well with the bulk density log, which shows high-amplitude variations ranging from 1.30 to 1.47 g/cm^3 (Figs. **F59** [Column 1], **F60**). The peak values >1.50 g/cm^3 (~106 and ~117 mbsf) correlate with intervals of low core recovery in Hole U1425B and dolomite layers in Section 346-U1425B-13X-1 and Core 16X, respectively. These dolomite layers are also well expressed in the resistivity logs with values exceeding 1 Ωm (Fig. **F59,** Column 4). The sonic curve is smooth. The resistivity curves are characterized by high-frequency oscillations. The base of logging Subunit Lia at ~132 mbsf fits well with the transition between lithologic Subunits IIA (dominantly diatom-bearing and diatom-rich clay) and IIB (diatom ooze with few clay intervals) placed in Section 20H-1 at ~131.90 m CSF-A (see **"Lithostratigraphy"**). This depth fits with a marked step in the NGR, density, and resistivity curves, which likely reflects the significant downhole increase in diatom content relative to terrigenous sediment.

Logging Subunit LIb: ~132 to 244 mbsf

Logging Subunit LIb is distinguished from logging Subunit LIa by lower values in total and spectral NGR, likely reflecting the abundance of nonradioactive elements within lithologic Subunit IIB (diatoms and other siliceous components, see **"Lithostratigraphy"**). A downhole increasing trend is also observed, with moderate- to high-amplitude swings (Fig. **F60**). Lower densities than those in logging Subunit LIa are observed from ~132 to ~187 mbsf (<1.40 g/cm^3), possibly reflecting an increased abundance of diatoms within lithologic Subunit IIB (diatom ooze, see **"Lithostratigraphy"**). Density slightly increases deeper than ~187 mbsf and shows higher amplitude oscillations. At the scale of logging Subunit LIb, the density log shows a positive downhole trend, reflecting compaction and/or a decrease in diatom content (Fig. **F59,** Column 3). Resistivity is also lower than within logging Subunit LIa, and the curve is relatively flat all along the logging subunit (Fig. **F59,** Column 4). Some distinct peaks in resistivity >0.6 Ωm seem to correlate in cores either with ash layers, dolomite intervals, or nodules (Section 346-U1425B-24H-7 and empty Core 31H). The sonic curve shows small-amplitude variations with few peaks at ~200 mbsf not correlating with clear lithologic features in the sediment. The prominent peaks in U, Th, and K observed at ~210 mbsf correspond to a prominent ash layer, which is >10 cm thick (interval 346-U1425D-25H-4, 44–74 cm). This ash layer is also clearly associated with a peak in density, magnetic susceptibility, and resistivity logs. It also correlates in the FMS images with an ~30 cm thick resistive horizon (light color, Fig. **F60,** Column 5).

The lowest part of logging Subunit LIb (from ~236 to 244 mbsf) is characterized by a slight decrease in gamma ray, density, and resistivity logs (Fig. **F59**). The base of logging Subunit LIb (~244 mbsf) approximates the depth of the lithologic Unit II/III boundary, placed at ~253.3 mbsf in Hole U1425B (Section 346-U1425B-35H-1) (see **"Lithostratigraphy"**).

Logging Subunit LII: ~244 to ~338 mbsf

Logging Unit LII starts with a small step in gamma ray, density, and resistivity logs (Fig. **F59**). Logging Unit LII is also distinguished from logging Unit LI by higher values in total NGR (between 40 and 85 gAPI) and its components U, Th, and K, possibly reflecting the increase in terrigenous content in lithologic Unit III compared to lithologic Unit II (see **"Lithostratigraphy"**). Regular high-amplitude cyclic swings are observed in both the gamma ray and density logs, with several orders of cycles varying from one to several meters in thickness (Fig. **F60**). The cyclic nature of the sediment record at intervals of ~8–10 m is especially well expressed (see also Fig. **F62** and FMS images in Fig. **F63**). U, Th, and K concentrations covary, suggesting that clay content controls these logs (Fig. **F60**). The low gamma ray and low density intervals correlate in cores with either diatom-rich or carbonate-rich intervals in lithologic Unit III (alternating layers of bioturbated diatom ooze and diatom-rich clay, see **"Lithostratigraphy"** and Fig. **F62**). The resistivity logs display higher values (generally between 0.55 and 0.65 Ωm) than in logging Subunit LIb and show regular cyclic swings correlating with the density log (Fig. **F59,** Column 4). The prominent double peaks in density (2.4 and 3.2 g/cm^3) and resistivity (>0.7 Ωm) observed at ~297 mbsf do not correlate with any lithologic feature in the cored sediment. The high values in the U log observed from ~255 to ~270 and ~278 to ~290 mbsf suggest organic-rich intervals. In logging Unit LII, the sonic logs show slightly higher amplitude variability compared to logging Unit LI.

The base of logging Unit LII (~338 mbsf) approximates the depth of the lithologic Subunit IIIA/IIIB boundary, placed at ~341.3 mbsf in Hole U1425B (Section 346-U1425B-53H-1) (see **"Lithostratigraphy"**).

Logging Unit LIII: ~338 mbsf to the bottom of the hole

Logging Unit LIII starts with a step in gamma ray, density, sonic, and resistivity logs (Fig. **F59**). The gamma ray and its component continue to show high-amplitude cyclic variability (Fig. **F60**). The values increase downhole to ~350 mbsf and decrease further at depth. The resistivity log has a positive downhole trend, with true resistivities ranging from 0.65 to 0.90 Ωm (Fig. **F59,** Column 4). Density increases from 1.4 to 1.6 g/cm^3 over the upper 5 m (~338–343 mbsf) and remains relatively constant below with values exceeding 1.6 g/cm^3. The three negative peaks observed from 350 to 356 mbsf are possibly related to borehole conditions presenting a diameter of 17 inches at these depths. The shift toward higher density and resistivity characterizing logging Unit LIII corresponds to the transition to lithologic Subunit IIIB (gray siliceous claystone) placed at 341.3 mbsf (see **"Lithostratigraphy"**) and the diagenetic boundary from biogenic opal-A to opal-CT, starting at ~342 mbsf (see **"Lithostratigraphy,"** Fig. **F22,** and **"Geochemistry"**). The increased gamma ray values suggest a relative increase in clay content, although XRD measurements show evidence of a decrease in clay minerals deeper than ~370 mbsf (Fig. **F8**). The high values in the U log observed from ~350 to ~387 mbsf probably characterize an interval enriched in organic matter.

FMS images

In Hole U1425B, the FMS resistivity data quality allows the borehole formation resistivity to be interpreted at several scales. Conductive intervals (dark color in the FMS image in Fig. **F60**) correlate with low gamma ray, low density, and low resistivity log values (Fig. **F59,** Columns 1–3). Conversely, more resistive intervals generally correlate with higher values in the gamma ray, bulk density, and resistivity logs. This relationship can be interpreted in terms of the relative abundance of clay/diatom in the sediment. As evidenced during Leg 128 at ODP Site 798 (deMenocal et al., 1992), clay has high K and Th contents and has relatively higher density and lower porosity than diatom-rich sediment. As a consequence, with the exception of ash and dolomite layers and intervals affected by major changes in density, conductive intervals in the FMS images tend to reflect intervals enriched in diatoms, whereas resistive intervals reflect relative high-terrigenous clay content. Such a relationship is also true at a smaller scale (see below).

At the scale of the borehole, the interval shallower than ~132 mbsf (logging Subunit LIa) is characterized by (relatively) medium conductivity (orange-colored upper interval in the FMS image in Fig. **F60**). Lower resistivity (dark color in the FMS image) is observed below, within logging Subunit LIb. This is interpreted as reflecting the significant downhole increase in diatom content within lithologic Subunit IIA compared to lithologic Subunit IIB (see **"Lithostratigraphy"**). Deeper than ~244 mbsf, within logging Units LII and LIII, the FMS images are characterized by higher resistivity, which reflects the increase in clay content in lithologic Unit III (see **"Lithostratigraphy"**). The change at ~244 mbsf appears ~10 m above the lithologic Unit II/III boundary placed at ~253 mbsf (see **"Lithostratigraphy"**). Deeper than 339 mbsf, logging Unit LIII is characterized by high resistivity (light color in the FMS image in Fig. **F60**), in agreement with the high density and resistivity observed within this unit (Fig. **F59,** Columns 3 and 4).

At a finer scale, the FMS images also reveal numerous resistive and conductive intervals, with thicknesses ranging from several tens of centimeters to a few meters (Figs. **F62, F63**). Figure **F64** illustrates an apparent cyclic nature of some resistive and conductive intervals on the FMS images from 290 to 325 mbsf. The cyclic pattern consists of ~3–5 m thick resistive intervals (light color in the FMS image), correlating with higher values in the gamma ray, bulk density, and resistivity logs (Type A intervals) and interpreted as reflecting relatively clay-rich intervals. These resistive intervals alternate with conductive intervals (dark color in the FMS image), generally correlating in core with laminated (diatomite or carbonate rich) intervals characterized by lower values in the gamma ray, bulk density, and resistivity logs (Type C intervals). These conductive intervals often contain higher frequency, smaller scale interbedded layers. The transition between Type A and Type C intervals is often marked by an intermediate level (Type B intervals), characterized by medium conductivity in the FMS images and medium density, gamma ray, and resistivity in logs. This pattern appears to be symmetrical (Types A, B, C, B, and A) or asymmetrical (Types A, B, C, A, B, and C), possibly indicating cyclic, more or less progressive, changes in productivity conditions. These very preliminary observations, however, need to be further examined by postexpedition shore-based research. The resistive–conductive cycles described above do not to occur shallower than ~245 mbsf. The higher frequency resistive–conductive cycles (<1 m in thickness) are also essentially observed deeper than ~245 mbsf (Fig. F63).

At a finer spatial resolution, some highly resistive layers (in white in the FMS images) are observed and most likely reflect either dolomite or ash layers. As an example, the ~30 cm thick resistive horizon observed on the FMS images at ~210 mbsf (light color, Fig. F60, Column 5) corresponds to a prominent ash layer in interval 346-U1425D-25H-4, 44–74 cm. This ash layer is also clearly associated with a maximum in the density, magnetic susceptibility, and resistivity logs and with a prominent maximum in U, Th, and K. The two resistive layers observed at ~104.5 and 105 mbsf on the images correlate with a low core recovery interval and a dolomite layer in interval 346-U1425B-13X-1, 0–9 cm.

In situ temperature and heat flow

APCT-3 downhole temperature measurements were performed in Hole U1425B at four depths, including the mudline. In situ temperatures range from 4.25°C at 37.3 m CSF-A to 10.2°C at 94.3 m CSF-A (Table T19), with a linear downhole increase indicating that the gradient is uniform with depth (Fig. F64). A linear fit of temperature versus depth gives a geothermal gradient of 104°C/km. This value is higher than was measured at Site 799 during Leg 128 (98°C/km; Ingle, Suyehiro, von Breymann, et al., 1990) and generally higher than what was expected in the Yamato Rise area (Langseth and Tamaki, 1992). This discrepancy may be explained by the fact that the geothermal gradient at Site U1425 was calculated from only three in situ measurements in the sediment as the result of coring difficulties deeper than 110 mbsf (see "Operations"). The bottom water temperature at this site is estimated to be 0.41°C, based on average mudline temperature in the three APCT-3 measurements. A heat flow of 96 mW/m^2 was obtained from the slope of the linear fit between in situ temperature and calculated in situ thermal resistance (Fig. F64) (Pribnow et al., 2000). This value is higher than the one calculated for Site 799 (92 mW/m^2).

Stratigraphic correlation and sedimentation rates

A composite section and splice (as defined in "Stratigraphic correlation and sedimentation rates" in the "Methods" chapter [Tada et al., 2015b]) were constructed for Site U1425 in an effort to establish a continuous sediment sequence using Holes U1425B and U1425D. Hole U1425A recovered only one core and was dedicated to training. Three cores were recovered from Hole U1425C, which were dedicated to future optically stimulated luminescence measurement without any onboard use. Holes U1425B and U1425D were cored, switching back and forth between the standard APC, XCB, and half APC to 407.2 m CSF-A at the base of Core 346-U1425B-61X and to 431.0 m CSF-A at the base of Core 346-U1425D-72H. Switching among coring devices allowed penetration of alternating hard layers and soft-sediment layers. Hole U1425E was cored to 113.1 m CSF-A at the base of Core 346-U1425E-13H in order to obtain additional core material. Splicing between Holes U1425B and U1425D enabled us to construct a continuous stratigraphic sequence, with the exception of three potential gaps, from the seafloor to the bottom of Core 346-U1425B-51H (336.91 m CSF-A). Deeper than 336.9 m CSF-A, poor recovery of sediment in both Holes U1425B and U1425D prohibited us from constructing a composite section.

Construction of CCSF-A scale

Definition of top (0 m CCSF-A)

The first cores in Holes U1425B, U1425D, and U1425E all recovered the mudline. We selected Core 346-U1425D-1H as the anchor core in order to avoid a whole-round sampling interval at Section 346-U1425B-1H-1 and defined the top as 0 m CCSF-A (as defined in "Stratigraphic correlation and sedimentation rates" in the "Methods" chapter [Tada et al., 2015b]).

Compositing of cores

The CCSF-A scale for Site U1425 is based on correlation of magnetic susceptibility and GRA data from the WRMSL and the Special Task Multisensor Logger, as well as RGB blue (B) data extracted from images acquired by the Section Half Imaging Logger (see "Physical properties" in the "Methods" chapter [Tada et al., 2015b] for details). Magnetic susceptibility and GRA bulk density were measured at 2.5 cm intervals for Holes U1425A and U1425B and at 5 cm intervals for Hole U1425C, whereas B was recovered at 0.5 cm intervals. Correlative horizons are most easily identified in the magnetic susceptibility and B data with the aid of GRA data when identical features of the variations were difficult to identify. Extremely fine scale correlations are best achieved using the 0.5 cm B data.

Core gaps

A partial stroke of the standard APC occurred at 104.6 m CSF-A during coring of Core 346-U1425B-12H because of an indurated layer (e.g., dolomite, see **"Lithostratigraphy"**). The following core (13X) successfully penetrated this hard layer, although the top of the core included fall-in. Although careful operations using a combination of the half APC (Core 346-U1425D-12H) and XCB (Core 346-U1425D-13X) in the next hole successfully cored this interval, the thickness of the hard layer between Cores 346-U1425B-12H and 13X and Cores 346-U1425D-12H and 13X remained unclear. Even during the third attempt (Hole U1425E), the recovery of Core 346-U1425E-12H was not sufficient, and the following core (13H) did not recover the interval. This difficult interval separates the splice segments above (Segment 1) and below (Segment 2) (Table **T20;** Fig. **F65B**).

Partial strokes of the standard APC also occurred at 211.63 and 210.89 m CSF-A during coring of Cores 346-U1425B-28H and 346-U1425D-25H, respectively, where a >40 cm thick ash layer was eventually recovered (see **"Lithostratigraphy"**). Because the tops of the following cores (346-U1425B-29H and 346-U1425D-26X) were not identical to one other, a potential gap at the bottom of the ash layer and below it remains, which separates the splice segments above (Segment 2) and below (Segment 3) (Table **T20;** Fig. **F65E**).

Core gaps aligned between Cores 346-U1425B-39H and 40X and between Cores 346-U1425D-35H and 36H because of the relatively large heave during coring operations at this site. Physical properties such as magnetic susceptibility, GRA density, NGR, and B values were not continuous beyond these boundaries (Fig. **F65E**). Therefore, the intervals between Cores 346-U1425B-39H and 40X and between Cores 346-U1425D-35H and 36H were potentially uncovered, which separates the splice segments above (Segment 3) and below (Segment 4) (Table **T20;** Fig. **F65E**).

Poor recovery and frequent coring disturbance (e.g., flow-in) made the sedimentary sequence significantly fragmented below Cores 346-U1425B-51H and 346-U1425D-45H (see **"Lithostratigraphy"**). Because this site was logged, the original stratigraphic relationships might be assigned to even the highly fragmented section recovered in these intervals using core-log comparison, as described below.

Summary

Based on three core gaps and the fragmented nature of the intervals from Cores 346-U1425B-52H through 61X and Cores 346-U1425D-46H through 72H, the CCSF-A scale given to Site U1425 cores is divided into five segments (Table **T20;** Fig. **F65**):

- Segment 1 consists of Cores 346-U1425A-1H, 346-U1425B-1H through 12H, and 346-U1425D-1H through 12H, which extends from 0 to ~110 m CCSF-A.
- Segment 2 consists of Cores 346-U1425B-13X through 28H and 346-U1425D-13X through 25H, which extends from ~110 to ~221 m CCSF-A.
- Segment 3 consists of Cores 346-U1425B-29H through 39H and 346-U1425D-26X through 35H, which extends from ~221 to ~292 m CCSF-A.
- Segment 4 consists of Cores 346-U1425B-40X through 51H and 346-U1425D-36H through 45H, which extends from ~292 to ~350 m CCSF-A.
- Segment 5 consists of Cores 346-U1425B-52H through 61X and 346-U1425D-46H through 72H, which extends from ~350 to ~446 m CCSF-A, where common vertical offsets of 15.53 and 15.40 m were assumed for the cores in Holes U1425B and U1425D, respectively.

Construction of CCSF-D scale

A combination of Holes U1425B and U1425D can cover all the stratigraphic intervals from Segments 1–4 to 336.91 m CSF-A (352.44 m CCSF-A). Because Hole U1425E was drilled 22 days after the drilling of Holes U1425B and U1425D, cores from Hole U1425E were not used for the splice, although a composite depth scale (CCSF-A) is supplied for Hole U1425E cores. Selected splice intervals are listed in Table **T21.**

We tried to construct a splice, avoiding whole-round sampling intervals and minimizing inclusion of disturbed intervals as much as possible. All the cores in Segment 1 were aligned properly and spliced completely.

For Segment 2, the 1.73 m thick interval (splice Segment 2-6 in Table **T21**) between 133.10 and 134.83 m CCSF-D (as defined in **"Stratigraphic correlation and sedimentation rates"** in the "Methods" chapter [Tada et al., 2015b]) was taken from Core 346-U1425B-19H, which showed a very homogeneous appearance with suspected drilling disturbance. We correlated this interval, however, to the top part of Core 346-U1425D-16H based on a resemblance in the magnetic susceptibility profiles.

In Segment 3, splicing between Cores 346-U1425B-29H and 346-U1425D-27H (splice Intervals 3-1 and 3-2 in Table **T21**) at 230.17 m CCSF-D was performed without pattern matching of physical properties; instead, splicing was only based on the fact that no jumps in magnetic susceptibility, GRA density, and B values were observed (Fig. **F65D**). A similar situation occurred for splicing between Cores 346-U1425D-33H and 346-U1425B-38H (splice Intervals 3-14 and 3-15 in Table **T21**) at 281.75 m CCSF-D (Fig, **F65E**).

In Segment 4, a 2.56 m thick homogeneous interval (splice Interval 4-5 in Table **T21**) from Core 346-U1425B-43H was spliced into the composite section between Cores 346-U1425D-38H and 39H. Although the homogeneous appearance of Core 346-U1425B-43H may reflect coring disturbance, we adopted it as a splice interval because all the physical properties such as magnetic susceptibility, GRA density, and B were mostly the same as the intervals above (Core 346-U1425D-38H) and below (Core 346-U1425D-39H). Cores 346-U1425D-40H and 346-U1425B-46H (splice Intervals 4-7 and 4-8 in Table **T21**) were also spliced at 320.65 m CCSF-D based only on the similarity of magnetic susceptibility, GRA density, and B values (Fig. **F65F**).

Estimation of gaps between cores based on core-log comparison

Because NGR was measured by sensors on the FMS-sonic and paleo combo tool strings during downhole logging in Hole U1425B (see **"Downhole measurements"**), we can align the spliced NGR profile with the wireline log depth below seafloor (WSF). The correlation between core NGR and total spectral gamma ray (HSGR) from downhole logging was good even at <0.1 m scale, which also enabled us to estimate the size of potential gaps between segments.

Figure **F66** shows the comparison between the corresponding intervals for NGR core splice and HSGR logging around Segment 1/2, 2/3, and 3/4 boundaries. The distance between correlative horizons above and below the Segment 1/2 boundary (Fig. **F66A**) was 9.02 m CCSF-D, whereas those for logging were 8.97 m WSF from the paleo combo tool string and 9.33 m WSF from the FMS-sonic tool string (Fig. **F66B**). Because both tool strings were separately run, there is an uncertainty in the WSF depth scale due to cable stretching and/or ship heave (see **"Downhole measurements"**), here estimated to ~30 cm. Therefore, no significant gap could be confidently recognized between Segments 1 and 2.

In the case of the Segment 2/3 boundary, the distance between correlative horizons above and below the boundary was 5.68 m CCSF-D for the core splice (Fig. **F66C**), whereas it was 5.73–5.83 m WSF for downhole logging (Fig. **F66D**). The uncertainty in wireline depth is small enough (<10 cm), and a gap of 10–20 cm between Segments 2 and 3 could explain the smaller distance in the NGR splice.

The distance of 6.43 m CCSF-D between correlative horizons above and below the Segment 3/4 boundary (Fig. **F66E**) is even larger than the 5.43–5.47 m WSF for logging, which suggests that there is no significant gap here. The larger distance in the core splice might be due to expansion of sediment during the coring process.

Although the sediment sequence below Cores 346-U1425B-51H and 346-U1425D-45H were fragmented by poor recovery and frequent flow-in disturbance, the NGR profiles from Holes U1425B and U1425D seem identical if the data taken from the flow-in intervals were removed (Fig. **F66G**). When these core data are compared to the HSGR log from the paleo combo tool string (see **"Downhole measurements"**), major fluctuation patterns are well matched throughout the interval between 340 and 410 m CCSF-A (Fig. **F66G**). Therefore, any data taken from the nonflow-in intervals plotted on the CCSF-A scale could be regarded as a reasonable property profile of Segment 5. It is also clear that a significant coring gap exists between 383 and 390 m CCSF-A.

Sedimentation rates

All age control datums, including biostratigraphic markers, paleomagnetic events, and tentatively dated tephra, were plotted on Figure **F67A** and listed in Table **T22.** Paleomagnetic datums constrained the sediment ages well for Subunits IA and IB. Therefore, ages of the Subunit IA/IB and IB/IIA boundaries were determined exclusively based on linear fits to paleomagetic datums. An apparent outlier in Subunit IB is the LO of *H. parviakitaensis* that was determined by "rare" occurrence of this species, which might suggest reworking (see Table **T22**). Within Subunit IIA, the depth-age relationship was narrowed by the lower limits defined by the LOs of *N. kamtschatica* and *D. bullatus* and the upper limits defined by the FOs of *G. praeinflata* and *H. parviakitaensis* (Fig. **F67A;** Table **T22**). The age of the Subunit IIA/IIB boundary was set to keep the sedimentation rate constant within Subunit IIA, thus satisfying these lower and upper limits. Because the LO and FO of *G. ikebei* were defined by rare occurrence from only one sample, they were considered reworked (see Table **T8**). Because an assumption of a single constant sedimentation rate within Subunit IIB disagrees with the constraints given by the FO of *L. pylomaticus* at 187.7 m CCSF-A and the LO of *L. parallelipes* at 198 m CCSF-A, we adopted these two datums as inflection points of depth-age lines. Between 137 and 187.7 m CCSF-A, the lower limit defined by the LO of *L. redondoensis* and the LO of *Thalassiosira jacksonii* and the upper limit defined by the FO of *D. bullatus* and the FO of *L. pylomaticus* narrowed a possible depth-age line. At 259 m CCSF-A, the LO of *C. nakasekoi* and the FO of

L. parallelipes define the age of the Subunit IIB/IIIA boundary. One of two outliers in Subunit IIB is the LO of *L. redondoensis* that was determined by rare occurrence of this species, which might suggest reworking (see Table **T7**). Another apparent inconsistency in the LO of *Thalassiosira schraderi* in Subunit IIB might be due to uncertainty in age assignment (7.6 Ma; Yanagisawa and Akiba, 1998), which was estimated as 7.0 Ma from the marginal sea by Koizumi (1992). For Subunits IIIA and IIIB, because the constraints were sparse after the removal of data taken from the intervals of flow-in disturbance, the age of the Subunit IIIA/IIIB boundary was determined to minimize the inflection point within the lower limit defined by the last common occurrence (LCO) of *Lychnocanoma magnacornuta* and the upper limit defined by the FO of *C. nakasekoi* (Fig. **F67A;** Table **T22**).

Sedimentation rates at Site U1425 range from 25.7 to 64.8 m/m.y. and are lower in Subunits IB, IIA, and the middle of Subunit IIB; moderate in Subunit IA; and higher in the upper and lower parts of Subunit IIB and Unit III (Fig. **F67B**). Low sedimentation rates in Subunit IIA and the middle of Subunit IIB are associated with very low GRA density, which suggests a decrease of detrital flux and relative increase of diatom fraction. Relatively high sedimentation rates in Subunits IIB and IIIA are associated with lower GRA density, which suggests that the diatom flux was higher during these periods. The lower sedimentation rate in Subunits IB and IIA, which is associated with an increase in GRA density, may indicate a decrease in diatom productivity and relative increase of the detrital fraction. An ensuing increase in sedimentation rate in Subunit IA keeping GRA density high suggests increased flux of detrital material during this period. Although possible compaction because of the dissolution of porous diatom frustules and the precipitation of opal-CT is suggested from the higher GRA density in Subunit IIIB (see **"Lithostratigraphy"** and **"Biostratigraphy"**), the sedimentation rate is rather higher here than in Subunit IIIA. Subunit IIIB is also characterized by higher NGR (Fig. **F66G**), which suggests a more enhanced detrital flux at that time.

References

Baker, P.A., and Kastner, M., 1981. Constraints on the formation of sedimentary dolomite. *Science,* 213(4504):214–216. **doi:10.1126/science.213.4504.214**

Blum, P., 1997. Physical properties handbook: a guide to the shipboard measurement of physical properties of deep-sea cores. *ODP Tech. Note,* 26. **doi:10.2973/odp.tn.26.1997**

Briucaud, A., Morel, A., and Prieur, L., 1981. Absorption by dissolved organic matter of the sea (yellow substance) in the UV and visible domains. *Limnol. Oceanogr.,* 26(1):43–53. **doi:10.4319/lo.1981.26.1.0043**

deMenocal, P.B, Bristow, J.F., and Stein, R., 1992. Paleoclimatic applications of downhole logs: Pliocene–Pleistocene results from Hole 798B, Sea of Japan. *Proc. ODP Sci. Results,* 127/128 (Pt. 1): College Station, TX (Ocean Drilling Program), 337–353. **doi:10.2973/odp.proc.sr.127128-1.143.1992**

Dickens, G.R., 2001. Sulfate profiles and barium fronts in sediment on the Blake Ridge: present and past methane fluxes through a large gas hydrate reservoir. *Geochim. Cosmochim. Acta,* 65(4):529–543. **doi:10.1016/S0016-7037(00)00556-1**

Emerson, S., and Hedges, J.I., 1988. Processes controlling the organic carbon content of open ocean sediments. *Paleoceanography,* 3(5):621–634. **doi:10.1029/PA003i005p00621**

Expedition 318 Scientists, 2011. Site U1359. *In* Escutia, C., Brinkhuis, H., Klaus, A., and the Expedition 318 Scientists, *Proc. IODP,* 318: Tokyo (Integrated Ocean Drilling Program Management International, Inc.). **doi:10.2204/iodp.proc.318.107.2011**

Föllmi, K.B., Cramp, A., Föllmi, K.E., Alexandrovich, J.M., Brunner, C., Burckle, L.H., Casey, M., deMenocal, P., Dunbar, R.B., Grimm, K.A., Holler, P., Ingle, J.C., Jr., Kheradyar, T., McEvoy, J., Nobes, D.C., Stein, R., Tada, R., von Breymann, M.T., and White, L.D., 1992. Dark–light rhythms in the sediments of the Japan Sea: preliminary results from Site 798, with some additional results from Sites 797 and 799. *In* Pisciotto, K.A., Ingle, J.C., Jr., von Breymann, M.T., Barron, J., et al., *Proc. ODP, Sci. Results,* 127/128 (Pt. 1): College Station, TX (Ocean Drilling Program), 559–576. **doi:10.2973/odp.proc.sr.127128-1.159.1992**

Fick, A., 1855. On liquid diffusion. *Philos. Mag.,* 294:30–39.

Gieskes, J.M., and Lawrence, J.R., 1981. Alteration of volcanic matter in deep-sea sediments: evidence from the chemical composition of interstitial waters from deep sea drilling cores. *Geochim. Cosmochim. Acta,* 45(10):1687–1703. **doi:10.1016/0016-7037(81)90004-1**

Gooday, A.J., 1993. Deep-sea benthic foraminiferal species which exploit phytodetritus: characteristic features and controls on distribution. *Mar. Micropaleontol.,* 22(3):187–205. **doi:10.1016/0377-8398(93)90043-W**

Ingle, J.C., Jr., Suyehiro, K., von Breymann, M.T., et al., 1990. *Proc. ODP, Init. Repts.,* 128: College Station, TX (Ocean Drilling Program). **doi:10.2973/odp.proc.ir.128.1990**

Isoda, Y., 2011. Climate change and physical process associated with the Tsushima Warm Current. *Mem. Fac. Fish. Sci., Hokkaido Univ.,* 53(2):2–12. **http://hdl.handle.net/2115/47547**

Jorissen, F.J., 1999. Benthic foraminiferal microhabitats below the sediment-water interface. *In* Sen Gupta, B.K. (Ed.), *Modern Foraminifera:* Dordrecht (Kluwer), 161–179. **doi:10.1007/0-306-48104-9_10**

Jorissen, F.J., de Stigter, H.C., and Widmark, J.G.V., 1995. A conceptual model explaining benthic foraminiferal microhabitats. *Mar. Micropaleontol.,* 26(1–4):3–15. **doi:10.1016/0377-8398(95)00047-X**

Jorissen, F.J., Fontanier, C., and Thomas, E., 2007. Paleoceanographical proxies based on deep-sea benthic foraminiferal assemblage characteristics. *In* Hillaire-Marcel, C. and De Vernal, A. (Eds.), *Proxies in Late Cenozoic Paleoceanography.* Dev. Mar. Geol., 263–325. **doi:10.1016/S1572-5480(07)01012-3**

Kamikuri, S., 2010. New late Neogene radiolarian species from the middle to high latitudes of the North Pacific. *Rev. Micropaleontol.,* 53(2):85–106. **doi:10.1016/j.revmic.2008.06.005**

Kastner, M., Keene, J.B., and Gieskes, J.M., 1977. Diagenesis of siliceous oozes, I. Chemical controls on the rate of opal-A to opal-CT transformation—an experimental study. *Geochim. Cosmochim. Acta,* 41(8):1041–1051. **doi:10.1016/0016-7037(77)90099-0**

Kim, K.-R., Rhee, T.S., and Kim, K., 1992. A note on initial nitrate and initial phosphate as tracers for the origin of East Sea (Japan Sea) Proper Water. *La Mer,* 30:149–155. **http://www.sfjo-lamer.org/la_mer/30-3/30-3-7.pdf**

Koizumi, I., 1992. Diatom biostratigraphy of the Japan Sea: Leg 127. *In* Pisciotto, K.A., Ingle, J.C., Jr., von Breymann, M.T., Barron, J., et al., *Proc. ODP, Sci. Results,* 127/128 (Pt. 1): College Station, TX (Ocean Drilling Program), 249–289. **doi:10.2973/odp.proc.sr.127128-1.127.1992**

Kucera, M., and Kennett, J.P., 2000. Biochronology and evolutionary implications of late Neogene California margin planktonic foraminiferal events. *Mar. Micropaleontol.,* 40(1–2):67–81. **doi:10.1016/S0377-8398(00)00029-3**

Langseth, M.G., and Tamaki, K., 1992. Geothermal measurements: thermal evolution of the Japan Sea basins and sediments. *In* Tamaki, K., Suyehiro, K., Allan, J., McWilliams, M., et al., *Proc. ODP, Sci. Results,* 127/128 (Pt. 2): College Station, TX (Ocean Drilling Program), 1297–1309. **doi:10.2973/odp.proc.sr.127128-2.227.1992**

Lyle, M., Koizumi, I., Richter, C., et al., 1997. *Proc. ODP, Init. Repts.,* 167: College Station, TX (Ocean Drilling Program). **doi:10.2973/odp.proc.ir.167.1997**

Maiya, S., 1978. Late Cenozoic planktonic foraminiferal biostratigraphy of the oil-field region of Northeast Japan. *In* Fujita, K., Ichikawa, K., Ichihara, M., Chiji, M., Unabara, K., Fujita, T., and Takayanagi, Y. (Eds.), *Cenozoic Geology of Japan:* Osaka (Osaka City Univ.), 35–60.

Martin, J.B., Gieskes, J.M., Torres, M., and Kastner, M., 1993. Bromide and iodine in Peru margin sediments and pore fluids: implication for fluid origins. *Geochim. Cosmochim. Acta,* 57(18):4377–4389. **doi:10.1016/0016-7037(93)90489-J**

Middelburg, J.J., de Lange, G.J., and van der Weijden, C.H., 1987. Manganese solubility control in marine pore waters. *Geochim. Cosmochim. Acta,* 51(3):759–763. **doi:10.1016/0016-7037(87)90086-X**

Miwa, M., 2014. Foraminifera. In *Sekiyu Kogyo Binran (Petroleum Technology Handbook) 2013:* Tokyo (Jpn. Assoc. Pet. Technol.), 223–227. (in Japanese)

Moore, T.S., Murray, R.W., Kurtz, A.C., and Schrag, D.P., 2004. Anaerobic methane oxidation and the formation of dolomite. *Earth Planet. Sci. Lett.,* 229(1–2):141–154. **doi:10.1016/j.epsl.2004.10.015**

Müller, P.J., and Suess, E., 1979. Productivity, sedimentation rate, and sedimentary organic matter in the oceans—I. Organic carbon preservation. *Deep-Sea Res., Part A,* 26(12):1347–1362. **doi:10.1016/0198-0149(79)90003-7**

Murata, K.J., and Nakata, J.K., 1974. Cristobalitic stage in the diagenesis of diatomaceous shale. *Science,* 184(4136):567–568. **doi:10.1126/science.184.4136.567**

Murray, R.W., Brumsack, H.J., von Breymann, M.T., Sturz, A.A., Dunbar, R.B., and Gieskes, J.M., 1992. Diagenetic reactions in deeply buried sediments of the Japan Sea: a synthesis of interstitial-water chemistry results from Legs 127 and 128. *In* Tamaki, K., Suyehiro, K., Allan, J., McWilliams, M., et al., *Proc. ODP, Sci. Results,* 127/128 (Pt. 2): College Station, TX (Ocean Drilling Program), 1261–1274. **doi:10.2973/odp.proc.sr.127128-2.177.1992**

Muza, J.P., 1992. Calcareous nannofossil biostratigraphy from the Japan Sea, Sites 798 and 799: evidence for an oscillating Pleistocene oceanographic frontal boundary. *In* Pisciotto, K.A., Ingle, J.C., Jr., von Breymann, M.T., Barron, J., et al., *Proc. ODP, Sci. Results,* 127/128 (Pt. 1): College Station, TX (Ocean Drilling Program), 155–169. **doi:10.2973/odp.proc.sr.127128-1.122.1992**

Nomura, R., 1992. Miocene benthic foraminifers at Sites 794, 795, and 797 in the Sea of Japan with reference to the foram sharp line in the Honshu arc. *In* Pisciotto, K.A., Ingle, J.C., Jr., von Breymann, M.T., Barron, J., et al., *Proc. ODP, Sci. Results,* 127/128 (Pt. 1): College Station, TX (Ocean Drilling Program), 493–540. **doi:10.2973/odp.proc.sr.127128-1.187.1992**

Pribnow, D., Kinoshita, M., and Stein, C., 2000. *Thermal Data Collection and Heat Flow Recalculations for Ocean Drilling Program Legs 101–180:* Hanover, Germany (Inst. Joint Geosci. Res., Inst. Geowiss. Gemeinschaftsauf. [GGA]). **http://www-odp.tamu.edu/publications/heatflow/ODPReprt.pdf**

Sayles, F.L., and Manheim, F., 1975. Interstitial solutions and diagenesis in deeply buried marine sediments: results from the Deep Sea Drilling Project. *Geochim. Cosmochim. Acta,* 39(2):103–127. **doi:10.1016/0016-7037(75)90165-9**

Shipboard Scientific Party, 1990. Site 799. *In* Ingle, J.C., Jr., Suyehiro, K., von Breymann, M.T., et al., *Proc. ODP, Init. Repts.,* 128: College Station, TX (Ocean Drilling Program), 237–402. **doi:10.2973/odp.proc.ir.128.106.1990**

Tada, R., 1991. Origin of rhythmical bedding in middle Miocene siliceous rocks of the Onnagawa Formation, northern Japan. *J. Sediment. Res.,* 61(7):1123–1145. **doi:10.1306/D426784D-2B26-11D7-8648000102C1865D**

Tada, R., 1994. Paleoceanographic evolution of the Japan Sea. *Palaeogeogr., Palaeoclimatol., Palaeoecol.,* 108(3–4):487–508. **doi:10.1016/0031-0182(94)90248-8**

Tada, R., and Iijima, A., 1992. Lithostratigraphy and compositional variation of Neogene hemipelagic sediments in the Japan Sea. *In* Tamaki, K., Suyehiro, K., Allan, J., McWilliams, M., et al., *Proc. ODP, Sci. Results,* 127/128 (Pt. 2): College Station, TX (Ocean Drilling Program), 1229–1260. **doi:10.2973/odp.proc.sr.127128-2.188.1992**

Tada, R., Irino, T., and Koizumi, I., 1999. Land-ocean linkages over orbital and millennial timescales recorded in late Quaternary sediments of the Japan Sea. *Paleoceanography,* 14(2):236–247. **doi:10.1029/1998PA900016**

Tada, R., Koizumi, I., Cramp, A., and Rahman, A., 1992. Correlation of dark and light layers, and the origin of their cyclicity in the Quaternary sediments from the Japan Sea. *In* Pisciotto, K.A., Ingle, J.C., Jr., von Breymann, M.T., Barron, J., et al., *Proc. ODP, Sci. Results,* 127/128 (Pt. 1): College Station, TX (Ocean Drilling Program), 577–601. **doi:10.2973/odp.proc.sr.127128-1.160.1992**

Tada, R., Murray, R.W., Alvarez Zarikian, C.A., Anderson, W.T., Jr., Bassetti, M.-A., Brace, B.J., Clemens, S.C., da Costa Gurgel, M.H., Dickens, G.R., Dunlea, A.G., Gallagher, S.J., Giosan, L., Henderson, A.C.G., Holbourn, A.E., Ikehara, K., Irino, T., Itaki, T., Karasuda, A., Kinsley, C.W., Kubota, Y., Lee, G.S., Lee, K.E., Lofi, J., Lopes, C.I.C.D., Peterson, L.C., Saavedra-Pellitero, M., Sagawa, T., Singh, R.K., Sugisaki, S., Toucanne, S., Wan, S., Xuan, C., Zheng, H., and Ziegler, M., 2015a. Expedition 346 summary. *In* Tada, R., Murray, R.W., Alvarez Zarikian, C.A., and the Expedition 346 Scientists, *Proc. IODP,* 346: College Station, TX (Integrated Ocean Drilling Program). **doi:10.2204/iodp.proc.346.101.2015**

Tada, R., Murray, R.W., Alvarez Zarikian, C.A., Anderson, W.T., Jr, Bassetti, M.-A., Brace, B.J., Clemens, S.C., Dickens, G.R., Dunlea, A.G., Gallagher, S.J., Giosan, L., da Costa Gurgel, M.H., Henderson, A.C.G., Holbourn, A.E., Ikehara, K., Irino, T., Itaki, T., Karasuda, A., Kinsley, C.W., Kubota, Y., Lee, G.S., Lee, K.E., Lofi, J., Lopes, C.I.C.D., Peterson, L.C., Saavedra-Pellitero, M., Sagawa, T., Singh, R.K., Sugisaki, S., Toucanne, S., Wan, S., Xuan, C., Zheng, H., and Ziegler, M., 2015b. Methods. *In* Tada, R., Murray, R.W., Alvarez Zarikian, C.A., and the Expedition 346 Scientists, *Proc. IODP,* 346: College Station, TX (Integrated Ocean Drilling Program). **doi:10.2204/iodp.proc.346.102.2015**

Tada, R., Murray, R.W., Alvarez Zarikian, C.A., Anderson, W.T., Jr., Bassetti, M.-A., Brace, B.J., Clemens, S.C., da Costa Gurgel, M.H., Dickens, G.R., Dunlea, A.G., Gallagher, S.J., Giosan, L., Henderson, A.C.G., Holbourn, A.E., Ikehara, K., Irino, T., Itaki, T., Karasuda, A., Kinsley, C.W., Kubota, Y., Lee, G.S., Lee, K.E., Lofi, J., Lopes, C.I.C.D., Peterson, L.C., Saavedra-Pellitero, M., Sagawa, T., Singh, R.K., Sugisaki, S., Toucanne, S., Wan, S., Xuan, C., Zheng, H., and Ziegler, M., 2015c. Site U1422. *In* Tada, R., Murray, R.W., Alvarez Zarikian, C.A., and the Expedition 346 Scientists, *Proc. IODP,* 346: College Station, TX (Integrated Ocean Drilling Program). **doi:10.2204/iodp.proc.346.103.2015**

Tada, R., Murray, R.W., Alvarez Zarikian, C.A., Anderson, W.T., Jr, Bassetti, M.-A., Brace, B.J., Clemens, S.C., Dickens, G.R., Dunlea, A.G., Gallagher, S.J., Giosan, L., da Costa Gurgel, M.H., Henderson, A.C.G., Holbourn, A.E., Ikehara, K., Irino, T., Itaki, T., Karasuda, A., Kinsley, C.W., Kubota, Y., Lee, G.S., Lee, K.E., Lofi, J., Lopes, C.I.C.D., Peterson, L.C., Saavedra-Pellitero, M., Sagawa, T., Singh, R.K., Sugisaki, S., Toucanne, S., Wan, S., Xuan, C., Zheng, H., and Ziegler, M., 2015d. Site U1423. *In* Tada, R., Murray, R.W., Alvarez Zarikian, C.A., and the Expedition 346 Scientists, *Proc. IODP,* 346: College Station, TX (Integrated Ocean Drilling Program). **doi:10.2204/iodp.proc.346.104.2015**

Tada, R., Murray, R.W., Alvarez Zarikian, C.A., Anderson, W.T., Jr, Bassetti, M.-A., Brace, B.J., Clemens, S.C., Dickens, G.R., Dunlea, A.G., Gallagher, S.J., Giosan, L., da Costa Gurgel, M.H., Henderson, A.C.G., Holbourn, A.E., Ikehara, K., Irino, T., Itaki, T., Karasuda, A., Kinsley, C.W., Kubota, Y., Lee, G.S., Lee, K.E., Lofi, J., Lopes, C.I.C.D., Peterson, L.C., Saavedra-Pellitero, M., Sagawa, T., Singh, R.K., Sugisaki, S., Toucanne, S., Wan, S., Xuan, C., Zheng, H., and Ziegler, M., 2015e. Site U1424. *In* Tada, R., Murray, R.W., Alvarez Zarikian, C.A., and the Expedition 346 Scientists, *Proc. IODP,* 346: College Station, TX (Integrated Ocean Drilling Program). **doi:10.2204/iodp.proc.346.105.2015**

von Breymann, M.T., Brumsack, H., and Emeis, K.C., 1992. Depositional and diagenetic behavior of barium in the Japan Sea. *In* Pisciotto, K.A., Ingle, J.C., Jr., von Breymann, M.T., Barron, J., et al., *Proc. ODP, Sci. Results,* 127/128 (Pt. 1): College Station, TX (Ocean Drilling Program), 651–665. **doi:10.2973/odp.proc.sr.127128-1.168.1992**

Xuan, C., and Channell, J.E.T., 2009. UPmag: MATLAB software for viewing and processing U channel or other pass-through paleomagnetic data. *Geochem., Geophys., Geosyst.,* 10(10):Q10Y07. **doi:10.1029/2009GC002584**

Yanagisawa, Y., and Akiba, F., 1998. Refined Neogene diatom biostratigraphy for the northwest Pacific around Japan, with an introduction of code numbers for selected diatom biohorizons. *Chishitsugaku Zasshi,* 104(6):395–414. **doi:10.5575/geosoc.104.395**

You, C.-F., Gieskes, J.M., Chen, R.F., Spivack, A., and Gamo, T., 1993. Iodide, bromide, manganese, boron, and dissolved organic carbon in interstitial waters of the organic carbon–rich marine sediments: observations in the Nankai accretionary prism. *In* Hill, I.A., Taira, A., Firth, J.V., et al., *Proc. ODP, Sci. Results,* 131: College Station, TX (Ocean Drilling Program), 165–174. **doi:10.2973/odp.proc.sr.131.116.1993**

Publication: 28 March 2015
MS 346-106

Figure F1. Bathymetric map of Expedition 346 sites (red circles) in the marginal sea surrounded by the Japanese Islands, the Korean Peninsula, and the Eurasian continent and the East China Sea. Sites previously drilled by the Deep Sea Drilling Project (DSDP) and Ocean Drilling Program (ODP) (white circles) are also shown. Also illustrated are surface current systems within and surrounding this marginal sea.

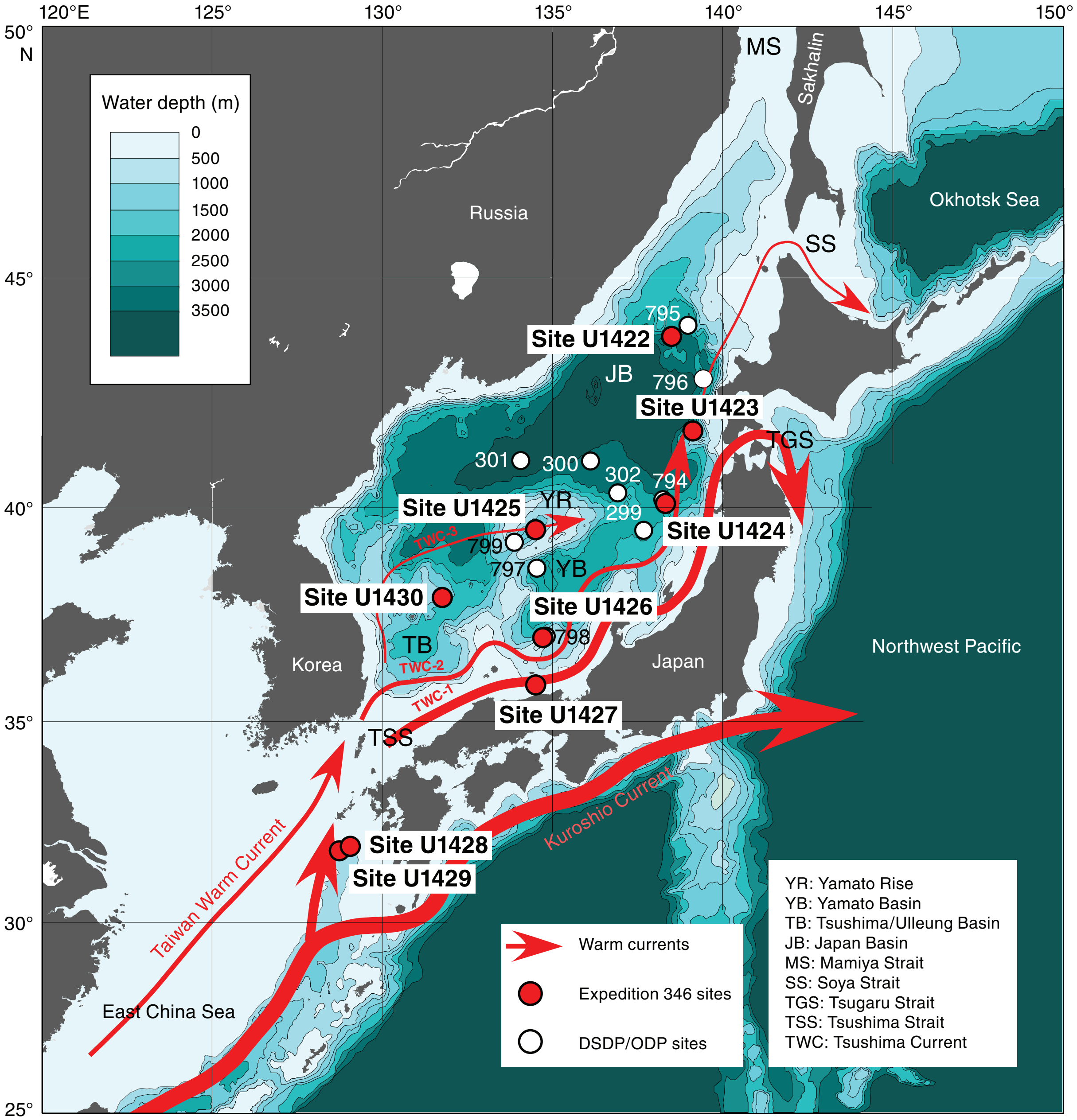

Figure F2. Primary seismic Line St7 1-2, Site U1425. CMP = common midpoint, SP = shot point.

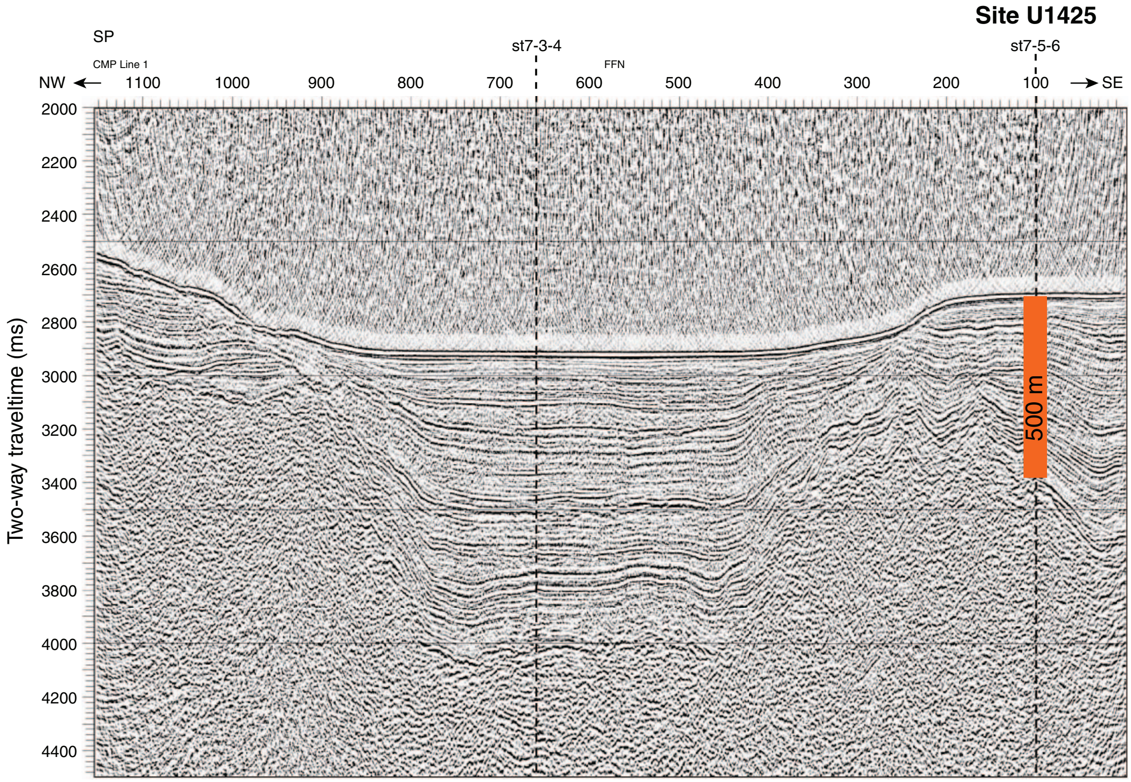

Figure F3. Lithologic summary, Hole U1425B. GRA = gamma ray attenuation.

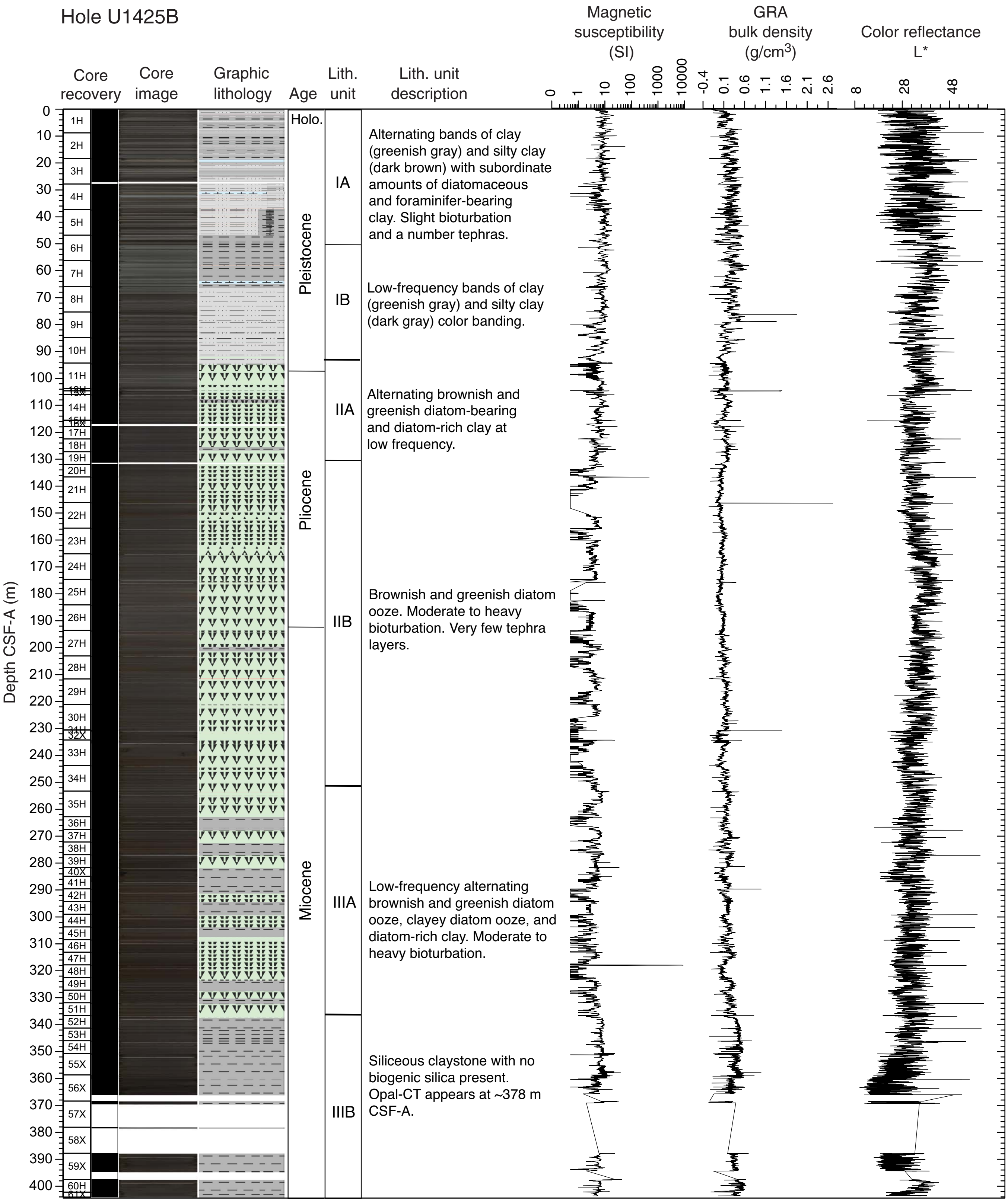

Figure F4. Lithologic summary, Hole U1425D. GRA = gamma ray attenuation.

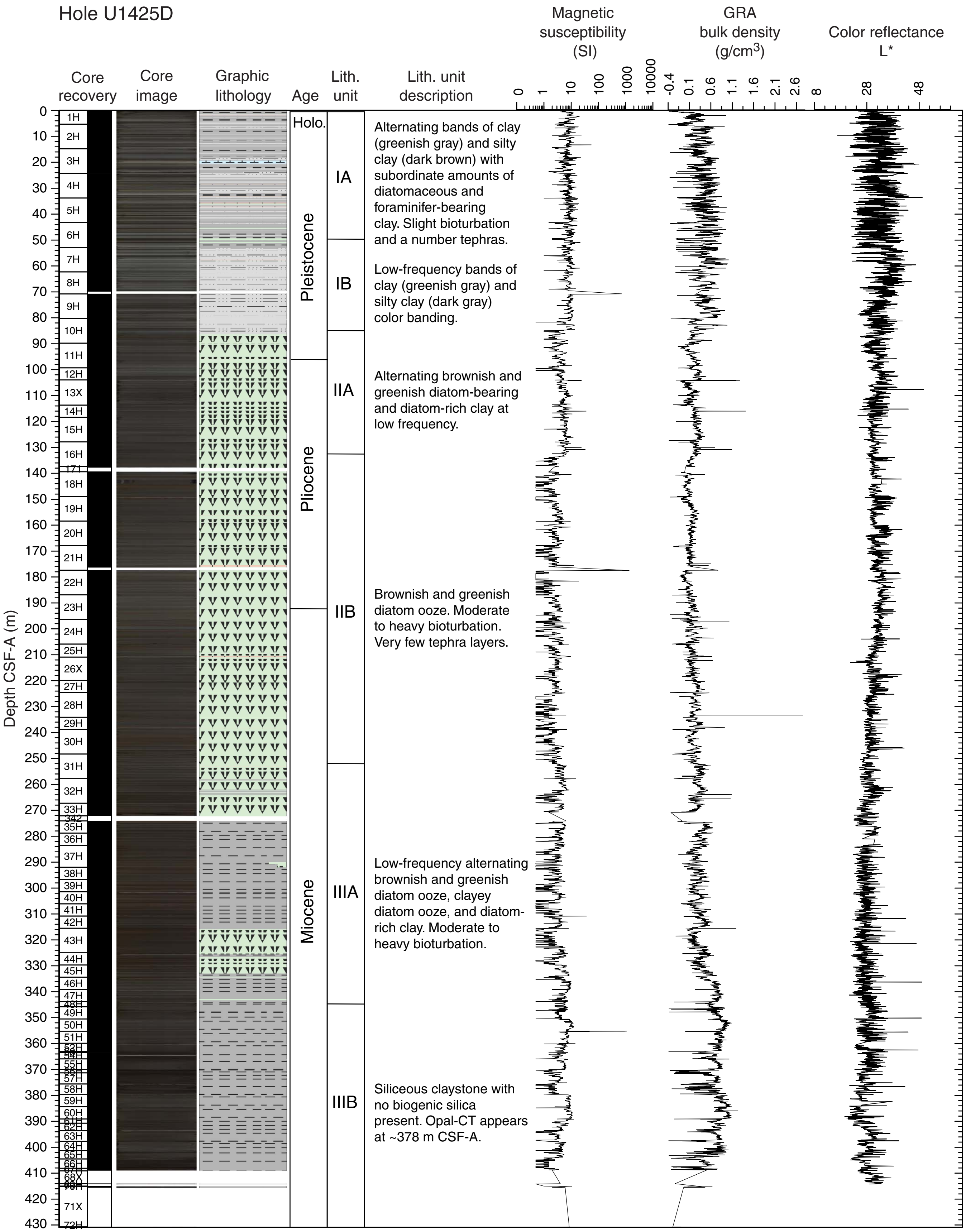

Figure F5. Lithologic summary, Hole U1425E. GRA = gamma ray attenuation.

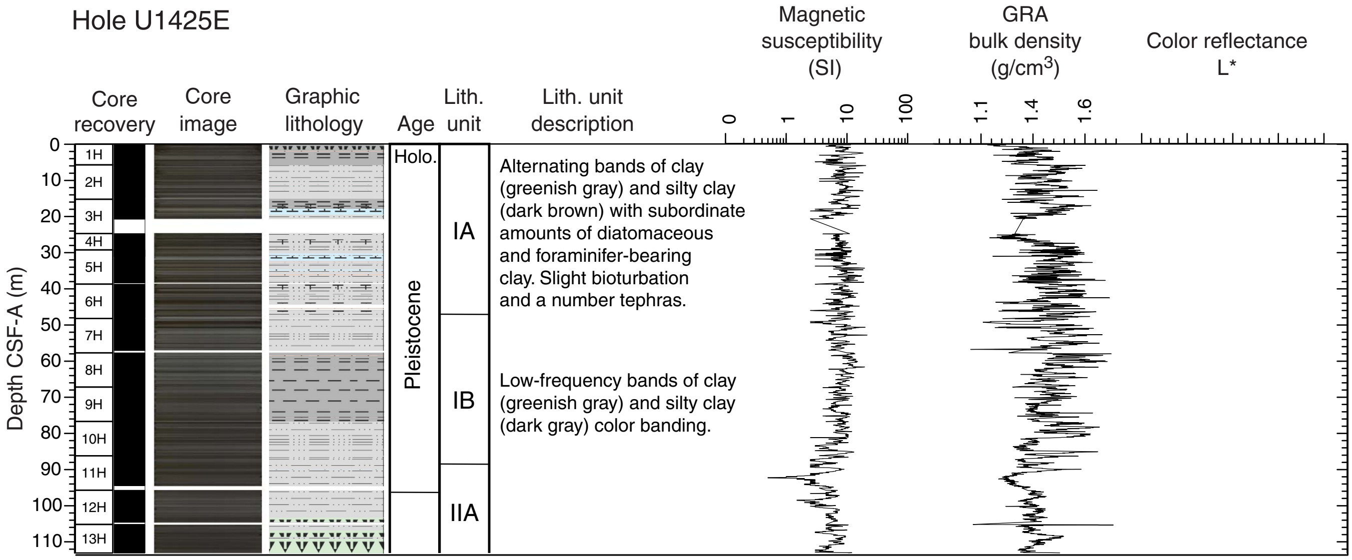

Figure F6. Hole-to-hole lithostratigraphic correlation, Site U1425. Note there is an uncertainty about the Unit I/II boundary as a result of slump folds in the sediment succession.

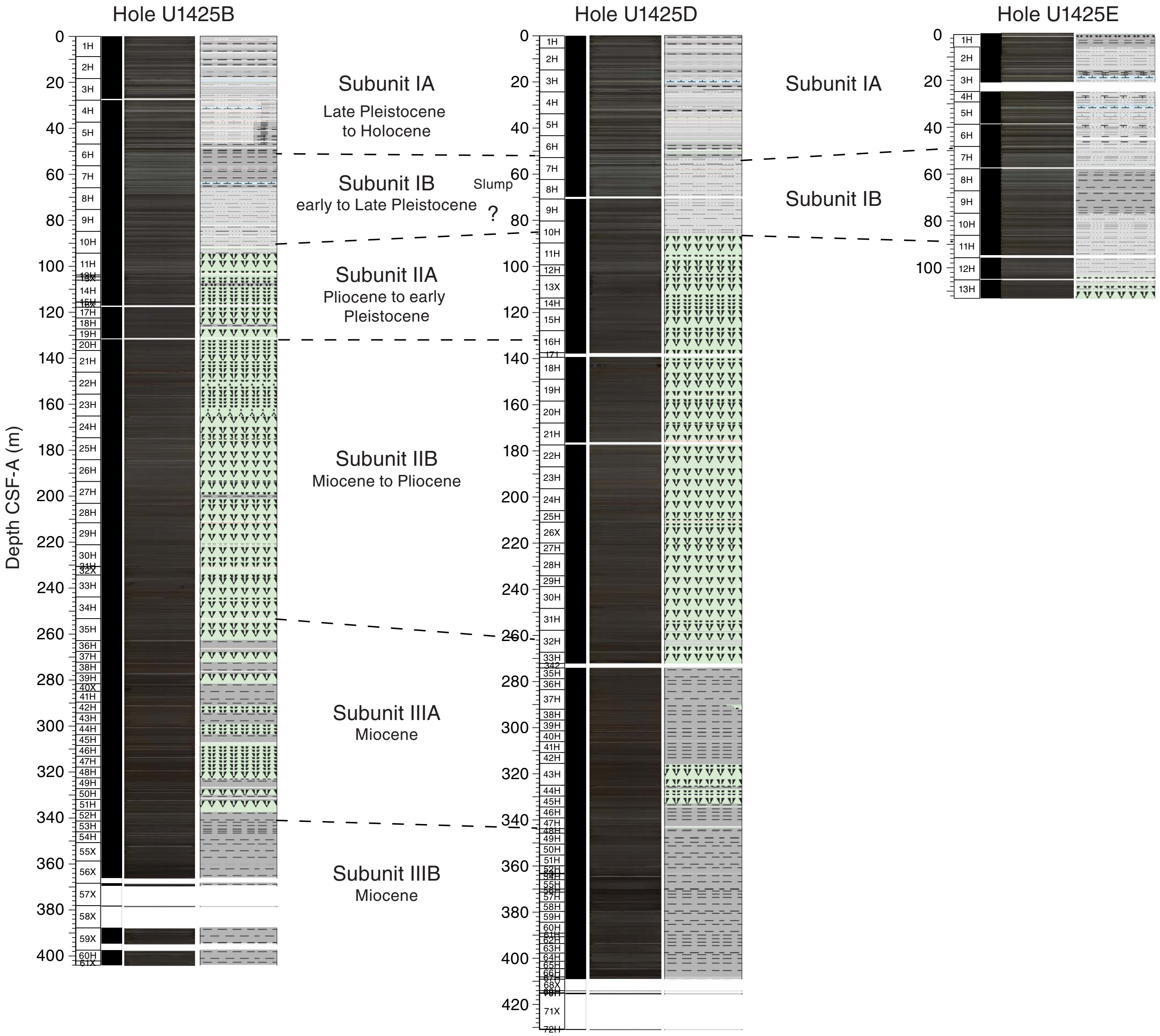

Figure F7. Distribution of the number of tephra layers and total thickness of tephra in each core, Hole U1425B.

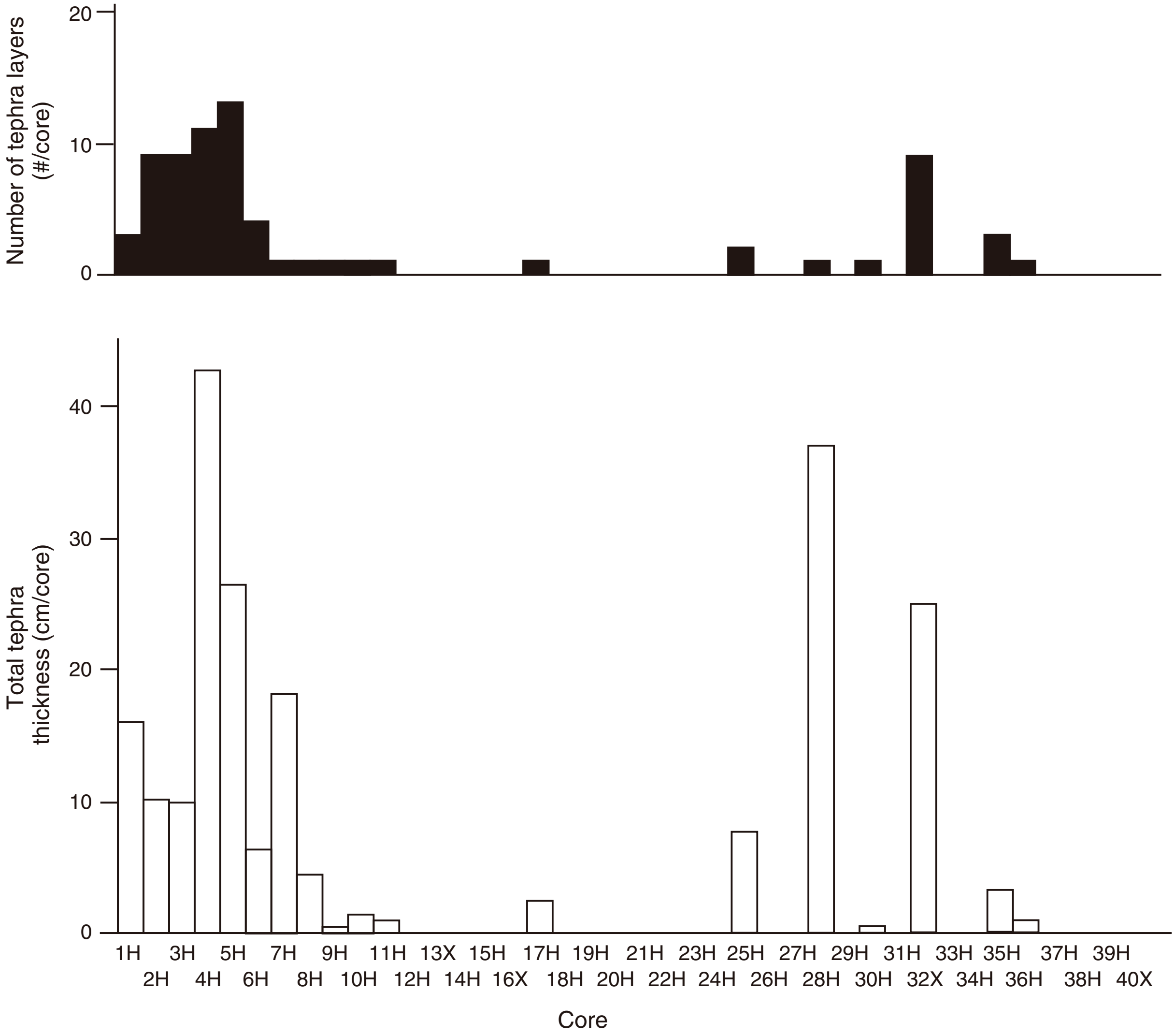

Figure F8. Variation of bulk sediment sample XRD peak intensity of identified minerals with depth, Site U1425.

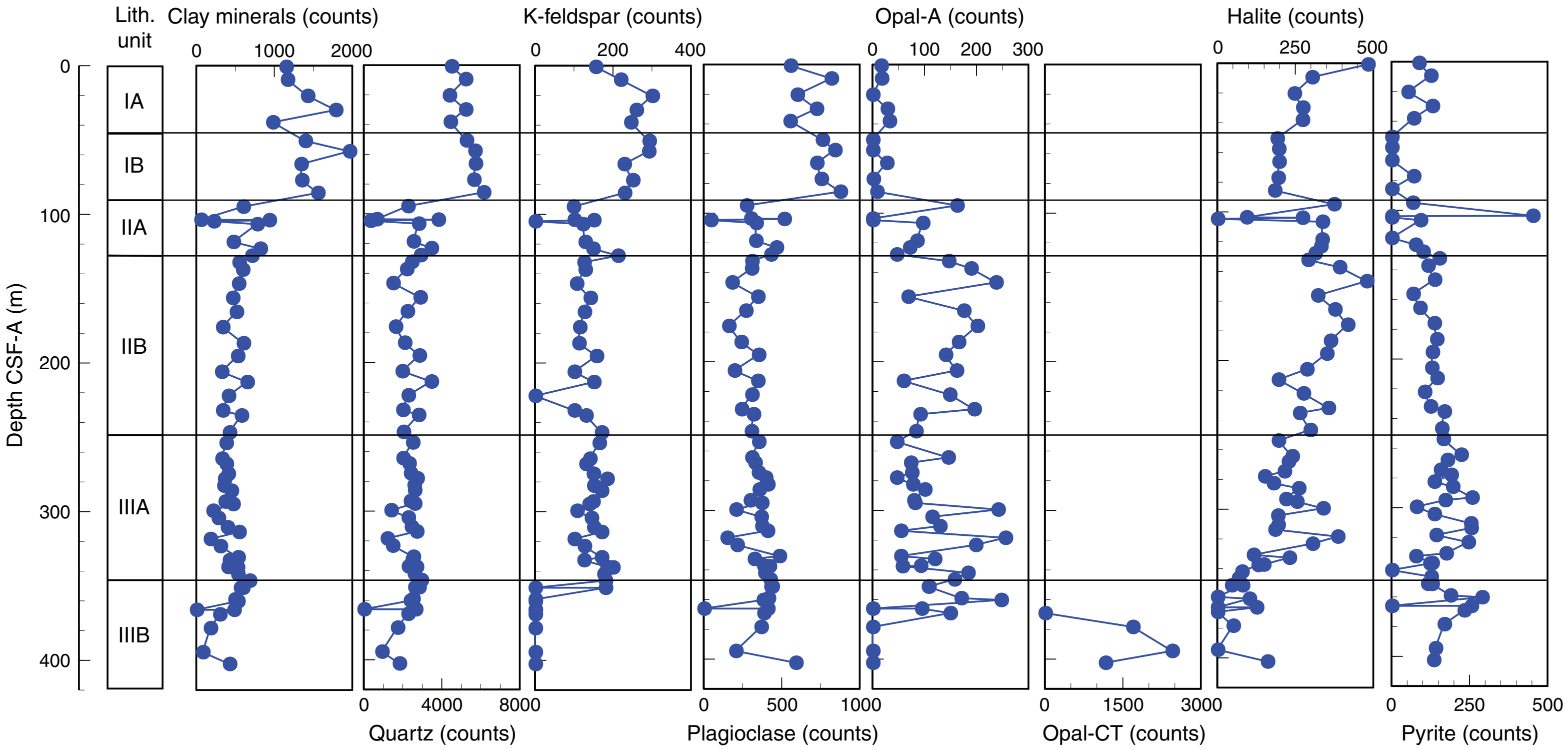

Figure F9. Photographs representative of Subunit IA, Hole U1425B. Note core images have been enhanced using a color contrast to highlight sedimentary structures.

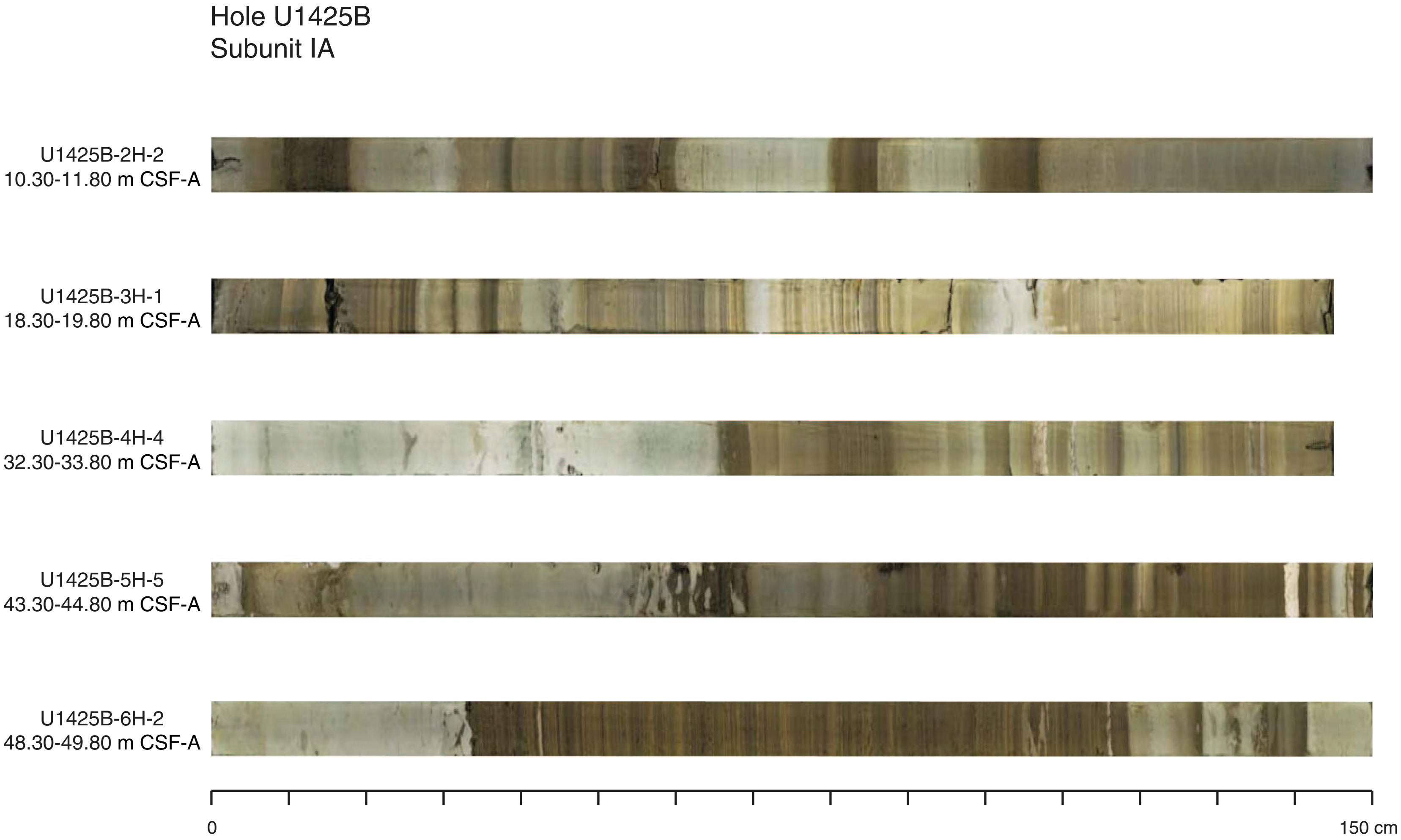

Figure F10. Detail of slightly bioturbated gray clay intercalated between light greenish gray and dark brown intervals in Subunit IA, Hole U1425B. Note core images have been enhanced using a color contrast to highlight sedimentary structures.

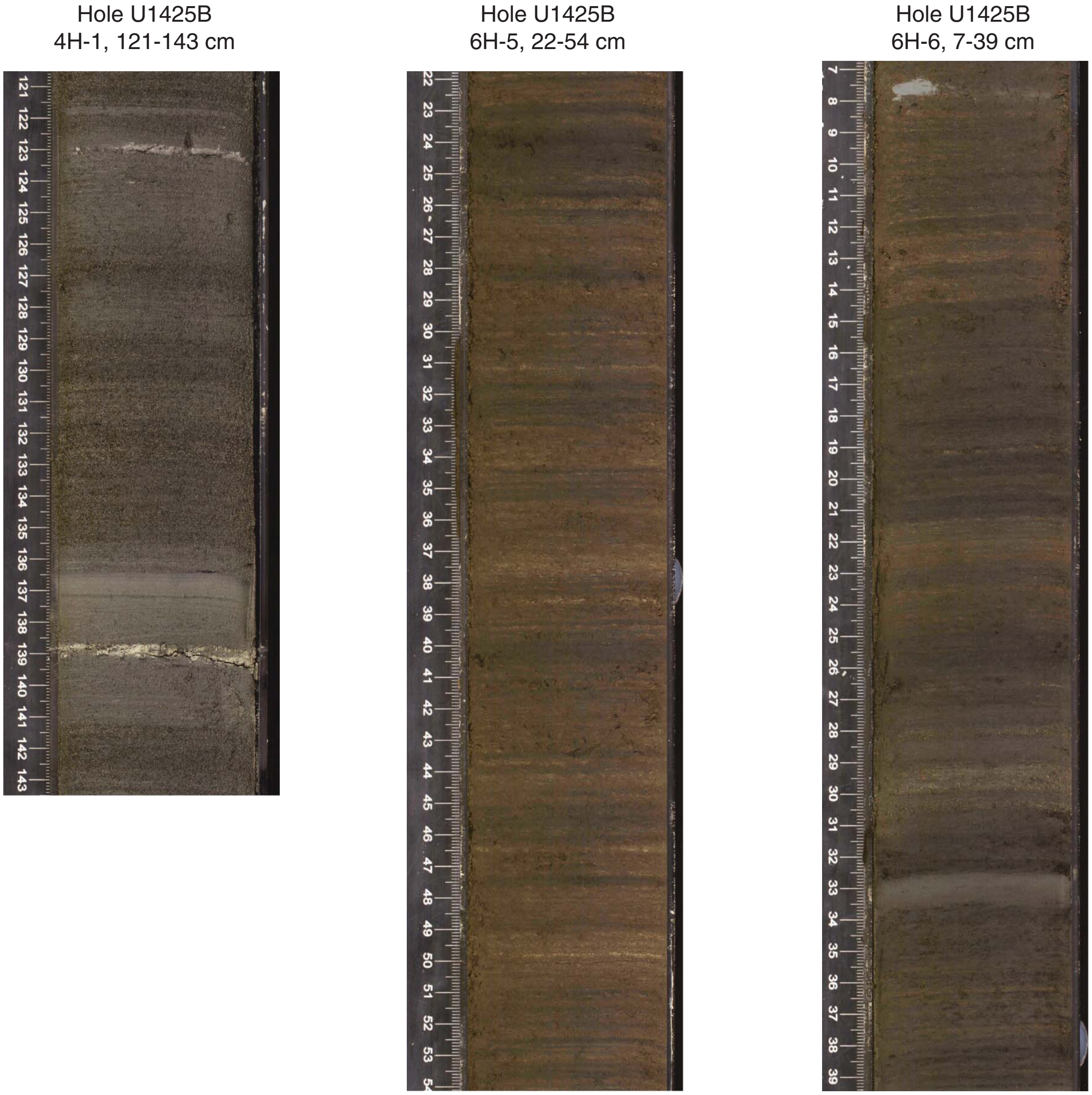

Hole U1425B
4H-1, 121-143 cm

Hole U1425B
6H-5, 22-54 cm

Hole U1425B
6H-6, 7-39 cm

Figure F11. Detail of dark brown laminated intervals in Subunit IA, Hole U1425B. Note core images have been enhanced using a color contrast to highlight sedimentary structures.

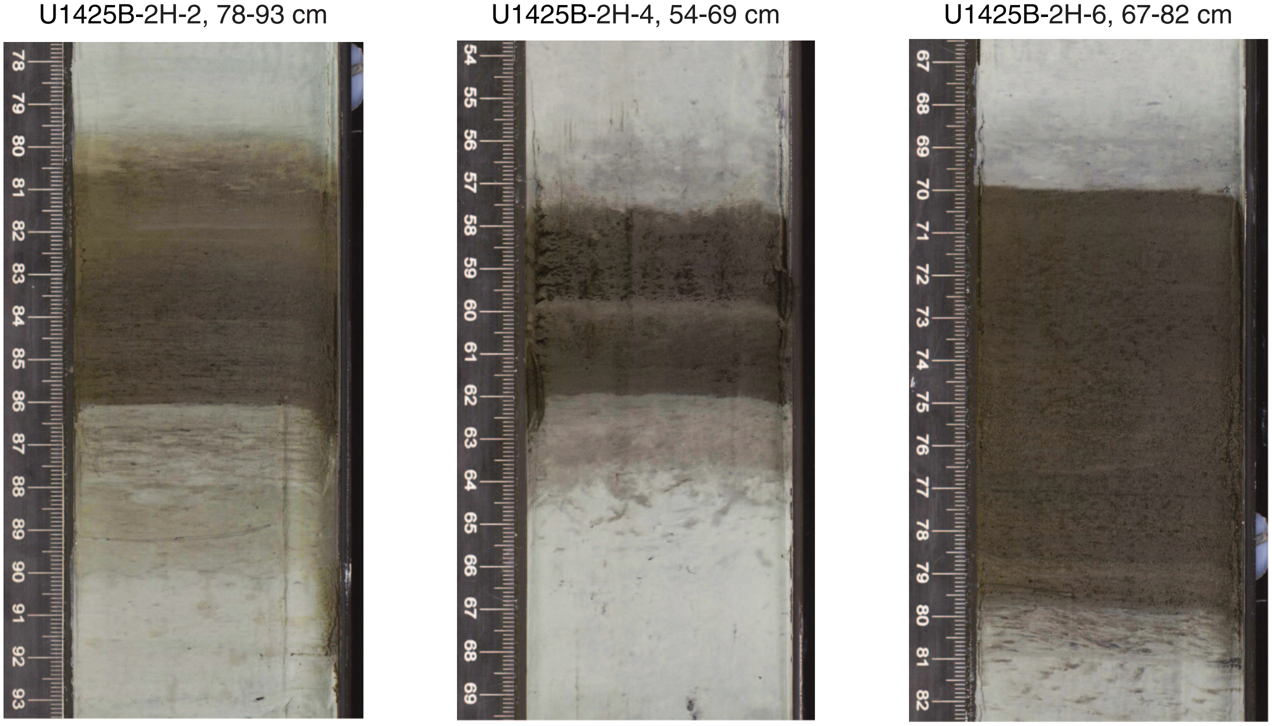

U1425B-2H-2, 78-93 cm

U1425B-2H-4, 54-69 cm

U1425B-2H-6, 67-82 cm

Figure F12. Detail of heavy bioturbation near the top of Subunit IA (interval 346-U1425B-1H-5, 86–107 cm). Note core images have been enhanced using a color contrast to highlight sedimentary structures.

Figure F13. Details of euhedral pyrite crystals (Section 346-U1425B-2H-5, 75 cm).

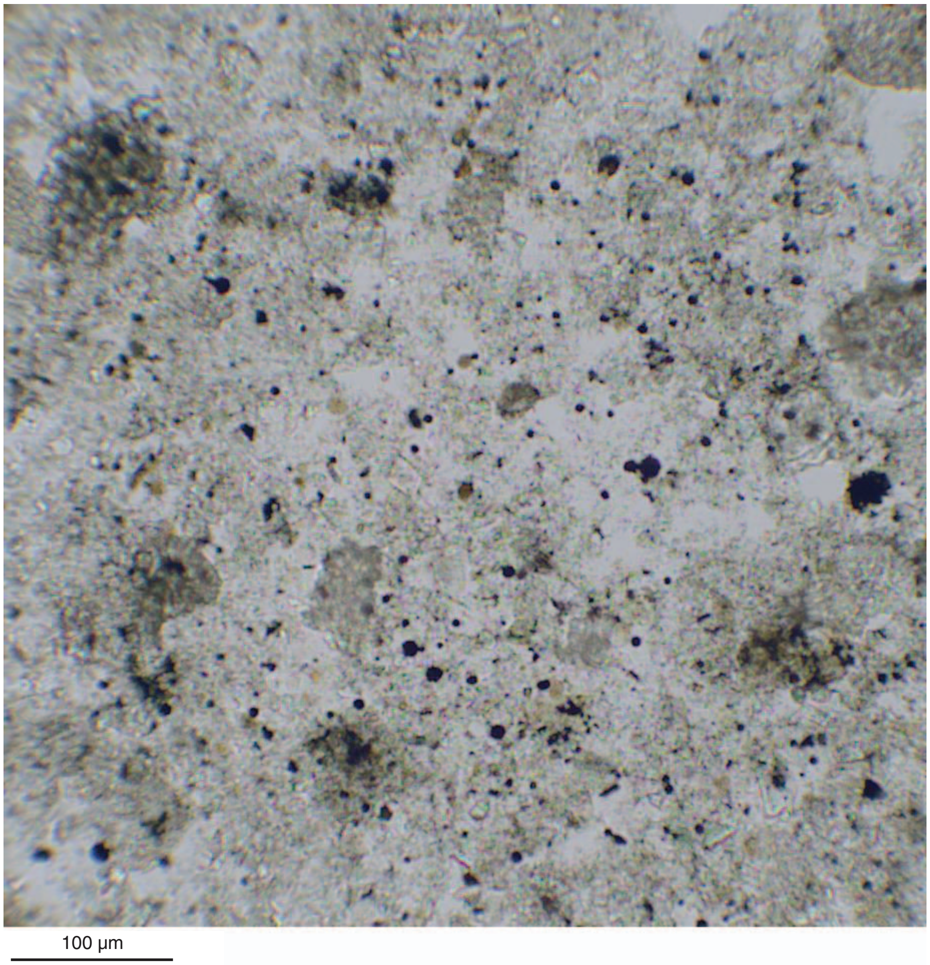

Figure F14. Photographs representative of Subunit IB, Hole U1425B. Note core images have been enhanced using a color contrast to highlight sedimentary structures.

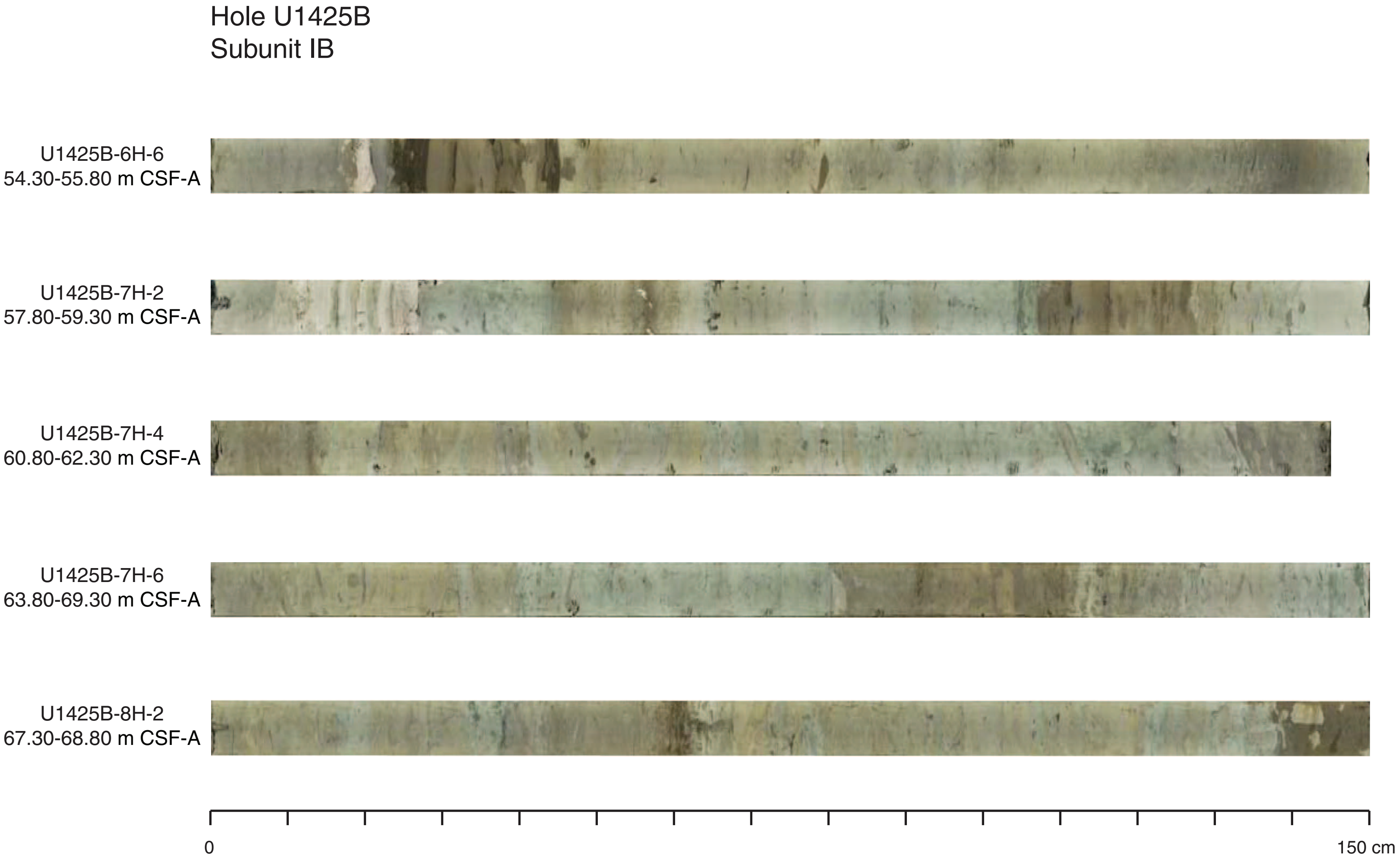

Figure F15. Photographs representative of Subunit IIA, Hole U1425B. Note core images have been enhanced using a color contrast to highlight sedimentary structures.

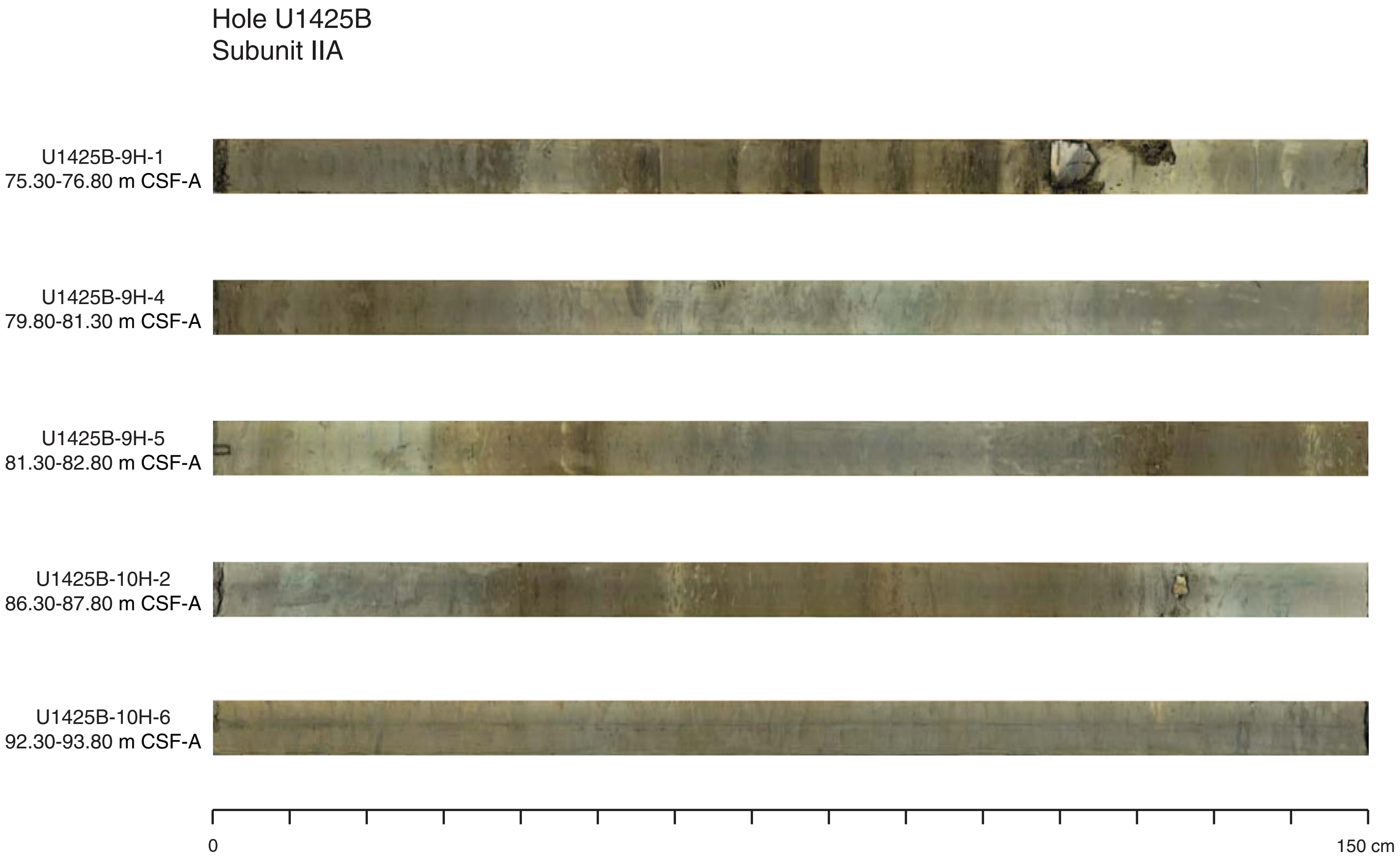

Figure F16. Photographs representative of Subunit IIB, Hole U1425B. Note core images have been enhanced using a color contrast to highlight sedimentary structures.

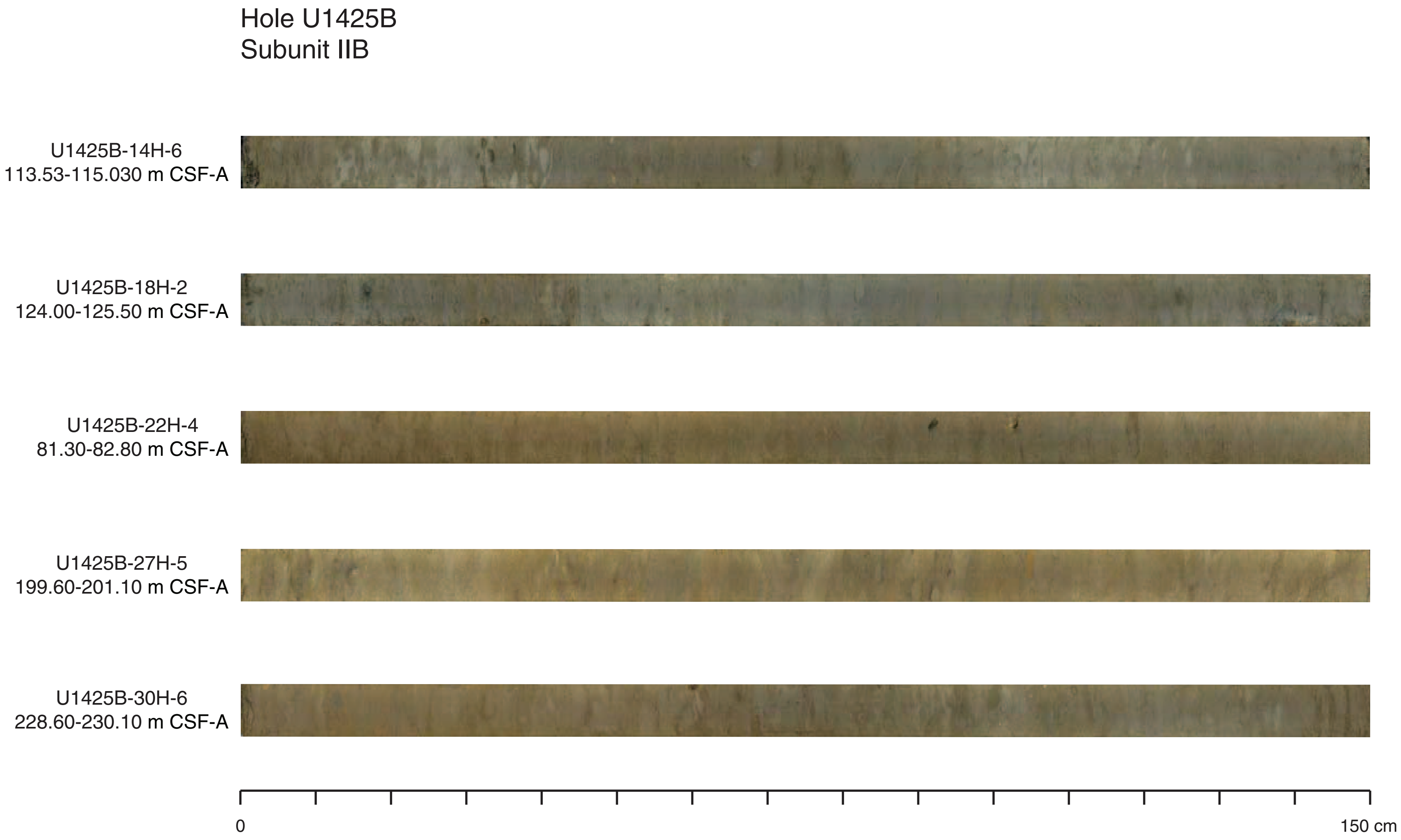

Figure F17. Detail of moderate to heavy bioturbation in Unit II, Hole U1425B. Note core images have been enhanced using a color contrast to highlight sedimentary structures.

U1425B-11H-6, 34-51 cm

U1425B-18H-4, 3-40 cm

U1425B-21H-5, 40-60 cm

Figure F18. Photographs and thin section photomicrographs of (**A**) a dolomite layer (interval 346-U1425B-13X-1, 0–10 cm) and (**B**) a dolomite concretion (interval 22H-1, 15–22 cm). Note core images have been enhanced using a color contrast to highlight sedimentary structures.

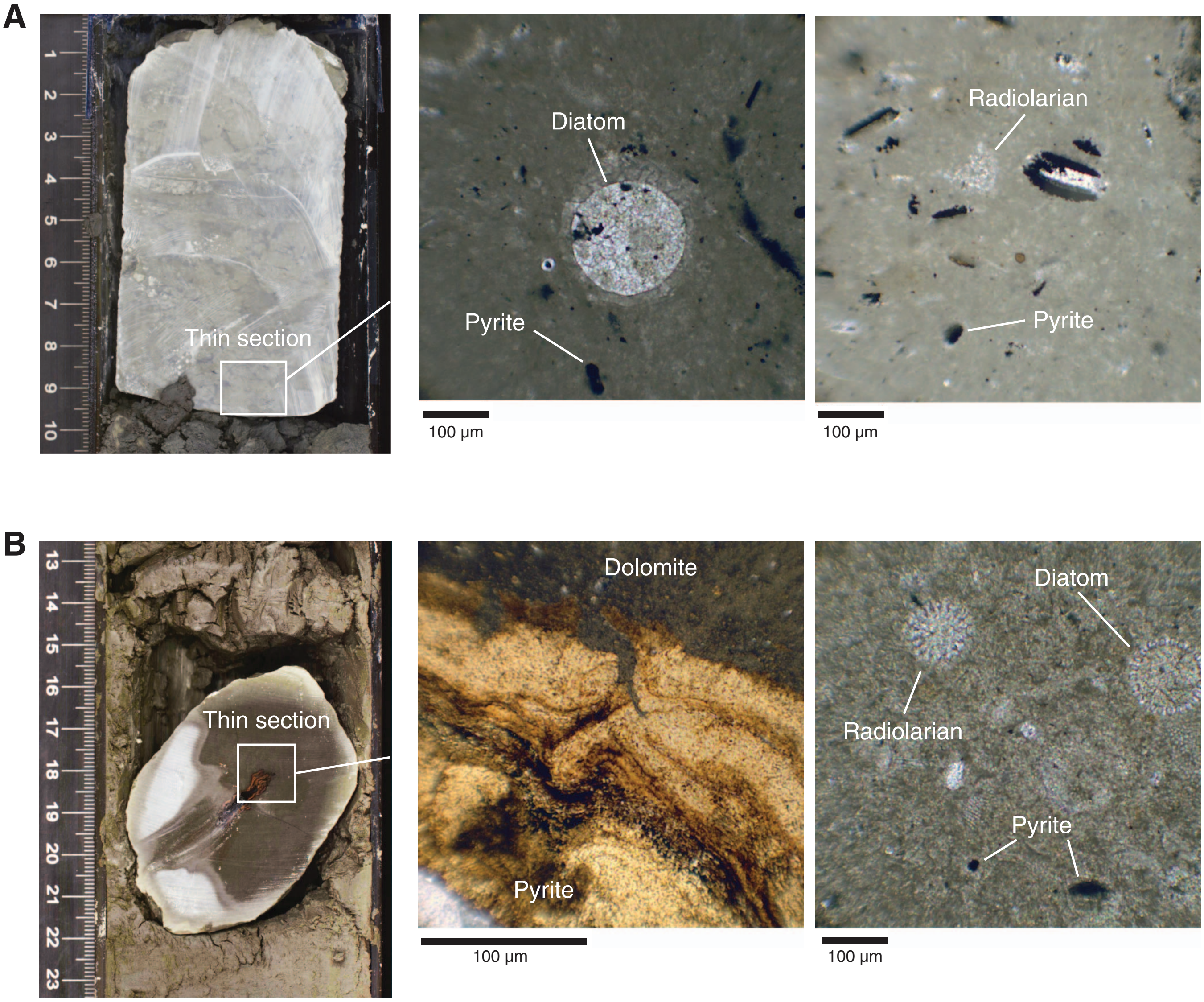

Figure F19. Photographs of slump folds at the Unit I/II boundary (Cores 346-U1425D-9H and 10H) and in Subunit IIIA (Core 38H). Note core images have been enhanced using a color contrast to highlight sedimentary structures.

U1425D-9H-2, 1-73 cm U1425D-10H-6, 50-123 cm U1425D-38H-1, 33-106 cm

Figure F20. Photomicrograph showing details of biosiliceous material found in Unit III (Section 346-U1425B-38H-3, 34 cm).

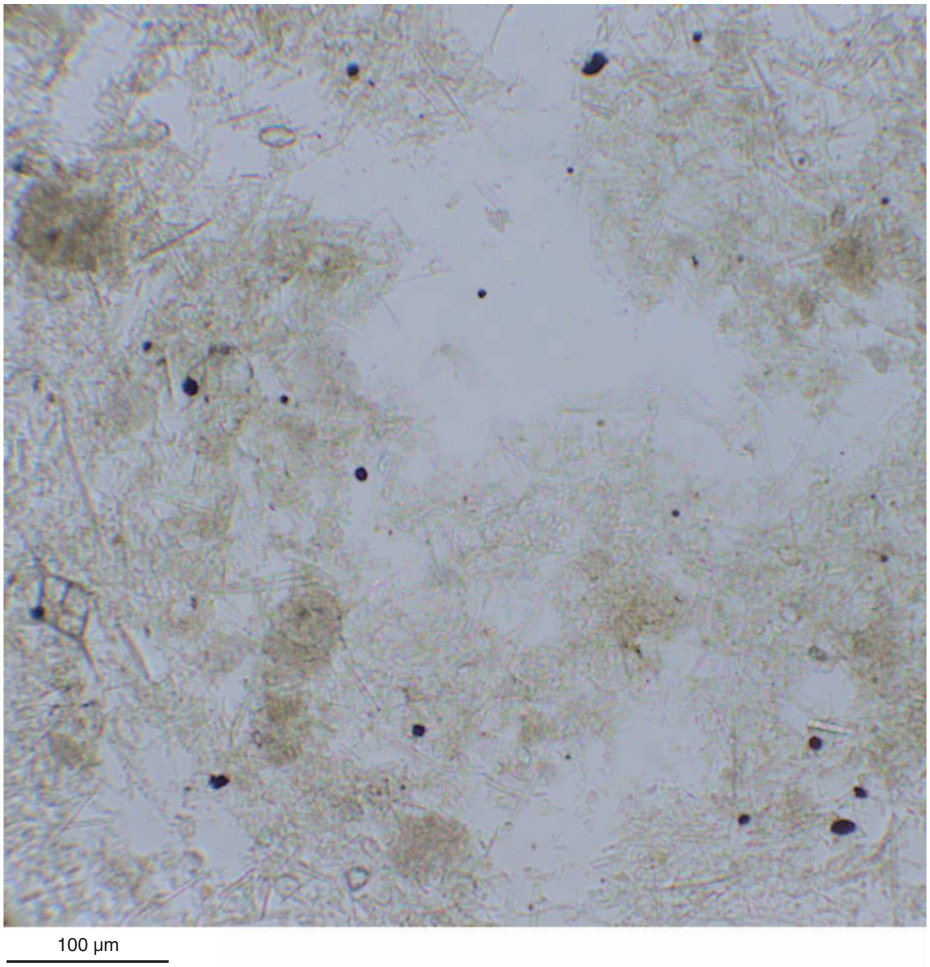

Figure F21. Photomicrographs showing details of the diagenesis of biogenic silica across the Subunit IIIA/IIIB boundary. **A.** Biosiliceous material (Section 346-U1425B-52H-1, 75 cm). **B.** Biosiliceous material disappears from dissolution and diagenetic transition to opal-CT (Section 346-U1425B-60H-4, 50 cm).

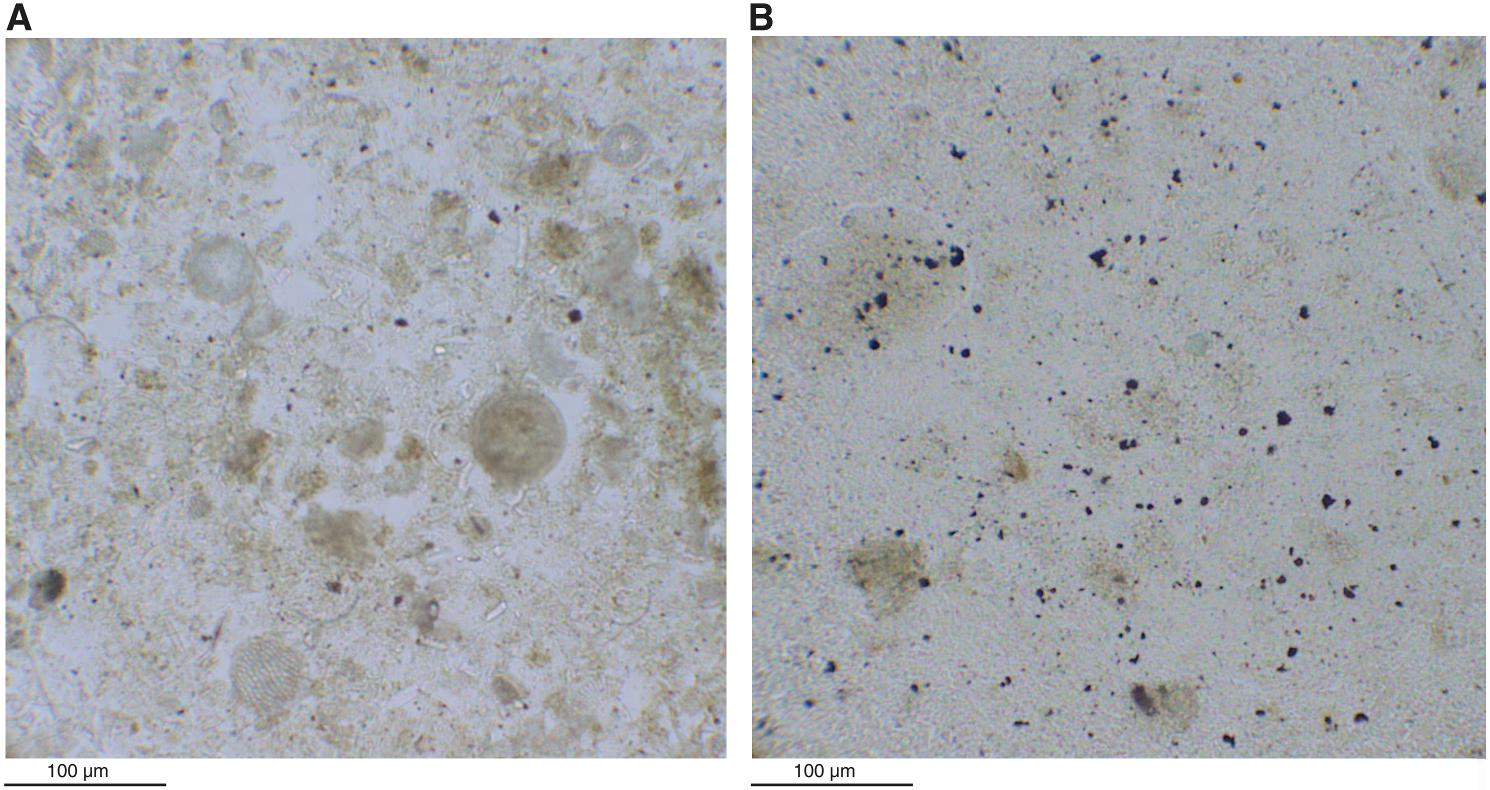

Figure F22. Downcore variations in opal-A and opal-CT with a switch between the two occurring at ~378 m CSF-A. X-ray diffraction (XRD) diagrams highlight well-defined peaks of cristobalite (C) and tridymite (T) in the lower section of Subunit IIIB, whereas there is only a clear peak in quartz (Q) in the upper portion of Subunit IIIB.

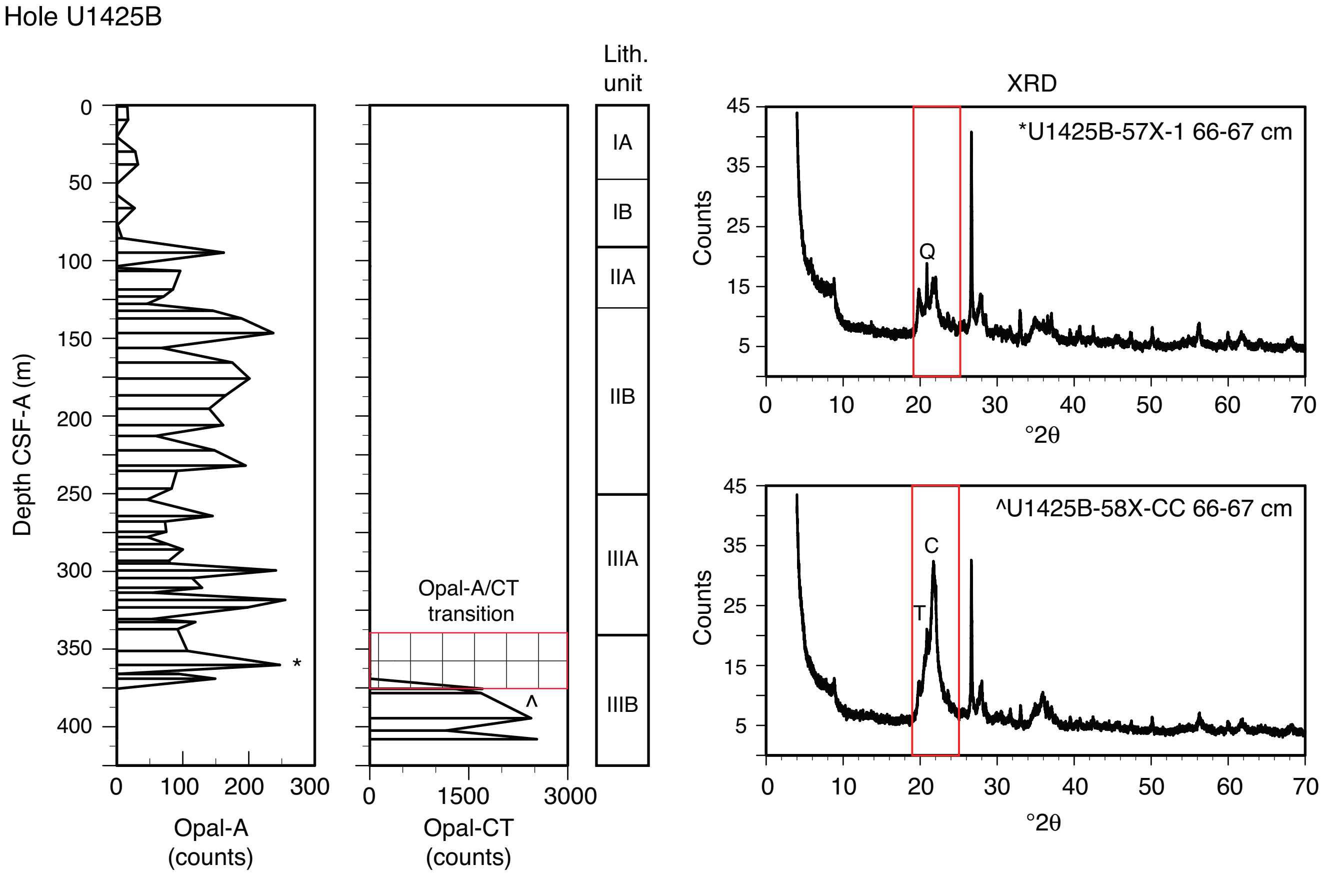

Figure F23. Photographs representative of Subunit IIIA, Hole U1425B. Note core images have been enhanced using a color contrast to highlight sedimentary structures.

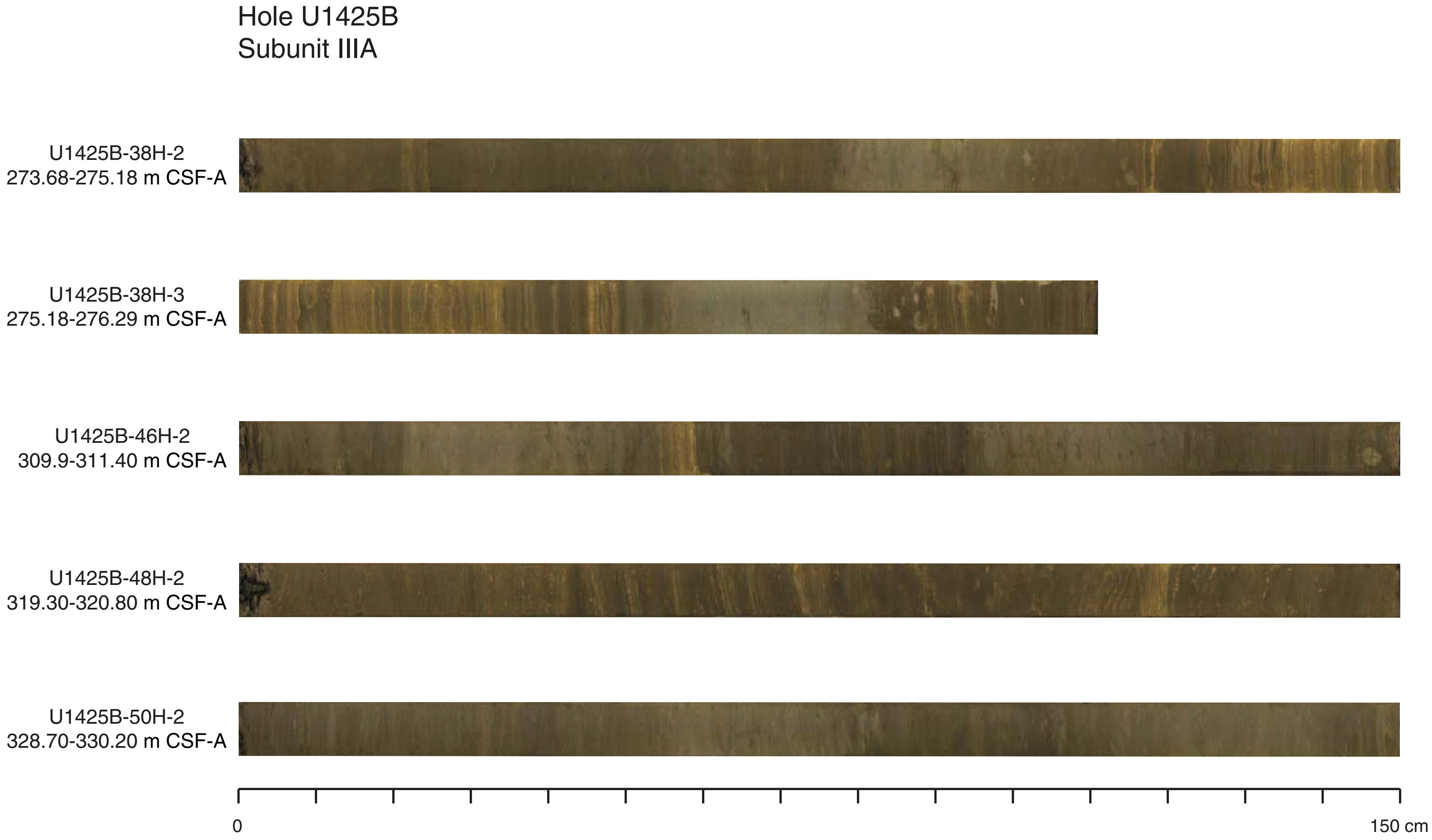

Figure F24. Photograph of a large vertical burrow in Subunit IIIA (interval 346-U1425D-44H-2, 71–113 cm). Note core image has been enhanced using a color contrast to highlight sedimentary structures.

Figure F25. Photograph of finely laminated diatom ooze in Subunit IIIA and IIIB (approximately middle to late Miocene age) from Holes U1425B and U1425D. Note core images have been enhanced using a color contrast to highlight sedimentary structures.

U1425B-38H-2, 128-149 cm

U1425B-38H-3, 0-39 cm

U1425D-35H-1, 4-44 cm

Figure F26. Photographs representative of Subunit IIIB, Hole U1425B. Note core images have been enhanced using a color contrast to highlight sedimentary structures.

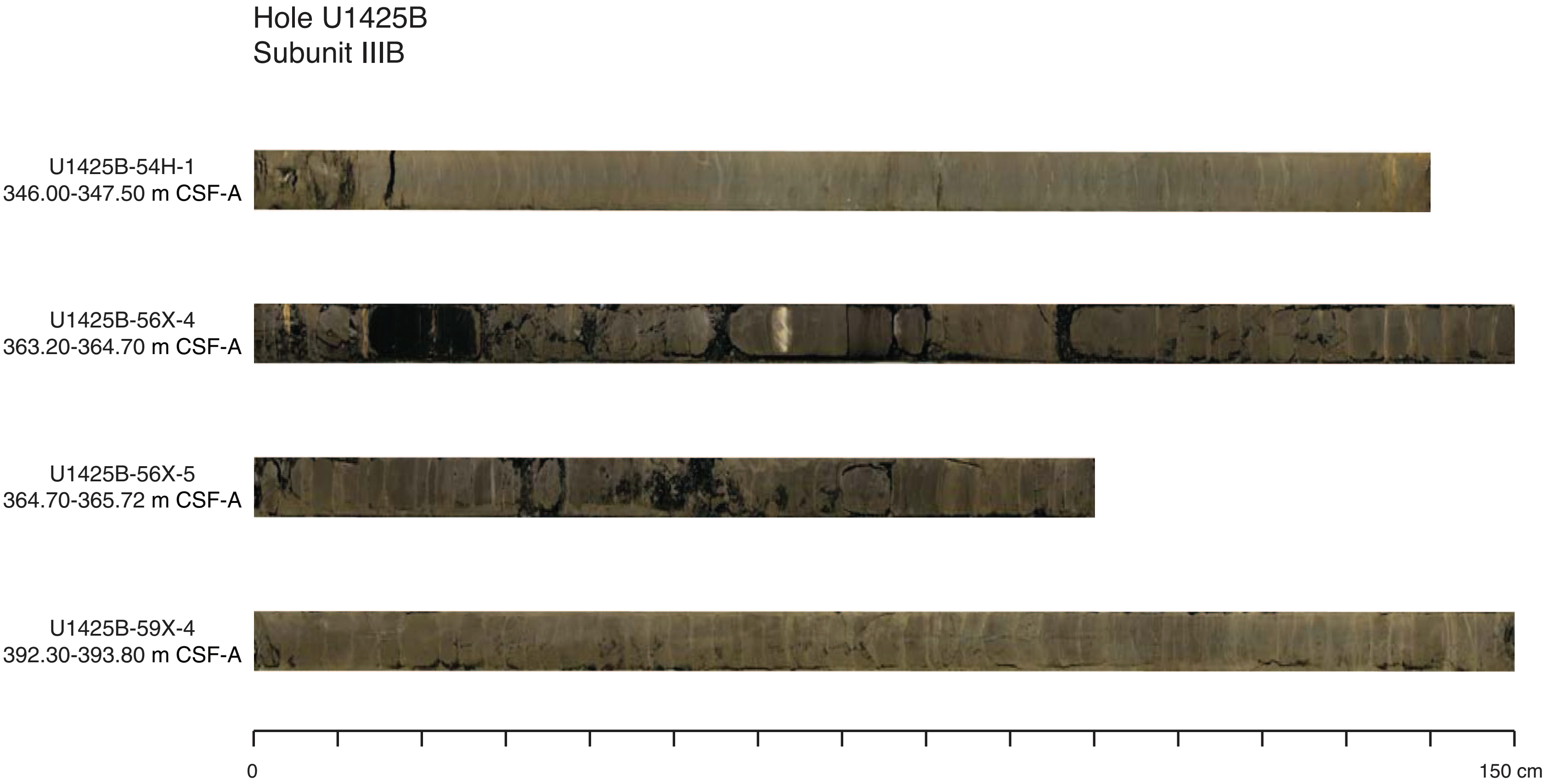

Figure F27. Photograph of parallel laminations in siliceous claystone from Subunit IIIB (interval 346-U1425B-56X-4, 131–148 cm). Note core images have been enhanced using a color contrast to highlight sedimentary structures.

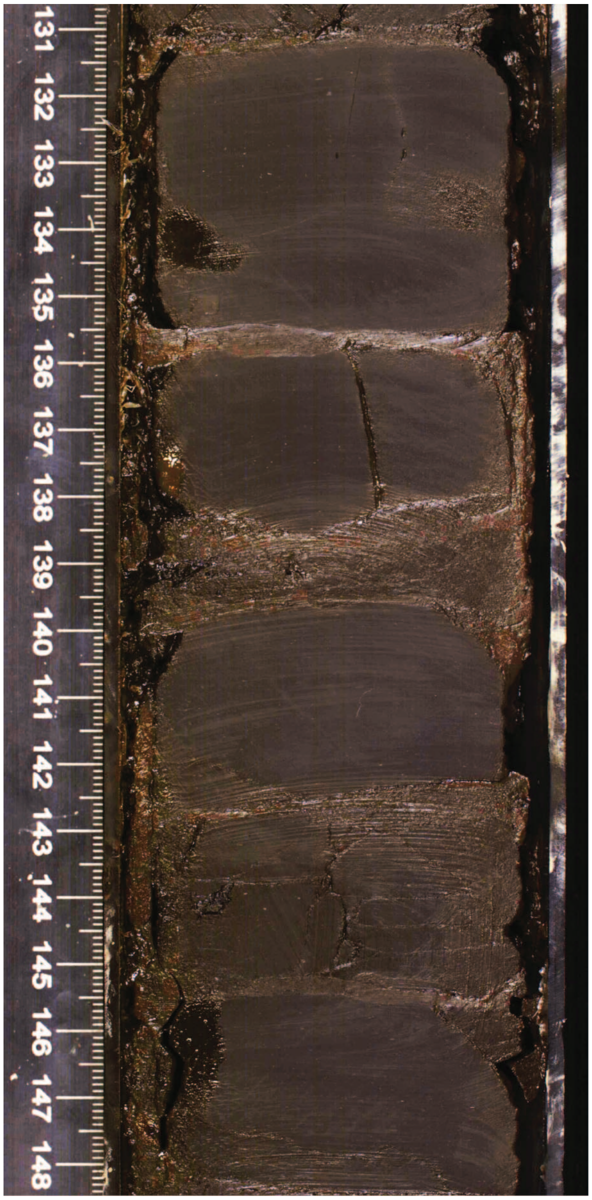

Figure F28. Photomicrograph showing presence of green glauconite minerals (Section 346-U1425D-64H-1, 107 cm).

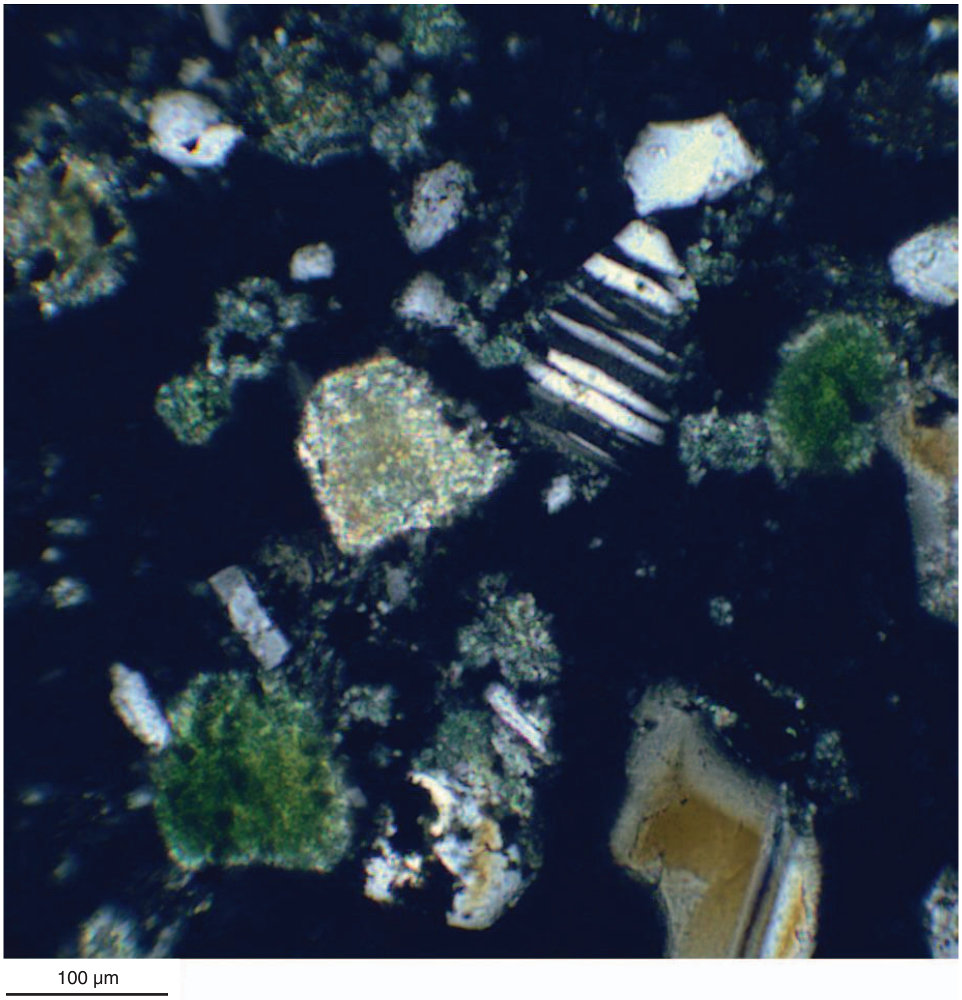

Figure F29. Integrated calcareous and siliceous microfossil biozonation, Site U1425.

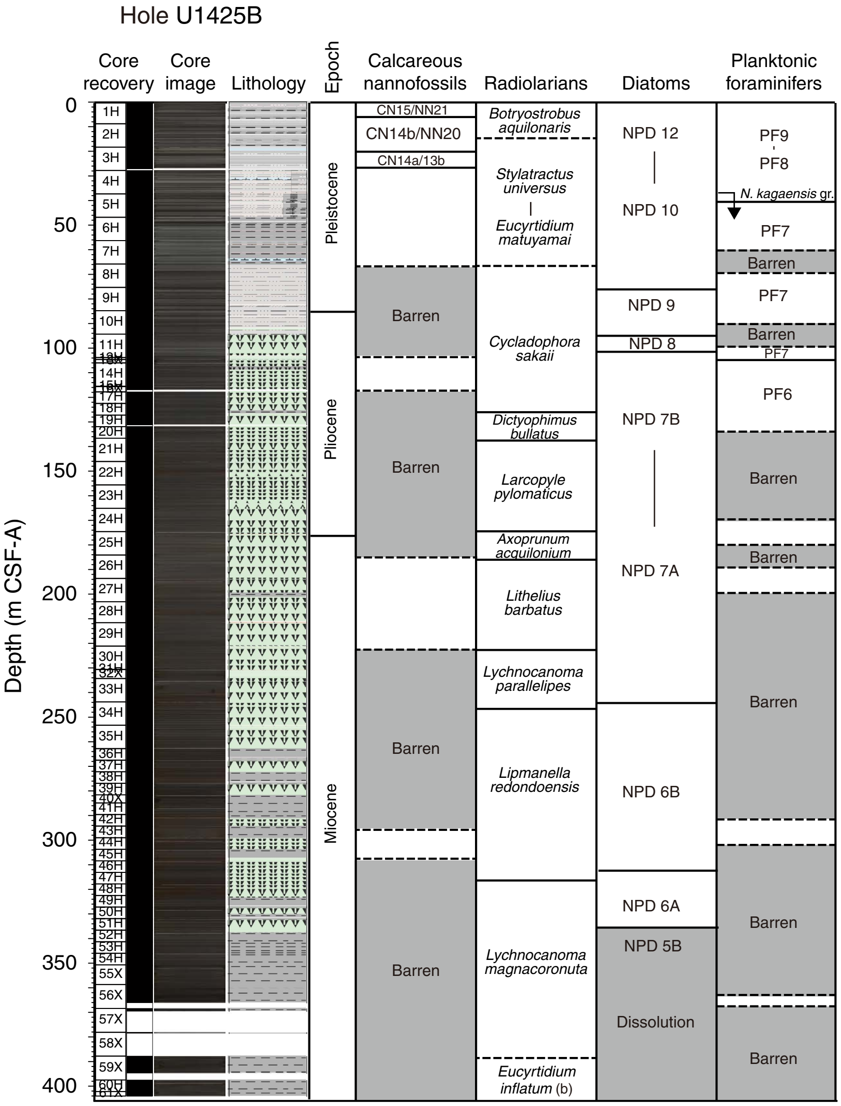

Figure F30. Age-depth profile, Site U1425. FO = first occurrence, LO = last occurrence, LCO = last common occurrence, RI = rapid increase, D/S = dextral/sinistral crossover.

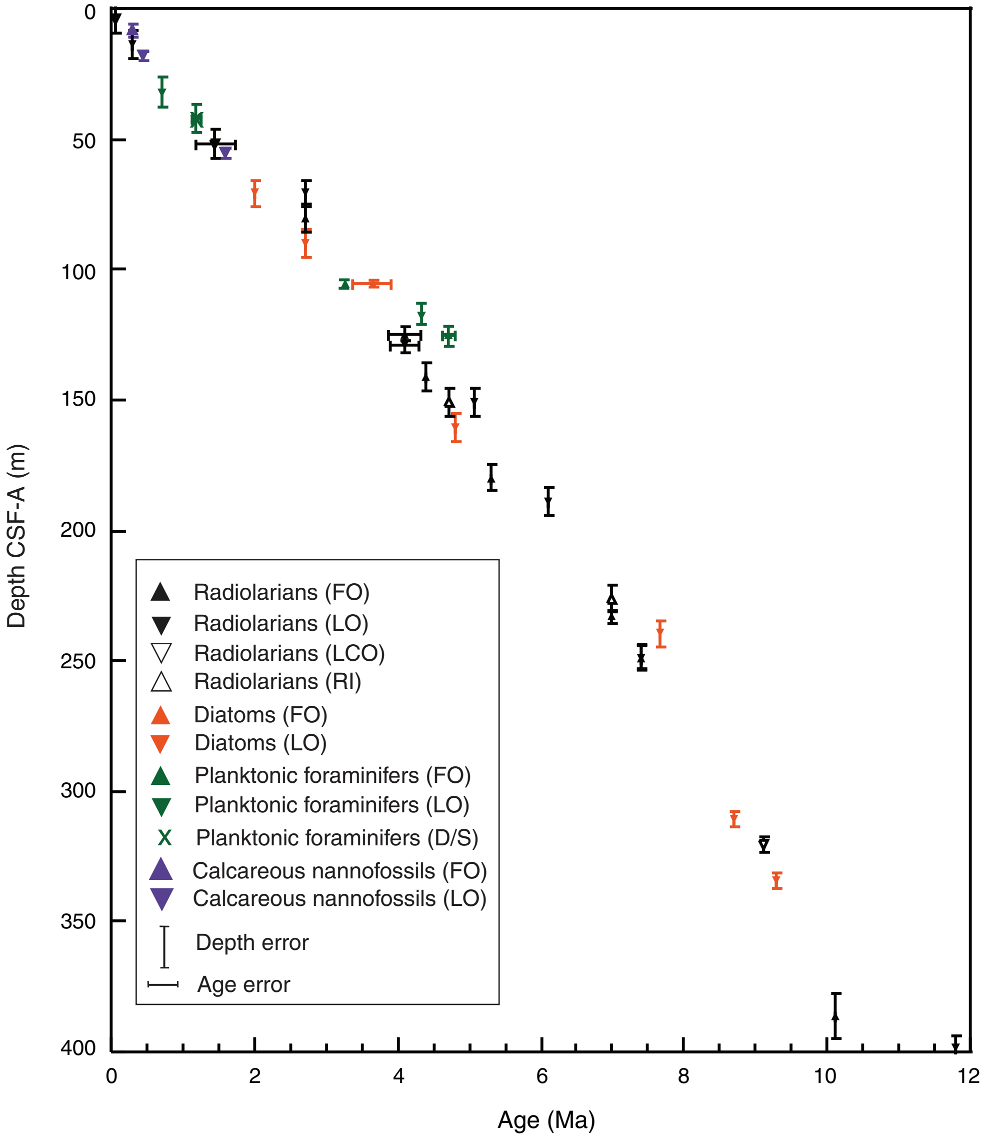

Figure F31. Distribution of siliceous and calcareous microfossils, Site U1425. B = barren, R = rare, F = few, C = common, A = abundant, D = dominant.

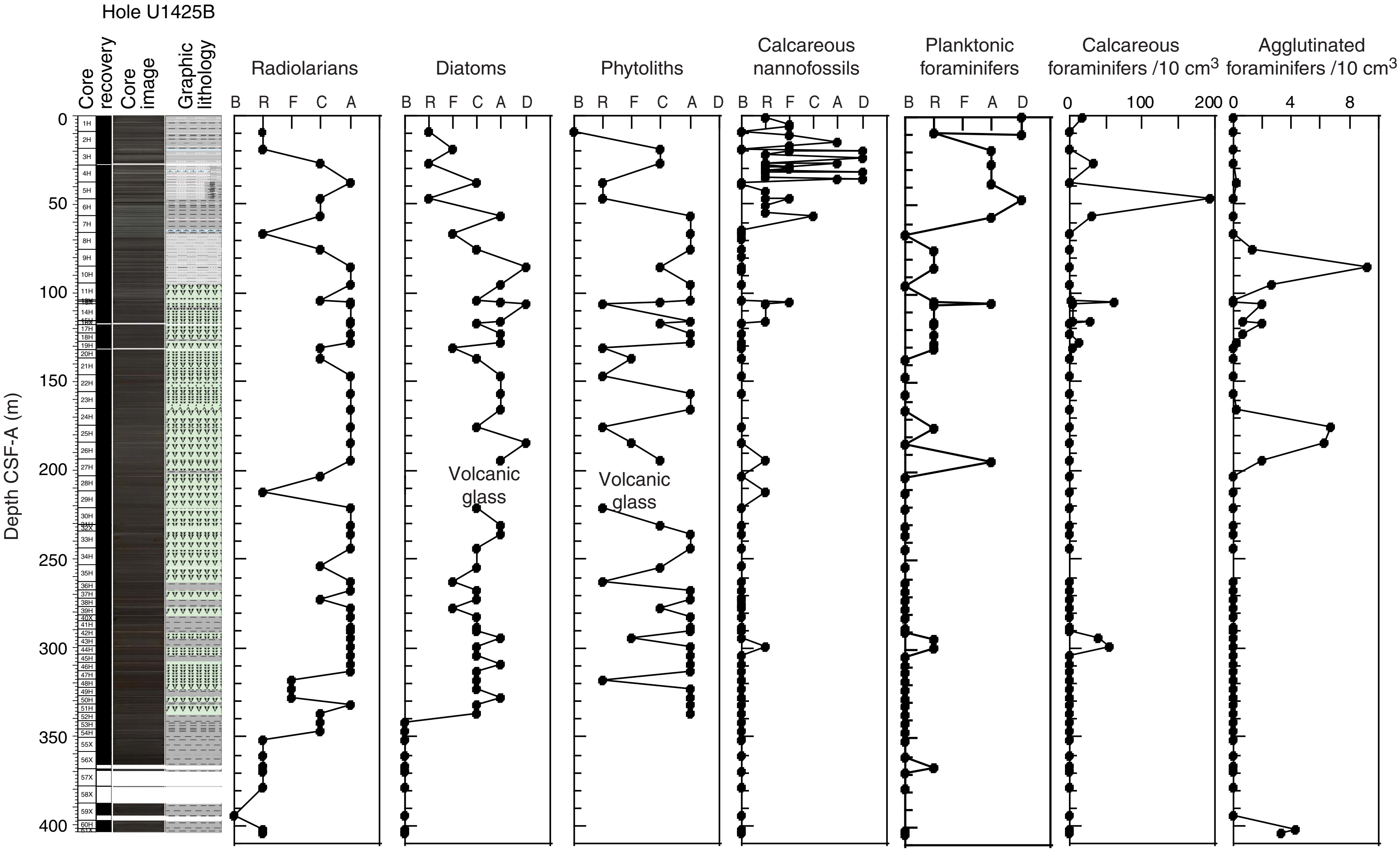

Figure F32. Calcareous nannofossils from Hole U1425B mudline sample and Sample 346-U1425B-1H-CC. Left: *Coccolithus pelagicus* coccosphere. Center and right: distal and proximal views of *C. pelagicus* coccoliths, respectively. Arrow indicates increased dissolution.

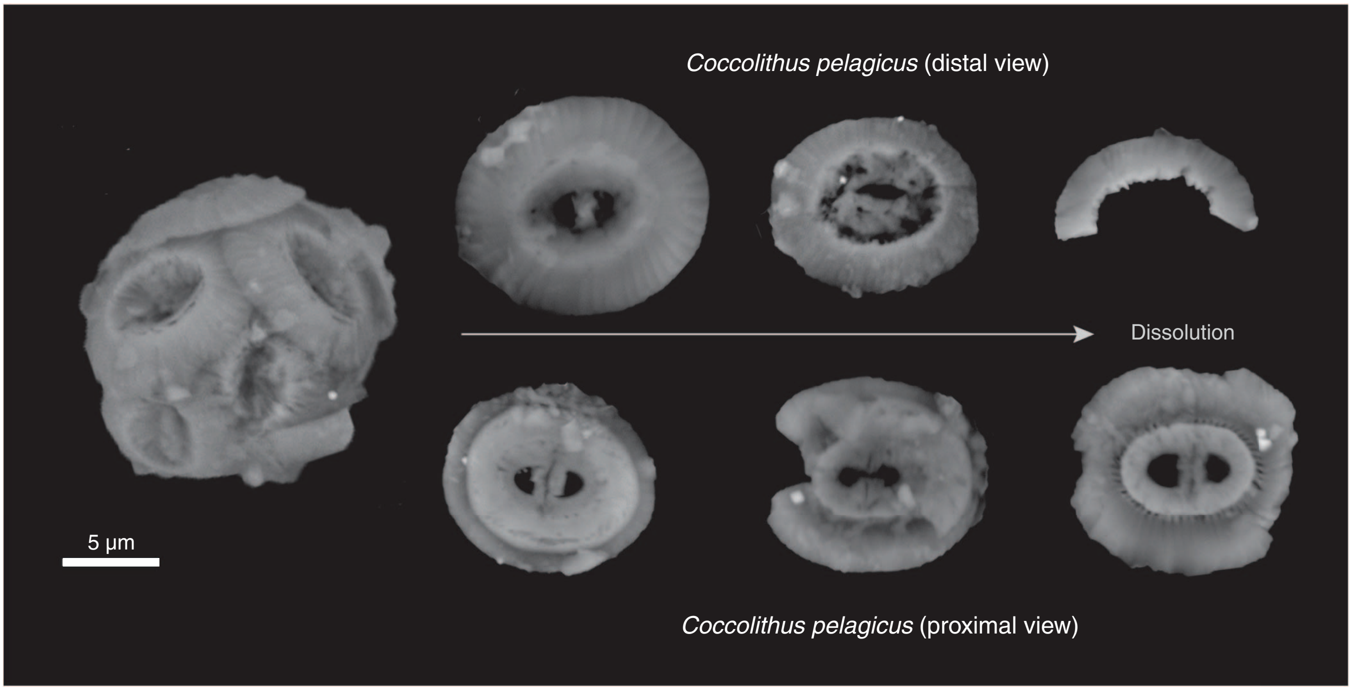

Figure F33. Distribution of foraminifers, Hole U1425B. The abundance of agglutinated and calcareous benthic foraminifers is expressed as a percentage of the total benthic foraminiferal assemblage. The percentage planktonic foraminifers relates to the total foraminiferal assemblage.

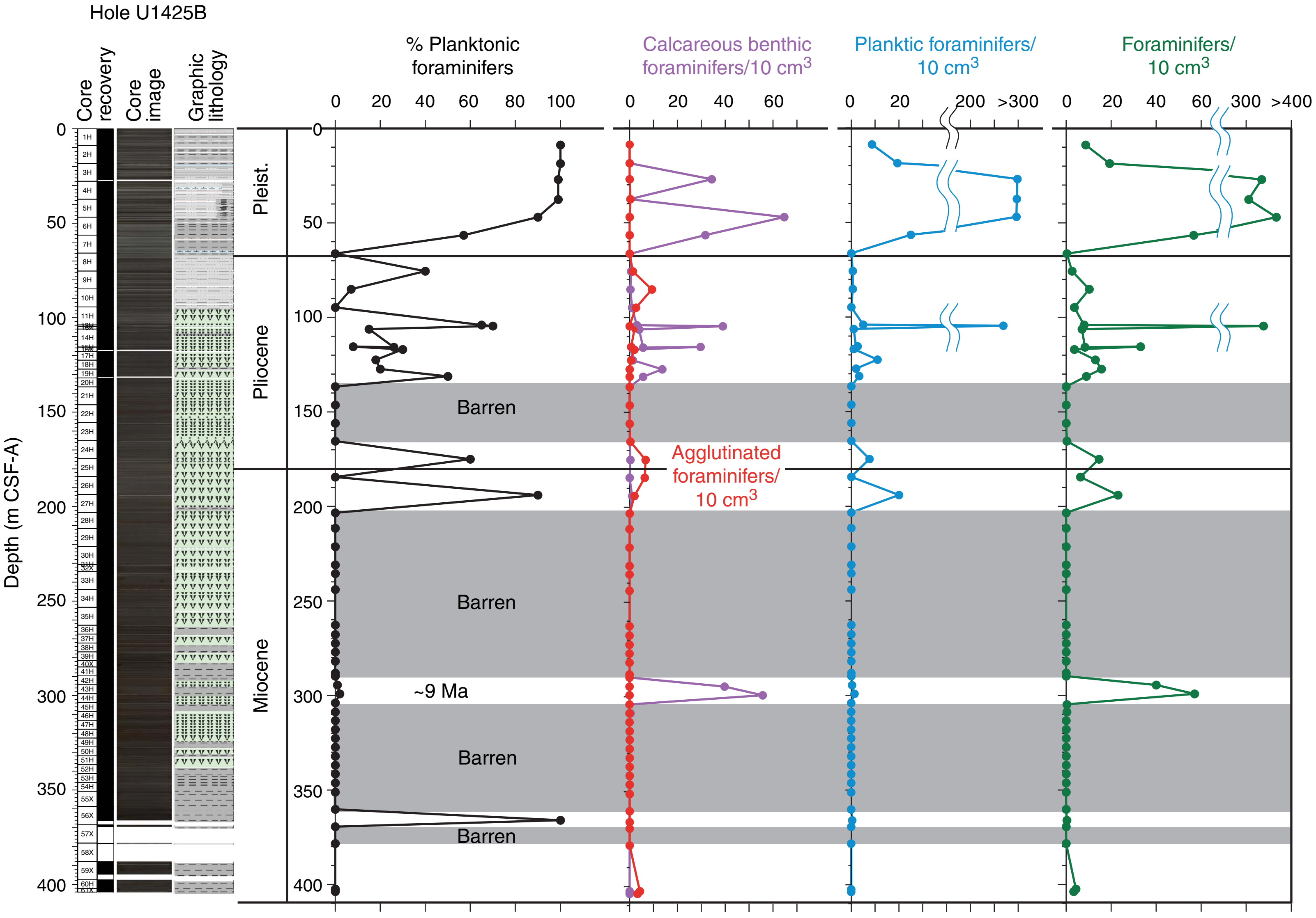

Figure F34. Planktonic foraminifers. Scale bars = 100 µm. **1, 1a.** *Neogloboquadrina* sp. with framboidal pyrite inside (Sample 346-U1425B-6H-CC); (1a) framboidal pyrite inside foraminiferal test. **2, 2a.** *Globigerinita glutinata* (Sample 346-U1425B-12H-1). **3–6, 5a.** *Neogloboquadrina dutertrei* sinistral cf. (Sample 346-U1425B-26H-CC). **7, 8.** *Globorotalia ikebei* (Sample 346-U1425B-17H-CC). **9, 9a.** *Orbulina* sp. showing partial dissolution and recrystallization (Sample 346-U1425B-17H-CC).

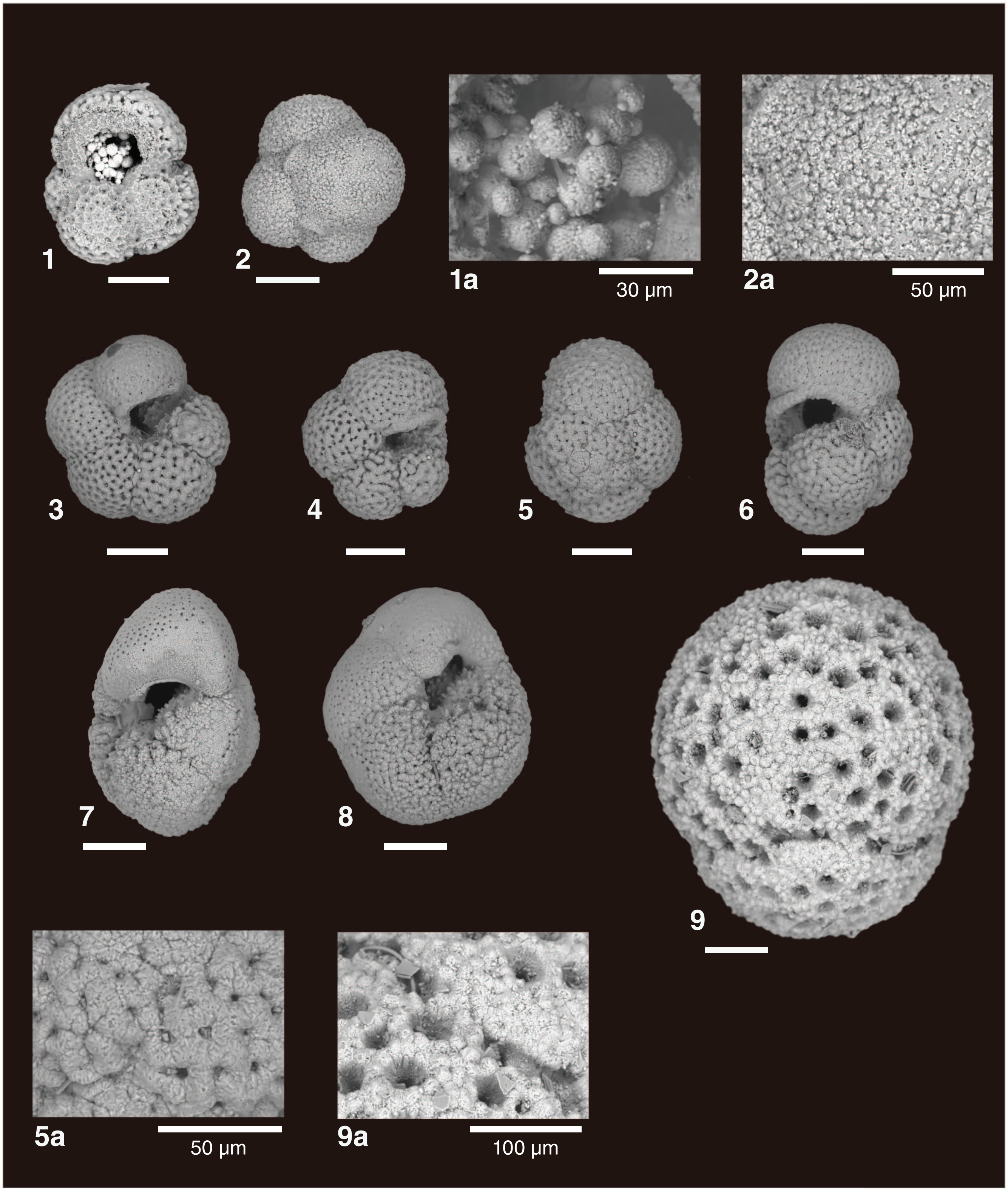

Figure F35. Benthic foraminifers. Scale bars = 50 µm. **1.** *Cassidulinoides tenuis* (Sample 346-U1425B-5H-CC). **2.** *Bolivina pacifica* (Sample 346-U1425B-5H-CC). **3.** *Bolivina* sp. (Sample 346-U1425B-5H-CC). **4, 5.** *Uvigerina yabei* (Sample 346-U1425B-15H-CC). **6.** *Cassidulina norcrossi* (Sample 346-U1425B-6H-CC). **7.** *Cassidulina* sp. (Sample 346-U1425B-6H-CC). **8.** *Sphaeroidina bulloides* (Sample 346-U1425B-12H-1, 76–81 cm). **9.** *Planulina wuellerstorfi* (Sample 346-U1423A-16H-CC). **10.** *Quinqueloculina akneriana* (Sample 346-U1425B-18H-CC). **11.** *Hoeglundina elegans* (Sample 346-U1425B-12H-1). **12, 13.** *Valvulineria sadonica* (Sample 346-U1425B-43H-CC).

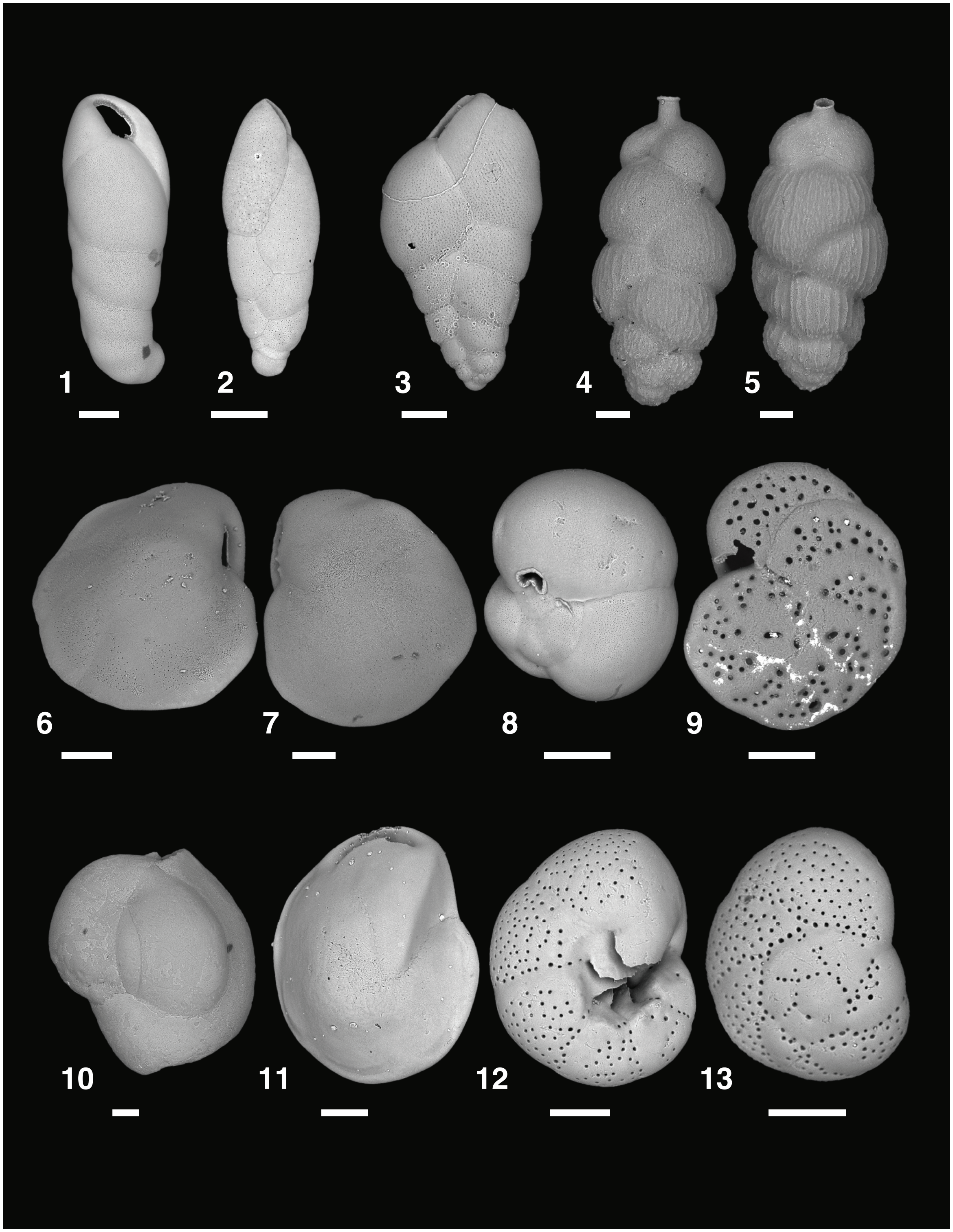

Figure F36. Calcareous and organically cemented, agglutinated foraminifers from the Hole U1425B mudline sample. Scale bars = 50 µm. **1, 2.** *Cassidulina teretis*. **3, 4.** *Haplophragmoides sphaeriloculum* (stained specimen). **5, 6, 13.** *Paratrochammina challengeri*; (13) with detail of aperture. **7, 8.** *Bolivina pacifica*. **9, 12.** *Miliammina echigoensis* (stained specimen). **10, 11.** *Reophax scorpiusus* with detail of wall structure. **14.** Overview of mudline benthic foraminiferal assemblage in slide. Scale = each side of the square is 3.5 mm.

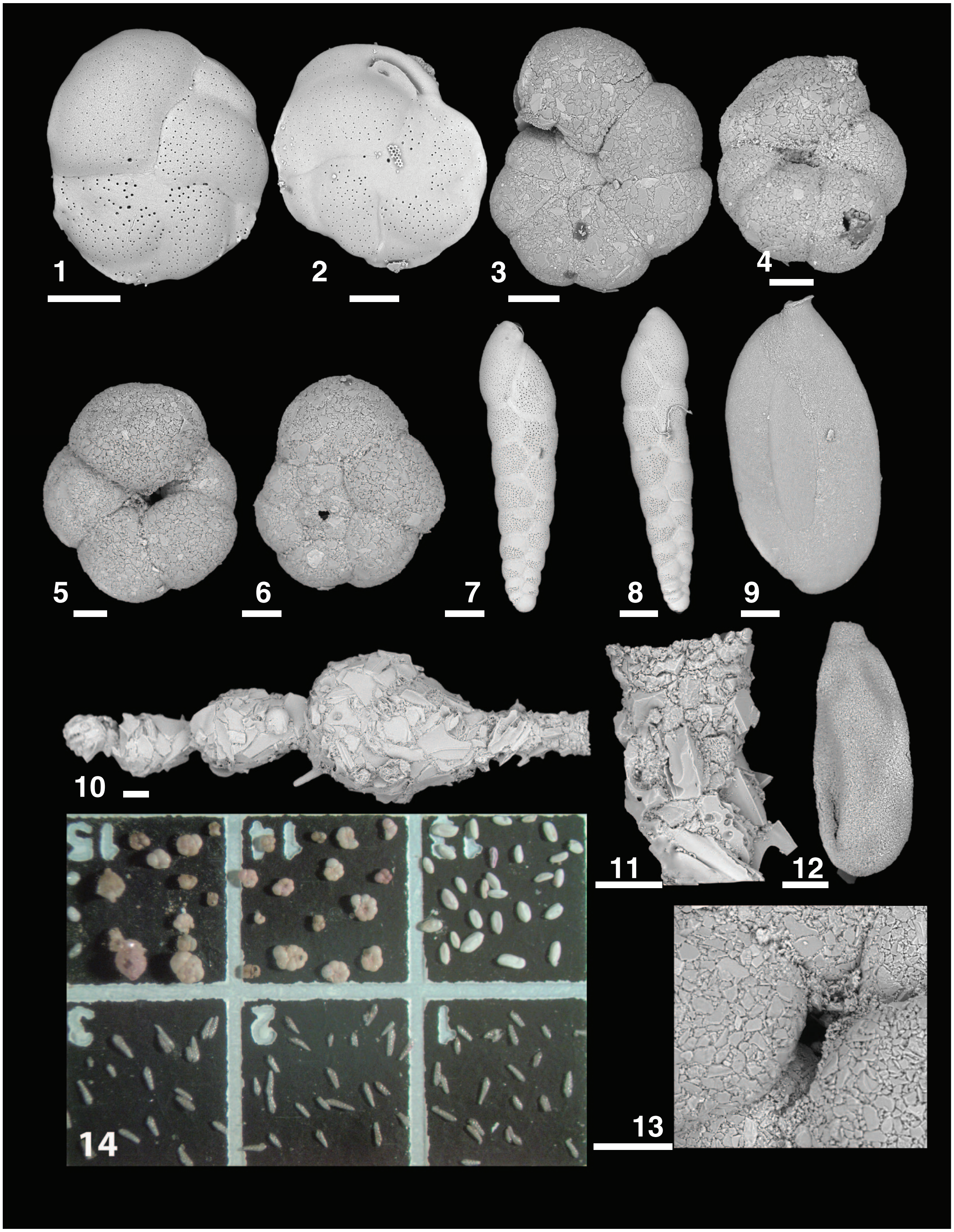

Figure F37. Original plan for interstitial water whole-round and Rhizon (Rh) sampling for Hole U1425A. The actual samples collected deviates from this plan and can be viewed in Table **T12.** IW-sq = squeezed interstitial water, ICP = inductively coupled plasma–atomic emission spectroscopy.

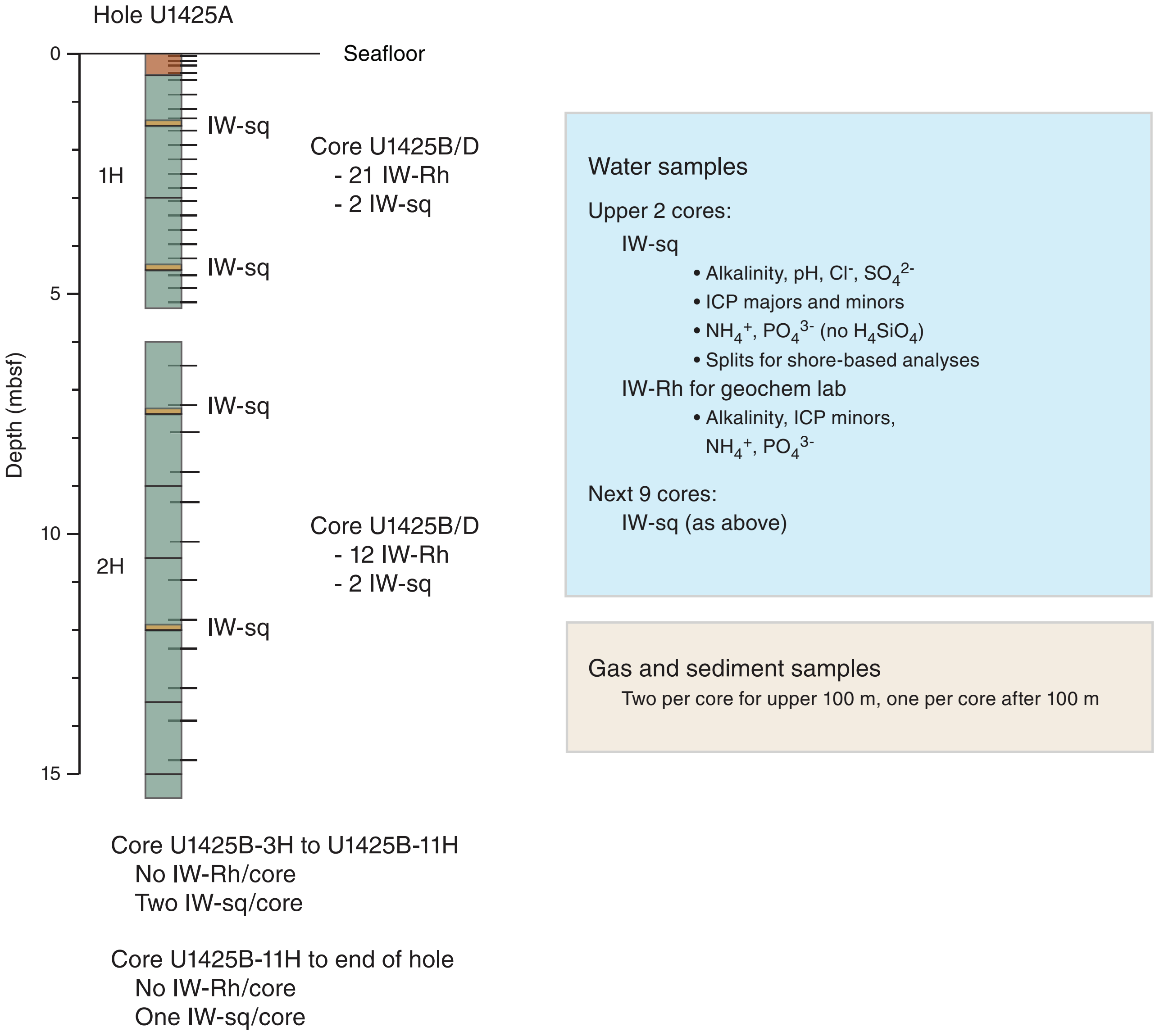

Figure F38. Solid-phase contents of discrete sediment samples, Site U1425. Unit II is shaded gray to emphasize the difference between units. TC = total carbon, TOC = total organic carbon, TN = total nitrogen.

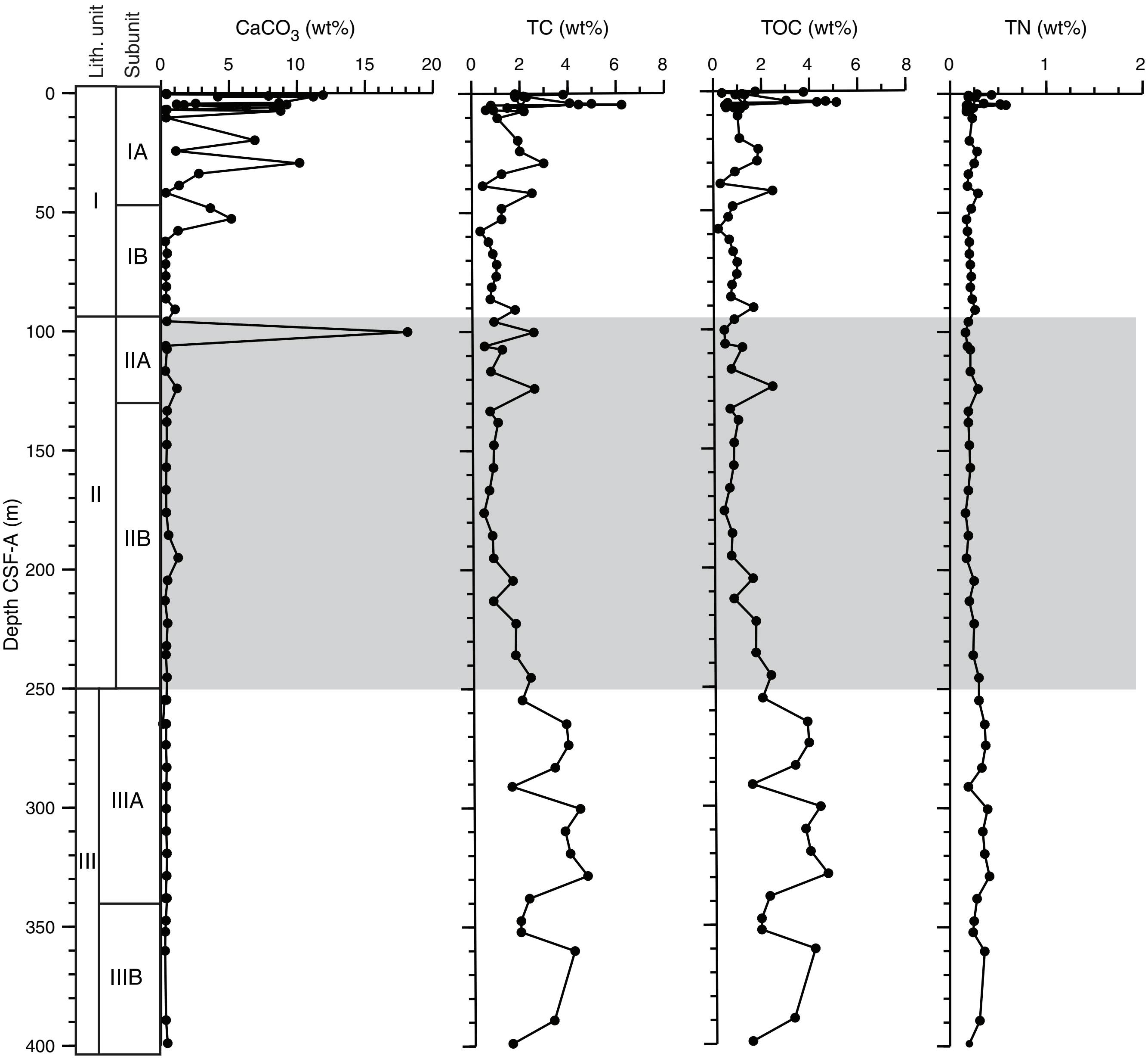

Figure F39. Dissolved manganese and iron profiles from squeezed samples, Site U1425.

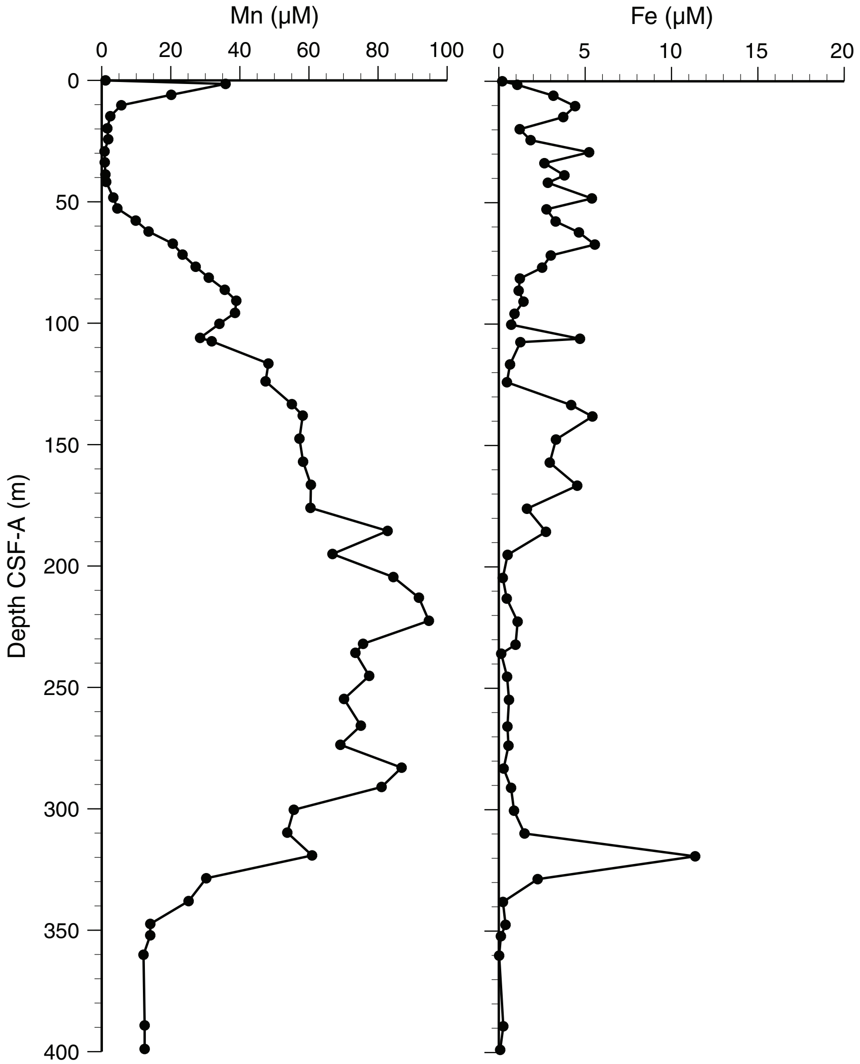

Figure F40. Dissolved manganese and iron profiles over the uppermost 9 m below the seafloor, Site U1425. IW-sq = squeezed interstitial water.

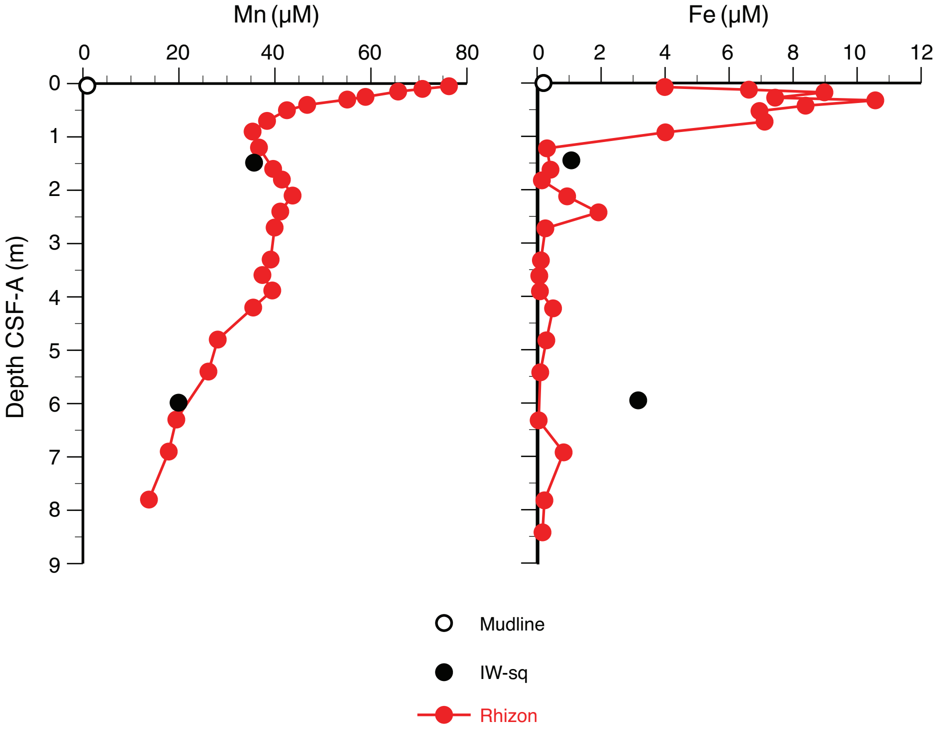

Figure F41. Dissolved sulfate concentrations, Site U1425. **A.** Full depth. Also shown are headspace CH_4 concentrations (on a linear scale). **B.** The upper 50 m below the seafloor, including squeezed interstitial water (IW-sq) and Rhizon samples.

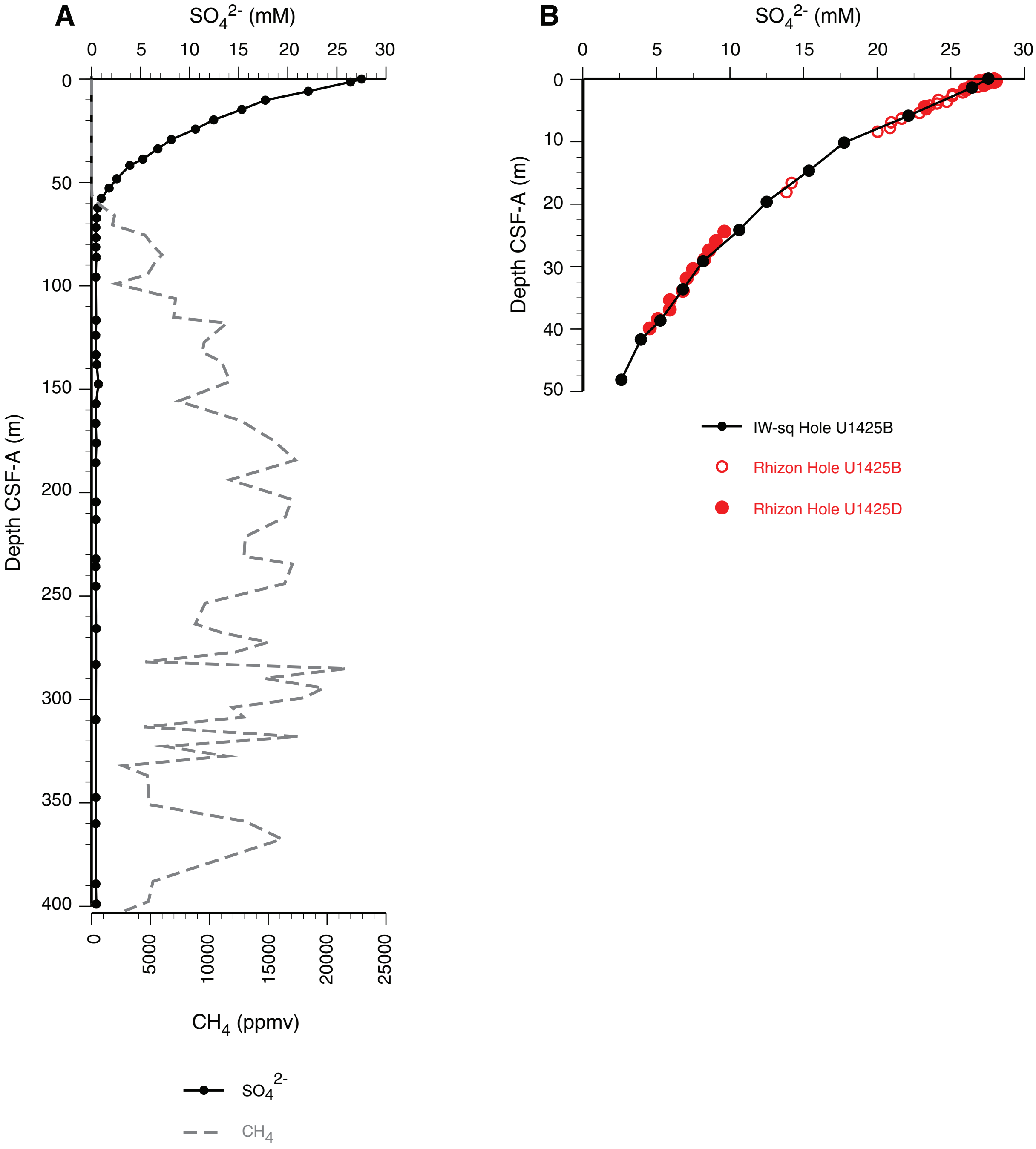

Figure F42. Dissolved barium profiles with depth, Site U1425. **A.** Full depth. **B.** Uppermost 20 m below the seafloor. IW-sq = squeezed interstitial water. High Ba concentrations are much higher than the calibration standards and are unconstrained. They are reported here only as preliminary results.

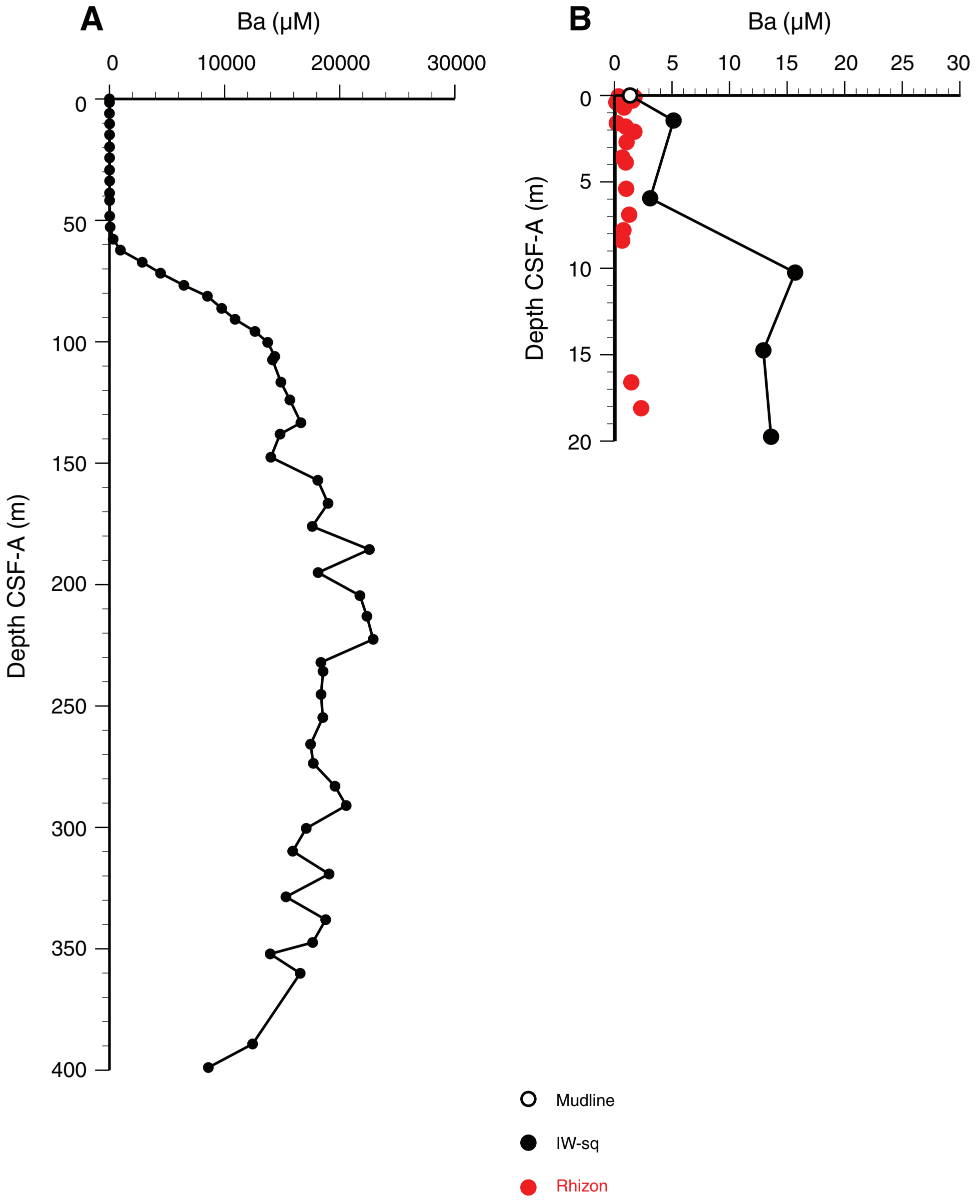

Figure F43. Headspace CH_4 concentrations with depth at Site U1425 with Sites U1422–U1424 for comparison. Note that values are not meaningful at depths where CH_4 surpasses saturation at 1 atm pressure (~10,000 ppm at 120 m CSF-A).

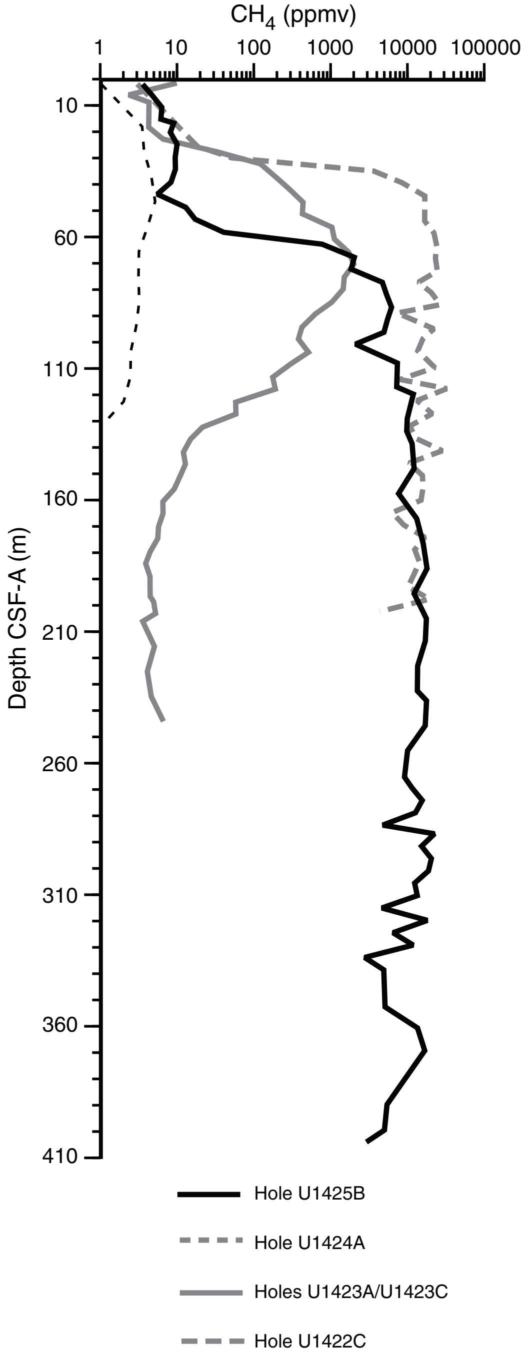

Figure F44. Dissolved alkalinity, ammonium, and phosphate profiles over the full depth, Site U1425. Constructed using IW-sq samples.

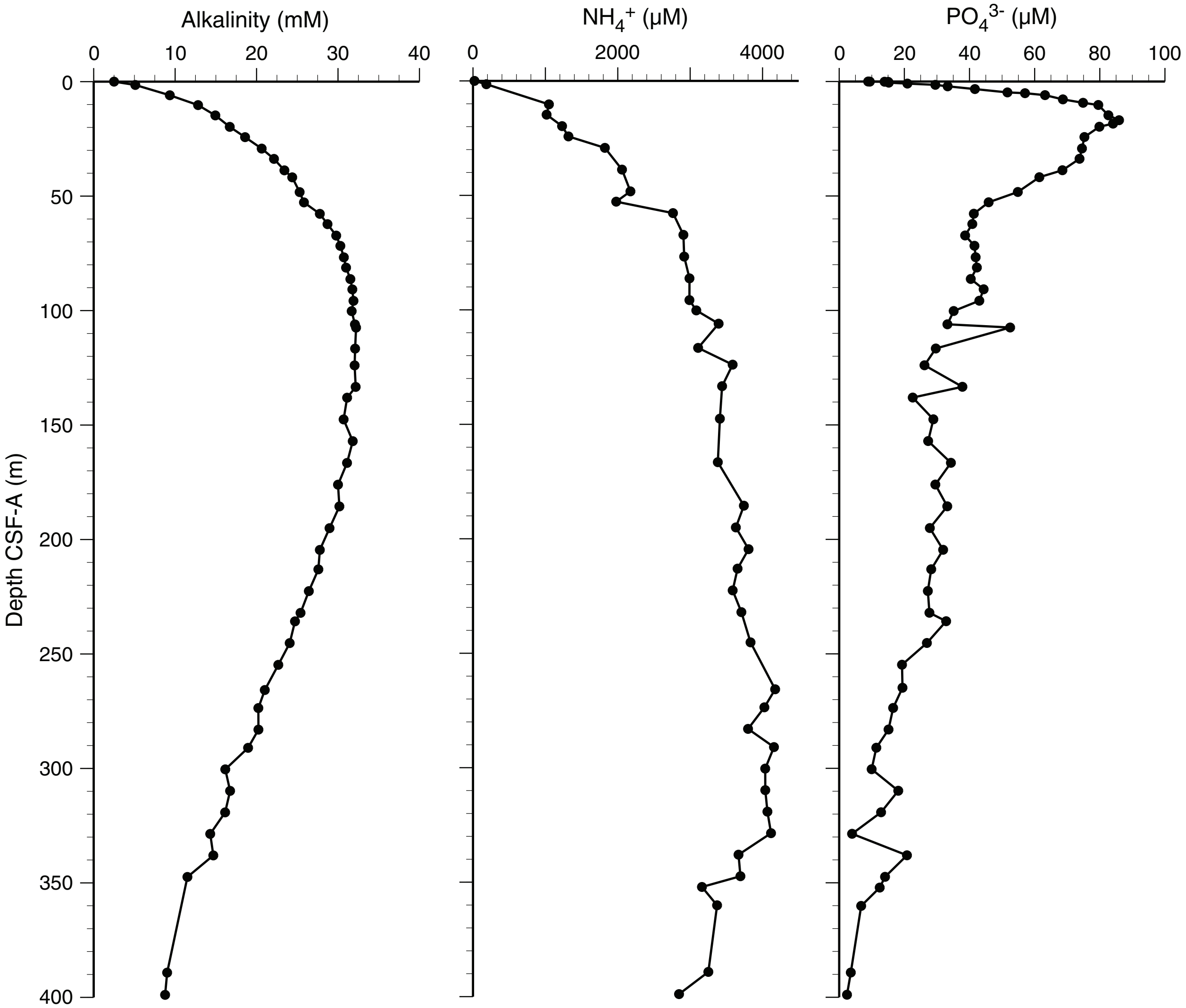

Figure F45. Dissolved alkalinity, ammonium, and phosphate profiles over shallow depth intervals, Site U1425. Constructed using squeezed interstitial water (IW-sq) and Rhizon samples.

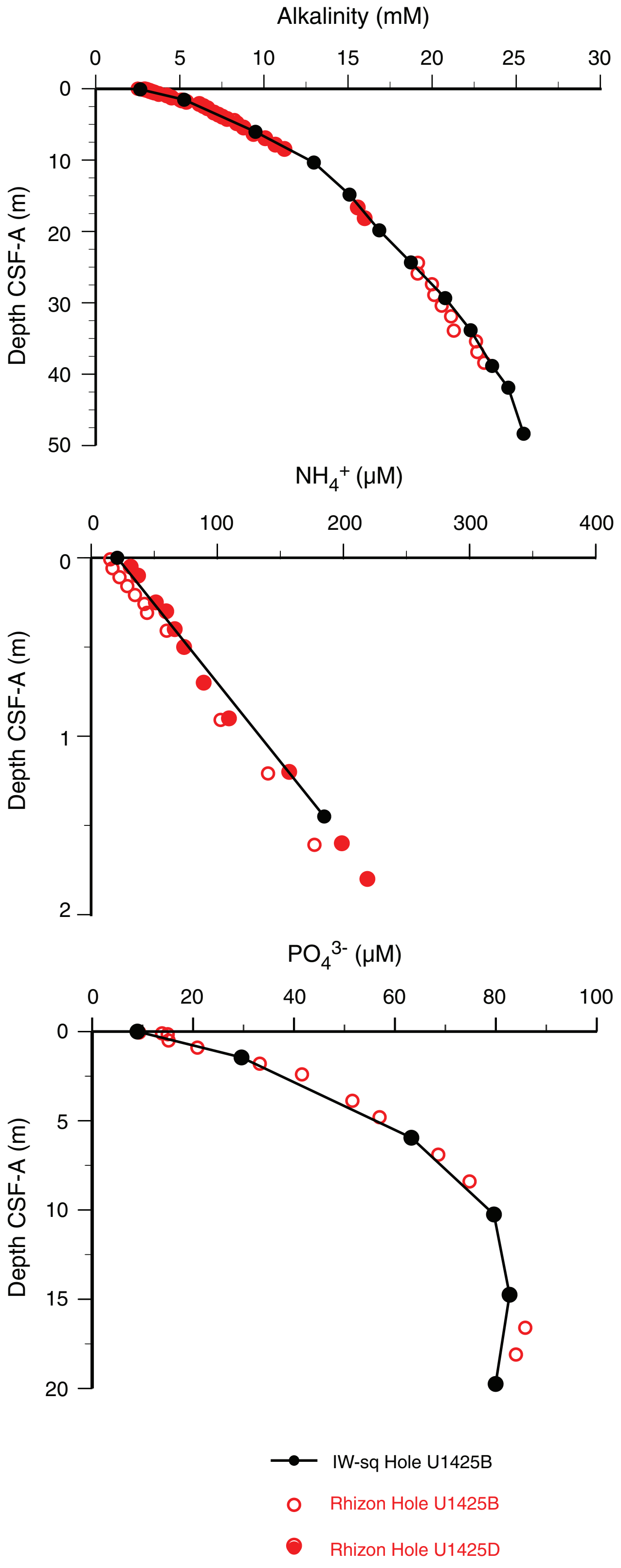

Figure F46. Concentrations of Br⁻, Site U1425.

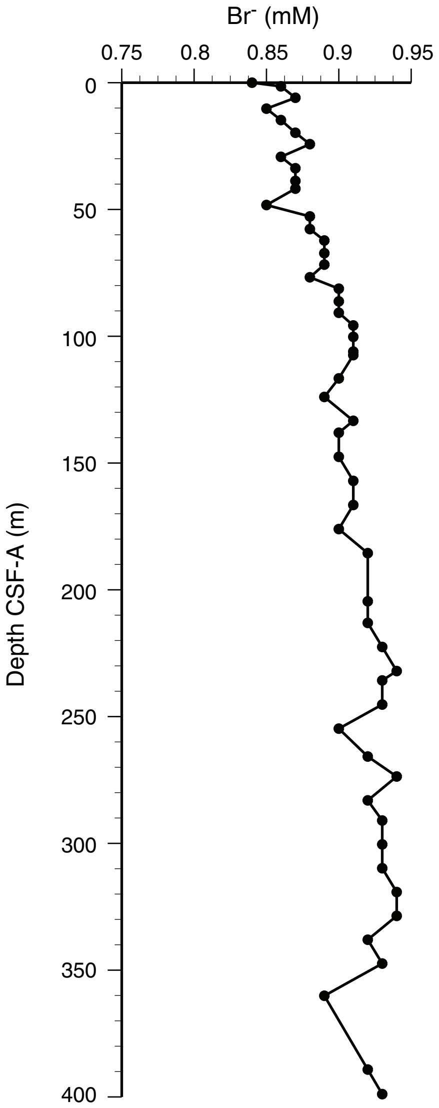

Figure F47. Absorbances of interstitial water samples at 227 and 325 nm wavelength according to depth, Site U1425. IW-sq = squeezed interstitial water.

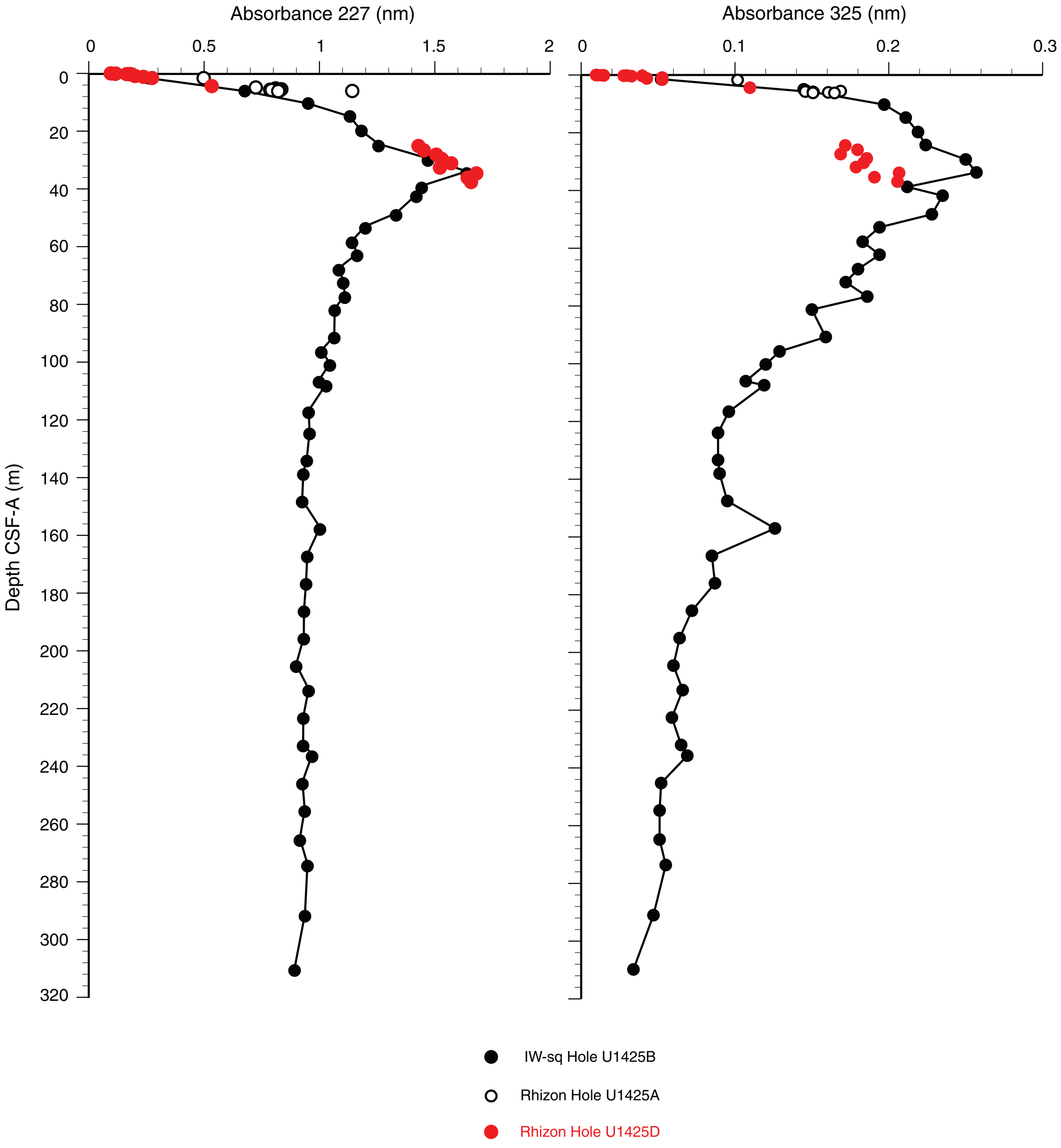

Figure F48. Dissolved calcium, magnesium, and strontium profiles across the full depth, Site U1425. Note the low in Ca concentration and the inflection in Mg concentration at ~53 m CSF-A.

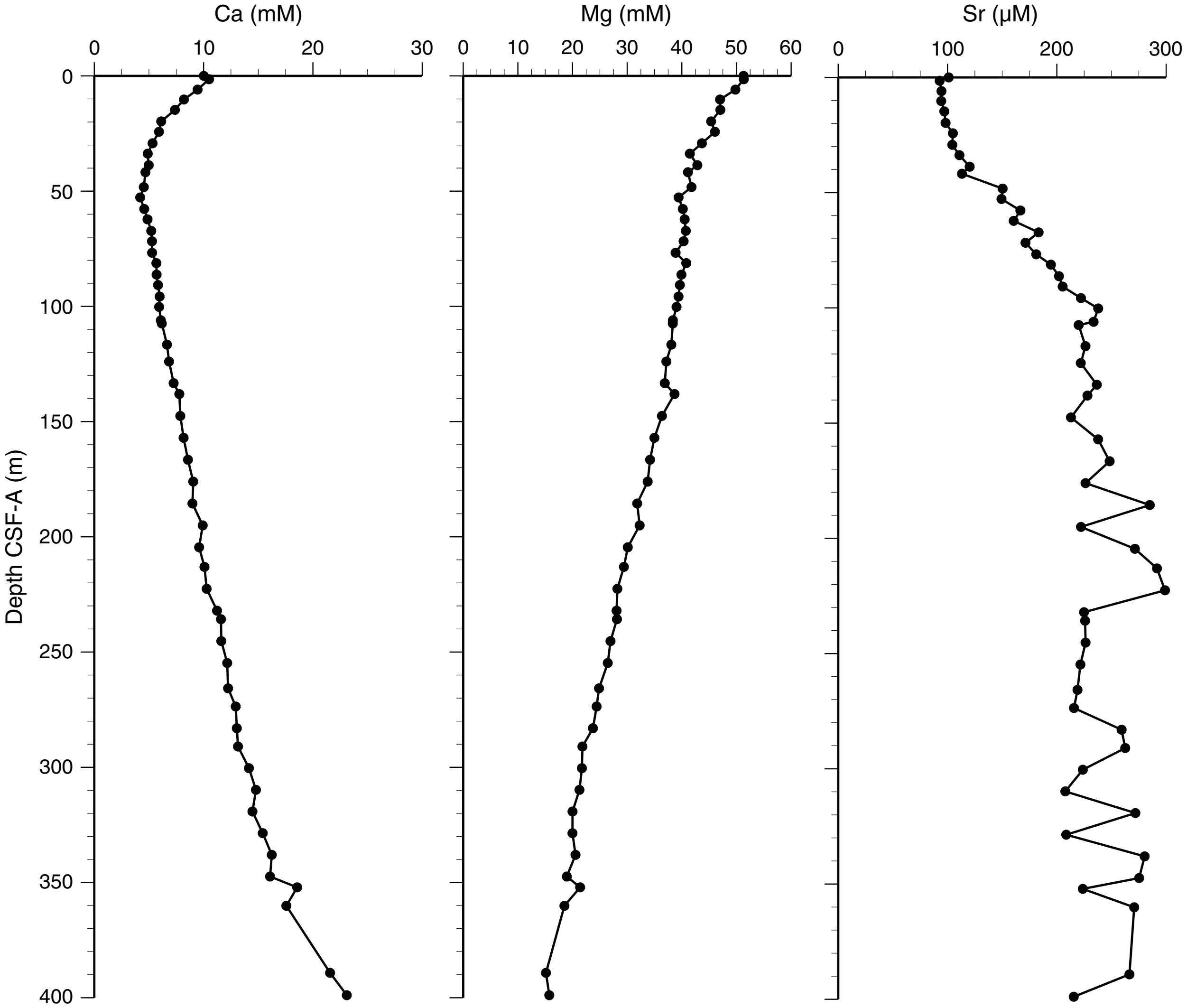

Figure F49. Dissolved calcium, magnesium, and strontium profiles across the upper 20 m, Site U1425. IW-sq = squeezed interstitial water.

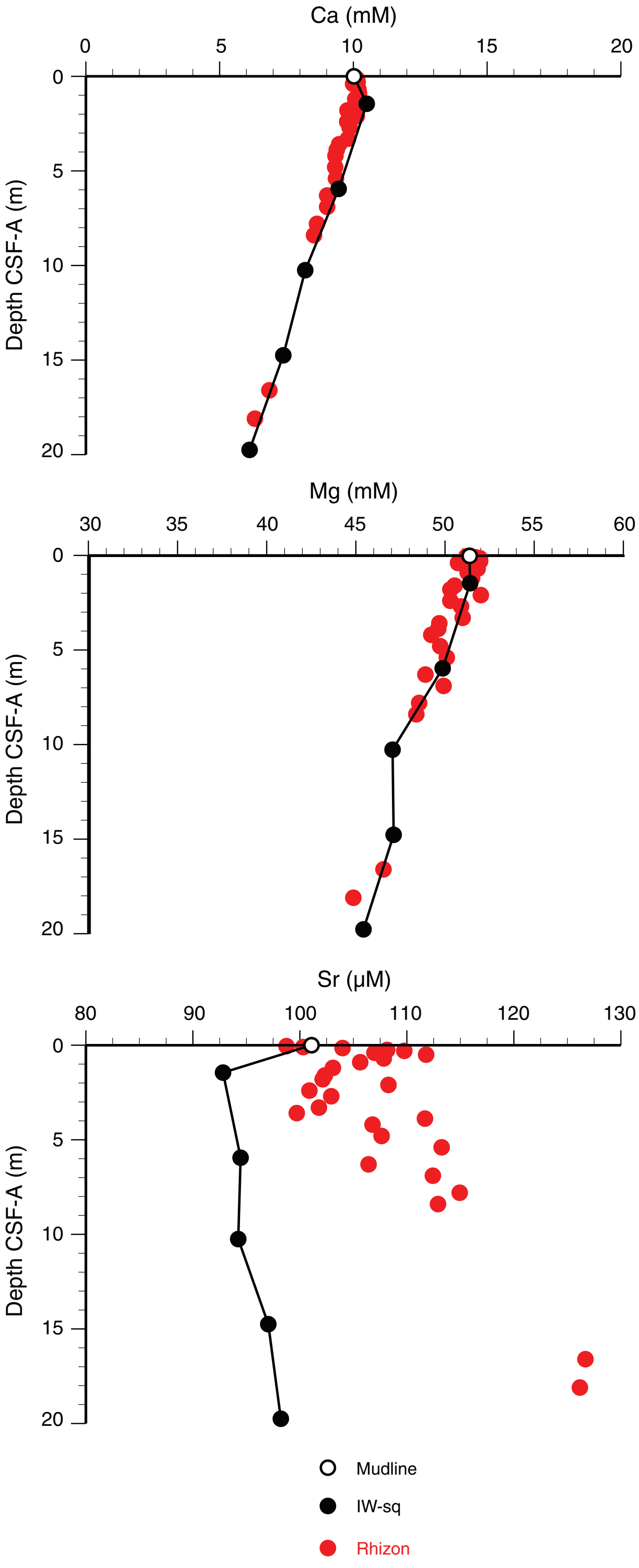

Figure F50. Dissolved chloride, sodium (left), and potassium (right) profiles across the full depth, Site U1425.

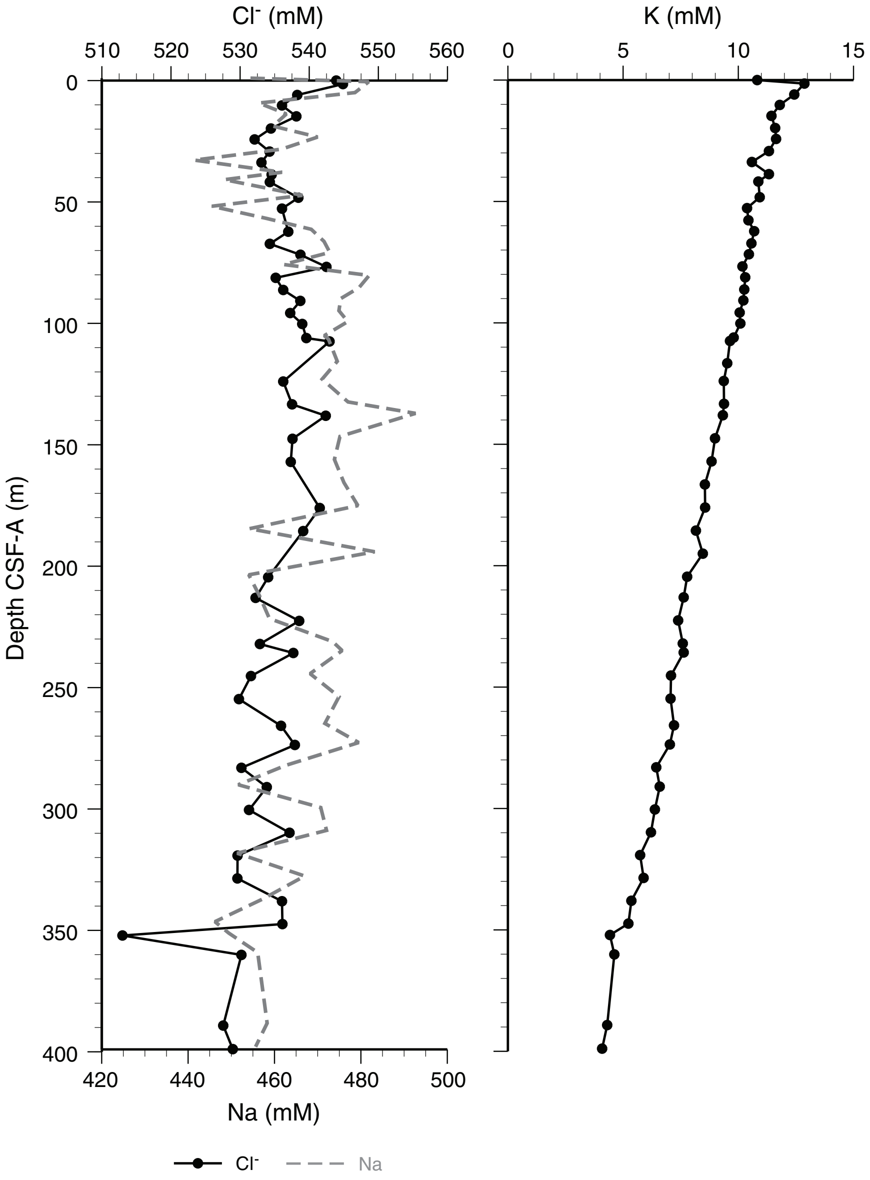

Figure F51. Dissolved sodium and potassium profiles across the upper 20 m, Site U1425. IW-sq = squeezed interstitial water.

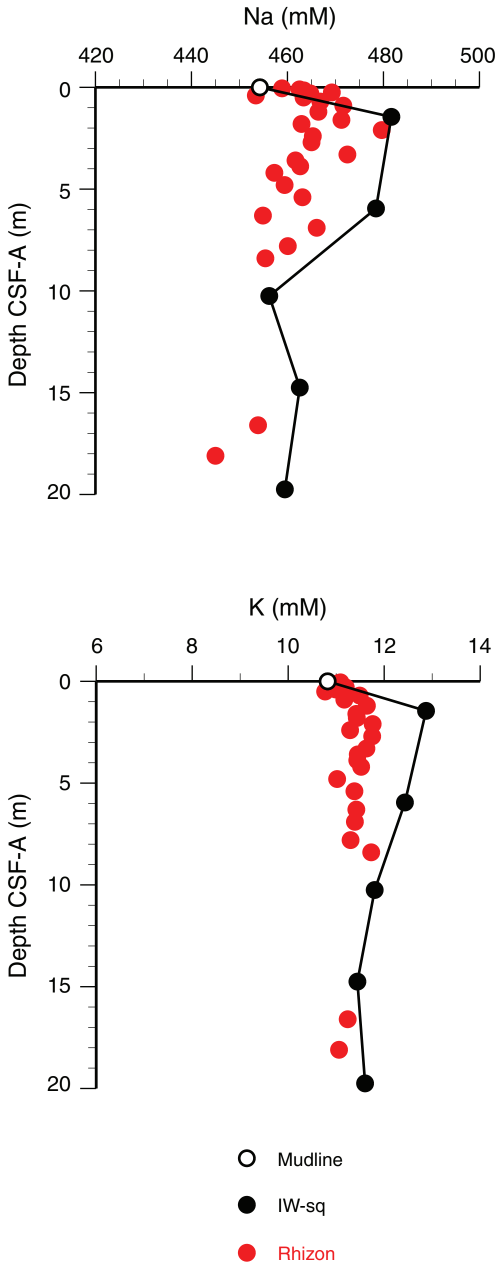

Figure F52. Dissolved boron, lithium, and silica profiles across the full depth, Site U1425.

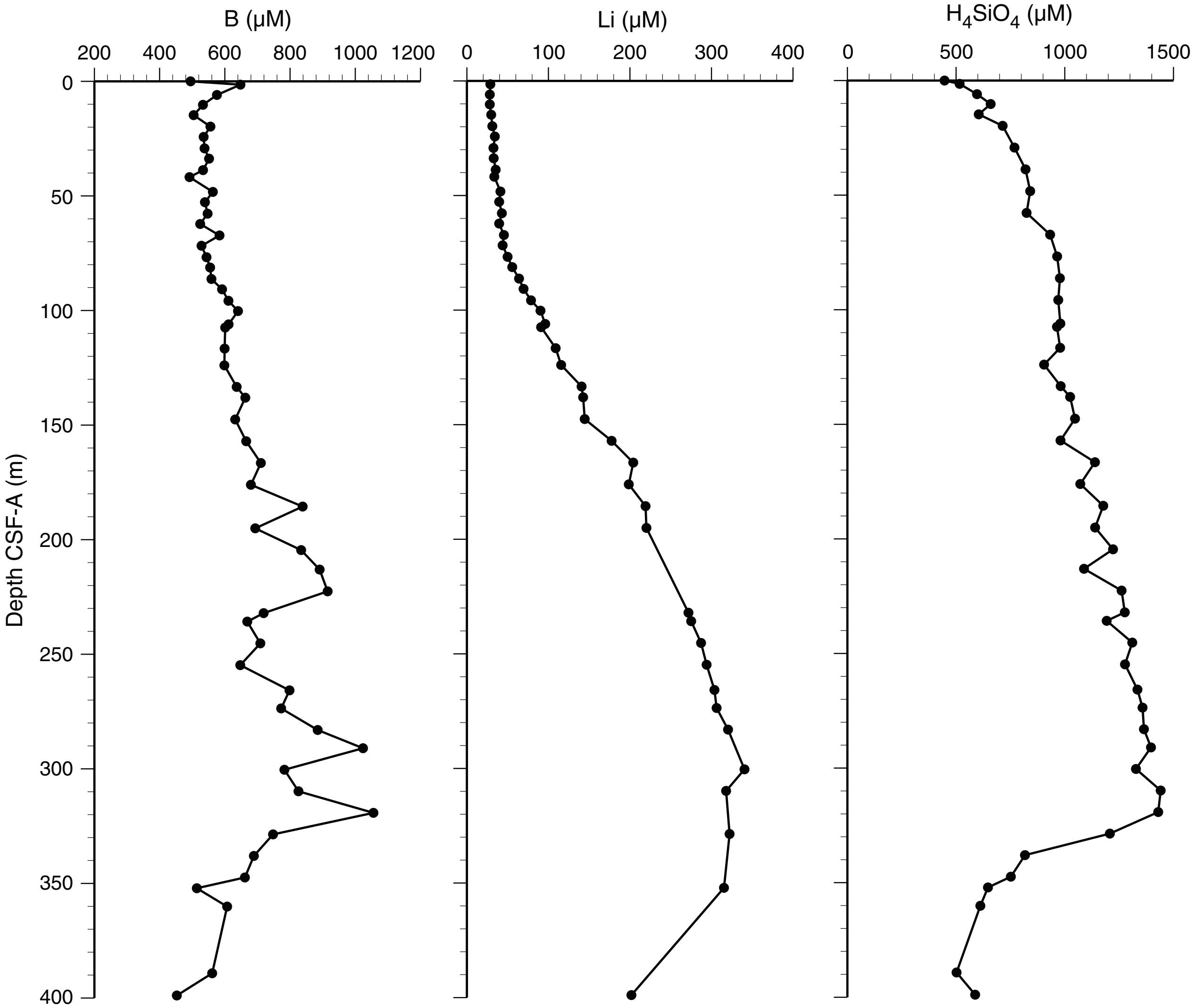

Figure F53. Paleomagnetism after 20 mT AF demagnetization, Site U1425. Chron column: black = normal polarity, white = reversed polarity, gray = zones or polarity boundaries without clear magnetostratigraphic interpretation. Inclination column: thin black dashed lines = expected geocentric axial dipole inclinations at the site latitude during reversed (left) and normal (right) polarities, triangles along the left side mark depths where discrete paleomagnetic cube samples were collected (orange = discrete samples measured during the expedition). Declination column: gray dots = measured declination values, green dots = declination values corrected using core orientation data collected by the FlexIT tool. Susceptibility column: SHMSL and WRMSL measured values are shown in magenta and gray dots, respectively. **A.** Hole U1425B shallower than 200 m CSF-A. (Continued on next three pages.)

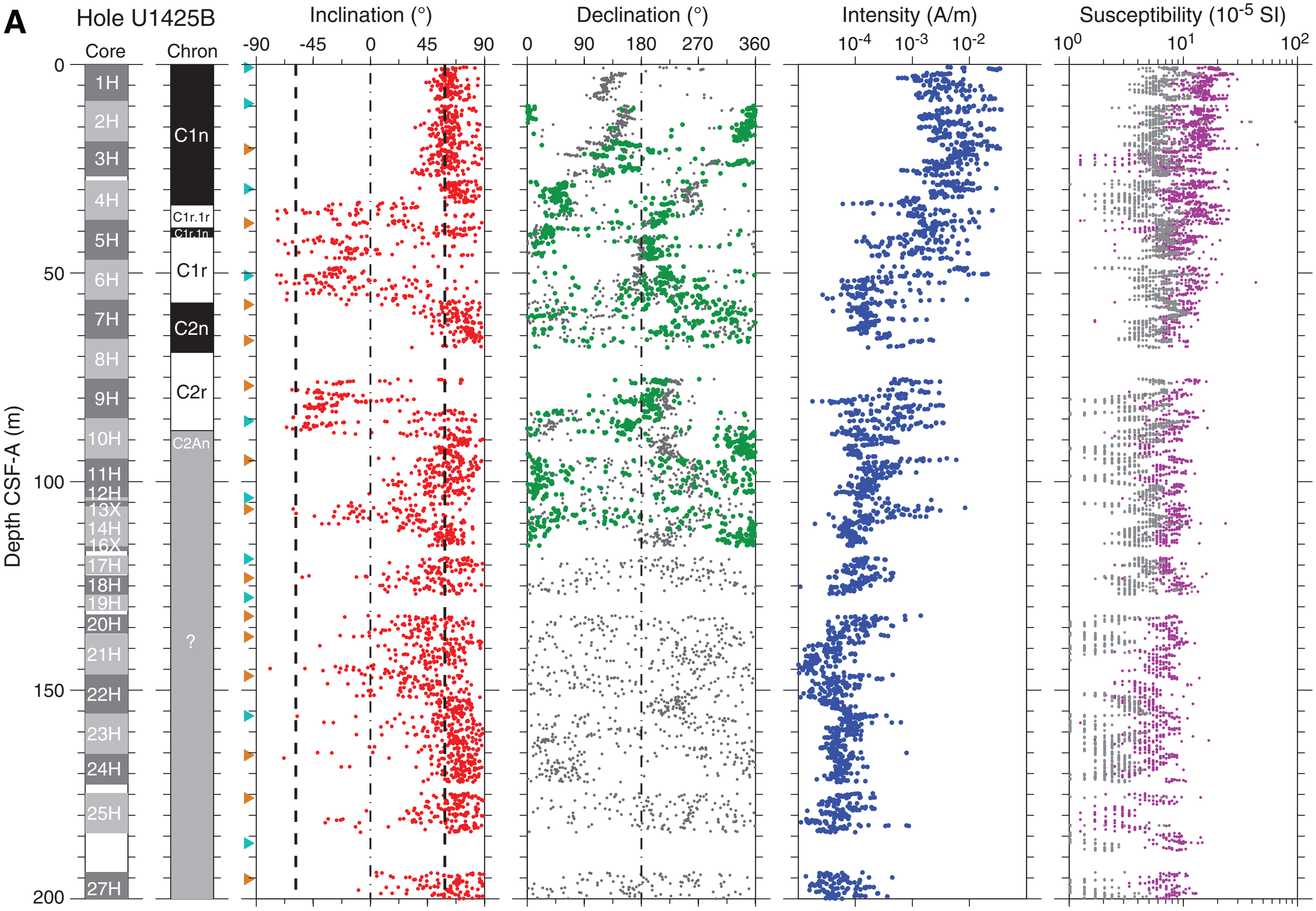

Figure F53 (continued). B. Hole U1425B deeper than 200 m CSF-A. (Continued on next page.)

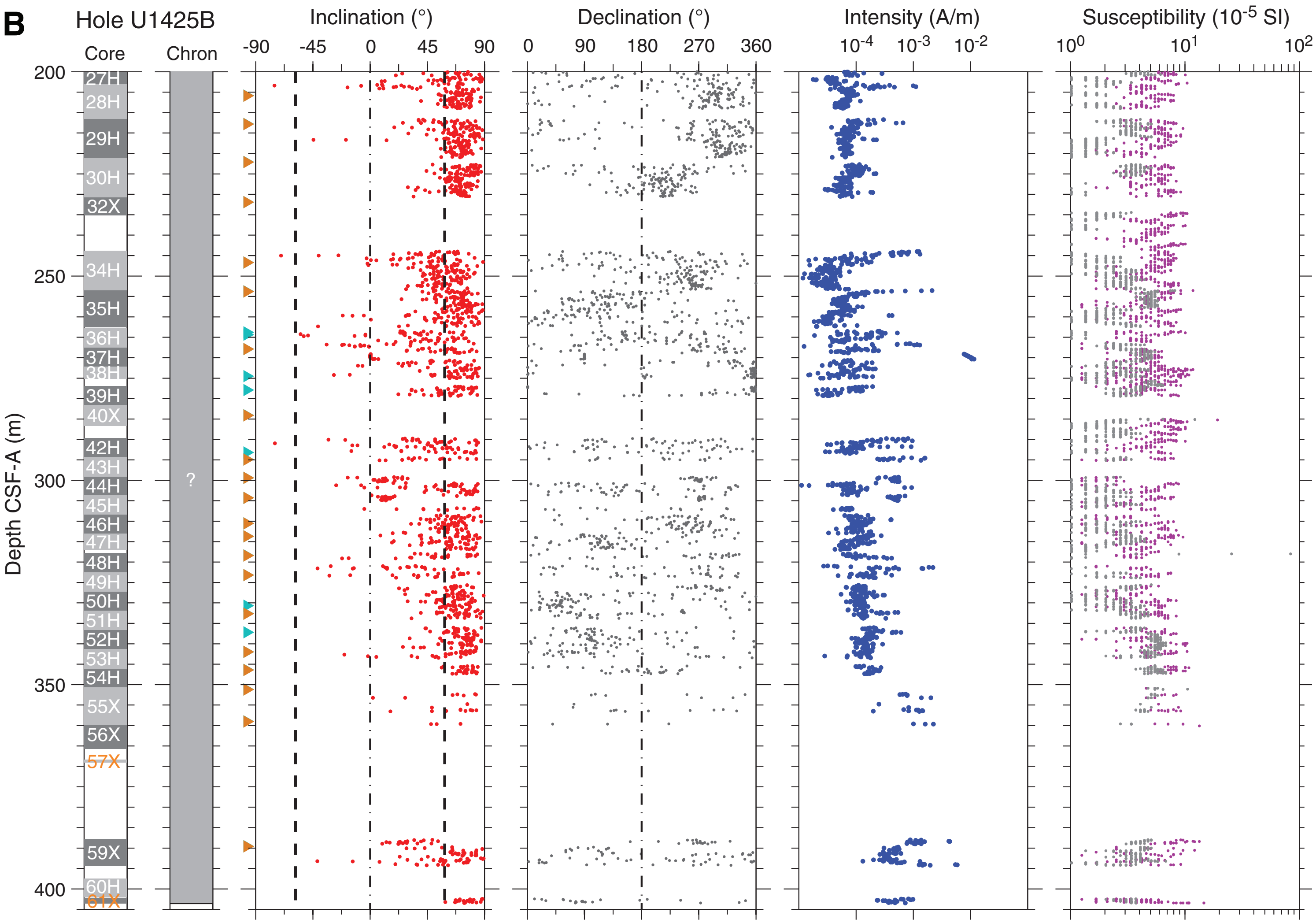

Figure F53 (continued). **C.** Hole U1425D shallower than 200 m CSF-A. (Continued on next page.)

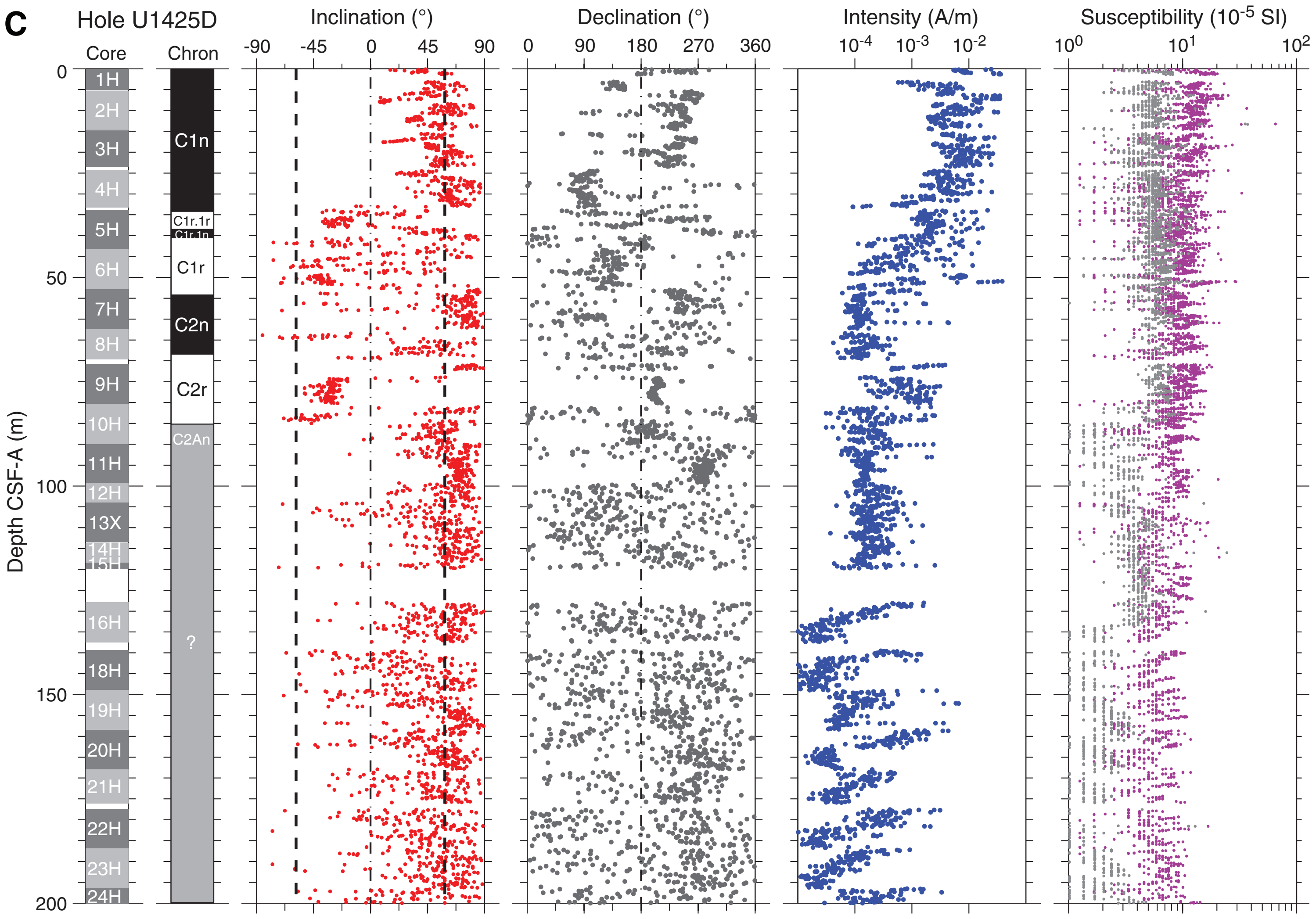

Figure F53 (continued). D. Hole U1425D deeper than 200 m CSF-A.

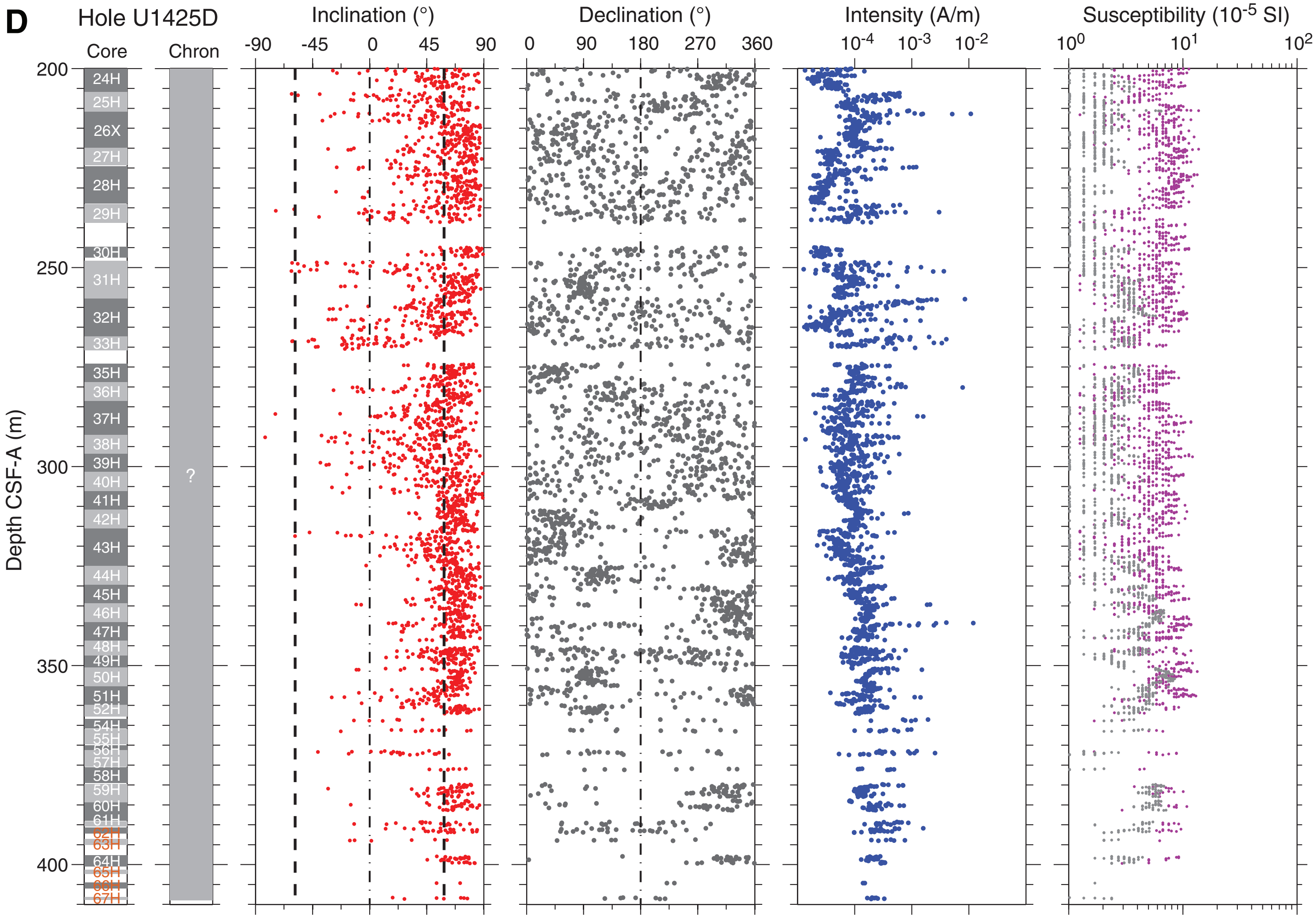

Figure F54. A–H. AF demagnetization results for eight discrete samples, Site U1425. For each sample, the left plot shows the intensity variation with progressive demagnetization. The middle and right plots show the NRM vector measured after each demagnetization treatment on an orthogonal projection (Zijderveld) and on an equal area projection, respectively. In the orthogonal projection plot, squares = horizontal projections, circles = vertical projections. In the equal area projection plot, closed circles = projection data with positive inclinations, open circles = projection data with negative inclinations. Note that on the orthogonal projection (Zijderveld) plot, NRM data before demagnetization have been removed to better display the demagnetized data.

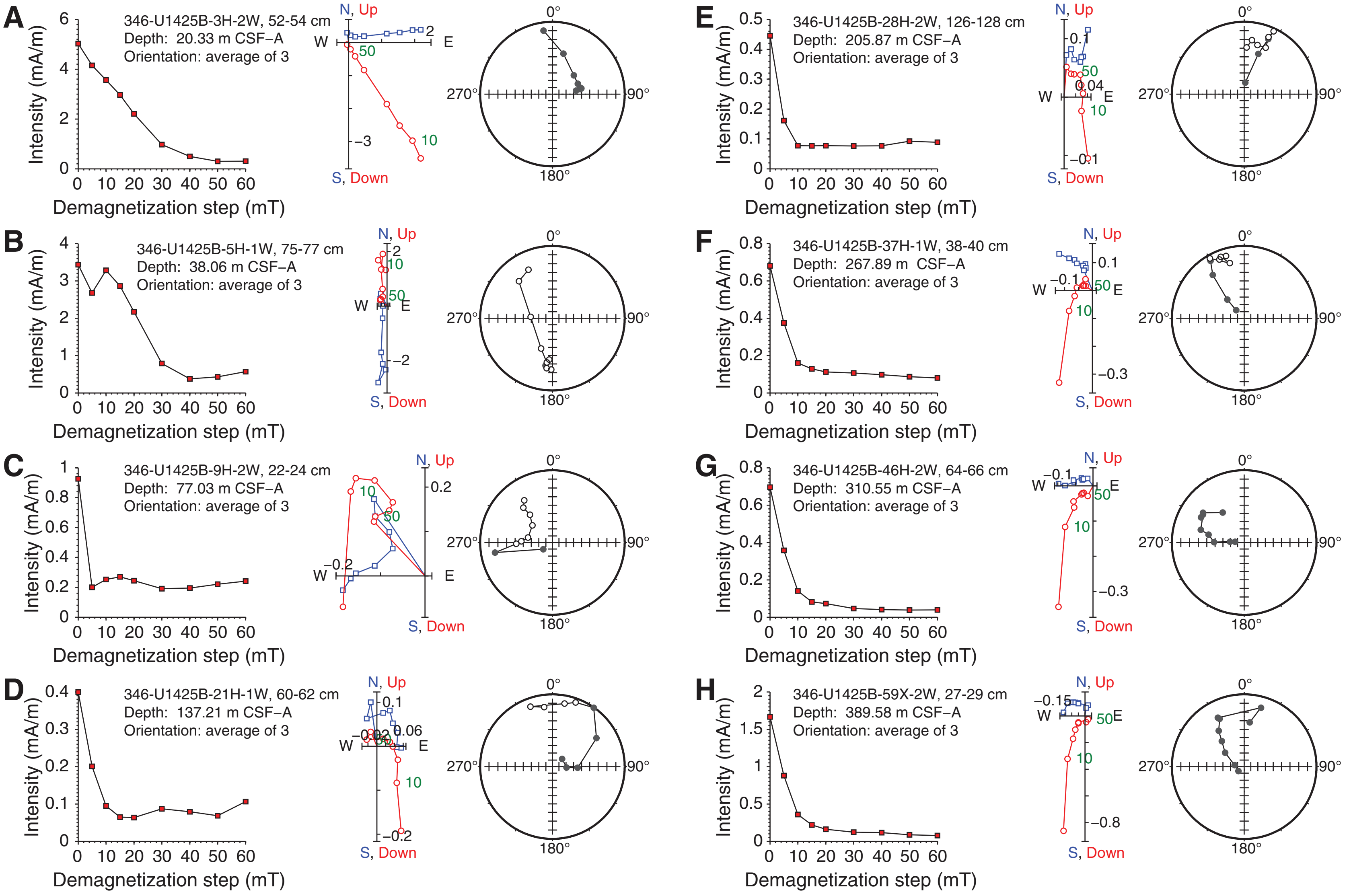

Figure F55. Suite of physical properties measured in Holes U1425B and U1425D. The first magnetic susceptibility panel shows WRMSL data of Hole U1425D, whereas the second panel shows point SHMSL susceptibility data of Hole U1425D. Gamma ray attenuation (GRA) bulk density is from Hole U1425D. Natural gamma radiation (NGR) is from Hole U1425D. *P*-wave velocity panel shows combined data from WRMSL of Holes U1425B and U1425D. Dashed horizontal lines = lithologic subunit boundaries, solid horizontal lines = lithologic unit boundaries.

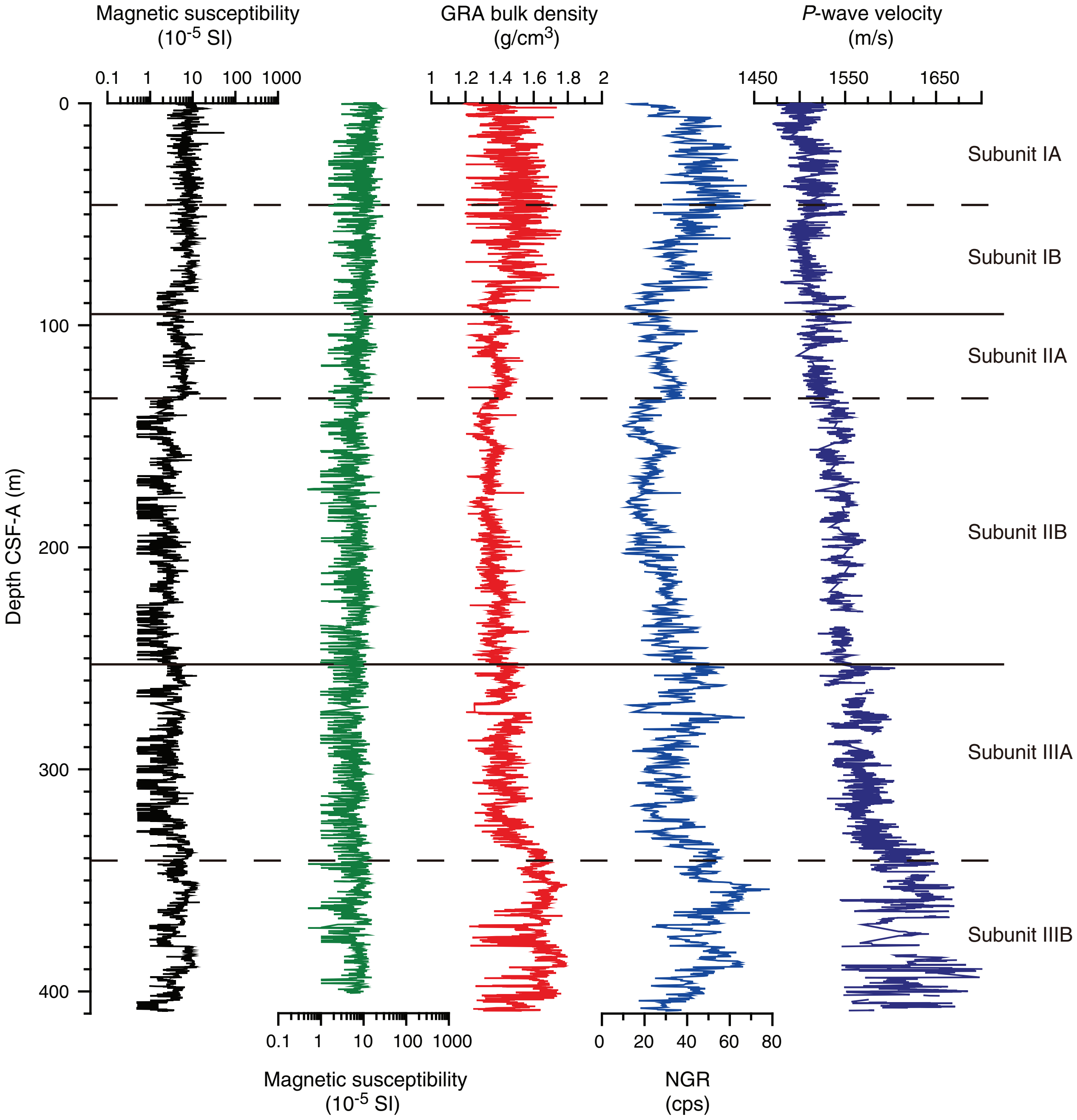

Figure F56. Discrete bulk density, grain density, porosity, water content, and shear strength, Site U1425. Solid symbols indicate measurements in dark layers. Dashed horizontal lines = lithologic subunit boundaries, solid horizontal lines = lithologic unit boundaries.

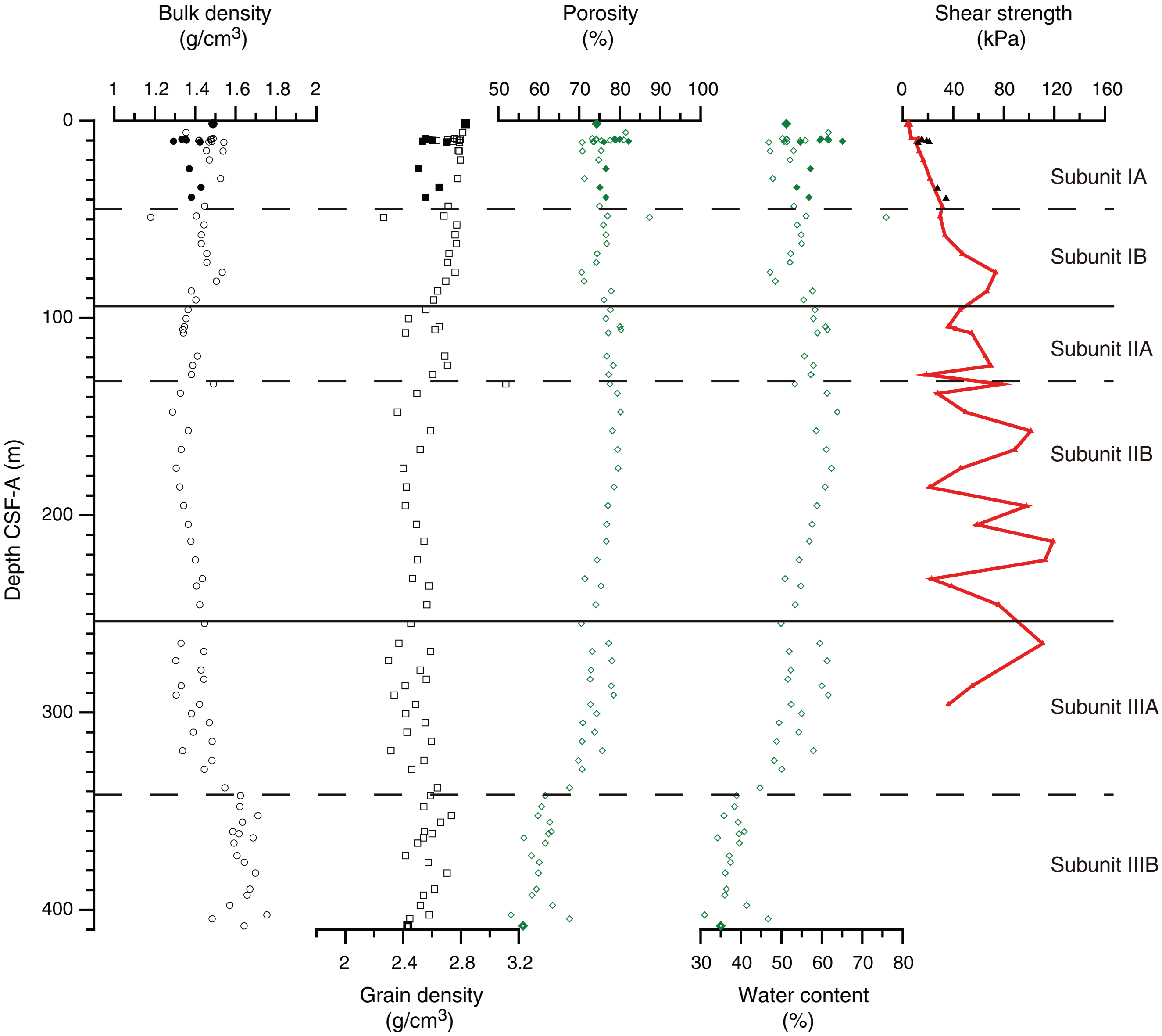

Figure F57. Relationship between lightness (L*) as a proxy for lithology, GRA bulk density (blue line), and discrete bulk density measured on organic-rich (solid circles) and hemipelagic (open circles) sediment. Dark and light gray shaded areas indicate massive dark and dark brown organic-rich layers, respectively, that appear to drive up low bulk density.

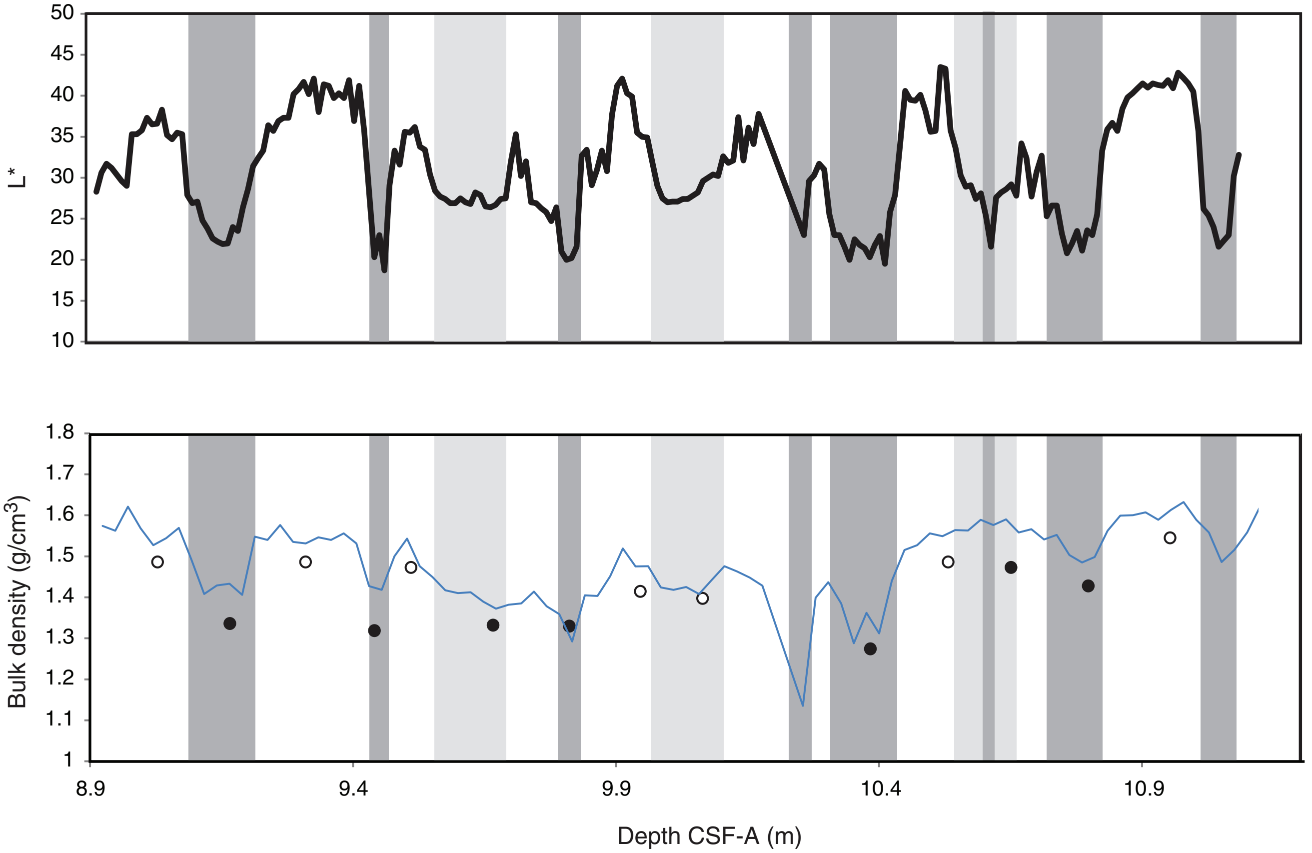

Figure F58. Color reflectance, Hole U1425D. Dashed horizontal lines = lithologic subunit boundaries, solid horizontal lines = lithologic unit boundaries.

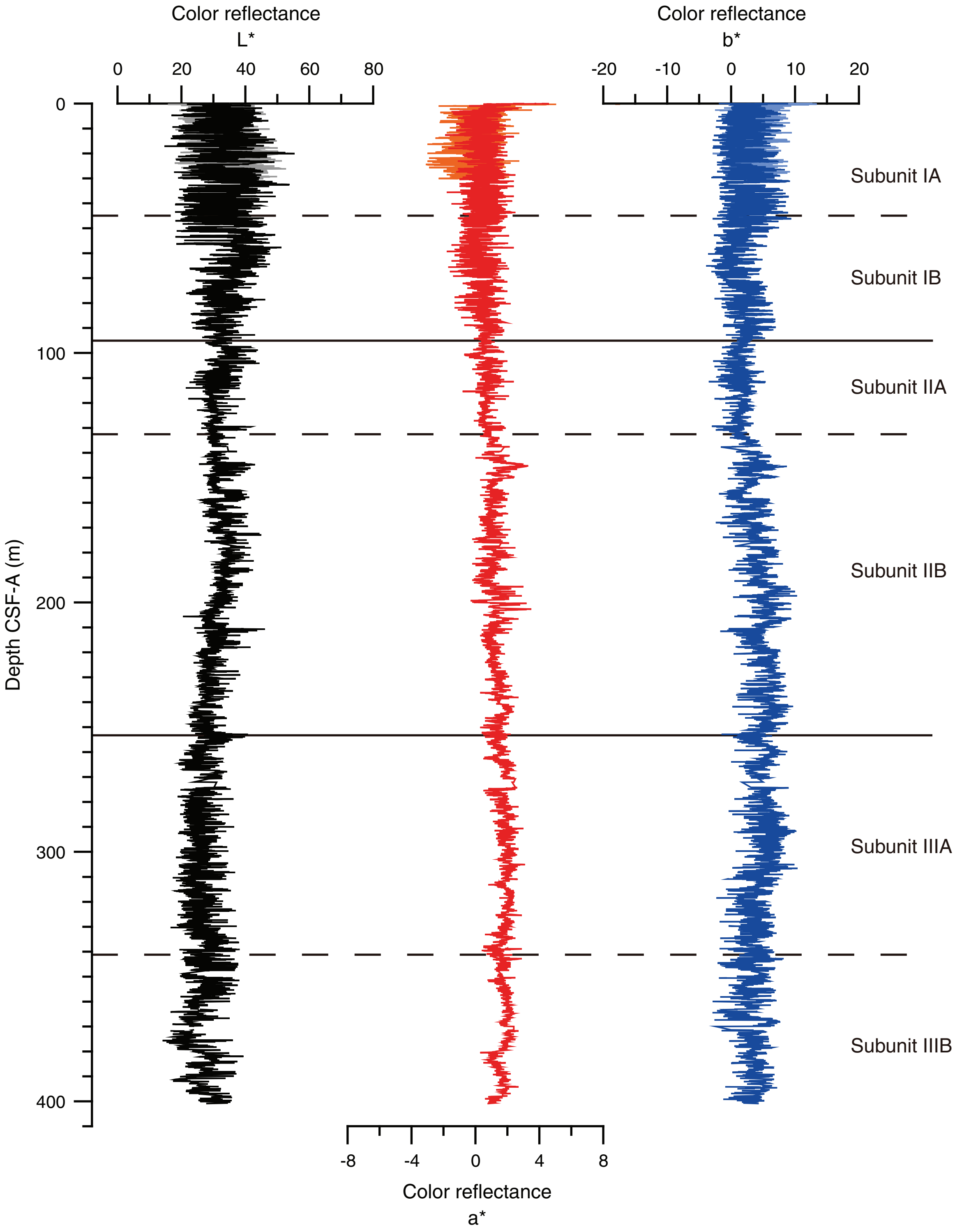

Figure F59. Downhole logs and logging units, Hole U1425B. HSGR = standard (total) gamma radiation, NGR = natural gamma radiation, RHOM = bulk density, GRA= gamma ray attenuation measured on core, RLA1 = shallow apparent resistivity, RT = “true” resistivity, MSS = Magnetic Susceptibility Sonde, HMSS = high-resolution MSS, LMSS= low-resolution MSS. FMS = Formation MicroScanner, V_P = P-wave velocity.

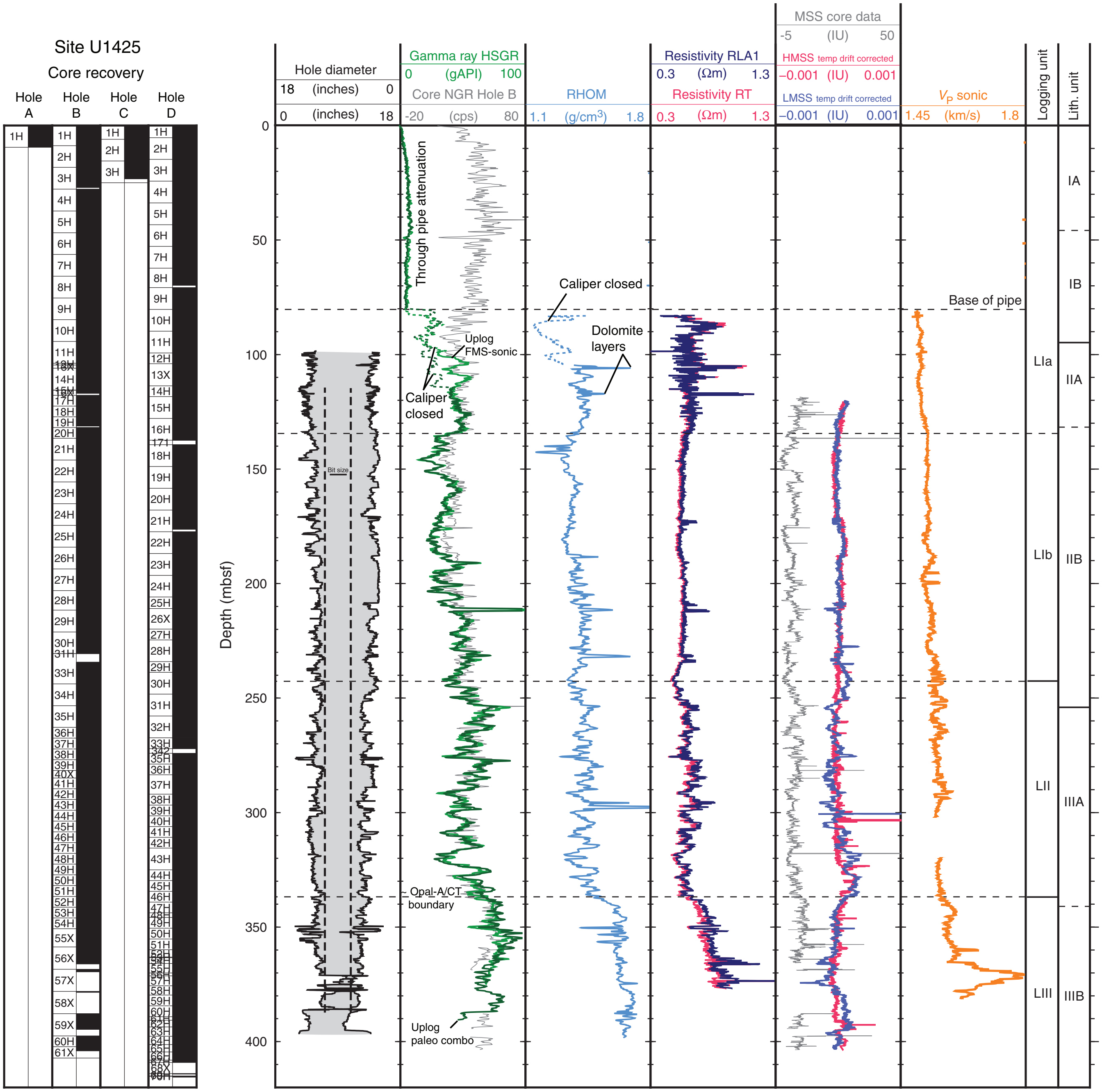

Figure F60. Natural gamma radiation logs, straight (nonoriented) Formation MicroScanner (FMS) images, and logging units, Hole U1425B. HSGR = standard (total) gamma radiation, HCGR = computed gamma radiation. Bold lines = triple combo tool string main pass, fine lines = FMS-sonic tool string main pass.

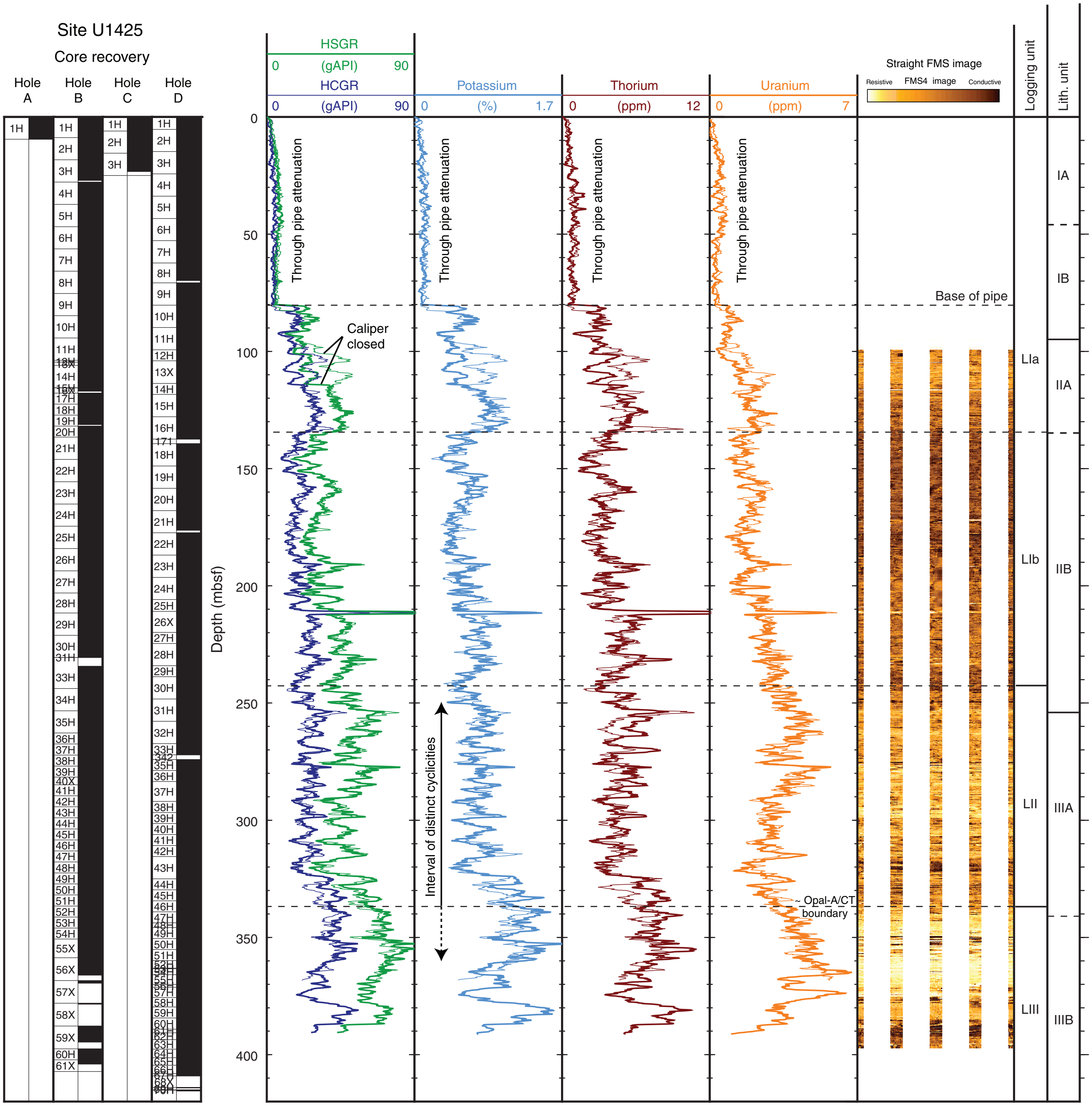

Figure F61. Logging operations summary diagram, Site U1425. FMS = Formation MicroScanner.

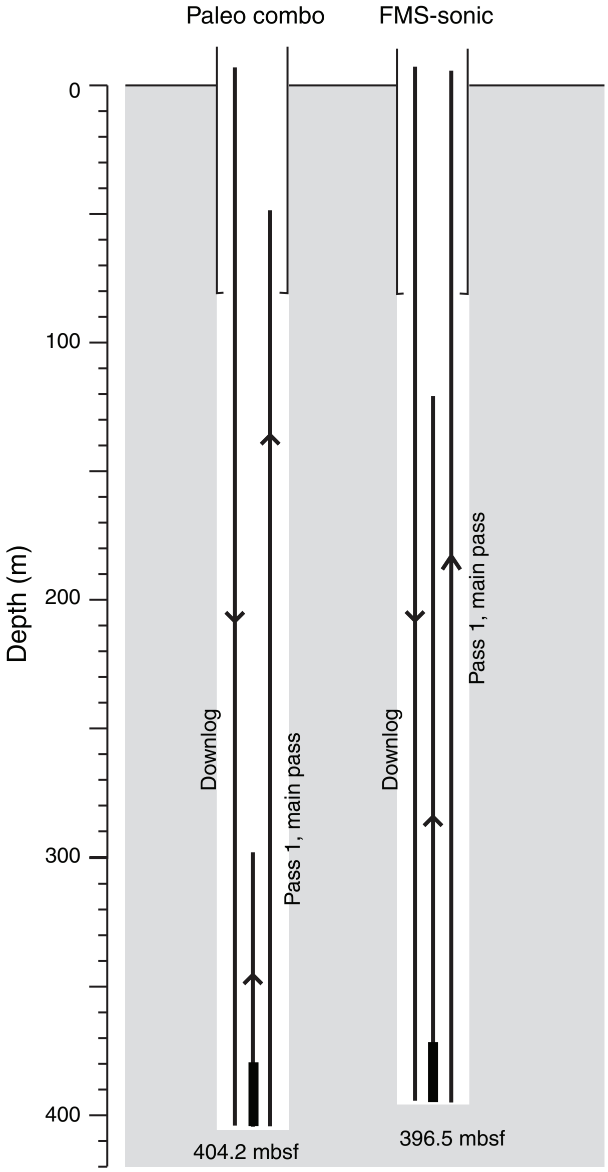

Figure F62. Correlation of downhole logs and straight (nonoriented) Formation MicroScanner (FMS) images (290–323 mbsf) in Hole U1425B, illustrating the cyclic nature of the sediment record at intervals of ~8–15 m. NGR = natural gamma radiation, HSGR = standard (total) natural gamma radiation, RHOM = bulk density, RT = "true" resistivity.

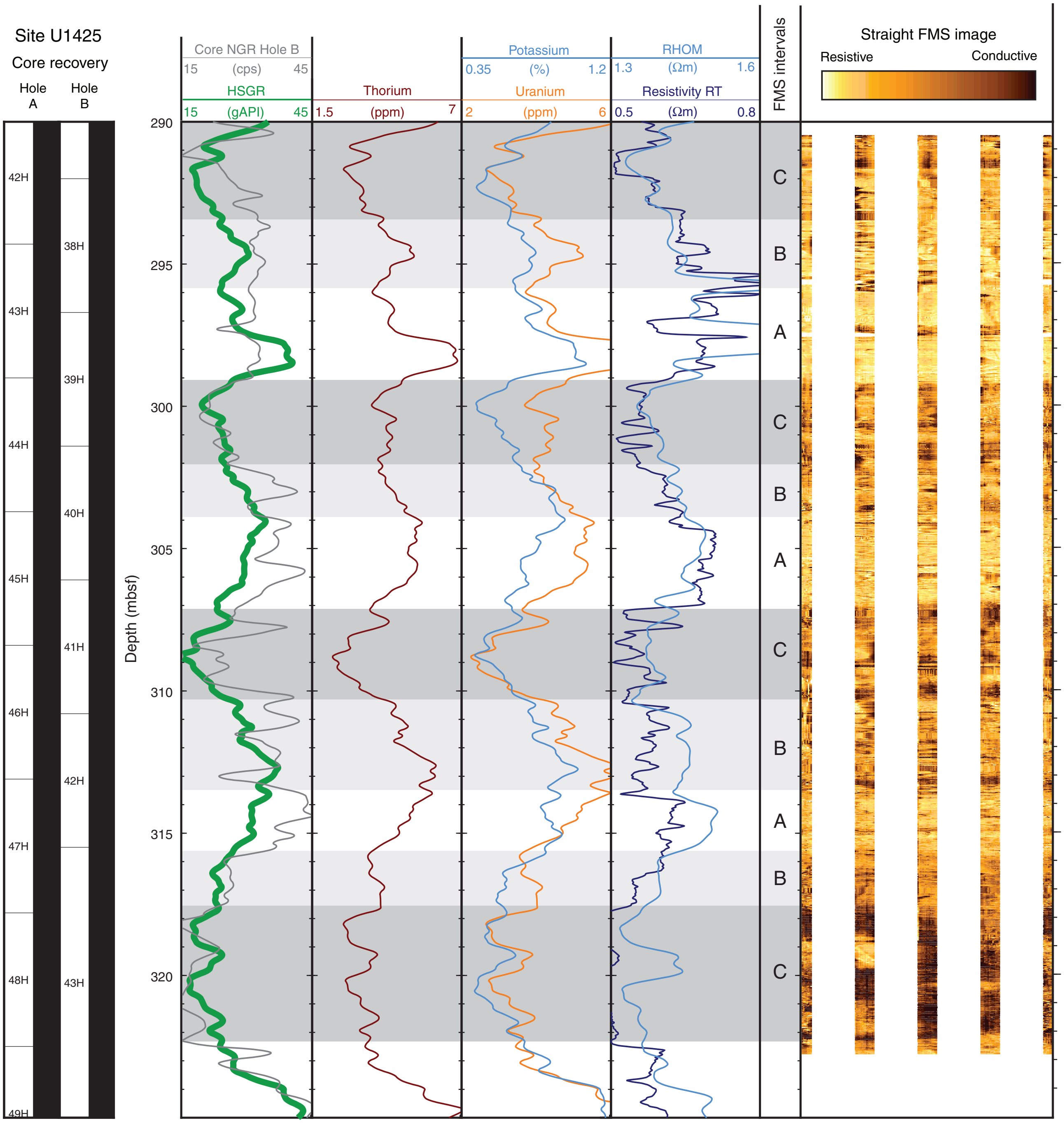

Figure F63. Straight (nonoriented) dynamic Formation MicroScanner (FMS) images in Hole U1425B, illustrating the high frequency cyclic nature of sediment records along several intervals.

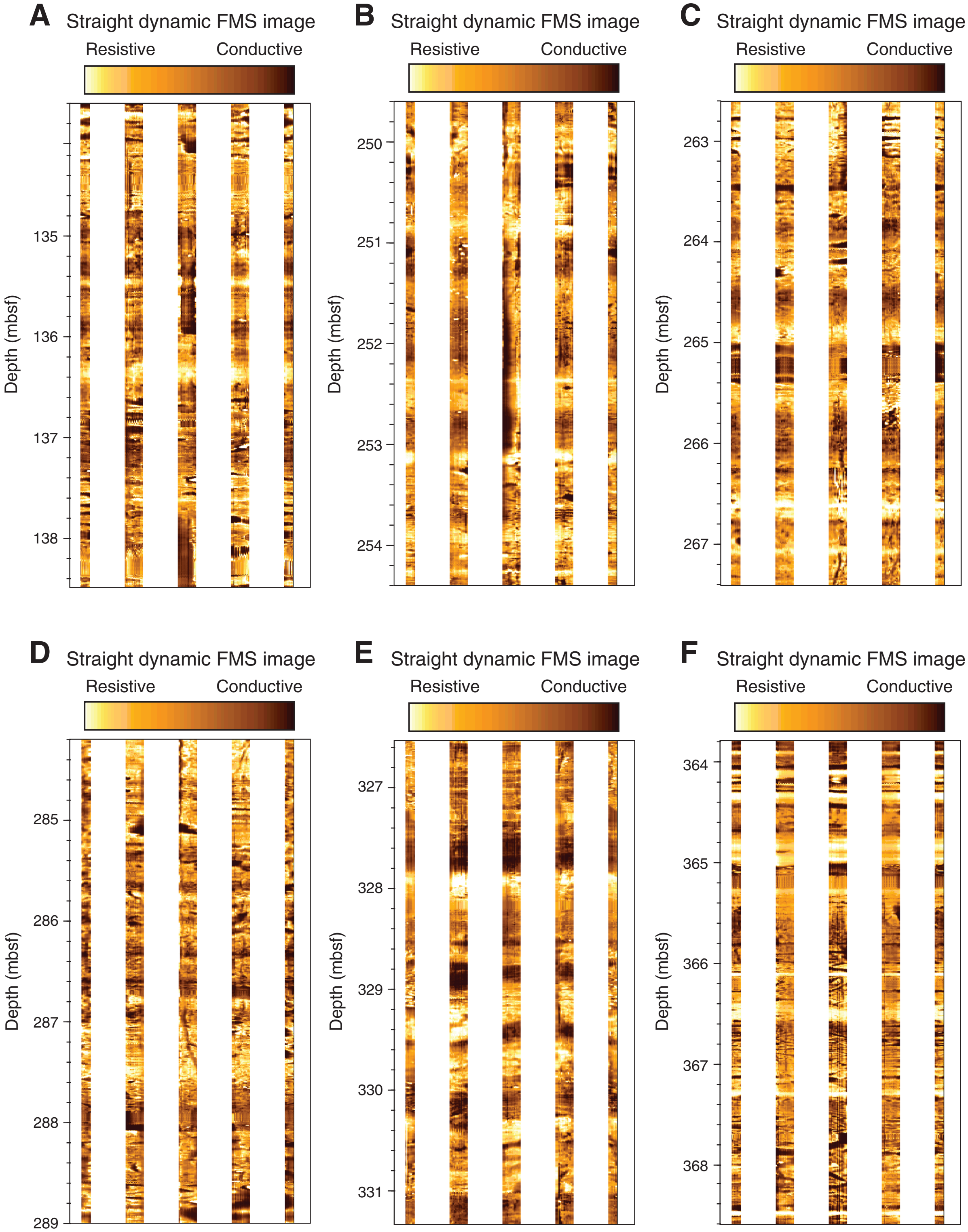

Figure F64. Plots of heat flow calculations, Hole U1425A. **A.** In situ sediment temperatures from advanced piston corer temperature tool (APCT-3) measurements with average values for Cores 346-U1425A-4H, 7H, and 10H (circles) and linear fit. **B.** In situ thermal conductivity data (squares) with calculated thermal resistance (solid line). **C.** Bullard plot of heat flow calculated from a linear fit of temperature vs. thermal resistance data.

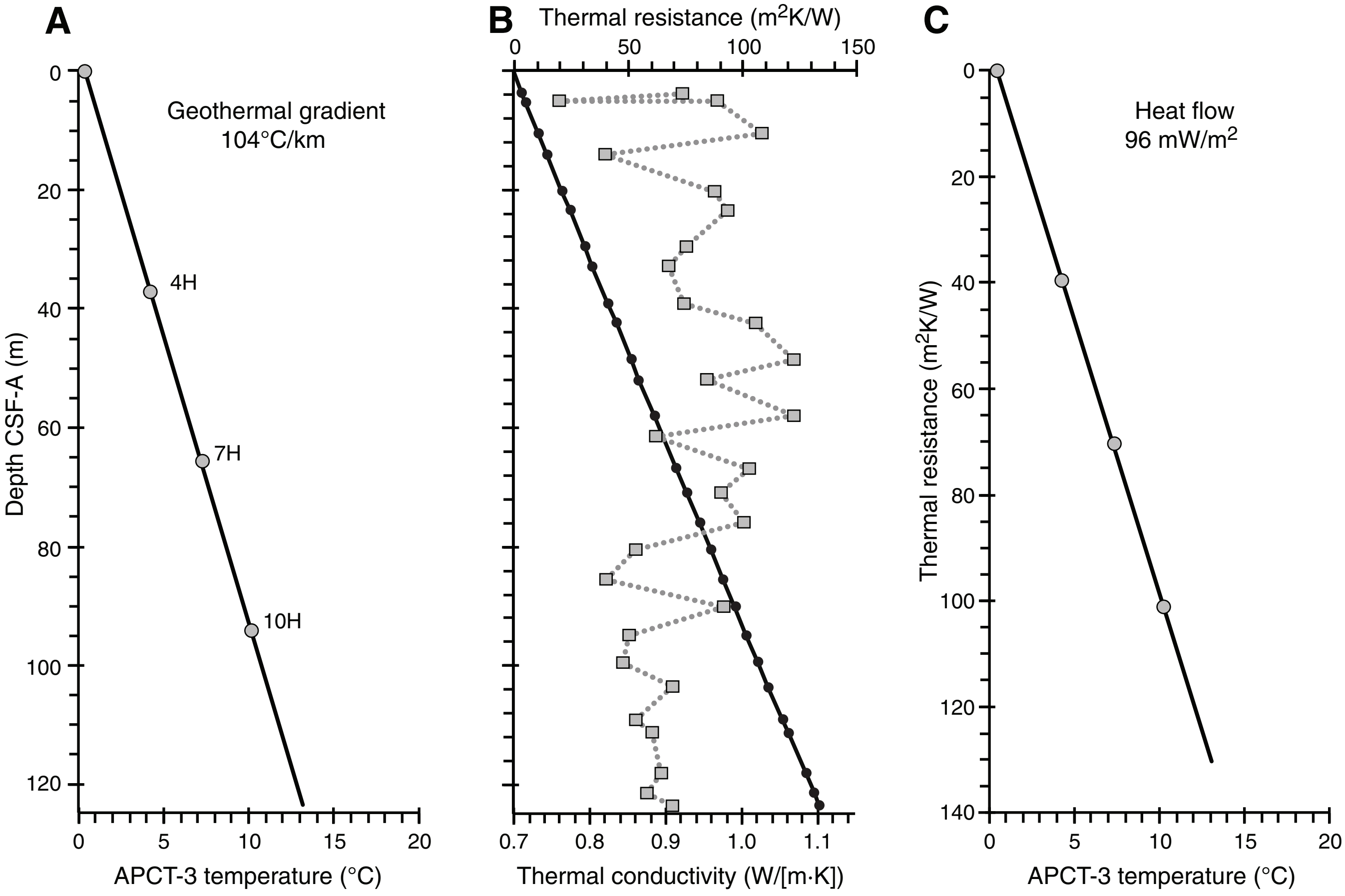

Figure F65. A–C. Alignment of the cores from Holes U1425B (red), U1425D (blue), and U1425E (orange) illustrated using natural gamma radiation (NGR) profiles. Spliced profile is also shown (black). (Continued on next page.)

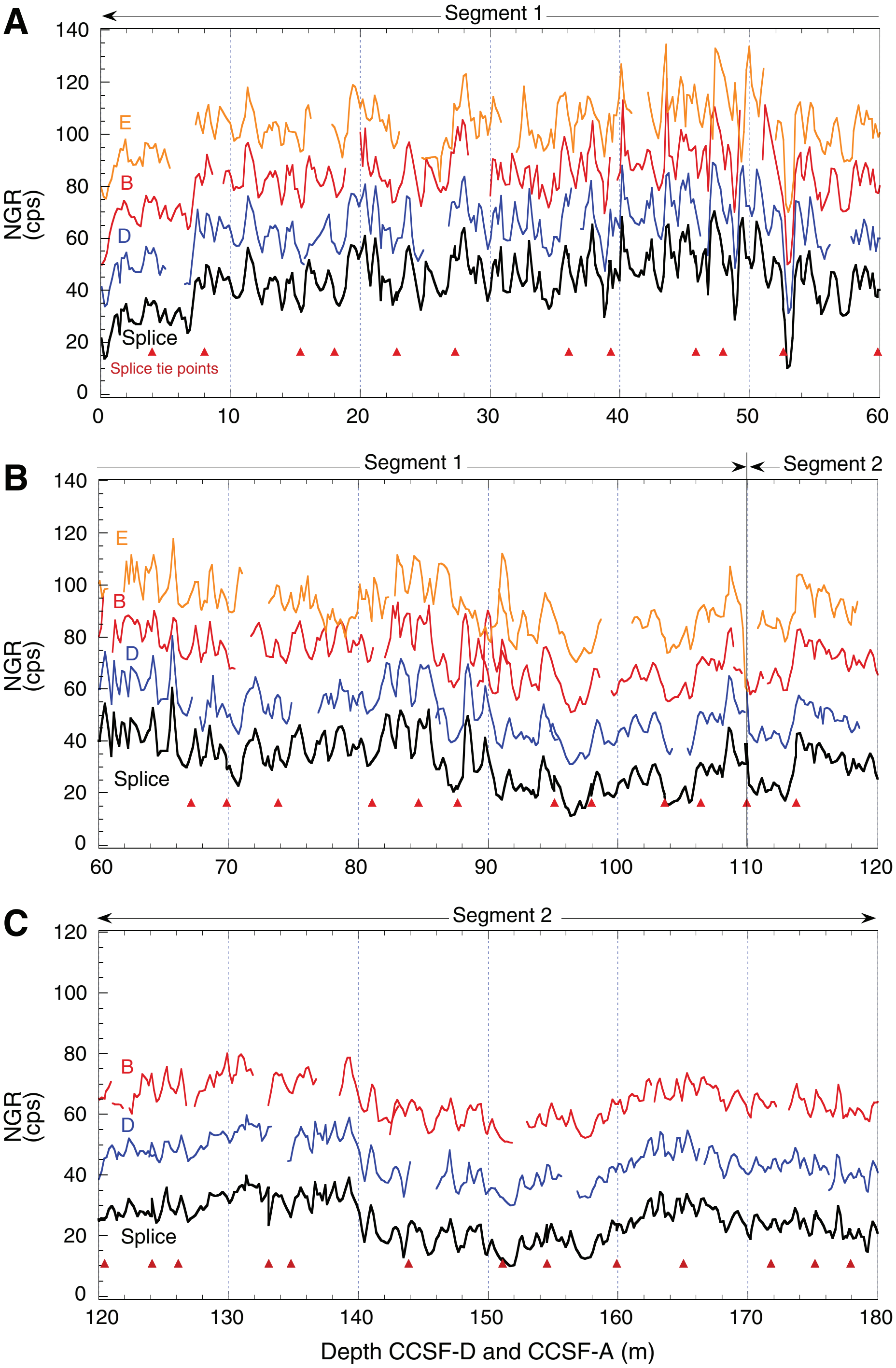

Figure F65 (continued). **D–F.** Red triangles indicate splice tie points.

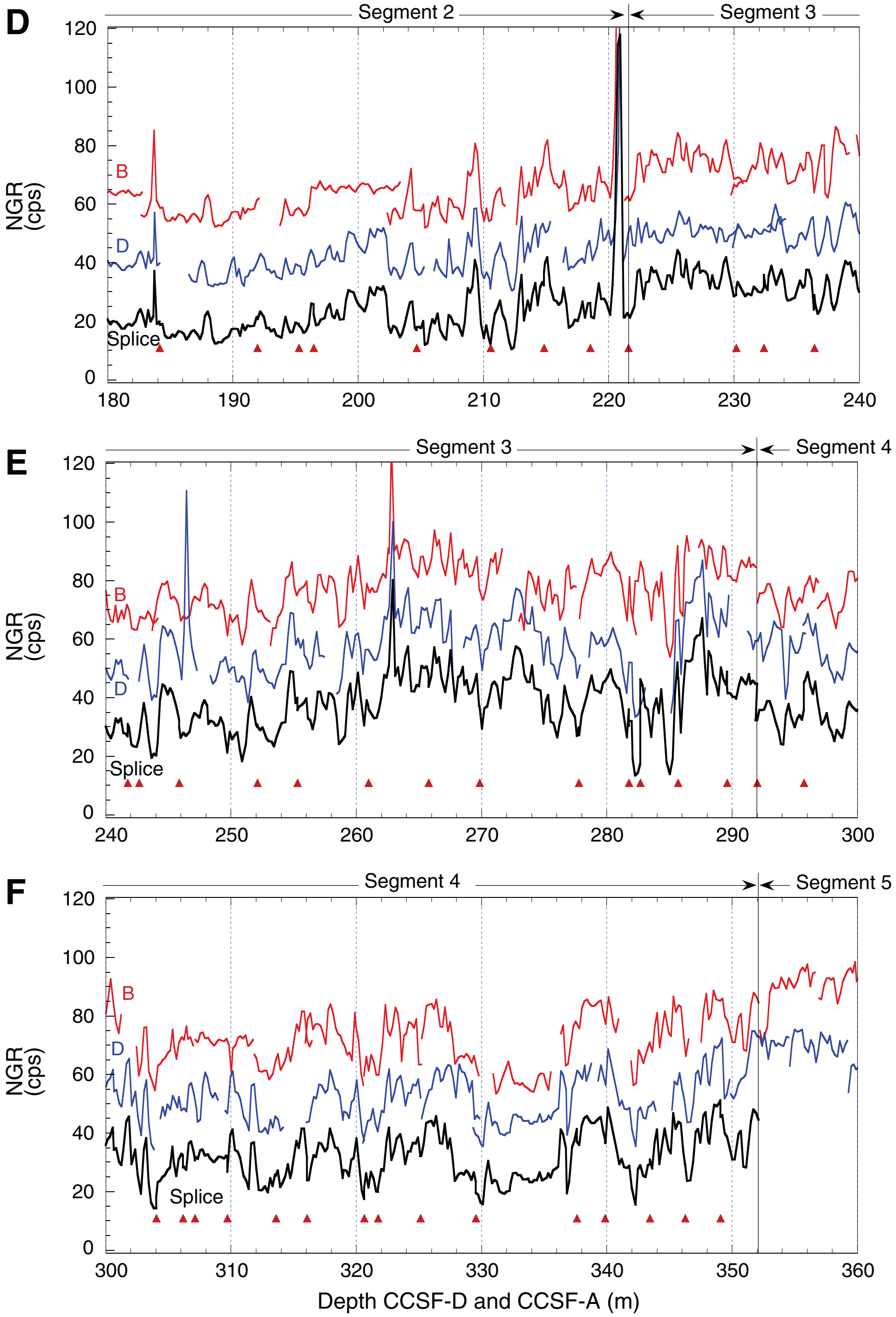

Figure F66. A–G. Correlation between core splice NGR and downhole logging total spectral gamma ray (HSGR) logs (green and orange curves) around the intervals between splice Segment 1/2, 2/3, and 3/4 boundaries and Segment 5. Distances between correlative horizons above and below segment boundaries are also shown. FMS = Formation MicroScanner. In B, between 96 and 114 m WSF, the HSGR data from the paleo combo tool string artificially deviate from the FMS-sonic tool string HSGR data to lower values as a result of the paleo combo caliper closure at ~114 m WSF (see **"Downhole measurements"**).

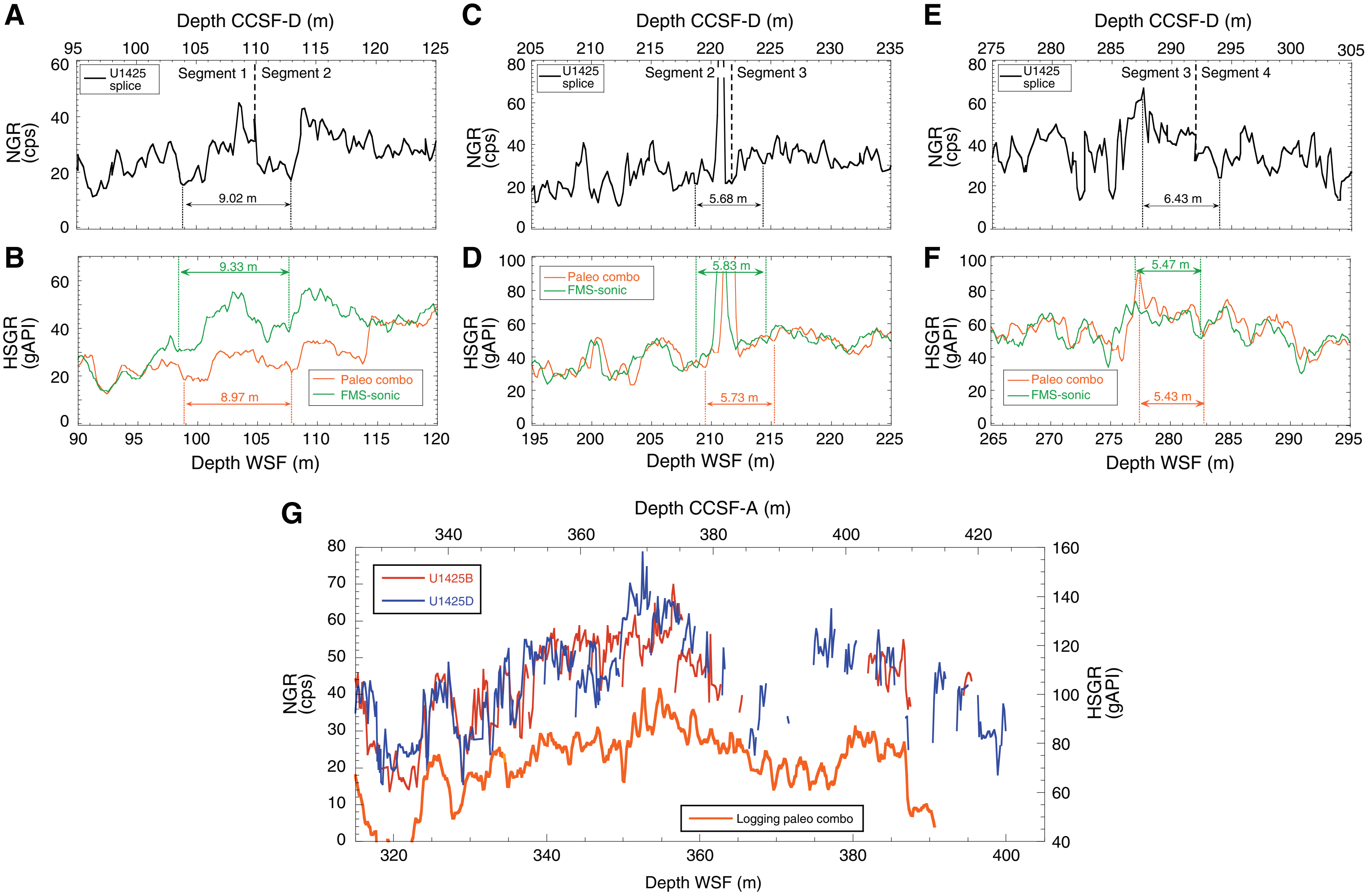

Figure F67. Age model and sedimentation rates, Site U1425. **A.** Synthesis of biostratigraphic, paleomagnetic, and tephra-based age control points and the depth age lines used to construct a preliminary age model. **B.** Average sedimentation rates calculated for each lithologic unit plotted with gamma ray attenuation (GRA) density.

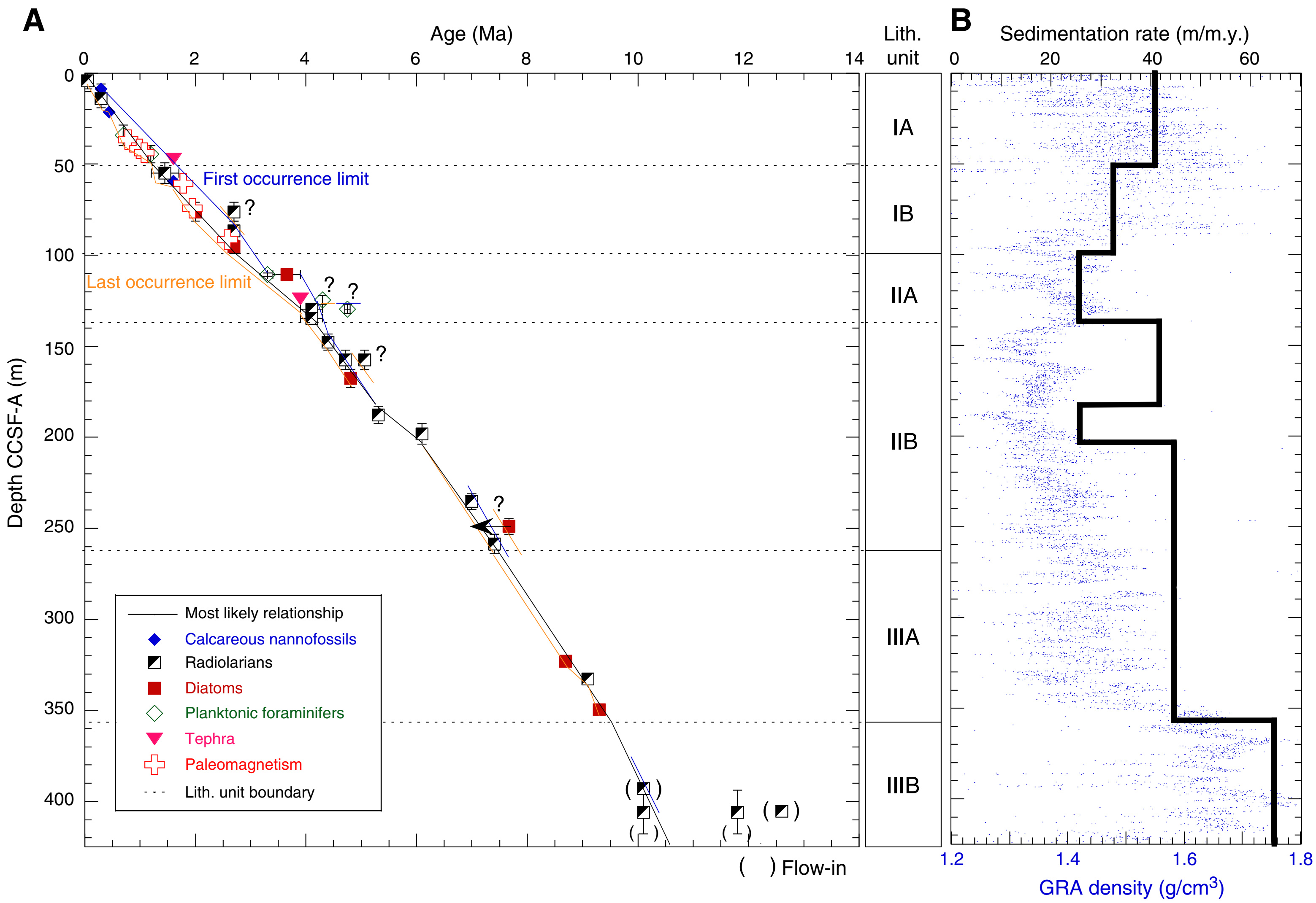

Table T1. Coring summary, Site U1425. (Continued on next three pages.)

Hole U1425A
Latitude: 39°9.4396′N
Longitude: 134°26.5505′E
Water depth (m): 1912.99
Date started (UTC): 1730 h 27 August 2013
Date finished (UTC): 0030 h 28 August 2013
Time on hole (days): 0.29
Seafloor depth DRF (m): 1924.4
Rig floor to sea level (m): 11.41
Penetration DSF (m): 19
Cored interval (m): 9.5
Recovered length (m): 9.81
Recovery (%): 103
Drilled interval (m): NA
Drilled interval: 0
Total cores: 1
APC cores: 1
XCB cores: 0
RCB cores: 0
Other cores: 0

Hole U1425B
Latitude: 39°29.4476′N
Longitude: 134°26.5502′E
Water depth (m): 1907.69
Date started (UTC): 0030 h 28 August 2013
Date finished (UTC): 1700 h 30 August 2013
Time on hole (days): 2.69
Seafloor depth DRF (m): 1919.1
Rig floor to sea level (m): 11.41
Penetration DSF (m): 407.2
Cored interval (m): 407.2
Recovered length (m): 397.25
Recovery (%): 98
Drilled interval (m): NA
Drilled interval: 0
Total cores: 61
APC cores: 51
XCB cores: 10
RCB cores: 0
Other cores: 0

Hole U1425C
Latitude: 39°29.4311′N
Longitude: 134°26.5501′E
Water depth (m): 1907.48
Date started (UTC): 1700 h 30 August 2013
Date finished (UTC): 2040 h 30 August 2013
Time on hole (days): 0.15
Seafloor depth DRF (m): 1918.9
Rig floor to sea level (m): 11.42
Penetration DSF (m): 25
Cored interval (m): 25
Recovered length (m): 23.21
Recovery (%): 93
Drilled interval (m): NA
Drilled interval: 0
Total cores: 3
APC cores: 3
XCB cores: 0
RCB cores: 0
Other cores: 0

Hole U1425D
Latitude: 39°29.4392′N
Longitude: 134°26.5395′E
Water depth (m): 1908.18
Date started (UTC): 2040 h 30 August 2013
Date finished (UTC): 0812 h 2 September 2013
Time on hole (days): 2.48
Seafloor depth DRF (m): 1919.6
Rig floor to sea level (m): 11.42
Penetration DSF (m): 431

Table T1 (continued). (Continued on next page.)

Cored interval (m): 427
Recovered length (m): 417.49
Recovery (%): 98
Drilled interval (m): 4
Drilled interval: 2
Total cores: 70
APC cores: 66
XCB cores: 4
RCB cores: 0
Other cores: 0

Hole U1425E
Latitude: 39°29.4392′N
Longitude: 134°26.5607′E
Water depth (m): 1908.6
Date started (UTC): 0530 h 24 September 2013
Date finished (UTC): 0112 h 25 September 2013
Time on hole (days): 0.82
Seafloor depth DRF (m): 1920.2
Rig floor to sea level (m): 11.60
Penetration DSF (m): 113.1
Cored interval (m): 113.1
Recovered length (m): 107.75
Recovery (%): 95
Drilled interval (m): NA
Drilled interval: 0
Total cores: 13
APC cores: 13
XCB cores: 0
RCB cores: 0
Other cores: 0

Site U1425 totals
Number of cores: 148
Penetration (m): 985.8
Cored (m): 981.8
Recovered (m): 955.51 (97%)

Core	Date (2013)	Time (h)	Top depth of cored interval DSF (m)	Bottom depth of cored interval DSF (m)	Interval advanced (m)	Top depth of recovered core CSF (m)	Bottom depth of recovered core CSF (m)	Length of core recovered (m)	Curated length (m)	Recovery (%)
346-U1425A-										
1H	28 Aug	0015	0.0	9.5	9.5	0.0	9.81	9.81	9.81	103
346-U1425B-										
1H	28 Aug	0110	0.0	8.8	8.8	0.0	8.82	8.82	8.82	100
2H	28 Aug	0200	8.8	18.3	9.5	8.8	18.63	9.83	9.83	103
3H	28 Aug	0235	18.3	27.8	9.5	18.3	27.09	8.79	8.79	93
4H	28 Aug	0350	27.8	37.3	9.5	27.8	37.68	9.83	9.88	103
5H	28 Aug	0430	37.3	46.8	9.5	37.3	47.01	9.71	9.71	102
6H	28 Aug	0505	46.8	56.3	9.5	46.8	56.58	9.78	9.78	103
7H	28 Aug	0545	56.3	65.8	9.5	56.3	66.27	9.97	9.97	105
8H	28 Aug	0620	65.8	75.3	9.5	65.8	75.63	9.83	9.83	103
9H	28 Aug	0655	75.3	84.8	9.5	75.3	85.17	9.87	9.87	104
10H	28 Aug	0740	84.8	94.3	9.5	84.8	94.82	10.02	10.02	105
11H	28 Aug	0810	94.3	103.8	9.5	94.3	104.04	9.74	9.74	103
12H	28 Aug	0850	103.8	104.6	0.8	103.8	104.61	0.81	0.81	101
13X	28 Aug	1030	104.6	106.0	1.4	104.6	106.31	1.71	1.71	122
14H	28 Aug	1115	106.0	115.5	9.5	106.0	115.81	9.81	9.81	103
15H	28 Aug	1215	115.5	115.6	0.1	115.5	115.53		0.03	
16X	28 Aug	1310	115.6	117.8	2.2	115.6	116.96	1.36	1.36	62
17H	28 Aug	1355	117.8	122.5	4.7	117.8	122.54	4.74	4.74	101
18H	28 Aug	1430	122.5	127.2	4.7	122.5	127.33	4.83	4.83	103
19H	28 Aug	1500	127.2	131.9	4.7	127.2	131.23	4.03	4.03	86
20H	28 Aug	1540	131.9	136.6	4.7	131.9	136.82	4.92	4.92	105
21H	28 Aug	1615	136.6	146.1	9.5	136.6	146.38	9.78	9.78	103
22H	28 Aug	1650	146.1	155.6	9.5	146.1	156.04	9.94	9.94	105
23H	28 Aug	1725	155.6	165.1	9.5	155.6	165.47	9.87	9.87	104
24H	28 Aug	1755	165.1	174.6	9.5	165.1	175.04	9.94	9.94	105
25H	28 Aug	1855	174.6	184.1	9.5	174.6	184.52	9.92	9.92	104
26H	28 Aug	1930	184.1	193.6	9.5	184.1	194.10	10.00	10.00	105
27H	28 Aug	2015	193.6	203.1	9.5	193.6	203.42	9.82	9.82	103

Table T1 (continued). (Continued on next page.)

Core	Date (2013)	Time (h)	Top depth of cored interval DSF (m)	Bottom depth of cored interval DSF (m)	Interval advanced (m)	Top depth of recovered core CSF (m)	Bottom depth of recovered core CSF (m)	Length of core recovered (m)	Curated length (m)	Recovery (%)
28H	28 Aug	2050	203.1	211.6	8.5	203.1	211.63	8.53	8.53	100
29H	28 Aug	2135	211.6	221.1	9.5	211.6	221.31	9.71	9.71	102
30H	28 Aug	2210	221.1	230.6	9.5	221.1	230.99	9.89	9.89	104
31H	28 Aug	2240	230.6	230.6	0.0	230.6	230.60	0.00	0.00	
32X	28 Aug	2340	230.6	234.3	3.7	230.6	235.51	4.91	4.91	133
33H	29 Aug	0010	234.3	243.8	9.5	234.3	244.03	9.73	9.73	102
34H	29 Aug	0045	243.8	253.3	9.5	243.8	253.46	9.66	9.66	102
35H	29 Aug	0150	253.3	262.8	9.5	253.3	262.73	9.43	9.43	99
36H	29 Aug	0235	262.8	267.5	4.7	262.8	267.77	4.97	4.97	106
37H	29 Aug	0305	267.5	272.2	4.7	267.5	272.49	4.99	4.99	106
38H	29 Aug	0355	272.2	276.9	4.7	272.2	277.13	4.93	4.93	105
39H	29 Aug	0425	276.9	281.6	4.7	276.9	281.97	5.07	5.07	108
40X	29 Aug	0515	281.6	284.9	3.3	281.6	287.05	5.45	5.45	165
41H	29 Aug	0545	284.9	289.6	4.7	284.9	289.85	4.95	4.95	105
42H	29 Aug	0630	289.6	294.3	4.7	289.6	294.58	4.98	4.98	106
43H	29 Aug	0700	294.3	299.0	4.7	294.3	299.24	4.94	4.94	105
44H	29 Aug	0740	299.0	303.7	4.7	299.0	304.05	5.05	5.05	107
45H	29 Aug	0815	303.7	308.4	4.7	303.7	308.76	5.06	5.06	108
46H	29 Aug	0850	308.4	313.1	4.7	308.4	313.37	4.97	4.97	106
47H	29 Aug	0925	313.1	317.8	4.7	313.1	318.10	5.00	5.00	106
48H	29 Aug	1010	317.8	322.5	4.7	317.8	322.74	4.94	4.94	105
49H	29 Aug	1040	322.5	327.2	4.7	322.5	327.47	4.97	4.97	106
50H	29 Aug	1115	327.2	331.9	4.7	327.2	332.25	5.05	5.05	107
51H	29 Aug	1145	331.9	336.6	4.7	331.9	336.91	5.01	5.01	107
52H	29 Aug	1220	336.6	341.3	4.7	336.6	341.57	4.97	4.97	106
53H	29 Aug	1300	341.3	346.0	4.7	341.3	346.35	5.05	5.05	107
54H	29 Aug	1350	346.0	350.7	4.7	346.0	351.25	5.25	5.25	112
55X	29 Aug	1555	350.7	358.7	8.0	350.7	360.27	9.57	9.57	120
56X	29 Aug	1720	358.7	368.4	9.7	358.7	366.07	7.37	7.37	76
57X	29 Aug	1905	368.4	378.1	9.7	368.4	369.52	1.12	1.12	12
58X	29 Aug	2030	378.1	387.8	9.7	378.1	378.46	0.36	0.36	4
59X	29 Aug	2125	387.8	397.5	9.7	387.8	394.66	6.86	6.86	71
60H	29 Aug	2210	397.5	402.2	4.7	397.5	402.50	5.00	5.00	106
61X	29 Aug	2345	402.2	407.2	5.0	402.2	404.04	1.84	1.84	37
				Total advanced (m):	407.2		Total recovered (m):	397.25		
346-U1425C-										
1H	30 Aug	1905	0.0	6.0	6.0	0.0	5.95	5.95	5.95	99
2H	30 Aug	1935	6.0	15.5	9.5	6.0	15.47	9.47	9.47	100
3H	30 Aug	2005	15.5	25.0	9.5	15.5	23.29	7.79	7.79	82
				Total advanced (m):	25.0		Total recovered (m):	23.21		
346-U1425D-										
1H	30 Aug	2115	0.0	5.3	5.3	0.0	5.28	5.28	5.28	100
2H	30 Aug	2145	5.3	14.8	9.5	5.3	14.77	9.47	9.47	100
3H	30 Aug	2215	14.8	24.3	9.5	14.8	24.22	9.42	9.42	99
4H	30 Aug	2245	24.3	33.8	9.5	24.3	33.91	9.61	9.61	101
5H	30 Aug	2315	33.8	43.3	9.5	33.8	43.55	9.75	9.75	103
6H	30 Aug	2340	43.3	52.8	9.5	43.3	53.04	9.74	9.74	103
7H	31 Aug	0010	52.8	62.3	9.5	52.8	62.63	9.83	9.83	103
8H	31 Aug	0040	62.3	70.8	8.5	62.3	69.8	7.50	7.50	88
9H	31 Aug	0115	70.8	80.3	9.5	70.8	80.68	9.88	9.88	104
10H	31 Aug	0210	80.3	89.8	9.5	80.3	90.18	9.88	9.88	104
11H	31 Aug	0245	89.8	99.3	9.5	89.8	99.68	9.88	9.88	104
12H	31 Aug	0320	99.3	104.0	4.7	99.3	104.25	4.95	4.95	105
13X	31 Aug	0400	104.0	113.7	9.7	104.0	113.85	9.85	9.85	102
14H	31 Aug	0430	113.7	118.4	4.7	113.7	118.60	4.90	4.90	104
15H	31 Aug	0535	118.4	127.9	9.5	118.4	128.01	9.61	9.61	101
16H	31 Aug	0605	127.9	137.4	9.5	127.9	137.75	9.85	9.85	104
171	31 Aug	0615			*****Drilled from 137.4 to 139.4 mbsf*****					
18H	31 Aug	0715	139.4	148.9	9.5	139.4	149.39	9.99	9.99	105
19H	31 Aug	0745	148.9	158.4	9.5	148.9	158.67	9.77	9.77	103
20H	31 Aug	0815	158.4	167.9	9.5	158.4	168.35	9.95	9.95	105
21H	31 Aug	0845	167.9	177.4	9.5	167.9	176.31	8.41	8.41	89
22H	31 Aug	0920	177.4	186.9	9.5	177.4	187.04	9.64	9.64	101
23H	31 Aug	1000	186.9	196.4	9.5	186.9	196.69	9.79	9.79	103
24H	31 Aug	1030	196.4	205.9	9.5	196.4	206.01	9.61	9.61	101
25H	31 Aug	1100	205.9	210.9	5.0	205.9	210.89	4.99	4.99	100
26X	31 Aug	1210	210.9	219.9	9.0	210.9	220.70	9.80	9.80	109

Table T1 (continued).

Core	Date (2013)	Time (h)	Top depth of cored interval DSF (m)	Bottom depth of cored interval DSF (m)	Interval advanced (m)	Top depth of recovered core CSF (m)	Bottom depth of recovered core CSF (m)	Length of core recovered (m)	Curated length (m)	Recovery (%)
27H	31 Aug	1345	219.9	224.6	4.7	219.9	224.55	4.65	4.65	99
28H	31 Aug	1415	224.6	234.1	9.5	224.6	234.14	9.54	9.54	100
29H	31 Aug	1510	234.1	238.8	4.7	234.1	239.07	4.97	4.97	106
30H	31 Aug	1545	238.8	248.3	9.5	238.8	248.29	9.49	9.49	100
31H	31 Aug	1630	248.3	257.8	9.5	248.3	257.89	9.59	9.59	101
32H	31 Aug	1705	257.8	267.3	9.5	257.8	267.22	9.42	9.42	99
33H	31 Aug	1740	267.3	272.1	4.8	267.3	272.11	4.81	4.81	100
342	31 Aug	1800			*****Drilled from 272.1 to 274.1 mbsf*****					
35H	31 Aug	1835	274.1	278.8	4.7	274.1	279.05	4.95	4.95	105
36H	31 Aug	1910	278.8	283.5	4.7	278.8	283.8	5.00	5.00	106
37H	31 Aug	1955	283.5	292.0	8.5	283.5	292.35	8.85	8.85	104
38H	31 Aug	2040	292.0	296.7	4.7	292.0	296.95	4.95	4.95	105
39H	31 Aug	2115	296.7	301.4	4.7	296.7	301.75	5.05	5.05	107
40H	31 Aug	2200	301.4	306.1	4.7	301.4	306.43	5.03	5.03	107
41H	31 Aug	2230	306.1	310.8	4.7	306.1	311.05	4.95	4.95	105
42H	31 Aug	2300	310.8	315.5	4.7	310.8	315.81	5.01	5.01	107
43H	31 Aug	2355	315.5	325.0	9.5	315.5	325.50	10.00	10.00	105
44H	1 Sep	0040	325.0	329.7	4.7	325.0	330.03	5.03	5.03	107
45H	1 Sep	0115	329.7	334.4	4.7	329.7	334.69	4.99	4.99	106
46H	1 Sep	0145	334.4	339.1	4.7	334.4	339.43	5.03	5.03	107
47H	1 Sep	0220	339.1	343.8	4.7	339.1	344.18	5.08	5.08	108
48H	1 Sep	0300	343.8	345.8	2.0	343.8	347.82	4.02	4.02	201
49H	1 Sep	0340	345.8	350.5	4.7	345.8	350.88	5.08	5.08	108
50H	1 Sep	0420	350.5	355.2	4.7	350.5	355.54	5.04	5.04	107
51H	1 Sep	0450	355.2	359.9	4.7	355.2	360.21	5.01	5.01	107
52H	1 Sep	0530	359.9	363.1	3.2	359.9	363.12	3.22	3.22	101
53H	1 Sep	0605	363.1	363.4	0.3	363.1	363.35	0.25	0.25	83
54H	1 Sep	0640	363.4	365.9	2.5	363.4	366.01	2.61	2.61	104
55H	1 Sep	0725	365.9	370.0	4.1	365.9	370.07	4.17	4.17	102
56H	1 Sep	0820	370.0	371.3	1.3	370.0	371.33	1.33	1.33	102
57H	1 Sep	0920	371.3	375.6	4.3	371.3	375.61	4.31	4.31	100
58H	1 Sep	1050	375.6	379.7	4.1	375.6	379.68	4.08	4.08	100
59H	1 Sep	1145	379.7	384.4	4.7	379.7	384.82	5.12	5.12	109
60H	1 Sep	1215	384.4	389.1	4.7	384.4	389.28	4.88	4.88	104
61H	1 Sep	1300	389.1	390.7	1.6	389.1	390.72	1.62	1.62	101
62H	1 Sep	1345	390.7	393.6	2.9	390.7	393.56	2.86	2.86	99
63H	1 Sep	1430	393.6	397.7	4.1	393.6	397.71	4.11	4.11	100
64H	1 Sep	1525	397.7	401.3	3.6	397.7	401.33	3.63	3.63	101
65H	1 Sep	1630	401.3	404.5	3.2	401.3	404.47	3.17	3.17	99
66H	1 Sep	1755	404.5	408.1	3.6	404.5	408.07	3.57	3.57	99
67H	1 Sep	2000	408.1	409.1	1.0	408.1	408.91	0.81	0.81	81
68X	1 Sep	2100	409.1	414.0	4.9	409.1	409.10	0.00	0.00	0
69H	1 Sep	2155	414.0	415.0	1.0	414.0	414.16	0.16	0.16	16
70H	1 Sep	2255	415.0	415.2	0.2	415.0	415.11	0.11	0.11	55
71X	2 Sep	0120	415.2	430.7	15.5	415.2	415.54	0.34	0.34	2
72H	2 Sep	0150	430.7	431.0	0.3	430.7	430.95	0.25	0.25	83
				Total advanced (m):	431.0		Total recovered (m):	417.49		
346-U1425E-										
1H	24 Sep	1100	0.0	5.7	5.7	0.0	5.69	5.69	5.69	100
2H	24 Sep	1130	5.7	15.2	9.5	5.7	15.06	9.36	9.36	99
3H	24 Sep	1205	15.2	24.7	9.5	15.2	20.75	5.55	5.55	58
4H	24 Sep	1240	24.7	29.2	4.5	24.7	31.10	6.40	6.40	142
5H	24 Sep	1315	29.2	38.7	9.5	29.2	38.39	9.19	9.19	97
6H	24 Sep	1350	38.7	48.2	9.5	38.7	48.06	9.36	9.36	99
7H	24 Sep	1425	48.2	57.7	9.5	48.2	57.07	8.87	8.87	93
8H	24 Sep	1500	57.7	67.2	9.5	57.7	67.15	9.45	9.45	99
9H	24 Sep	1530	67.2	76.7	9.5	67.2	76.60	9.40	9.40	99
10H	24 Sep	1600	76.7	86.2	9.5	76.7	86.11	9.41	9.41	99
11H	24 Sep	1635	86.2	95.7	9.5	86.2	94.49	8.29	8.29	87
12H	24 Sep	1705	95.7	105.2	9.5	95.7	104.61	8.91	8.91	94
13H	24 Sep	1750	105.2	113.1	7.9	105.2	113.07	7.87	7.87	100
				Total advanced (m):	113.1		Total recovered (m):	107.75		

DRF = drilling depth below rig floor, DSF = drilling depth below seafloor, CSF = core depth below seafloor. APC = advanced piston corer, XCB = extended core barrel, RCB = rotary core barrel. H = APC system, X = XCB system, numeric core type = drilled interval. NA = not applicable.

Table T2. XRD analysis of bulk samples, Site U1425.

Core, section, interval (cm)	Top depth CSF-A (m)	Smectite (counts)	Illite (counts)	Kaolinite + chlorite (counts)	Opal-A (counts)	Opal-CT (counts)	Quartz (counts)	K-feldspar (counts)	Plagioclase (counts)	Calcite (counts)	Halite (counts)	Pyrite (counts)	Dolomite (counts)
346-U1425B-													
1H-1, 78.0–79.0	0.78	248	503	397	16	0	4488	155	555	1401	482	87	0
2H-1, 59.0–60.0	9.39	232	509	425	17	0	5208	219	816	545	303	125	0
3H-2, 51.0–52.0	20.31	321	666	437	0	0	4377	300	598	2493	246	52	0
4H-2, 51.0–52.0	29.81	354	849	581	28	0	5211	259	721	0	273	130	0
5H-1, 78.0–79.0	38.08	146	483	348	32	0	4423	245	552	0	272	70	0
6H-3, 82.0–83.0	50.62	269	707	418	0	0	5251	292	759	631	191	0	0
7H-1, 129.0–130.0	57.59	398	957	606	0	0	5686	291	839	0	196	0	0
8H-1, 40.0–41.0	66.20	242	676	422	27	0	5711	228	723	0	197	0	0
9H-2, 21.0–22.0	77.01	269	661	419	1	0	5630	250	752	0	194	70	0
10H-1, 76.0–77.0	85.56	280	829	446	8	0	6131	229	874	0	183	0	0
11H-1, 53.0–54.0	94.83	94	298	206	162	0	2250	98	273	0	373	67	0
11H-7, 32.0–35.0	103.62	56	0	0	0	0	649	100	300	0	93	452	0
12H-1, 11.0–12.0	103.91	188	455	289	0	0	3806	150	514	0	272	0	0
13X-1, 7.0–9.0	104.67	220	0	0	0	0	328	0	44	0	0	0	4567
14H-1, 61.0–62.0	106.61	163	377	237	96	0	2798	122	334	0	336	92	0
17H-1, 74.0–75.0	118.54	120	195	156	85	0	2531	128	332	0	335	0	0
18H-1, 59.0–60.0	123.09	110	425	281	71	0	3448	148	464	0	331	76	0
19H-1, 59.0–60.0	127.79	157	301	251	46	0	2898	212	429	0	313	100	0
20H-1, 36.0–37.0	132.26	125	257	163	146	0	2448	125	307	0	290	152	0
21H-1, 59.0–60.0	137.19	100	320	171	189	0	2186	128	305	0	391	116	0
22H-1, 49.0–50.0	146.59	107	247	185	237	0	1484	106	180	0	478	137	0
23H-1, 59.0–60.0	156.19	72	225	166	68	0	2875	141	345	0	321	68	0
24H-1, 49.0–50.0	165.59	116	244	151	175	0	2219	126	268	0	376	90	0
25H-1, 128.0–129.0	175.88	61	162	112	201	0	1614	114	159	0	417	136	0
26H-2, 109.0–110.0	186.69	94	306	200	165	0	2081	112	238	0	362	144	0
27H-2, 20.0–21.0	195.30	82	267	178	140	0	2831	157	350	0	350	130	0
28H-2, 128.0–129.0	205.88	0	197	125	161	0	1956	100	195	0	286	128	0
29H-1, 122.0–123.0	212.82	157	334	157	59	0	3448	150	345	0	195	145	0
30H-1, 99.0–100.0	222.09	91	198	120	148	0	2265	0	307	0	275	105	0
32X-1, 130.0–131.0	231.90	55	174	106	195	0	1989	100	241	0	355	124	0
33H-1, 100.0–101.0	235.30	106	282	187	91	0	2797	130	317	0	263	168	0
34H-2, 140.0–141.0	246.70	136	206	80	83	0	2018	170	304	0	297	160	0
35H-1, 50.0–51.0	253.80	87	201	91	46	0	2495	164	351	0	195	165	0
36H-2, 100.0–101.0	264.36	92	139	95	145	0	2000	140	307	0	239	222	0
37H-1, 40.0–41.0	267.90	100	176	105	73	0	2305	130	327	0	227	178	0
38H-2, 82.0–83.0	274.50	94	218	94	75	0	2385	149	349	0	214	156	0
39H-1, 101.0–102.0	277.91	100	151	109	46	0	2719	184	395	0	151	190	0
40X-1, 87.0–88.0	282.47	109	163	78	77	0	2568	150	409	0	179	136	0
41H-1, 100.0–101.0	285.90	50	276	120	100	0	2594	170	354	0	260	195	0
42H-3, 58.0–59.0	293.18	50	241	76	79	0	2377	148	297	0	219	257	0
43H-1, 59.0–60.0	294.89	80	263	124	81	0	2593	138	370	0	254	171	0
44H-1, 39.0–40.0	299.39	0	147	64	241	0	1385	107	205	0	338	79	0
45H-1, 59.0–60.0	304.29	60	145	74	114	0	2264	144	366	0	193	136	0
46H-2, 63.0–64.0	310.53	92	195	109	129	0	2428	150	371	0	194	253	0
47H-1, 59.0–60.0	313.69	125	248	171	54	0	2699	170	407	0	184	254	0
48H-1, 59.0–60.0	318.39	0	108	69	255	0	1193	100	148	0	385	142	0
49H-1, 69.0–70.0	323.19	78	160	67	198	0	1466	126	212	0	304	245	0
50H-3, 49.0–50.0	330.69	172	263	97	54	0	2527	170	483	0	115	174	0
51H-1, 71.0–72.0	332.61	136	187	98	119	0	2470	125	323	0	230	77	0
52H-1, 59.0–60.0	337.19	100	215	88	92	0	2275	184	383	0	148	129	0
52H-1, 90.0–91.0	337.50	150	279	96	57	0	2688	199	419	0	130	122	0
53H-1, 67.0–68.0	341.97	156	247	126	183	0	2576	176	390	0	78	0	0
54H-1, 39.0–40.0	346.39	157	333	190	157	0	2938	180	424	0	67	126	0
55X-1, 46.0–47.0	351.16	246	236	111	108	0	2604	0	437	0	45	115	0
54H-CC, 0.0–1.0	351.20	80	392	91	107	0	2816	180	429	0	80	129	0
56X-1, 30.0–31.0	359.00	241	176	75	170	0	2509	0	413	0	0	188	0
55X-CC, 0.0–5.0	360.22	59	377	94	247	0	2376	0	380	0	102	289	0
56X-CC, 0.0–2.0	366.02	0	0	0	0	0	0	0	0	0	0	0	726
56X-CC, 0.0–5.0	366.02	68	348	64	94	0	2645	0	409	0	125	255	0
57X-1, 66.0–67.0	369.06	0	298	0	149	0	2254	0	384	0	0	232	0
58X-CC, 0.0–5.0	378.35	0	178	0	0	1686	1719	0	366	0	50	168	0
59X-CC, 0.0–2.0	394.51	0	80	0	0	2443	916	0	204	0	0	140	0
60H-CC, 32.0–37.0	402.45	255	129	39	0	1160	1811	0	589	0	160	134	0

Table T3. Visible tephra layers thicker than 0.5 cm, Hole U1425B.

Core, section, interval (cm)	Thickness (cm)	Color	Occurrence
346-U1425B-			
1H-2, 33–41	8.0	Gray	Layered
1H-2, 141–147	1.0	Gray	Layered
1H-5, 137–144	7.0	Dark gray	Layered
2H-2, 57–58	1.0	Dark gray	Layered
2H-3, 34–35	1.0	Light gray	Layered
2H-3, 54–54.5	0.5	Gray	Layered
2H-4, 46–51	5.0	Gray	Layered
2H-4, 96.5–97	0.5	Light gray	Layered
2H-5, 65.5–66	0.5	Light gray	Layered
2H-5, 100.5–101	0.5	Dark gray	Layered
2H-5, 116.5–117	0.5	Dark gray	Layered
2H-7, 55–58	1.0	Dark gray	Layered
3H-1, 4.5–7	0.5	Brownish gray	Layered
3H-1, 45–46	1.0	Gray	Layered
3H-2, 43.5–44.5	1.0	Light gray	Layered
3H-3, 18.7–19.2	0.5	Light gray	Layered
3H-3, 74.5–75	0.5	Light gray	Layered
3H-4, 33.5–36.5	3.0	Light gray	Layered
3H-5, 17.5–18.5	1.0	Dark gray	Layered
3H-5, 99–100.5	1.5	Gray	Layered
3H-6, 51.5–52	0.5	Gray	Layered
4H-1, 37–37.7	0.7	White	Layered
4H-1, 103–110.7	7.7	Light gray	Layered
4H-1, 141.8–142.5	0.7	Light gray	Layered
4H-2, 29.2–30.4	1.2	Light gray	Layered
4H-2, 64.3–65.1	0.8	Light gray	Layered
4H-4, 106.5–108	1.5	Light gray	Layered
4H-4, 111.1–111.7	0.6	Light gray	Layered
4H-4, 134–134.5	0.5	Light gray	Layered
4H-4, 135.2–135.8	0.6	Light gray	Layered
4H-6, 117.7–118.5	0.8	White	Layered
4H-7, 8.3–34.7	26.4	Gray	Layered
5H-1, 48.3–53.5	5.2	Light gray	Layered
5H-1, 87.4–90	2.6	Gray	Layered
5H-1, 101.5–102.5	1.0	White	Layered
5H-2, 79.3–80.3	1.0	White	Layered
5H-2, 85.3–87.8	2.5	White	Layered
5H-2, 104.8–106.5	1.7	White	Layered
5H-3, 88.2–88.7	0.5	Light gray	Layered
5H-3, 133–133.7	0.7	White	Layered
5H-4, 32–32.7	0.7	White	Layered
5H-5, 0–4	4.0	Gray	Layered
5H-5, 138.3–140	1.7	Light brownish white	Layered
5H-5, 146–147	1.0	Light gray	Layered
5H-6, 115.2–119	3.8	White	Layered
6H-2, 42.4–43	0.6	Gray	Layered
6H-2, 115.9–116.5	0.6	Gray	Layered
6H-4, 89.2–90.9	1.7	White	Layered
6H-6, 18.5–21.5	3.0	Light gray	Layered
7H-2, 9–27	18.0	White	Layered
8H-6, 118–122.5	4.5	Light gray	Layered
9H-6, 19–26	0.5	Dark gray	Layered
10H-2, 87.8–89.3	1.5	Gray	Layered
11H-6, 140.5–141.5	1.0	Light gray	Layered
17H-2, 31–33.5	2.5	Gray	Layered
25H-1, 109–116.2	7.2	Dark gray	Layered
25H-1, 118.5–119	0.5	Dark gray	Layered
28H-6, 61.3–98	36.7	Gray	Layered
30H-1, 71–72	0.5	Light gray	Layered
32H-1, 3–8.5	5.5	Light gray	Layered
32H-1, 12.5–16	3.0	Light gray	Layered
32H-1, 33–40	7.0	Light gray	Layered
32H-1, 112–119	0.5	Gray	Patched
32H-1, 126–129	3.0	Gray	Patched
32H-2, 6–14	1.0	Light gray	Patched
32H-2, 44–46	2.0	Light gray	Layered
32H-2, 56–58	2.0	Light gray	Patched
32H-2, 66–76	1.0	Light gray	Patched
35H-1, 135–136	0.5	Light gray	Patched
35H-2, 4.5–6.2	1.7	Light gray	Layered
35H-2, 6.5–9.5	1.0	Light gray	Patched
36H-4, 59–60	1.0	Light gray	Layered

Table T4. Preservation and estimated abundance of diatoms, Hole U1425B. (Continued on next page.)

Core, section, interval (cm)	Top depth CSF-A (m)	Bottom depth CSF-A (m)	Preservation	Abundance	*Actinocyclus curvatulus*	*Actinocyclus oculatus*	*Actinoptychus senarius*	*Aulacoseira* spp.	*Azpeitia endoi*	*Chaetoceros* spp. and similar spores	*Coscinodiscus marginatus*	*Cyclotella striata*	*Denticulopsis dimorpha*	*Denticulopsis katayamae*	*Denticulopsis praelauta*	*Fragilariopsis doliolus*	*Neodenticula kamtschatica*	*Neodenticula koizumii*	*Neodenticula seminae*	*Odontella aurita*	*Paralia sulcata*	*Proboscia curvirostris*	*Rhizosolenia barboi*	*Rhizosolenia styliformis*	*Rouxia californica*	*Shionodiscus oestrupii*	*Stephanopyxis turris*	*Stephanopyxis* spp.	*Thalassionema nitzschioides*	*Thalassionema schraderi*	*Thalassiosira antiqua*	*Thalassiosira eccentrica*	*Thalassiosira jacksonii*	*Thalassiosira leptopus*	*Thalassiosira manifesta*	*Thalassiosira nidulus*	*Thalassiosira pacifica*	*Thalassiosira trifulta*	*Thalassiothrix frauenfeldii*	Phytolith abundance	Comments
346-U1425B-																																									
1H-CC	8.77	8.82	M	R		R				R																														B	
2H-CC	18.58	18.63	G	F	F				R	F							R				R	R				C			A											C	
3H-CC	27.04	27.09	G	R			R															R				R													R	C	
4H-CC	37.58	37.63	G	C						A		R					R	R	R		R								A										R	R	
5H-CC	46.96	47.01	G	R						R																														R	
6H-CC	56.53	56.58	G	A	R				R	A		R			R				R		C			R		F			A											A	
7H-CC	66.22	66.27	G	F						A											F					R			F											A	
8H-CC	75.58	75.63	G	C						A					R	R	R	C			R					F			A							R				A	
9H-CC	85.12	85.17	G	D	F	A			R	C	A							A	R		R			R		F	R	F	A											C	
10H-CC	94.77	94.82	G	A		F				C	F				R		A	F								C		R	A							R				A	
11H-CC	103.99	104.04	G	C		R				F	A				R		A	R											R											A	
12H-1, 76–81	104.56	104.61	G	A						C	F				F		A	C		R			R			F		F	A											C	
13X-CC	106.26	106.31	G	D		R		F		C	A						A						R			F		F	A										F	R	
14H-CC	115.76	115.81	G	A						C	R				R		C				R					R			C			R								A	
15H-CC	115.50	115.53	G	A		A	F			A	R						C				F					R		F	F			R								A	
16X-CC	116.92	116.96	G	C							R				R		C				F			R					F										R	C	
17H-CC	122.49	122.54	G	A						F	A						C				F					C		F	F					R						A	
18H-CC	127.28	127.33	G	A			R				A				R		A				R			R		F	R													A	
19H-CC	131.17	131.23	G	F	R					R	R						F												R											R	
20H-CC	136.66	136.72	G	C							R						A				F					R		F			R							R		F	
21H-CC	146.33	146.38	G	A							A						A							R				F	F											R	
22H-CC	155.99	156.04	G	A						R	F						A									F		F	F											A	
23H-CC	165.42	165.47	G	A							A						A				R			R		F		F	R				C			R				A	
24H-CC	174.99	175.04	G	C	R						R						A						R			F		F	F											R	
25H-CC	184.47	184.52	G	D							A						A							C		R		F	A				C							F	
26H-CC	194.05	194.10	G	A																													F							C	
27H-CC	203.37	203.42																																							Fine volcanic glass
28H-6, 98–103	211.58	211.63																																							Fine volcanic glass
29H-CC	221.26	221.31	G	C			R			A	A																													R	
30H-CC	230.94	230.99	G	A			R			R	A																R			R										C	
32X-CC	235.46	235.51	G	A	R		A			F	A										R		R				F			R										A	
33H-CC	243.98	244.03	G	C						R													R							A										A	
34H-CC	254.80	254.85	G	C			R			R	R										F									C										C	
35H-CC	262.68	262.73	G	F	F																				R															R	
36H-CC	267.72	267.77	G	C			F			C	F												R		F				C											A	
37H-CC	272.44	272.49	G	C			F			F													R		F				C											A	
38H-CC	277.08	277.13	G	F			F			F	C												R						R	R										C	
39H-CC	281.91	281.97	G	C			F			F	F														F				F											A	
40X-CC	288.19	288.24	G	C			A			R											R		F		A				F											A	

Table T4 (continued).

Core, section, interval (cm)	Top depth CSF-A (m)	Bottom depth CSF-A (m)	Preservation	Abundance	*Actinocyclus curvatulus*	*Actinocyclus oculatus*	*Actinoptychus senarius*	*Aulacoseira* spp.	*Azpeitia endoi*	*Chaetoceros* spp. and similar spores	*Coscinodiscus marginatus*	*Cyclotella striata*	*Denticulopsis dimorpha*	*Denticulopsis katayamae*	*Denticulopsis praelauta*	*Fragilariopsis doliolus*	*Neodenticula kamtschatica*	*Neodenticula koizumii*	*Neodenticula seminae*	*Odontella aurita*	*Paralia sulcata*	*Proboscia curvirostris*	*Rhizosolenia barboi*	*Rhizosolenia styliformis*	*Rouxia californica*	*Shionodiscus oestrupii*	*Stephanopyxis turris*	*Stephanopyxis* spp.	*Thalassionema nitzschioides*	*Thalassionema schraderi*	*Thalassiosira antiqua*	*Thalassiosira eccentrica*	*Thalassiosira jacksonii*	*Thalassiosira leptopus*	*Thalassiosira manifesta*	*Thalassiosira nidulus*	*Thalassiosira pacifica*	*Thalassiosira trifulta*	*Thalassiothrix frauenfeldii*	Phytolith abundance	Comments
41H-CC	289.80	289.85	G	C			A			F	F												R		F				R											A	
42H-CC	294.53	294.58	G	A	F		A			F	R										R		R		C				A											F	
43H-CC	299.19	299.24	G	C			A			R	R			R											C				R											A	
44H-CC	304.00	304.05	G	C	R		C			F	F			F							R				A				C											A	
45H-CC	308.71	308.76	G	A	R		A			F				F							F								R						F					A	
46H-CC	313.32	313.37	G	C			A			F				C							R								C						R					A	
47H-CC	318.05	318.10	G	C						F				A																										R	
48H-CC	322.69	322.74	G	C	R	R	C			F	F			A							R								C						R					A	
49H-CC	327.42	327.47	G	A			C			C	A			A											A				A						R					A	
50H-CC	332.15	332.20	G	C			A	R		F	F			A							C								F								R			A	
51H-CC	336.86	336.91	G	C						F	F		A	A											R				A											A	
52H-CC	341.52	341.57		B																																					
53H-CC	346.30	346.35		B																																					
54H-CC	351.20	351.25		B																																					
55X-CC	360.22	360.27		B																																					
56X-CC	366.02	366.07		B																																					
57X-CC	369.47	369.52		B																																					
58X-CC	378.35	378.40		B																																					
59X-CC	394.51	394.53		B																																					
60H-CC	402.45	402.50		B																																					
61X-CC	403.83	403.87		B																																					

Preservation: G = good, M = moderate. Abundance: D = dominant, A = abundant, C = common, F = few, R = rare, B = barren, ? = does not allow an assessment of this property. Shaded intervals = barren.

Table T5. Microfossil bioevents, Site U1425.

Core, Section, interval (cm)		Event		Age	Depth CSF-A (m)				Depth CCSF-A (m)			
Top	Bottom	type	Bioevents and epoch boundaries	(Ma)	Top	Bottom	Midpoint	±	Top	Bottom	Midpoint	±
346-U1425B-	346-U1425B-											
1H, mudline	1H-CC	R	LO *Lychnocanoma sakaii*	0.05	0	8.77	4.39	4.39	0.00	8.77	4.39	4.39
1H-5W, 11	2H-2W, 59	CN	FO *Emiliania huxleyi*	0.29	6.11	10.89	8.50	2.39	6.11	11.45	8.78	2.67
1H-CC	2H-CC	R	LO *Spongodiscus* sp.	0.29	8.77	18.58	13.68	4.91	8.77	19.14	13.95	5.18
3H-1W, 108–109	3H-2W, 46–47	CN	LO *Pseudoemiliania lacunosa*	0.44	19.38	20.26	19.82	0.44	20.96	21.84	21.40	0.44
3H-CC	4H-CC	PF	LO *Neogloboquadrina kagaensis* group	0.7	27.04	37.58	32.31	5.27	28.62	39.68	34.15	5.53
4H-CC	5H-CC	PF	X *Neogloboquadrina pachyderma* (D to S)	1.14–1.24	37.58	46.96	42.27	4.69	39.68	49.37	44.53	4.84
5H-CC	6H-CC	R	LO *Axoprunum acquilonium*	1.2–1.7	46.96	56.53	51.75	4.79	49.37	60.63	55.00	5.63
6H-5W, 123–124	6H-CC	CN	LO *Calcidiscus macintyrei*	1.6	54.03	56.53	55.28	1.25	58.13	60.63	59.38	1.25
7H-CC	8H-CC	D	LO *Neodenticula koizumii*	2.0	66.22	75.58	70.90	4.68	70.90	81.41	76.15	5.26
Pliocene/Pleistocene boundary				2.59								
7H-CC	8H-CC	R	LO *Hexacontium parviakitaensis*	2.7	66.22	75.58	70.90	4.68	70.90	81.41	76.15	5.26
8H-CC	9H-CC	R	FO *Cycladophora davisiana*	2.7	75.58	85.12	80.35	4.77	81.41	91.77	86.59	5.18
9H-CC	10H-CC	D	LO *Neodenticula kamtschatica*	2.7	85.12	94.77	89.95	4.83	91.77	99.04	95.41	3.64
12H-1, 76–81	13X-CC	PF	FO *Globorotalia praeinflata*	3.3	104.56	106.26	105.41	0.85	109.60	111.54	110.57	0.97
12H-1, 76–81	13X-CC	D	FO *Neodenticula koizumii*	3.4–3.9	104.56	106.26	105.41	0.85	109.60	111.54	110.57	0.97
16X-CC	17H-CC	PF	LO *Globorotalia ikebei*	4.3	116.92	122.49	119.71	2.79	122.30	126.95	124.63	2.33
17H-CC	18H-CC	PF	FO *Globorotalia ikebei*	4.7–4.8	122.49	127.28	124.89	2.40	126.95	132.07	129.51	2.56
17H-CC	18H-CC	R	FO *Hexacontium parviakitaensis*	3.9–4.3	122.49	127.28	124.89	2.40	126.95	132.07	129.51	2.56
18H-CC	19H-CC	R	LO *Dictyophimus bullatus*	3.9–4.3	127.28	131.17	129.23	1.94	132.07	136.96	134.52	2.45
20H-CC	21H-CC	R	FO *Dictyophimus bullatus*	4.4	136.66	146.33	141.50	4.84	143.23	152.05	147.64	4.41
21H-CC	22H-CC	R	RI *Siphocampe arachnea* group	4.71	146.33	155.99	151.16	4.83	152.05	162.77	157.41	5.36
21H-CC	22H-CC	R	LO *Lipmanella redondoensis*	5.06	146.33	155.99	151.16	4.83	152.05	162.77	157.41	5.36
22H-CC	23H-CC	D	LO *Thalassiosira jacksonii*	4.81	155.99	165.42	160.71	4.72	162.77	172.54	167.66	4.88
24H-CC	25H-CC	R	FO *Larcopyle pylomaticus*	5.3	174.99	184.47	179.73	4.74	182.94	192.46	187.70	4.76
Miocene/Pliocene boundary				5.33								
25H-CC	26H-CC	R	LO *Lychnocanoma parallelipes*	6.1	184.47	194.05	189.26	4.79	192.46	203.61	198.03	5.57
29H-CC	30H-CC	R	RI *Lithelius barbatus*	7.0	221.26	230.94	226.10	4.84	230.86	239.53	235.20	4.34
29H-CC	30H-CC	R	FO *Axoprunum acquilonium*	7.0	221.26	230.94	226.10	4.84	230.86	239.53	235.20	4.34
32X-CC	33H-CC	D	LO *Thalassiosira schraderi*	7.67	235.46	243.98	239.72	4.26	244.53	253.28	248.90	4.38
33H-CC	34H-CC	R	LO *Cycladophora nakasekoi*	7.4	243.98	254.80	249.39	5.41	253.28	264.04	258.66	5.38
33H-CC	34H-CC	R	FO *Lychnocanoma parallelipes*	7.4	243.98	254.80	249.39	5.41	253.28	264.04	258.66	5.38
45H-CC	46H-CC	D	LO *Denticulopsis katayamae*	8.7	308.71	313.32	311.02	2.31	320.84	325.42	323.13	2.29
47H-CC	48H-CC	R	LCO *Lychnocanoma magnacornuta*	9.1	318.05	322.69	320.37	2.32	330.05	335.74	332.89	2.85
50H-CC	51H-CC	D	LO *Denticulopsis dimorpha*	9.3	332.15	336.86	334.51	2.36	346.77	352.39	349.58	2.81
58X-CC	60H-CC	R	FO *Cycladophora nakasekoi*	10.1	378.35	402.45	390.40	12.05	393.88	417.98	405.93	12.05
58X-CC	60H-CC	R	LO *Eucyrtidium inflatum*	11.8	378.35	402.45	390.40	12.05	393.88	417.98	405.93	12.05
346-U1425D-	346-U1425D-											
57H-CC	58H-CC	R	FO *Lychnocanoma magnacornuta*	10.1	375.56	379.63	377.60	2.03	390.96	395.03	393.00	2.03
58H-CC	59H-CC	R	LO *Eucyrtidium inflatum*	11.8	379.63	384.77	382.20	2.57	395.03	400.17	397.60	2.57
60H-CC	61H-CC	R	RD *Cyrtocapsella tetrapera*	12.6	389.23	390.67	389.95	0.72	404.63	406.07	405.35	0.72

R = radiolarian, F = foraminifer, CN = calcareous nannofossil, D = diatom. LO = last occurrence, LCO = last common occurrence, FO = first occurrence, RI = rapid increase, RD = rapid decrease. D to S = dextral to sinistral.

Table T6. Preservation and estimated abundance of calcareous nannofossils, Site U1425. (Continued on next two pages.)

Core, section, interval (cm)	Top depth CSF-A (m)	Bottom depth CSF-A (m)	Preservation	Abundance	*Braarudosphaera bigelowii*	*Calcidiscus leptoporus*	*Calcidiscus macintyrei*	*Coccolithus pelagicus*	*Emiliania huxleyi*	*Gephyrocapsa caribbeanica*	*Gephyrocapsa margerelii/muellerae*	*Gephyrocapsa oceanica* s.s.	*Gephyrocapsa omega*	*Gephyrocapsa* spp. (>4 µm)	*Gephyrocapsa* spp. large (>5.5 µm)	*Gephyrocapsa* spp. small (<4 µm)	*Helicosphaera carteri*	*Pontosphaera* spp.	*Pseudoemiliania lacunosa*	*Reticulofenestra minuta*	*Reticulofenestra minutula*	*Reticulofenestra pseudoumbilica*	*Reticulofenestra* spp.	*Umbilicosphaera sibogae*
346-U1425B-																								
1H-1, 53	0.53	0.53	M	R								F				F								
1H-4, 63	5.13	5.13	M	F	R			R	A	R			F			R		R						
1H-5, 11	6.11	6.11	P	F				C	A			F				C								
1H-CC	8.77	8.82		B																				
2H-2, 59	10.89	10.89	P	F				F						F		C								
2H-4, 124	14.54	14.54	P	A												D								
2H-6, 76	17.06	17.06	P	F				R								C	R							
2H-CC	18.58	18.63		B																				
3H-1, 108–109	19.38	19.39	G	D				C								D								
3H-2, 46–47	20.26	20.27	M	F				C		F		F				C	R		F	F	F			R
3H-3, 78	22.08	22.08	M	R												F								
3H-4, 60	23.40	23.40	G	D				C								D								
3H-6, 60	26.40	26.40	P	R				R		R						R								
3H-CC	27.04	27.09	M	A				C		R		F		F		C		R						
4H-1, 112–113	28.92	28.93	P	F		R		C		R	R	F	R			F					R			
4H-1, 57–58	28.37	28.38	P	R				R		R														
4H-1, 83–84	28.63	28.64	M	F				F				C	R	F	R	C			R				R	
4H-1, 9–10	27.89	27.90	P	R				R		R		R				R			R					
4H-2, 25–26	29.55	29.56	M	F				C		R		F		F		R							R	
4H-3, 0–1	30.80	30.81	P	R				R																
4H-3, 48–49	31.28	31.29	M	D				F								D								
4H-3, 76–77	31.56	31.57	P	R				F								C		R						
4H-5, 118–119	34.98	34.99	P	R				F								F								
4H-6, 9–10	35.39	35.40	G	A	R											D								
4H-6, 22–23	35.52	35.53	M	D	R			R								D								
4H-CC	37.58	37.63		B																				
5H-2, 25–26	39.05	39.06		B																				
5H-4, 40–41	42.20	42.21	P	R	R																			
5H-7 33–34	46.45	46.46	M	R				R														*		
5H-CC	46.96	47.01	M	F				C								R								
6H-3, 45–46	50.25	50.26	P	R				R																
6H-5, 123–124	54.03	54.04	M	R						R		R		R										
6H-CC	56.53	56.58	M	C		C	C	C		R						R					R			
7H-6, 98–99	64.78	64.79		B																				
7H-CC	66.22	66.27		B																				
8H-3, 30–31	69.10	69.11		B																				
8H-CC	75.58	75.63		B																				
9H-3, 90–91	79.20	79.21		B																				
9H-CC	85.12	85.17		B																				
10H-2, 72–73	87.02	87.03		B																				
10H-CC	94.77	94.82		B																				
11H-CC	103.99	104.04		B																				
12H-1, 76–81	104.56	104.61	P	F				R			F					A								
13X-CC	106.26	106.31	P	R												R								
14H-CC	115.76	115.81	P	R												F								
15H-CC	115.50	115.53	M	R												F								
16X-CC	116.92	116.96		B																				
17H-CC	122.49	122.54		B																				
18H-CC	127.28	127.33		B																				
19H-CC	131.17	131.23		B																				
20H-CC	136.66	136.72		B																				
21H-CC	146.33	146.38		B																				
22H-CC	155.99	156.04		B																				
22H-CC	165.42	165.00																						
24H-CC	174.99	175.04		B																				
25H-CC	184.47	184.52		B																				

Table T6 (continued). (Continued on next page.)

Core, section, interval (cm)	Top depth CSF-A (m)	Bottom depth CSF-A (m)	Preservation	Abundance	*Braarudosphaera bigelowii*	*Calcidiscus leptoporus*	*Calcidiscus macintyrei*	*Coccolithus pelagicus*	*Emiliania huxleyi*	*Gephyrocapsa caribbeanica*	*Gephyrocapsa margerelii/muellerae*	*Gephyrocapsa oceanica* s.s.	*Gephyrocapsa omega*	*Gephyrocapsa* spp. (>4 µm)	*Gephyrocapsa* spp. large (>5.5 µm)	*Gephyrocapsa* spp. small (<4 µm)	*Helicosphaera carteri*	*Pontosphaera* spp.	*Pseudoemiliania lacunosa*	*Reticulofenestra minuta*	*Reticulofenestra minutula*	*Reticulofenestra pseudoumbilica*	*Reticulofenestra* spp.	*Umbilicosphaera sibogae*
26H-CC	194.05	194.10	P	R				R																
27H-CC	203.37	203.42		B																				
28H-6	211.58	211.63	M	R												R								
29H-CC	221.26	221.31		B																				
30H-CC	230.94	230.99		B																				
32X-CC	235.46	235.51		B																				
33H-CC	243.98	244.03		B																				
34H-CC	253.40	253.45		B																				
35H-CC	262.68	262.73		B																				
36H-CC	267.72	267.77		B																				
37H-4, 23–24	271.84	271.85		B																				
37H-CC	272.44	272.49		B																				
38H-3, 33–34	275.51	275.52		B																				
38H-3, 5–6	275.23	275.24		B																				
38H-CC	277.08	277.13		B																				
39H-CC	281.91	281.97		B																				
40X-CC	288.19	288.24		B																				
41H-CC	289.80	289.85		B																				
42H-CC	294.53	294.58		B																				
43H-CC	299.19	299.24	P	R				R												F				
44H-CC	304.00	304.05		B																				
45H-CC	308.71	308.76		B																				
46H-CC	313.32	313.37		B																				
47H-CC	318.05	318.10		B																				
48H-CC	322.69	322.74		B																				
49H-CC	327.42	327.47		B																				
50H-CC	332.15	332.20		B																				
51H-CC	336.86	336.91		B																				
52H-CC	341.52	341.57		B																				
53H-CC	346.30	346.35		B																				
54H-CC	351.20	351.25		B																				
55X-CC	360.22	360.27		B																				
56X-CC	351.20	351.25		B																				
57X-CC	369.47	369.52		B																				
58X-CC	378.35	378.40		B																				
59X-CC	394.51	394.53		B																				
60X-CC	402.45	402.50		B																				
61X-CC	403.83	403.87		B																				
346-U1425D-																								
4H-2, 75	26.55	26.55	M	F				C		R	R	F		R		F					R			
4H-5, 75	31.05	31.05	G	D				C								D					C			
4H-6, 75	32.55	32.55	M	F		R		A		F		C		C		D					C		F	
13X-CC	113.80	113.85		B																				
14H-CC	118.39	118.43		B																				
15H-CC	127.96	128.01		B																				
16H-CC	137.70	137.75		B																				
18H-CC	149.34	149.39		B																				
19H-CC	158.62	158.67		B																				
59H-CC	384.77	384.82		B																				
60H-CC	389.23	389.28		B																				
61H-CC	390.67	390.72		B																				
62H-CC	393.51	393.56		B																				
63H-CC	397.66	397.71		B																				
64H-CC	401.28	401.33		B																				
65H-CC	404.42	404.47		B																				
66H-CC	408.02	408.07		B																				
67H-CC	408.86	408.91		B																				
69H-CC	414.11	414.16		B																				
70H-CC	415.10	415.11		B																				

Table T6 (continued).

Core, section, interval (cm)	Top depth CSF-A (m)	Bottom depth CSF-A (m)	Preservation	Abundance	*Braarudosphaera bigelowii*	*Calcidiscus leptoporus*	*Calcidiscus macintyrei*	*Coccolithus pelagicus*	*Emiliania huxleyi*	*Gephyrocapsa caribbeanica*	*Gephyrocapsa margerelii/muellerae*	*Gephyrocapsa oceanica* s.s.	*Gephyrocapsa omega*	*Gephyrocapsa* spp. (>4 µm)	*Gephyrocapsa* spp. large (>5.5 µm)	*Gephyrocapsa* spp. small (<4 µm)	*Helicosphaera carteri*	*Pontosphaera* spp.	*Pseudoemiliania lacunosa*	*Reticulofenestra minuta*	*Reticulofenestra minutula*	*Reticulofenestra pseudoumbilica*	*Reticulofenestra* spp.	*Umbilicosphaera sibogae*
71X-CC	415.32	415.33		B																				
72H-1	430.70	430.95		B																				

Preservation: G = good, M = moderate, P = poor. Abundance: D = dominant, A = abundant, C = common, F = few, R = rare, B = barren. Shaded intervals = barren.

Table T7. Preservation and estimated abundance of radiolarians, Site U1425. (Continued on next page.)

Core, section, interval (cm)	Top depth CSF-A (m)	Bottom depth CSF-A (m)	Preservation	Abundance	*Actinomma boreale*	*Actinomma leptodermum*	*Amphimelissa setosa*	*Axoprunum acquilonium*	*Carpocanarium papillosum*	*Ceratospyris borealis*	*Cornutella profunda*	*Cycladophora cornutoides*	*Cycladophora davisiana*	*Cycladophora funakawai*	*Cycladophora nakasekoi*	*Cycladophora sakaii*	*Cyrtocapsella tetrapera*	*Cyrtopera languncula*	*Dictyocoryne profunda*	*Dictyocoryne truncatum*	*Dictyophimus bullatus*	*Eucyrtidium inflatum*	*Hexacontium akitaensis*	*Hexacontium parviakitaensis*	*Larcopyle polyacantha* group	*Larcopyle pylomaticus*	*Lithelius barbatus*	*Lychnocanoma magnacornuta*	*Lychnocanoma parallelipes*	*Lychnocanoma sakaii*	*Peripyramis circumtexta*	*Peripyramis woodringi*	*Phorticium pylonium* group	*Siphocampe arachnea* group	*Sphaeropyle langii*	*Sphaeropyle robusta*	*Spongodiscus* sp.	*Spongopyle osculosa*	*Stichocorys delmontensis*	*Stichocorys peregrina*	*Stichocorys* spp. group	*Stichocorys wolffii*	*Stylatractus universus*	*Stylochlamydium venustum*	*Stylochlamydium bensoni*	*Thecosphaera japonica*	*Thecosphaera pseudojaponica*	*Theocorys redondoensis*
346-U1425B-																																																
1H-CC	8.77	8.82	P	R						R			F					P							F					F																		
2H-CC	18.58	18.63	M	R			F			C			C			P									F	F							P	P			R				R							
3H-CC	27.04	27.09	M	C						A			A																					P			A											
4H-CC	37.58	37.63	G	A						F			A						P	F					C								C	F														
5H-CC	46.96	47.01	G	C						A																																						
6H-CC	56.53	56.58	M	C						C			F							R					C						A																	
7H-CC	66.22	66.27	P	R				A					F													R						C		P														
8H-CC	75.58	75.63	M	C				C		C		P	F											R		F						F		F	P											R		
9H-CC	85.12	85.17	G	A	P	P		R		C	P							P			P			F		C								R										F		F	P	
10H-CC	94.77	94.82	G	A							F					F								F		R					P			P												F	P	
11H-CC	103.99	104.04	G	C				C		F	F													C	P	P						F		F	P			P								F	F	
12H-1, 76–81	104.56	104.61	G	A				C			P					C		P						F	F	C						P		F	R			C						F		F	P	
13X-CC	106.26	106.31	G	A				F			R					R								C		C								F				P						F		F		
14H-CC	115.76	115.81	G	A				F			F					C								C		F					P	P		F	R			R						F		R		
15H-CC	115.50	115.53	G	A				P			P					F								C								P		P										C		F	R	
16X-CC	116.92	116.96	G	A				C			F					C								C		R						R	P	F	F									R		F		
17H-CC	122.49	122.54	G	A				F								C								R											F			P						F		R		
18H-CC	127.28	127.33	G	A				C			R					C									P							P	P	C							P					F	F	
19H-CC	131.17	131.23	G	C				P								C					F					F								C														
20H-CC	136.66	136.72	G	C				P			F					C					R				F									F							P					R		
21H-CC	146.33	146.38	G	A				R			R					C										C								A				F								P		
22H-CC	155.99	156.04	G	A				P			F					F										F						R		F					P	F	P			F		P		P
23H-CC	165.42	165.47	G	A				R			F					C									P	F																		A			P	
24H-CC	174.99	175.04	G	A				R			C				P	F		R							P	P												F						C				R
25H-CC	184.47	184.52	G	A				P			P					C		P									F					P												P				P
26H-CC	194.05	194.10	G	A				P			C					C											F		P									C						C		P		C
27H-CC	203.37	203.42	G	C				F			C					F		P									F					P												C				R
28H-6, 98–103	211.58	211.63	G	R												C											R		R		P			R														
29H-CC	221.26	221.31	G	A				P			F					C											A		C			R						R	R	F	F							R
30H-CC	230.94	230.99	G	A				R	P		P					A											R		F						P						P							F
32X-CC	235.46	235.51	G	A					P		P	P				A											R		F										P									
33H-CC	243.98	244.03	G	A							F	P				C													F				P	F		F			P		P			C				F
34H-CC	253.40	253.46	M	C					R		R			F	A	R																P		P					F		F			R				F
35H-CC	262.68	262.73	G	A					R		F				C										P																							F
36H-CC	267.72	267.77	G	A					P		F				A			R																														
37H-CC	272.44	272.49	G	C					P						A																														C			P
38H-CC	277.08	277.13	G	A					A		F				A																								R		F				F			F
39H-CC	281.91	281.97	G	A					C		F				A																																	F
40X-CC	288.19	288.24	G	A					C		C				A																								F		C			P				P
41H-CC	289.80	289.85	G	A											A																							F	F		A	P						F
42H-CC	294.53	294.58	G	A					F		F	P			A																																	P

Table T7 (continued).

Core, section, interval (cm)	Top depth CSF-A (m)	Bottom depth CSF-A (m)	Preservation	Abundance	*Actinomma boreale*	*Actinomma leptodermum*	*Amphimelissa setosa*	*Axoprunum acquilonium*	*Carpocanarium papillosum*	*Ceratospyris borealis*	*Cornutella profunda*	*Cycladophora cornutoides*	*Cycladophora davisiana*	*Cycladophora funakawai*	*Cycladophora nakasekoi*	*Cycladophora sakaii*	*Cyrtocapsella tetrapera*	*Cyrtopera languncula*	*Dictyocoryne profunda*	*Dictyocoryne truncatum*	*Dictyophimus bullatus*	*Eucyrtidium inflatum*	*Hexacontium akitaensis*	*Hexacontium parviakitaensis*	*Larcopyle polyacantha* group	*Larcopyle pylomaticus*	*Lithelius barbatus*	*Lychnocanoma magnacornuta*	*Lychnocanoma parallelipes*	*Lychnocanoma sakaii*	*Peripyramis circumtexta*	*Peripyramis woodringi*	*Phorticium pylonium* group	*Siphocampe arachnea* group	*Sphaeropyle langii*	*Sphaeropyle robusta*	*Spongodiscus* sp.	*Spongopyle osculosa*	*Stichocorys delmontensis*	*Stichocorys peregrina*	*Stichocorys* spp. group	*Stichocorys wolffii*	*Stylatractus universus*	*Stylochlamydium venustum*	*Stylochlamydium bensoni*	*Thecosphaera japonica*	*Thecosphaera pseudojaponica*	*Theocorys redondoensis*
43H-CC	299.19	299.24	G	A					F		F	F			A			R																					F		C							P
44H-CC	304.00	304.05	G	A					F		F	F			A																	R						F	P		F							F
45H-CC	308.71	308.76	G	A					F		F	F		F	A										F						P							F										F
46H-CC	313.32	313.37	M	A					F		P				C										A														P									C
47H-CC	318.05	318.10	G	F							P					P									F																							
48H-CC	322.69	322.74	G	F							P	P													F			F										P										F
49H-CC	327.42	327.47	G	F					P		P				C										C													P										
50H-CC	332.15	332.20	G	A							P				A													P																				
51H-CC	336.86	336.91	M	C							F	P			A										F			P			P																	F
52H-CC	341.52	341.57	M	C											A													R											P		P							P
53H-CC	346.30	346.35	M	C					P		C				F										F			C										F	C		C							F
54H-CC	351.20	351.25	P	R					F		F				F										C			P										F										P
55X-CC	360.22	360.27	P	R					C		P				P													F												P	P							
56X-CC	366.02	366.07	P	R							P	P			F													P				P						F										
57X-CC	369.47	369.52	P	R											P																																	
58X-CC	378.35	378.40	P	R											P																										P							
59X-CC	394.51	394.53		B																																												
60H-CC	402.45	402.50	M	R													P					F			P													F	P		C		P					P
61X-CC	403.83	403.87	P	R					P																P																							
346-U1425D-																																																
57H-CC	375.56	375.61	P	R					R		P												R					F										R										F
58H-CC	379.63	379.68	P	R					R		R																											F			P							R
59H-CC	384.77	384.82	P	R							F											C																										C
60H-CC	389.23	389.28	P	R																		P																										P
61H-CC	390.67	390.72	P	R							P						A					F																										C
62H-CC	393.51	393.56	P	R							F											C																F										C
63H-CC	397.66	397.71	P	R													P					R			F									P					F		C							
64H-CC	401.28	401.33	P	R													A					P																					P					
65H-CC	404.42	404.47	P	R													C					R																										
66H-CC	408.02	408.07	P	R																																												
67H-CC	408.86	408.91	P	R													F								F																							P
69H-CC	414.11	414.16	P	R																																												
70H-CC	415.10	415.11		B																																												

Preservation: G = good, M = moderate, P = poor. Abundance: D = dominant, A = abundant, C = common, F = few, R = rare, P = present, B = barren. Shaded intervals = barren.

Table T8. Preservation and estimated abundance of planktonic foraminifers, Site U1425. (Continued on next two pages.)

Core, section, interval (cm)	Top depth CSF-A (m)	Bottom depth CSF-A (m)	Preservation	Abundance	% Planktonic foraminifers	*Globigerina bulloides*	*Globigerina umbilicata*	*Globigerina quinqueloba*	*Globigerina* sp.	*Globigerinita glutinata*	*Globigerinoides* sp.	*Globorotalia ikbei*	*Globorotalia praeinflata*	*Neogloboquadrina* cf. *dutertrei* (s)	*Neogloboquadrina* cf. *asanoi*	*Neogloboquadrina dutertrei*	*Neogloboquadrina incompta*	*Neogloboquadrina kagaensis* and *Neogloboquadrina inglei*	*Neogloboquadrina pachyderma*	*Neogloboquadrina pachyderma* (d)	*Neogloboquadrina pachyderma* (s)	*Neogloboquadrina* sp.	*Orbulina suturalis*	*Orbulina* sp.	*Orbulina universa*	Total number of planktonic foraminifers	Comment
346-U1425A-																											
1H, mudline	0.00	0.00	G	D		39	1									1				1	46					88	
1H-CC	9.76	9.81	G	D	99	18	1									1				1	22	1				44	
346-U1425B-																											
1H-CC	8.77	8.82	G	R	50	8		4											6	3	5					26	
2H-CC	18.58	18.63	M	A	100	15													7	4	32					58	
3H-CC	27.04	27.09	M	A	99	40	10	1								1			3		40	2				97	
4H-CC	37.58	37.63	M	A	99	18		1										6	6		54	2				87	
5H-CC	46.96	47.01	M	D	90	42	14	1							2			19		10	7	1				96	
6H-CC	56.53	56.58	M	A	57	36	1	5							4			7		16		6				75	
7H-CC	66.22	66.27		B																						0	
8H-CC	75.58	75.63	P	R	40	1										1										2	
9H-CC	85.12	85.17	P	R	7													1								2	
10H-CC	94.77	94.82		B																						0	
11H-CC	103.99	104.04	P	R	65	12	1											1		1						15	
12H-1, 76–81	104.56	104.61	M	A	70	26	6			1	1		2		10	7	5	18		17	1				4	98	
13X-CC	106.26	106.31	P	R	15	1														2						3	
14H-CC	115.76	115.81	P	R	26	2											2				1				1	6	
15H-CC	115.50	115.53	M	R	8	3	2															1			2	8	
16X-CC	116.92	116.96	M	R	30	1	1									1										3	
17H-CC	122.49	122.54	P	R	18	7						3				6					6	8		2	1	33	Yellow-color tests are abundant
18H-CC	127.28	127.33	P	R	20	3										1							1			6	Yellow-color tests are abundant
19H-CC	131.17	131.23	P	R	50					2												7				9	Yellow-color tests are abundant
20H-CC	136.66	136.72		B																						0	
21H-CC	146.33	146.38		B																						0	
22H-CC	155.99	156.04		B																						0	
23H-CC	165.42	165.47		B																						0	
24H-CC	174.99	175.04	P	R	60	8				1										1	6	6				22	Yellow-color tests are abundant
25H-CC	184.47	184.52		B																						0	
26H-CC	194.05	194.10	P	A	90	2								33						1	21	2				60	Yellow-color tests are abundant
27H-CC	203.37	203.42		B																						0	
28H-6, 98–103	211.58	211.63		B																						0	
29H-CC	221.26	221.31		B																						0	

Table T8 (continued). (Continued on next page.)

Core, section, interval (cm)	Top depth CSF-A (m)	Bottom depth CSF-A (m)	Preservation	Abundance	% Planktonic foraminifers	*Globigerina bulloides*	*Globigerina umbilicata*	*Globigerina quinqueloba*	*Globigerina* sp.	*Globigerinita glutinata*	*Globigerinoides* sp.	*Globorotalia ikbei*	*Globorotalia praeinflata*	*Neogloboquadrina* cf. *dutertrei* (s)	*Neogloboquadrina* cf. *asanoi*	*Neogloboquadrina dutertrei*	*Neogloboquadrina incompta*	*Neogloboquadrina kagaensis* and *Neogloboquadrina inglei*	*Neogloboquadrina pachyderma*	*Neogloboquadrina pachyderma* (d)	*Neogloboquadrina pachyderma* (s)	*Neogloboquadrina* sp.	*Orbulina suturalis*	*Orbulina* sp.	*Orbulina universa*	Total number of planktonic foraminifers	Comment
30H-CC	230.94	230.99		B																						0	
32X-CC	235.46	235.51		B																						0	
33H-CC	243.98	244.03		B																						0	
34H-CC	253.40	253.45		B																						0	
35H-CC	262.68	262.73		B																						0	
36H-CC	267.72	267.77		B																						0	
37H-CC	272.44	272.49		B																						0	
38H-CC	277.08	277.13		B																						0	
39H-CC	281.91	281.97		B																						0	
40X-CC	288.19	288.24		B																						0	
41H-CC	289.80	289.85		B																						0	
42H-CC	294.53	294.58		R	1	1																				1	
43H-CC	299.19	299.24		R	2	4																				4	
44H-CC	304.00	304.05		B																						0	
45H-CC	308.71	308.76		B																						0	
46H-CC	313.32	313.37		B																						0	
47H-CC	318.05	318.10		B																						0	
48H-CC	322.69	322.74		B																						0	
49H-CC	327.42	327.47		B																						0	
50H-CC	332.15	332.20		B																						0	
51H-CC	336.86	336.91		B																						0	
52H-CC	341.52	341.57		B																						0	
53H-CC	346.30	346.35		B																						0	
54H-CC	351.20	351.25		B																						0	
55X-CC	360.22	360.27		B																						0	
56X-CC	366.02	366.07		R	100	1																				1	
57X-CC	369.47	369.52		B																						0	
58X-CC	378.35	378.40		B																						0	
59X-CC	378.35	378.40		B																						0	
60X-CC	402.45	402.50		B																						0	
61X-CC	403.83	403.87		B																						0	
346-U1425D-																											
13X-CC	113.80	113.85	P	R		3																				3	

Table T8 (continued).

Core, section, interval (cm)	Top depth CSF-A (m)	Bottom depth CSF-A (m)	Preservation	Abundance	% Planktonic foraminifers	*Globigerina bulloides*	*Globigerina umbilicata*	*Globigerina quinqueloba*	*Globigerina* sp.	*Globigerinita glutinata*	*Globigerinoides* sp.	*Globorotalia ikbei*	*Globorotalia praeinflata*	*Neogloboquadrina* cf. *dutertrei* (s)	*Neogloboquadrina* cf. *asanoi*	*Neogloboquadrina dutertrei*	*Neogloboquadrina incompta*	*Neogloboquadrina kagaensis* and *Neogloboquadrina inglei*	*Neogloboquadrina pachyderma*	*Neogloboquadrina pachyderma* (d)	*Neogloboquadrina pachyderma* (s)	*Neogloboquadrina* sp.	*Orbulina suturalis*	*Orbulina* sp.	*Orbulina universa*	Total number of planktonic foraminifers	Comment
14H-CC	118.39	118.43	P	R		7	1		3												1	1				13	Yellow-color tests are abundant
15H-CC	127.96	128.01	M	R		3														2	3				3	11	
16H-CC	137.70	137.75		B																						0	
18H-CC	149.34	149.39		B																						0	
19H-CC	158.62	158.67		B																						0	
59H-CC	384.77	384.82		B																						0	
60H-CC	389.23	389.28		B																						0	
61H-CC	390.67	390.72		B																						0	
63H-CC	397.66	397.71		B																						0	
64H-CC	401.28	401.33		B																						0	
65H-CC	404.42	404.47		B																						0	
66H-CC	408.02	408.07		B																						0	
67H-CC	408.86	408.91		B																						0	
69H-CC	414.11	414.16		B																						0	
70H-CC	415.10	415.11		B																						0	
71X-CC	415.32	415.33		B																						0	
72H-1	430.70	430.95		B																						0	

Preservation: G = good, M = moderate, P = poor. Abundance: D = dominant, A = abundant, R = rare, B = barren. Shaded intervals = barren.

Table T9. Benthic foraminifers, Site U1425. This table is available in an oversized format.

Table T10. Calcium carbonate, total carbon (TC), total organic carbon (TOC), and total nitrogen (TN) contents on interstitial water squeeze cake sediment samples, Site U1425.

Core, section, interval (cm)	Top depth CSF-A (m)	Calcium carbonate (wt%)	TC (wt%)	TOC (wt%)	TN (wt%)
346-U1425A-					
1H-1, 145–150	1.45	4.18	1.82	1.32	0.26
1H-4, 145–150	5.95	6.27	2.06	1.31	0.24
346-U1425B-					
1H-1, 145–150	1.45	11.20	2.28	0.93	0.19
1H-4, 145–150	5.95	8.26	1.49	0.50	0.18
2H-1, 145–150	10.25	0.37	1.07	1.02	0.23
3H-1, 145–150	19.75	6.90	1.92	1.09	0.20
3H-4, 145–150	24.25	1.09	2.00	1.87	0.28
4H-1, 145–150	29.25	9.79	2.99	1.82	0.25
4H-4, 145–150	33.75	2.78	1.24	0.90	0.19
5H-1, 145–150	38.75	1.33	0.45	0.29	0.18
5H-4, 0–5	41.80	0.35	2.50	2.46	0.29
6H-1, 145–150	48.25	3.63	1.23	0.80	0.22
6H-4, 145–150	52.75	5.17	1.23	0.61	0.17
7H-1, 145–150	57.75	1.25	0.34	0.19	0.18
7H-4, 145–150	62.25	0.31	0.68	0.65	0.20
8H-1, 145–150	67.25	0.45	0.86	0.81	0.20
8H-4, 145–150	71.75	0.33	1.02	0.98	0.21
9H-1, 145–150	76.75	0.34	1.00	0.96	0.22
9H-4, 145–150	81.25	0.39	0.81	0.76	0.21
10H-1, 145–150	86.25	0.35	0.75	0.71	0.23
10H-4, 145–150	90.75	1.03	1.78	1.65	0.26
11H-1, 145–150	95.75	0.42	0.90	0.85	0.19
11H-4, 145–150	100.25	17.74	2.55	0.43	0.16
13X-1, 145–150	106.05	0.35	0.50	0.46	0.18
14H-1, 145–150	107.45	0.43	1.24	1.18	0.21
16X-1, 102–107	116.62	0.31	0.76	0.72	0.21
18H-1, 145–150	123.95	1.17	2.57	2.43	0.29
20H-1, 145–150	133.35	0.45	0.72	0.66	0.19
21H-1, 145–150	138.05	0.41	1.05	1.00	0.19
22H-1, 145–150	147.55	0.42	0.87	0.82	0.20
23H-1, 145–150	157.05	0.39	0.85	0.80	0.21
24H-1, 145–150	166.55	0.37	0.68	0.63	0.19
25H-1, 145–150	176.05	0.39	0.45	0.40	0.16
26H-1, 145–150	185.55	0.55	0.80	0.73	0.19
27H-1, 145–150	195.05	1.26	0.84	0.69	0.17
28H-1, 145–150	204.55	0.48	1.64	1.58	0.25
29H-1, 145–150	213.05	0.29	0.83	0.79	0.20
30H-1, 145–150	222.55	0.48	1.76	1.70	0.25
32X-1, 145–150	232.05	0.40	ND	ND	ND
33H-1, 145–150	235.75	0.36	1.74	1.69	0.24
34H-1, 145–150	245.25	0.44	2.37	2.32	0.30
35H-1, 145–150	254.75	0.40	2.01	1.96	0.30
36H-2, 145–150	264.81	0.14	3.84	3.82	0.36
38H-1, 143–148	273.63	0.36	3.92	3.88	0.37
40X-1, 145–150	283.05	0.41	3.36	3.31	0.33
42H-1, 140–145	291.00	0.39	1.57	1.52	0.19
44H-1, 140–145	300.40	0.39	4.40	4.35	0.39
46H-1, 140–145	309.80	0.38	3.77	3.73	0.34
48H-1, 140–145	319.20	0.43	3.98	3.93	0.36
50H-1, 140–145	328.60	0.41	4.70	4.65	0.41
52H-1, 140–145	338.00	0.33	2.27	2.23	0.28
54H-1, 140–145	347.40	0.36	1.92	1.88	0.25
55X-1, 140–150	352.10	0.31	1.92	1.88	0.24
56X-1, 140–145	360.10	0.30	4.15	4.11	0.36
59X-1, 140–145	389.20	0.37	3.29	3.24	0.31
60H-1, 140–145	398.90	0.49	1.56	1.50	0.20

ND = not determined.

Table T11. Calcium carbonate, total carbon (TC), total organic carbon (TOC), and total nitrogen (TN) contents of sediment samples from light and dark intervals, Hole U1425B.

Core, section, interval (cm)	Top depth CSF-A (m)	Calcium carbonate (wt%)	TC (wt%)	TOC (wt%)	TN (wt%)
346-U1425B-					
1H-1, 14–16	0.14	0.38	1.81	1.76	0.28
1H-1, 46–48	0.46	0.41	3.81	3.76	0.43
1H-1, 75–77	0.75	11.91	1.80	0.37	0.19
1H-1, 113–115	1.13	7.91	2.16	1.21	0.20
1H-3, 105–107	4.05	8.67	4.08	3.04	0.35
1H-3, 132–134	4.32	2.54	4.99	4.68	0.52
1H-4, 16–18	4.66	1.14	4.45	4.32	0.53
1H-4, 26–28	4.76	9.24	6.24	5.13	0.58
1H-4, 38–40	4.88	1.69	0.81	0.61	0.17
1H-5, 87–89	6.87	0.42	0.59	0.54	0.17
1H-5, 96–98	6.96	0.30	0.91	0.87	0.21
1H-5, 144–146	7.44	8.80	2.18	1.13	0.17

Table T12. Interstitial water chemistry, Site U1425. This table is available in an oversized format.

Table T13. Color measurements (absorbance) of interstitial water, Site U1425. (Continued on next page.)

Core, section, interval (cm)	Top depth CSF-A (m)	Top depth CCSF-A (m)	Sample type	Alkalinity (mM)	Absorbance 227 nm	Absorbance 325 nm
346-U1425A-						
1H-1, 145–150	1.45	3.83	IW-Sq	7.79	0.495	0.101
1H-4, 20	4.70	7.08	IW-Rh		0.721	0.144
1H-4, 50	5.00	7.38	IW-Rh		0.807	0.145
1H-4, 80	5.30	7.68	IW-Rh		0.832	0.168
1H-4, 95	5.45	7.83	IW-Rh		0.783	0.145
1H-4, 108	5.58	7.96	IW-Rh		0.789	0.150
1H-4, 125	5.75	8.13	IW-Rh		0.825	0.160
1H-4, 140	5.90	8.28	IW-Rh		1.139	0.150
1H-4, 145–150	5.95	8.33	IW-Sq	10.90	0.818	0.164
346-U1425B-						
1H-1, 145–150	1.45	1.45	IW-Sq	5.11	0.259	0.052
1H-4, 145–150	5.95	5.95	IW-Sq	9.35	0.676	0.151
2H-1, 145–150	10.25	10.81	IW-Sq	12.82	0.951	0.197
2H-4, 145–150	14.75	15.31	IW-Sq	14.94	1.132	0.211
3H-1, 145–150	19.75	21.33	IW-Sq	16.71	1.182	0.219
3H-4, 145–150	24.25	25.83	IW-Sq	18.59	1.256	0.224
4H-1, 145–150	29.25	31.35	IW-Sq	20.63	1.470	0.250
4H-4, 145–150	33.75	35.85	IW-Sq	22.14	1.638	0.257
5H-1, 145–150	38.75	41.16	IW-Sq	23.42	1.443	0.212
5H-4, 0–5	41.80	44.21	IW-Sq	24.38	1.420	0.235
6H-1, 145–150	48.25	52.35	IW-Sq	25.29	1.332	0.228
6H-4, 145–150	52.75	56.85	IW-Sq	25.82	1.199	0.194
7H-1, 145–150	57.75	62.43	IW-Sq	27.77	1.141	0.183
7H-4, 145–150	62.25	66.93	IW-Sq	28.71	1.163	0.194
8H-1, 145–150	67.25	73.08	IW-Sq	29.78	1.084	0.180
8H-4, 145–150	71.75	77.58	IW-Sq	30.29	1.103	0.172
9H-1, 145–150	76.75	83.40	IW-Sq	30.72	1.110	0.186
9H-4, 145–150	81.25	87.90	IW-Sq	30.99	1.066	0.150
10H-1, 145–150	86.25	90.52	IW-Sq	31.52		
10H-4, 145–150	90.75	95.02	IW-Sq	31.76	1.064	0.159
11H-1, 145–150	95.75	100.84	IW-Sq	31.90	1.008	0.129
11H-4, 145–150	100.25	105.34	IW-Sq	31.80	1.045	0.120
13X-1, 145–150	106.05	111.33	IW-Sq	32.08	0.998	0.107
14H-1, 145–150	107.45	112.87	IW-Sq	32.22	1.029	0.119
16X-1, 102–107	116.62	122.00	IW-Sq	32.10	0.953	0.096
18H-1, 145–150	123.95	128.74	IW-Sq	32.04	0.957	0.089
20H-1, 145–150	133.35	139.91	IW-Sq	32.17	0.945	0.089
21H-1, 145–150	138.05	143.77	IW-Sq	31.12	0.930	0.090
22H-1, 145–150	147.55	154.33	IW-Sq	30.69	0.925	0.095

Table T13 (continued).

Core, section, interval (cm)	Top depth CSF-A (m)	Top depth CCSF-A (m)	Sample type	Alkalinity (mM)	Absorbance 227 nm	Absorbance 325 nm
23H-1, 145–150	157.05	164.17	IW-Sq	31.81	1.002	0.126
24H-1, 145–150	166.55	174.50	IW-Sq	31.11	0.947	0.085
25H-1, 145–150	176.05	184.04	IW-Sq	30.00	0.942	0.087
26H-1, 145–150	185.55	195.11	IW-Sq	30.17	0.933	0.072
27H-1, 145–150	195.05	203.68	IW-Sq	28.96	0.932	0.064
28H-1, 145–150	204.55	213.98	IW-Sq	27.77	0.899	0.060
29H-1, 145–150	213.05	222.65	IW-Sq	27.59	0.953	0.066
30H-1, 145–150	222.55	231.14	IW-Sq	26.42	0.930	0.059
32X-1, 145–150	232.05	241.12	IW-Sq	25.40	0.929	0.065
33H-1, 145–150	235.75	245.05	IW-Sq	24.72	0.968	0.069
34H-1, 145–150	245.25	254.49	IW-Sq	24.07	0.926	0.052
35H-1, 145–150	254.75	263.98	IW-Sq	22.67	0.936	0.051
36H-2, 145–150	264.81	274.89	IW-Sq	21.01	0.915	0.051
38H-1, 143–148	273.63	283.42	IW-Sq	20.22	0.948	0.055
40X-1, 145–150	283.05	293.36	IW-Sq	20.23		
42H-1, 140–145	291.00	303.74	IW-Sq	18.96	0.937	0.047
44H-1, 140–145	300.40	313.14	IW-Sq	16.16		
46H-1, 140–145	309.80	321.90	IW-Sq	16.75	0.892	0.034
48H-1, 140–145	319.20	332.25	IW-Sq	16.14		
346-U1425D-						
1H-1, 0–5	0.00	0.00	IW-Rh	2.50	0.092	0.009
1H-1, 5	0.05	0.05	IW-Rh	2.66	0.114	0.010
1H-1, 10	0.10	0.10	IW-Rh	2.71	0.111	0.013
1H-1, 15	0.15	0.15	IW-Rh	2.87	0.112	0.014
1H-1, 20	0.20	0.20	IW-Rh	2.98	0.176	0.029
1H-1, 25	0.25	0.25	IW-Rh	3.07	0.161	0.027
1H-1, 30	0.30	0.30	IW-Rh	3.12	0.174	0.039
1H-1, 40	0.40	0.40	IW-Rh	3.29	0.182	0.032
1H-1, 90	0.90	0.90	IW-Rh	4.15	0.198	0.052
1H-1, 120	1.20	1.20	IW-Rh	4.42	0.234	0.042
1H-2, 10	1.60	1.60	IW-Rh	4.99	0.271	0.052
1H-3, 140	4.40	4.40	IW-Rh	8.25	0.530	0.109
4H-1, 10	24.40	26.83	IW-Rh	19.16	1.426	0.171
4H-2, 10	25.90	28.33	IW-Rh	19.14	1.449	0.179
4H-3, 10	27.40	29.83	IW-Rh	19.99	1.503	0.168
4H-4, 10	28.90	31.33	IW-Rh	20.13	1.527	0.185
4H-5, 10	30.40	32.83	IW-Rh	20.57	1.568	0.183
4H-6, 10	31.90	34.33	IW-Rh	21.13	1.519	0.178
5H-1, 10	33.90	36.97	IW-Rh	21.29	1.677	0.206
5H-2, 10	35.40	38.47	IW-Rh	22.61	1.639	0.190
5H-3, 10	36.90	39.97	IW-Rh	22.69	1.654	0.205

IW-Sq = interstitial water from whole-round squeezing, IW-Rh = interstitial water from Rhizons.

Table T14. Headspace (HS) gas concentrations, Site U1425. (Continued on next page.)

Core, section, interval (cm)	Top depth CSF-A (m)	Sample type	Sediment volume (cm^3)	CH_4 (ppmv) GC3 measured	CH_4 (ppmv) NGA-FID measured	CH_4 (ppmv) GC3 normalized	CH_4 (ppmv) NGA-FID normalized
346-U1425A-							
1H-2, 0–5	1.50	HS	3.8		3		3
1H-5, 0–5	6.00	HS	4.4		4		5
346-U1425B-							
1H-2, 0–5	1.50	HS	4.0		0		0
1H-5, 0–5	6.00	HS	4.0		3		4
2H-2, 0–5	10.30	HS	4.2		5		6
2H-5, 0–5	14.80	HS	4.5		5		6
2H-6, 0–5	16.30	HS	4.0		7		9
3H-2, 0–5	19.80	HS	3.0		5		8
3H-5, 0–5	24.30	HS	4.0		8		10
4H-2, 0–5	29.30	HS	3.6		7		9
4H-5, 0–5	33.80	HS	3.2		6		9
5H-2, 0–5	38.80	HS	3.0		5		8
5H-5, 0–5	43.30	HS	3.0		3		5
6H-2, 0–5	48.30	HS	3.0		8		13
6H-5, 0–5	52.80	HS	3.0		10		17
7H-2, 0–5	57.80	HS	3.2		25		39
7H-5, 0–5	62.30	HS	3.0		446		744
8H-2, 0–5	67.30	HS	3.0		1,175		1,959
8H-5, 0–5	71.80	HS	3.0		1,068		1,779
9H-2, 0–5	76.80	HS	3.0		2,725		4,541
9H-5, 0–5	81.30	HS	3.0		3,072		5,121
10H-2, 0–5	86.30	HS	3.0		3,589		5,981
10H-5, 0–5	90.80	HS	3.0		3,183		5,305
11H-2, 0–5	95.80	HS	3.2		3,043		4,755
11H-5, 0–5	100.30	HS	3.0		1,215		2,025
12H-1, 71–76	104.51	HS	—		3,347		—
13X-CC, 11–16	106.21	HS	—		4,931		—
14H-2, 0–5	107.50	HS	3.0		4,274		7,124
16X-1, 97–102	116.57	HS	3.2		4,462		6,972
17H-2, 0–5	119.30	HS	3.0		6,892		11,487
19H-2, 0–5	128.63	HS	4.0		7,648		9,560
20H-2, 0–5	133.40	HS	4.0		7,527		9,409
21H-2, 0–5	138.10	HS	4.0		8,848		11,060
22H-2, 0–5	147.60	HS	3.8		8,932		11,753
23H-2, 0–5	157.10	HS	3.5		5,160		7,371
24H-2, 0–5	166.60	HS	3.0		7,617		12,694
25H-2, 0–5	176.10	HS	3.0		9,265		15,442
26H-2, 0–5	185.60	HS	4.0	13,855		17,319	
27H-2, 0–5	195.10	HS	3.0	7,042		11,736	
28H-2, 0–5	204.60	HS	3.2	10,869		16,983	
29H-2, 0–5	213.10	HS	3.2	10,531		16,455	
30H-2, 0–5	222.60	HS	3.0	7,836		13,059	
32X-2, 0–5	232.10	HS	2.5	6,472		12,944	
33H-2, 0–5	235.80	HS	2.8	9,552		17,057	
34H-2, 0–5	245.30	HS	3.3	10,824		16,400	
35H-2, 0–5	254.80	HS	2.5	4,826		9,651	
36H-3, 0–5	264.86	HS	3.0	5,284		8,807	
37H-2, 0–5	269.00	HS	3.0	6,636		11,060	
38H-2, 0–5	273.68	HS	3.0	8,997		14,994	
39H-2, 0–5	278.40	HS	3.0	7,343		12,238	
40X-2, 0–5	283.10	HS	3.0	2,749		4,581	
41H-2, 0–5	286.40	HS	3.0	12,997		21,662	
42H-2, 0–5	291.10	HS	3.4	9,990		14,691	
43H-2, 0–5	295.80	HS	3.4	13,409		19,720	
44H-2, 0–5	300.50	HS	2.6	9,389		18,056	
45H-2, 0–5	305.13	HS	3.4	8,125		11,949	
46H-2, 0–5	309.90	HS	3.0	7,752		12,920	
47H-2, 0–5	314.60	HS	3.0	2,677		4,462	
48H-2, 0–5	319.30	HS	3.0		10,502		17,503
49H-2, 0–5	324.00	HS	2.6		3,246		6,241
50H-2, 0–5	328.70	HS	2.6		5,949		11,440
51H-2, 0–5	333.40	HS	3.6		1,919		2,666
52H-2, 0–5	338.10	HS	2.6		2,461		4,733
53H-2, 0–5	342.80	HS	—		4,421		—

Table T14 (continued).

Core, section, interval (cm)	Top depth CSF-A (m)	Sample type	Sediment volume (cm^3)	CH_4 (ppmv) GC3 measured	CH_4 (ppmv) NGA-FID measured	CH_4 (ppmv) GC3 normalized	CH_4 (ppmv) NGA-FID normalized
54H-2, 0–5	347.50	HS	—		3,248		—
55X-2, 0–5	352.20	HS	2.7		2,656		4,918
56X-2, 0–5	360.20	HS	2.3		5,986		13,013
57X-1, 41–46	368.81	HS	3.0		9,697		16,161
59X-2, 0–5	389.30	HS	3.6		3,756		5,217
60H-2, 0–5	399.00	HS	4.0		3,864		4,830
61X-1, 137–142	403.57	HS	4.0		2,247		2,808

GC3 = gas analyzer (C_1–C_3), NGA = natural gas analyzer (C_1–C_7), FID = flame ionization detector. — = not measured.

Table T15. FlexIT tool core orientation data, Hole U1425B.

Core	Orientation angle (°)	Orientation standard (°)
346-U1425B-		
2H	203.59	1.05
3H	41.59	0.51
4H	152.17	0.82
5H	15.01	0.38
6H	41.51	0.99
7H	266.54	0.79
8H	201.79	0.39
9H	336.47	0.36
10H	122.68	0.18
11H	115.35	0.31
12H	66.27	0.14
14H	130.49	0.62

Table T16. Core disturbance intervals, Site U1425. (Continued on next five pages.)

Core, section, interval (cm)	Comments on disturbance	Drilling disturbance intensity
346-U1425B-		
1H-1, 0–66	Soupy	Slight to moderate
1H-2, 17–50	Slurry	Moderate to high
1H-2, 140–150	Tilted	
2H-1, 0–105		Slight to moderate
2H-CC, 0–14		Slight
3H-1, 0–19	Void and tilted	High
3H-5, 95–96	Tilted	
3H-CC, 0–29		Slight
4H-1, 0–7		Slight
4H-5, 78–87	Deformed	
4H-6, 113–108	Microfault	
4H-7, 8–35	Soupy ash	
5H-2, 112–115	Void	Destroyed
5H-3, 0–10	Deformed	
5H-5, 0–20	Deformed	
5H-5, 50–60	Deformed	
6H-1, 0–150	Disturbed, tilted, microfault	Moderate
6H-2, 30–35	Deformed	
6H-2, 105–110	Microfault	
6H-2, 135–140	Microfault	
6H-6, 20–45	Ash and deformed	
7H-1, 27–33	Microfault	
7H-2, 25–32	Ash and deformed	
7H-4, 135–140	Microfault	
7H-5, 25–53	Microfault	

Table T16 (continued). (Continued on next page.)

Core, section, interval (cm)	Comments on disturbance	Drilling disturbance intensity
7H-6, 80–85	Microfault	
8H-1, 0–10	Deformed	
8H-1, 25–35	Microfault	Moderate to high
8H-1, 80–150	Tilted	
8H-2, 0–7	Microfault	
8H-2, 40–50	Tilted	
8H-2, 69–72	Microfault?	
8H-2, 60–150	Mass transfer deposit	
8H-3, 0–150	Mass transfer deposit	
8H-4, 0–150	Mass transfer deposit	
8H-5, 0–150	Mass transfer deposit	
8H-6, 0–150	Mass transfer deposit	
8H-7, 0–150	Mass transfer deposit	
9H-1, 100–107	Slightly disturbed by IRD, took off when measuring samples	
9H-2, 0–110	Mass transfer deposit	
9H-3, 50–60	Nodule conclusion?	
9H-6, 130–150	Tilted + microfault	
9H-6, 145–150		Moderate
10H-1, 0–10	Disturbed	
11H-CC, 0–11		Slight
12H-1, 38–58		Moderate
13X-1, 10–49		Moderate
13X-1, 95–105	Disturbed	
13X-1, 138–142	Void	Destroyed
13X-CC, 0–21		Slight to moderate
14H-1, 0–27	Fall-in	Moderate
16X-1, 0–107		Slight
16X-CC, 0–29		Slight
17H-1, 0–40	Disturbed	
18H-1, 0–9		Slight to moderate
18H-3, 85–94		Moderate
19H-1, 0–20	Fall-in, core top disturbance	High
19H	Flow-in	High
20H-1, 0–22		Slight to moderate
21H-1, 0–14	Fall-in	Slight
22H-1, 0–22	Nodule conclusion?	Moderate
23H-1, 0–2		Slight
23H-CC, 0–26		Slight
24H-5, 96–150	Flow-in	High
24H-6, 0–150	Flow-in	High
24H-7, 0–73	Flow-in	High
24H-CC, 0–21	Flow-in	High
25H-2, 80–95	Microfault	
26H-3, 0–50	Suck in	High
26H-4, 0–150	Suck in	High
26H-5, 0–150	Suck in	High
26H-6, 0–150	Suck in	High
26H-7, 0–75	Suck in	High
26H-CC, 0–25	Suck in	High
27H-6, 0–20	Disturbance?	
28H-5, 0–150	Mass transfer deposit?	
28H-6, 0–46	Suck in	Moderate
28H-6, 46–103	Soupy	Moderate to high
30H-1, 0–150		Slight
32X	Biscuit	Moderate to high
33H-1, 0–17	Soupy	High
33H-3, 46–80	Microfault	
34H-1, 0–19		Moderate to high
35H-1, 0–20	Disturbed	
36H-1, 0–56	Biscuit	High
39H-2, 100–150	Suck in	High
39H-3, 0–150	Flow-in	
39H-4, 0–150	Flow-in	
40X	Biscuit	High
40X-1, 0–150	Biscuit	High
40X-2, 0–9	Mixed and tilted part	
40X-2, 18–21	Mixed and tilted part	
40X-2, 55–80	Mixed and tilted part	
40X-2, 90–98	Mixed and tilted part	

Table T16 (continued). (Continued on next page.)

Core, section, interval (cm)	Comments on disturbance	Drilling disturbance intensity
40X-2, 103–113	Mixed and tilted part	
40X-2, 116–127	Mixed and tilted part	
40X-2, 131–141	Mixed and tilted part	
40X-3, 10–33	Mixed and tilted part	
40X-3, 45–55	Mixed and tilted part	
40X-3, 62–118	Mixed and tilted part	
40X-4, 0–20	Mixed and tilted part	
41H	Flow-in	Moderate to high
42H-3, 81–150	Mass transfer deposit?	
42H-4, 0–64	Microfault and mass transfer deposit?	
43H-1, 0–3		Slight
43H-1, 86–150	Flow-in	Slight
43H-2, 0–150	Flow-in	Slight
43H-3, 0–121	Flow-in	Slight
43H-4, 0–57	Flow-in	Slight
43H-CC, 0–16	Flow-in	Slight
44H-1, 0–18		Slight to moderate
44H-4, 1–15	Tilted	
45H-1, 0–13		Slight
45H-3, 68–111	Tilted	
45H-4, 0–70	Tilted	
45H-CC, 22–27		Moderate to high
46H-1, 0–8	Suck in	Slight
46H-CC, 0–14		Slight
47H-1, 0–19		Slight
47H-CC, 0–13		Slight
48H-1, 0–12		Slight
48H-2, 0–150	Tilted	
48H-4, 0–51	Tilted	
48H-CC, 0–3		Slight
49H-1, 0–4		Slight
49H-2, 0–150	Slightly deformed	
49H-3, 16–30	Slightly deformed	
49H-CC, 0–25		Slight
50H-1, 0–9		Slight
50H-CC, 0–3		Slight
51H-1, 0–7		Slight
51H-2, 41–150	Tilted	
51H-3, 0–150	Tilted	
52H-1, 0–9		Slight
52H-1, 75–86	Microfault	
52H-1, 104–113	Microfault	
52H-CC, 0–28		Slight
53H-1, 0–4		Slight
53H-1, 12–33	Tilted	
53H-2, 64–151	Flow-in	
53H-3, 0–150	Flow-in	
53H-4	Flow-in	
54H-1, 0–20	Void	Moderate
54H-2, 0–150		Slight to moderate
54H-3, 0–102	Void	Destroyed
54H-4, 0–65	Flow-in	
54H-CC, 4–24	Biscuit	Moderate to high
54H-CC, 37–45		Inter-biscuit mud
55X-1, 0–150		Inter-biscuit mud
55X-2, 0–13		Inter-biscuit mud
55X-2, 27–39		Inter-biscuit mud
55X-2, 48–99		Inter-biscuit mud
55X-2, 110–150		Inter-biscuit mud
55X-3, 0–102		Inter-biscuit mud
55X-3, 107–150		Inter-biscuit mud
55X-4, 0–38		Inter-biscuit mud
55X-4, 42–93		Inter-biscuit mud
55X-5, 0–151		Inter-biscuit mud
55X-6, 0–116		Inter-biscuit mud
55X-7, 0–24		Inter-biscuit mud
55X-7, 36–54		Inter-biscuit mud
56X-1, 0–150	Biscuit	High
56X-2, 0–150	Biscuit	High

Table T16 (continued). (Continued on next page.)

Core, section, interval (cm)	Comments on disturbance	Drilling disturbance intensity
56X-3, 0–150	Biscuit	High
56X-4, 0–150	Biscuit	Moderate to high
56X-4, 0–14		Inter-biscuit mud
56X-4, 28–58		Inter-biscuit mud
56X-4, 77–99		Inter-biscuit mud
56X-4, 108–151		Inter-biscuit mud
56X-5, 0–78		Inter-biscuit mud
56X-5, 0–102	Biscuit	Moderate to high
56X-CC, 0–35	Biscuit	Moderate to high
57X-1, 0–67	Biscuit	High
57X-CC, 0–45	Biscuit	High
58X-CC, 0–36	Biscuit	High
59X-1, 0–17		Inter-biscuit mud
59X-1, 32–47		Inter-biscuit mud
59X-1, 121–150		Inter-biscuit mud
59X-2, 0–49		Inter-biscuit mud
59X-2, 60–65		Inter-biscuit mud
59X-2, 84–85		Inter-biscuit mud
59X-2, 92–95		Inter-biscuit mud
59X-2, 105–124		Inter-biscuit mud
59X-3, 25–31		Inter-biscuit mud
59X-3, 107–128		Inter-biscuit mud
59X-4, 15–16		Inter-biscuit mud
59X-5, 50–61		Inter-biscuit mud
60H		High
61X-1, 0–21	Disturbed	
61X-1, 129–142	Disturbed	
346-U1425D-		
1H-1, 0–11		Slight
1H-2, 0–150	Crack	Moderate
1H-CC, 0–13		Slight
2H-3, 113–114	Void	Destroyed
2H-CC, 0–13		Slight
3H-1, 0–70	Fall-in	Moderate to high
3H-2, 77–78	Void	Destroyed
3H-7, 0–57	Bowed	Destroyed
4H-1, 0–5		Slight to moderate
4H-3, 19–20	Void	Destroyed
4H-4, 82–83.5	Void	Destroyed
4H-7, 18–35	Crack	Moderate to high
5H-1, 0–5		Slight
5H-2, 67–68	Void	Destroyed
5H-CC, 7–16		Slight
6H-1, 30–49	Soupy	Moderate
6H-2, 139–141	Void	Destroyed
6H-CC, 7–17		Slight
7H-1, 77–85	Void	High
7H-2, 55–60	Void	High
7H-3, 97–102	Soupy	Moderate to high
8H-1, 0–105		High
8H-2, 105–106	Void	High
8H-2, 137–138	Void	High
8H-3, 18–20	Void	High
8H-3, 30–33	Void	High
8H-3, 44–47	Void	High
8H-3, 70–71	Void	High
8H-3, 95–96	Void	High
8H-4, 71–72	Void	High
8H-4, 106–107	Void	High
8H-4, 121–125	Void	High
8H-5, 93–94	Void	High
8H-5, 99–101	Void	High
8H-5, 108–109	Void	High
9H-2, 107–113	Void	High
9H-3, 41–46	Void	High
10H-1, 0–77	Soupy	High
11H-1, 0–21	Soupy	High
12H-1, 0–29	Soupy	High
13X	Crack	High

Table T16 (continued). (Continued on next page.)

Core, section, interval (cm)	Comments on disturbance	Drilling disturbance intensity
14H-1, 28–32	Crack	Moderate
15H	Flow-in	Moderate
16H-1, 17–20	Void	High
16H-1, 125–127	Void	High
18H-1, 0–10	Soupy	Slight
20H-1, 0–12		Slight
21H-1, 0–69	Soupy	High
21H-3, 18–30	Suck in	Moderate
23H-1, 0–29	Mousse-like	Slight to moderate
24H-7, 16–42	Bowed	Moderate to high
25H-1, 0–23		Moderate
25H-1, 23–26	Void	Destroyed
26X	Biscuit	Slight
26X-CC, 0–35		Slight to moderate
27H	Stretched	High
28H-1, 0–6		Slight
28H-CC, 0–17		Slight
29H-1, 0–10		Slight
29H-CC, 0–4		Slight
30H	Stretched	High
31H-1, 0–33		Slight to moderate
31H-2, 70–73	Void	Destroyed
33H-2, 122–133	Flow-in	Slight
33H-3, 25–50		Moderate
33H-4, 0–114		High
38H-1, 0–10		Slight
41H		Slight
41H-1	Tilted	
41H-2, 0–130	Tilted	
42H-1, 0–10	Disturbed	Moderate
43H-1, 0–10		Moderate
44H-1, 0–13		Moderate
45H-1, 0–18		Moderate
45H-1, 23–25	Void	Moderate
47H-1, 0–13		Moderate to high
48H-1, 0–150		Slight
49H-1, 0–5		Moderate
49H-3, 0–3		Slight
50H-1, 0–10		Slight
51H-1, 0–3		Slight
51H-3, 84–111	Flow-in	Slight
52H-1, 0–10		Slight
52H-2, 70–140	Suck in	High
52H-CC, 0–32	Suck in	Moderate to high
53H-CC, 0–25		Moderate to high
54H-1, 26–35		Moderate to high
54H-1, 52–150	Suck in	High
54H-1, 98–111	Void	
54H-2, 0–93	Slurry	High
54H-CC, 0–18	Slurry	High
55H-1, 0–12		Moderate
55H-1, 66–150	Suck in	Moderate to high
55H-2, 0–150	Suck in	Moderate to high
55H-3, 0–83	Suck in	Moderate to high
55H-CC, 0–34	Suck in	Moderate to high
56H-1, 0–128	Slurry	High
57H-1, 117–150		Moderate
57H-2, 0–150	Suck in	Moderate to high
57H-3, 0–116	Suck in	Moderate to high
57H-CC, 0–15	Suck in	Moderate to high
58H-1, 0–6	Soupy	Slight
58H-2, 47–150	Suck in	Moderate to high
58H-3, 0–150	Suck in	Moderate to high
58H-4, 0–63	Suck in	Moderate to high
58H-4, 63–75		High
58H-CC, 0–15	Slurry	High
59H-3, 50–130	Suck in	Moderate to high
59H-CC, 0–45	Suck in	Moderate to high
60H-1, 39–50	Crack	Moderate

Table T16 (continued).

Core, section, interval (cm)	Comments on disturbance	Drilling disturbance intensity
60H-2, 50–150	Suck in	Moderate to high
60H-3, 0–100	Suck in	Moderate to high
60H-4, 0–61	Suck in	Moderate to high
60H-CC, 0–27	Suck in	Moderate to high
61H-1, 0–15	Fall-in	Moderate to high
61H-1, 97–132	Suck in	Moderate to high
61H-CC, 0–30	Suck in	Moderate to high
62H-1, 0–14	Fall-in	Moderate to high
62H-1, 130–150		Moderate
62H-2, 0–107	Suck in	Moderate to high
62H-CC, 0–29	Suck in	Moderate to high
63H-1, 0–9	Fall-in	Moderate to high
63H-1, 41–61		High
63H-1, 61–150	Suck in	Moderate to high
63H-2, 0–150	Suck in	Moderate to high
63H-3, 0–63	Suck in	Moderate to high
63H-3, 63–106	Slurry	High
64H-1, 0–24	Fall-in	High
64H-2, 52–130	Suck in	Moderate to high
64H-3, 0–51	Suck in	Moderate to high
64H-CC, 0–32	Suck in	Moderate to high
65H-1, 0–105	Slump material?	Slight
65H-2, 0–78	Slump material?	Moderate to high
65H-3, 0–70	Suck in	High
65H-3, 70–129	Slurry	High
66H-1, 24–150	Slurry	High
66H-2, 0–147	Slurry	High
66H-3, 0–55	Slurry	High
67H-1, 0–19	Slurry	High
67H-1, 52–76	Slurry	High
69H-CC, 0–16	Slurry	High
70H-CC, 0–11	Slurry	High
71X-CC, 0–34	Slurry	High
72H-1, 0–25	Slurry	High

IRD = ice-rafted debris.

Table T17. NRM inclination, declination, and intensity data after 20 mT peak field AF demagnetization, Site U1425.

Core, section, interval (cm)	Depth CSF-A (m)	Inclination (°)	Declination (°)	FlexIT-corrected declination (°)	Intensity (A/m)
346-U1425B-					
1H-1	0				
1H-1, 5	0.05				
1H-1, 10	0.1				
1H-1, 15	0.15				
1H-1, 20	0.2				
1H-1, 25	0.25				
1H-1, 30	0.3				
1H-1, 35	0.35				
1H-1, 40	0.4				
1H-1, 45	0.45				
1H-1, 50	0.5				
1H-1, 55	0.55				
1H-1, 60	0.6				
1H-1, 65	0.65				
1H-1, 70	0.7	73.5	209.3		0.00418
1H-1, 75	0.75	75.8	220.3		0.00471
1H-1, 80	0.8	64.9	234.9		0.00816
1H-1, 85	0.85	70.6	214.9		0.0076
1H-1, 90	0.9	82.5	120.1		0.00766
1H-1, 95	0.95	67.5	255.4		0.02191
1H-1, 100	1	59	254.5		0.033702
1H-1, 105	1.05	56.1	254.6		0.034573
1H-1, 110	1.1	65.4	256.4		0.024431
1H-1, 115	1.15	67.1	277.6		0.025867
1H-1, 120	1.2	60.5	276.3		0.030684
1H-1, 125	1.25	61.5	274.1		0.028512
1H-1, 130	1.3	56.6	273.8		0.030843
1H-1, 135	1.35	51.7	274		0.02974
1H-1, 140	1.4				
1H-1, 145	1.45				
1H-1, 150	1.5				
1H-2	1.5				
1H-2, 5	1.55				
1H-2, 10	1.6				
1H-2, 15	1.65	67.1	187.3		0.00806
1H-2, 20	1.7				
1H-2, 25	1.75				
1H-2, 30	1.8				
1H-2, 35	1.85				
1H-2, 40	1.9				
1H-2, 45	1.95				
1H-2, 50	2				
1H-2, 55	2.05	61.5	133.1		0.0018
1H-2, 60	2.1	59.7	144.9		0.00274
1H-2, 65	2.15	63.5	148		0.00325
1H-2, 70	2.2	59.4	151.6		0.00445
1H-2, 75	2.25	59.4	155		0.00463
1H-2, 80	2.3	57.7	146.6		0.00417
1H-2, 85	2.35	60.6	139.1		0.00373
1H-2, 90	2.4	61.4	132.5		0.00296
1H-2, 95	2.45	66.7	138.3		0.00226
1H-2, 100	2.5	65.7	147.3		0.00245
1H-2, 105	2.55	61.5	145.5		0.00327
1H-2, 110	2.6	59.1	150.2		0.00218
1H-2, 115	2.65	57.9	141.4		0.00174
1H-2, 120	2.7	55.2	146.1		0.00157
1H-2, 125	2.75	64.6	148.9		0.00112

Blank cells indicate depth levels where data were either not available (i.e., FlexIT-corrected declination data for nonoriented cores) or removed because of disturbance, voids, or measurement edge effects. Only a portion of this table appears here. The complete table is available in **ASCII.**

Table T18. Polarity boundaries, Site U1425.

Core, section, interval (cm)		Polarity boundary	Age (Ma)	Depth CSF-A (m)				Depth CCSF-D (m)			
Top	Bottom			Top	Bottom	Midpoint	±	Top	Bottom	Midpoint	±
346-U1425B-	346-U1425B-										
4H-4, ~40	4H-5, ~90	(B) C1n (Brunhes/Matuyama)	0.781	32.70	34.70	**33.70**	1.00	34.80	36.80	**35.80**	1.00
5H-1, ~90	5H-2, ~140	(T) C1r.1n (Jaramillo)	0.988	38.20	40.20	**39.20**	1.00	40.61	42.61	**41.61**	1.00
5H-3, ~80	5H-3, ~140	(B) C1r.1n (Jaramillo)	1.072	41.10	41.70	**41.40**	0.30	43.51	44.11	**43.81**	0.30
6H-7, ~40	7H-2, ~40	(T) C2n (Olduvai)	1.778	56.20	58.20	**57.20**	1.00	60.88	62.88	**61.88**	1.00
8H-3, ~20	8H-3, ~120	(B) C2n (Olduvai)	1.945	69.00	70.00	69.50	0.50	74.83	75.83	75.33	0.50
10H-2, ~40	10H-2, ~110	(T) C2An.1n (Matuyama/Gauss)	2.581	86.70	88.90	**87.80**	1.10	90.97	93.17	**92.07**	1.10
346-U1425D-	346-U1425D-										
4H-6, ~140	5H-1, ~140	(B) C1n (Brunhes/Matuyama)	0.781	33.20	35.20	**34.20**	1.00	36.27	38.27	**37.27**	1.00
5H-3, ~120	5H-4, ~70	(T) C1r.1n (Jaramillo)	0.988	38.00	39.00	**38.50**	0.50	41.07	42.07	**41.57**	0.50
5H-5, ~40	5H-5, ~100	(B) C1r.1n (Jaramillo)	1.072	40.20	40.80	40.50	0.30	43.27	43.87	43.57	0.30
7H-1, ~70	7H-2, ~60	(T) C2n (Olduvai)	1.778	53.50	54.90	**54.20**	0.70	58.39	59.79	**59.09**	0.70
8H-4, ~125	8H-5, ~45	(B) C2n (Olduvai)	1.945	67.40	69.40	68.40	1.00	72.81	74.81	73.81	1.00
10H-3, ~150	10H-4, ~80	(T) C2An.1n (Matuyama/Gauss)	2.581	84.80	85.60	**85.20**	0.40	90.36	91.16	**90.76**	0.40

Bold = boundaries that are relatively well defined. B = bottom, T = top.

Table T19. Results from APCT-3 temperature profiles, Site U1425.

Core	Minimum temperature at mudline (°C)	Average temperature at mudline (°C)	Depth CSF-A (m)	In situ temperature (°C)	Thermal resistance (m^2K/W)
346-U1425B-					
4H	0.24	0.23	37.3	4.25	39.51
7H	0.22	0.43	65.8	7.34	70.21
10H	0.22	0.56	94.3	10.20	101.37
Average:	0.22	0.41			

In situ temperatures were determined using TP-Fit software by Martin Heesemann. Thermal resistance was calculated from thermal conductivity data (see **"Physical properties"**) corrected for in situ conditions (see **"Downhole measurements"** in the "Methods" chapter [Expedition 346 Scientists, 2015b]).

Table T20. Vertical offsets applied to cores in order to align a specific feature in adjacent cores, Site U1425. This table is available in an **oversized format.**

Table T21. Splice intervals, Site U1425. (Continued on next page.)

Splice segment	Hole, core, section	Depth in section (cm)	Depth CSF-A (m)	Depth CCSF-D (m)	Hole, core, section	Depth in section (cm)	Depth CSF-A (m)	Depth CCSF-D (m)	Data used to tie
	346-				346-				
1-1	U1425D-1H-1	0	0.00	0.00	U1425D-1H-3	99	3.99	3.99	
1-2	U1425B-1H-3	98	3.98	3.99	U1425B-1H-6	49	7.99	7.99	Blue
1-3	U1425D-2H-2	12	6.92	7.99	U1425D-2H-7	21	14.32	15.38	Blue
1-4	U1425B-2H-5	3	14.83	15.38	U1425B-2H-6	116	17.46	18.02	Blue
1-5	U1425D-3H-2	92	17.22	18.02	U1425D-3H-5	122	22.02	22.81	Blue
1-6	U1425B-3H-2	143	21.23	22.81	U1425B-3H-5	142	25.72	27.31	Blue
1-7	U1425D-4H-1	58	24.88	27.31	U1425D-4H-7	34	33.64	36.07	Blue
1-8	U1425B-4H-5	17	33.97	36.07	U1425B-4H-7	57	37.18	39.28	Blue
1-9	U1425D-5H-2	92	36.22	39.28	U1425D-5H-6	148	42.78	45.84	Blue
1-10	U1425B-5H-5	14	43.44	45.84	U1425B-5H-6	75	45.55	47.96	Blue
1-11	U1425D-6H-1	130	44.60	47.96	U1425D-6H-4	144	49.23	52.59	Blue
1-12	U1425B-6H-2	19	48.49	52.59	U1425B-6H-6	146	55.76	59.86	Blue
1-13	U1425D-7H-2	67	54.97	59.86	U1425D-7H-7	44	62.24	67.13	Blue
1-14	U1425B-7H-5	16	62.46	67.13	U1425B-7H-6	139	65.19	69.86	Blue
1-15	U1425D-8H-2	86	64.46	69.86	U1425D-8H-5	73	68.41	73.82	Blue
1-16	U1425B-8H-2	69	67.99	73.82	U1425B-8H-7	45	75.25	81.07	Blue
1-17	U1425D-9H-3	129	75.06	81.07	U1425D-9H-6	35	78.62	84.64	Blue
1-18	U1425B-9H-2	118	77.98	84.64	U1425B-9H-4	121	81.01	87.66	Blue
1-19	U1425D-10H-2	31	82.11	87.66	U1425D-10H-7	26	89.56	95.12	Blue
1-20	U1425B-10H-5	5	90.85	95.12	U1425B-10H-6	139	93.69	97.97	Blue
1-21	U1425D-11H-3	29	93.09	97.97	U1425D-11H-6	141	98.71	103.58	Blue
1-22	U1425B-11H-3	119	98.49	103.58	U1425B-11H-5	99	101.29	106.38	Blue
1-23	U1425D-12H-1	112	100.42	106.38	U1425D-12H-4	66	103.97	109.92	Blue
2-1	U1425D-13X-1	0	104.00	109.80	U1425D-13X-3	91	107.91	113.71	
2-2	U1425B-14H-2	79	108.29	113.71	U1425B-14H-7	3	115.06	120.48	Blue
2-3	U1425D-14H-1	56	114.26	120.48	U1425D-14H-4	8	117.90	124.12	Blue
2-4	U1425B-17H-2	35	119.65	124.12	U1425B-17H-3	88	121.68	126.15	Blue
2-5	U1425D-15H-2	87	120.77	126.15	U1425D-15H-7	32	127.72	133.10	Blue
2-6	U1425B-19H-1	11	127.31	133.10	U1425B-19H-2	34	129.04	134.83	MS
2-7	U1425D-16H-1	36	128.26	134.83	U1425D-16H-7	39	137.31	143.89	MS
2-8	U1425B-21H-2	7	138.17	143.89	U1425B-21H-6	130	145.40	151.12	Blue
2-9	U1425D-18H-4	70	144.60	151.12	U1425D-18H-6	112	148.02	154.54	Blue
2-10	U1425B-22H-2	16	147.76	154.54	U1425B-22H-5	102	153.12	159.90	Blue
2-11	U1425D-19H-3	15	152.05	159.90	U1425D-19H-6	81	157.21	165.06	Blue
2-12	U1425B-23H-2	84	157.94	165.06	U1425B-23H-7	7	164.67	171.79	Blue
2-13	U1425D-20H-4	75	163.65	171.79	U1425D-20H-6	112	167.02	175.17	Blue
2-14	U1425B-24H-2	61	167.21	175.17	U1425B-24H-4	35	169.95	177.90	Blue
2-15	U1425D-21H-2	26	169.66	177.90	U1425D-21H-6	50	175.90	184.14	Blue
2-16	U1425B-25H-2	5	176.15	184.14	U1425B-25H-7	38	183.98	191.97	Blue
2-17	U1425D-22H-4	108	182.98	191.97	U1425D-22H-6	139	186.29	195.28	Blue
2-18	U1425B-26H-2	13	185.73	195.28	U1425B-26H-2	128	186.88	196.44	Blue
2-19	U1425D-23H-1	70	187.60	196.44	U1425D-23H-6	143	195.83	204.67	Blue

Table T21 (continued).

Splice segment	Hole, core, section	Depth in section (cm)	Depth CSF-A (m)	Depth CCSF-D (m)	Hole, core, section	Depth in section (cm)	Depth CSF-A (m)	Depth CCSF-D (m)	Data used to tie
2-20	U1425B-27H-2	94	196.04	204.67	U1425B-27H-6	84	201.94	210.58	Blue
2-21	U1425D-24H-4	13	201.03	210.58	U1425D-24H-6	138	205.28	214.82	Blue
2-22	U1425B-28H-2	79	205.39	214.82	U1425B-28H-4	1	209.11	218.54	Blue
3-1	U1425B-29H-1	0	211.60	221.20	U1425B-29H-6	147	220.57	230.17	
3-2	U1425D-27H-1	38	220.28	230.17	U1425D-27H-2	109	222.49	232.38	Blue, GRA, MS
3-3	U1425B-30H-2	119	223.79	232.38	U1425B-30H-5	75	227.85	236.44	Blue
3-4	U1425D-28H-3	83	228.43	236.44	U1425D-28H-7	64	233.74	241.75	Blue
3-5	U1425B-32X -2	58	232.68	241.75	U1425B-32X-2	150	233.60	242.66	Blue
3-6	U1425D-29H-1	11	234.21	242.66	U1425D-29H-3	32	237.42	245.87	Blue
3-7	U1425B-33H-2	76	236.56	245.87	U1425B-33H-6	102	242.82	252.12	Blue
3-8	U1425D-30H-3	87	242.67	252.12	U1425D-30H-5	107	245.87	255.32	Blue
3-9	U1425B-34H-2	78	246.08	255.32	U1425B-34H-6	43	251.73	260.97	Blue
3-10	U1425D-31H-2	114	250.94	260.97	U1425D-31H-5	143	255.73	265.76	Blue
3-11	U1425B-35H-3	24	256.54	265.76	U1425B-35H-5	132	260.62	269.85	Blue
3-12	U1425D-32H-1	140	259.20	269.85	U1425D-32H-7	44	267.14	277.79	Blue
3-13	U1425B-37H-1	7	267.57	277.79	U1425B-37H-3	103	271.53	281.75	Blue
3-14	U1425D-33H-3	27	270.57	281.75	U1425D-33H-4	73	271.53	282.71	Blue, GRA, MS
3-15	U1425B-38H-1	72	272.92	282.71	U1425B-38H-3	73	275.91	285.69	Blue
3-16	U1425D-35H-1	67	274.77	285.69	U1425D-35H-4	39	278.69	289.61	Blue
3-17	U1425B-39H-2	86	279.26	289.61	U1425B-39H-4	63	281.66	292.01	Blue
4-1	U1425B-40X-1	0	281.60	291.91	U1425B-40X-3	82	285.42	295.73	
4-2	U1425D-37H-1	16	283.66	295.73	U1425D-37H-8	19	291.96	304.03	Blue
4-3	U1425B-42H-2	19	291.29	304.03	U1425B-42H-3	82	293.42	306.17	Blue
4-4	U1425D-38H-2	43	293.93	306.17	U1425D-38H-2	140	294.90	307.14	Blue
4-5	U1425B-43H-1	9	294.39	307.14	U1425B-43H-2	116	296.96	309.71	Blue, GRA, MS
4-6	U1425D-39H-1	27	296.97	309.71	U1425D-39H-3	118	300.88	313.62	Blue, GRA, MS
4-7	U1425B-44H-2	37	300.87	313.62	U1425B-44H-4	12	303.34	316.08	Blue
4-8	U1425D-40H-1	17	301.57	316.08	U1425D-40H-4	52	306.14	320.65	Blue
4-9	U1425B-46H-1	16	308.56	320.65	U1425B-46H-1	126	309.66	321.75	Blue, GRA, MS
4-10	U1425D-41H-1	132	307.42	321.75	U1425D-41H-4	51	310.82	325.15	Blue
4-11	U1425B-47H-1	5	313.15	325.15	U1425B-47H-4	46	317.56	329.55	Blue
4-12	U1425D-43H-1	32	315.82	329.55	U1425D-43H-6	91	323.91	337.64	Blue
4-13	U1425B-49H-1	143	323.93	337.64	U1425B-49H-3	66	326.16	339.88	Blue
4-14	U1425D-44H-1	67	325.67	339.88	U1425D-44H-4	2	329.23	343.44	Blue
4-15	U1425B-50H-2	11	328.81	343.44	U1425B-50H-4	23	331.63	346.25	Blue
4-16	U1425D-45H-1	115	330.85	346.25	U1425D-45H-3	98	333.68	349.08	Blue
4-17	U1425B-51H-2	15	333.55	349.08	U1425B-51H-CC	29	336.91	352.44	Blue

GRA = gamma-ray attenuation, MS = magnetic susceptibility, Blue = RGB blue datum.

Table T22. Constrained tie points for depth-age relationship, Site U1425.

Selected ties for depth-age lines	Event type	Bioevents and epoch boundaries	Depth CCSF-A(m)	Depth range (±)	Age (Ma)	Age range (±)	Sedimentation rate (m/m.y.)
Core top			*0.00*		*0.000*		
	R	LO *Lychnocanoma sakaii*	4.39	4.39	0.050	0.000	40.9
	CN	FO *Emiliania huxleyi*	8.78	2.67	0.290	0.000	
	R	LO *Spongodiscus* sp.	13.96	5.19	0.290	0.000	
	CN	LO *Pseudoemiliania lacunosa*	21.40	0.44	0.440	0.000	
	PF	LO *Neogloboquadrina kagaensis*	34.15	5.53	0.700	0.000	
	PM	Bottom of C1n (Brunhes/Matuyama)	36.54	0.73	0.781	0.000	
	PM	Top of C1r.1n (Jaramillo)	41.59	0.02	0.988	0.000	
	PM	Bottom of C1r.1n (Jaramillo)	43.69	0.12	1.072	0.000	
	PF	*Neogloboquadrina pachyderma* (S to D)	44.53	4.85	1.190	0.050	
	T	Om-SK110	47.10	0.01	1.600	0.000	
Unit IA/IB			*50.94*		*1.244*		
	R	LO *Axoprunum acquilonium*	55.00	5.63	1.450	0.250	32.6
	CN	LO *Calcidiscus macintyrei*	59.38	1.25	1.600	0.000	
	PM	Top of C2n (Olduvai)	60.49	1.40	1.778	0.000	
	PM	Bottom of C2n (Olduvai)	74.35	0.53	1.945	0.000	
	D	LO *Neodenticula koizumii*	76.16	5.26	2.000	0.000	
	R	LO *Hexacontium parviakitaensis*	76.16	5.26	2.700	0.000	
	R	FO *Cycladophora davisiana*	86.59	5.18	2.700	0.000	
	PM	Top of C2An.1n (Matuyama/Gauss)	91.42	0.66	2.581	0.000	
	D	LO *Neodenticula kamtschatica*	95.41	3.63	2.700	0.000	
Unit IB/IIA			*99.09*		*2.722*		
	PF	FO *Globorotalia praeinflata*	110.57	0.97	3.300	0.000	25.7
	D	FO *Neodenticula koizumii*	110.57	0.97	3.650	0.250	
	T	Znp-Ohta	124.09	0.01	3.900	0.000	
	PF	LO *Globorotalia ikebei*	124.63	2.33	4.300	0.000	
	PF	FO *Globorotalia ikebei*	129.51	2.56	4.750	0.050	
	R	FO *Hexacontium parviakitaensis*	129.51	2.56	4.100	0.200	
	R	LO *Dictyophimus bullatus*	134.52	2.44	4.100	0.200	
Unit IIA/IIB			*137.02*		*4.200*		
	R	FO *Dictyophimus bullatus*	147.64	4.41	4.400	0.000	41.7
	R	RI *Siphocampe arachnea* group	157.41	5.36	4.710	0.000	
	R	LO *Lipmanella redondoensis*	157.41	5.36	5.060	0.000	
	D	LO *Thalassiosira jacksonii*	167.66	4.88	4.810	0.000	
Biostrat			*182.94*		*5.300*		
	R	FO *Larcopyle pylomaticus*	187.70	4.76	5.300	0.000	25.8
	R	LO *Lychnocanoma parallelipes*	198.04	5.58	6.100	0.000	
Biostrat			*203.61*		*6.100*		
	R	RI *Lithelius barbatus*	235.20	4.34	7.000	0.000	44.7
	R	FO *Axoprunum acquilonium*	235.20	4.34	7.000	0.000	
	D	LO *Thalassiosira schraderi*	248.91	4.38	7.670	0.000	
	R	LO *Cycladophora nakasekoi*	258.66	5.38	7.400	0.000	
	R	FO *Lychnocanoma parallelipes*	258.66	5.38	7.400	0.000	
Unit IIB/IIIA			*262.53*		*7.419*		
	D	LO *Denticulopsis katayamae*	323.13	2.29	8.700	0.000	44.7
	R	LCO *Lychnocanoma magnacornuta*	332.90	2.84	9.100	0.000	
	D	LO *Denticulopsis dimorpha*	349.58	2.81	9.300	0.000	
Unit IIIA/IIIB			*356.83*		*9.528*		
	R	FO *Lychnocanoma magnacornuta* (flow-in)	393.00	2.04	10.100	0.000	64.8
	R	RD *Cyrtocapsella tetrapera* (flow-in)	405.35	0.72	12.600	0.000	
Biostrat			*393.88*		*10.100*		
	R	FO *Cycladophora nakasekoi* (flow-in at bottom)	405.93	12.05	10.100	0.000	
	R	LO *Eucyrtidium inflatum* (flow-in at bottom)	405.93	12.05	11.800	0.000	

R = radiolarian, PF = planktonic foraminifer, CN = calcareous nannofossil, D = diatom, PM = paleomagnetism, T = tephra, LCO = last common occurrence. LO = last occurrence, FO = first occurrence, RI = rapid increase, RD = rapid decrease. S to D = sinistral to dextral coiling.